UNIVERSIDADE FEDERAL DO CEARÁ
CENTRO DE CIÊNCIAS
PROGRAMA DE PÓS-GRADUAÇÃO EM QUÍMICA

DAVINO MACHADO ANDRADE NETO

RAPID SONOCHEMISTRY APPROACH PRODUCES MAGNETIC NANOPARTICLES FOR MR IMAGING AND ELECTROCHEMICAL SENSORS

FORTALEZA
2021

DAVINO MACHADO ANDRADE NETO

RAPID SONOCHEMISTRY APPROACH PRODUCES MAGNETIC NANOPARTICLES FOR MR IMAGING AND ELECTROCHEMICAL SENSORS

Tese apresentada ao Programa de Pós-Graduação em Química da Universidade Federal do Ceará, como requisito parcial à obtenção do título de Doutor em Química. Área de concentração: Química.

Orientador: Prof. Dr. Pierre Basílio Almeida Fechine.

FORTALEZA

2021

Dados Internacionais de Catalogação na Publicação
Universidade Federal do Ceará
Sistema de Bibliotecas
Gerada automaticamente pelo módulo Catalog, mediante os dados fornecidos pelo(a) autor(a)

A566r Andrade Neto, Davino Machado.
Rapid sonochemistry approach produces magnetic nanoparticles for MR imaging and electrochemical sensors / Davino Machado Andrade Neto. – 2021.
153 f. : il. color.

Tese (doutorado) – Universidade Federal do Ceará, Centro de Ciências, Programa de Pós-Graduação em Química, Fortaleza, 2021.
Orientação: Prof. Dr. Pierre Basílio Almeida Fechine..

1. Sonochemistry approach. 2. Magnetic nanoparticles. 3. Contrast Agent. 4. Electrochemical Sensors. I. Título.

CDD 540

DAVINO MACHADO ANDRADE NETO

RAPID SONOCHEMISTRY APPROACH PRODUCES INTERESTING MAGNETIC NANOPARTICLES FOR MRI AND ELECTROCHEMICAL SENSORS

Tese apresentada ao Programa de Pós-Graduação em Química da Universidade Federal do Ceará, como requisito parcial à obtenção do título de Doutor em Química. Área de concentração: Química.

Aprovada em: ___/___/_____.

BANCA EXAMINADORA

_____
Prof. Dr. Pierre Basílio Almeida Fechine
Universidade Federal do Ceará (UFC)

_____
Prof. Dr. Adriana Nunes Correia
Universidade Federal do Ceará (UFC)

_____
Prof. Dr. Claudenilson Clemente
Universidade Federal do Ceará (UFC)

_____
Prof. Dr. Juliano Casagrande Denardin
Universidade de Santiago de Chile (USACH)

_____
Prof. Dr. Ralph Santos-Oliveira
Fundação Centro Universitário Estadual da Zona Oeste (UEZO)

À minha família e a todos os meus professores.

“Em algum lugar, alguma coisa incrível está esperando para ser descoberta” *Carl Sagan*.

ACNOWLEDGMENTS

First of all, I extend my heartfelt gratitude to my advisor, Pierre Basílio, for his invaluable guidance and partnership over the years. I feel fortunate to have had the opportunity to work with him from my scientific initiation to the completion of my doctorate. Under his tutelage, I not only honed my technical research skills but also learned to be more compassionate, courteous, and patient. These qualities will stay with me for the rest of my life, particularly in my future relationships with my students.

I would also like to extend my gratitude to the members of my research group, GQMAT, where I made friends for life. GQMAT played a critical role in my success, fostering a collaborative and supportive environment through knowledge sharing, social gatherings, and mutual support. I am deeply thankful to my friends Tiago Melo, Anderson Valério, Victor Moreira, Rafael Melo, Denis Valony, Fernando Lima, Alvernes Cruz, Elayne Valério, Clinton Simplicio, and Eduardo Viana.

I would also like to express my gratitude to the Electrochemistry and Corrosion Group of UFC for their pivotal role in my success. I am especially thankful to Professor Adriana Nunes for her unwavering support, advice, and mentorship throughout my time in the group. I would also like to acknowledge the significant contributions of Camila Pinheiro, whose insightful conversations and guidance were invaluable. I was warmly welcomed into the group by all its members, making me feel as though I was part of GQMAT. I would like to extend a special thank you to Raissa Costa, Natalia Gomes, Luís Paulo, and Professors Paulo Naftali and Pedro de Lima Neto.

Making high-quality science in Brazil requires strong scientific partnerships, and I am grateful to have been blessed with a supportive network of individuals who went above and beyond in their contributions to my work. I extend my heartfelt thanks to Luelc Souza for his unwavering support in the area of microscopy, Professor Juliano Denardin for his expertise in magnetic measurements, Thiago Soares and Igor Vasconcelos for their contributions in the Mössbauer measurements, Luzia Kalyne, João Sousa, and Lyara Freitas for their invaluable experiments in cell cultures, Juan Gallo and Manuel Bañobre-López for their efforts in measuring relaxivity, Helena Becker for providing natural water samples, and Ronaldo Nascimento, Jhonyson Guedes, and Hélio Nascimento for conducting high-efficiency liquid chromatography analyses.

Balancing the demands of my doctoral work and my employment at the University of the International Integration of Lusophony Afro-Brazilian (UNILAB) and the Federal

Institute of Education, Science and Technology of Ceará (IFCE) was no small feat, but I was fortunate enough to have a team of colleagues and managers who made the journey less challenging. I am deeply grateful to Livia Paulia, Camila Peixoto, Ethanielda de Lima, and Tatyane Barros from UNILAB, as well as João Paulo Cordeiro, Roger Almeida, João Rufino, and Rafael Almeida from IFCE.

I also wish to express my sincerest gratitude to all of the teachers and mentors I have had throughout my life. Their dedication and hard work have been instrumental in shaping me into the person I am today. While I am thankful to each and every one of them, I would like to give special recognition to the professors from my undergraduate and graduate studies in chemistry at the Federal University of Ceará: Ronaldo Nascimento, Edilberto Rocha, Jair Mafezoli, Francisco Belmino, Izaura Cirino, Nágila Ricardo, and Antônio Gomes.

Finally, I would like to express my heartfelt gratitude to my family for their unwavering support throughout my academic journey. Without their help and encouragement, completing this doctoral thesis would have been a monumental challenge, if not impossible. A special thank you goes to my beloved wife, Dayany Barros, my parents, Ana Veiga Ferrer and Iraldo Machado, and my stepfather, Luciano Fernandes. They are my inspiration and the reason I wake up each day with a smile on my face. This thesis is dedicated to them, as a token of my appreciation and love.

ABSTRACT

The synthetic methodology impacts the performance of magnetic nanoparticles (MNPs) in several applications, including biological, sensing, and separation. In this respect, the most used approach to preparing these nanomaterials, thermal decomposition, has proven to be time-consuming, expensive, and laborious, which indicates the need for alternative synthetic methods. Sonochemistry has received increasing attention in nanomaterials synthesis because of its ability to increase the speed of nanomaterials' production. In this sense, this work consolidates the developed sonochemistry methodology by applying the produced MNPs as a contrast agent for magnetic resonance imaging (MRI) and an electrochemical sensor for carbendazim (CBZ). Concerning the contrast agent, it is reported the use of a commercially available amino-phosphonate compound, diethylenetriaminepenta (methylene phosphonic acid, DTPMP), to functionalize Fe_3O_4 nanoparticles (NPs). Several characterization techniques were performed to study the properties of DTPMP-functionalized MNPs. Furthermore, relaxivity and cytotoxicity analyses confirmed the MRI contrast agent potential of the DTPMP-coated Fe_3O_4 NPs, presenting a non-cytotoxicity profile and high values of transverse relaxivity (357–417 mM^{-1} s^{-1}). Regarding the electrochemical sensor, it was developed a highly efficient electrochemical sensor for CBZ using polyethylenimine-functionalized MNPs (@BPEI). Furthermore, a pathway for the electrooxidation reaction of CBZ was proposed based on electrochemical measurements and the oxidation products detected by mass spectrometry. Then, an electroanalytical methodology was developed using @BPEI. Our findings suggest that oxidation of CBZ occurs through the insertion of hydroxyl radicals and that the redox reaction involves the same number of protons and electrons. The LOD and LOQ values of the electroanalytical method are 3.87×10^{-8} to 6.40×10^{-8} and 6.17×10^{-8} to 7.34×10^{-8} mol L^{-1}, respectively, which are lower than the maximum permitted level for CBZ in Brazilian regulation. Additionally, an electroanalytical methodology was successfully developed for CBZ detection in natural waters. Therefore, we can firmly affirm that this work contributed to different research fields, but connected by materials science, from analytical chemistry to medical imaging diagnosis.

Keywords: sonochemistry approach; magnetic nanoparticles; contrast agent; electrochemical sensors.

RESUMO

A metodologia sintética impacta na performance das nanopartículas magnéticas (MNPs) em diversas aplicações, incluindo biológicas, em sensores e separação. Nessa perspectiva, algumas estratégias de síntese podem ser dispendiosas, demoradas e de difícil execução, o que leva a procura por metodologias alternativas. O método sonoquímico tem recebido atenção em síntese de nanomateriais, pois ele pode aumentar a velocidade da produção dos nanomaterias. Nesse sentido, este trabalho consolidou a abordagem sonoquímica desenvolvida em nosso grupo, aplicando as nanopartículas produzidas como agentes de contraste para imagem por ressonância magnética nuclear (RMN) e sensor eletroquímico para o pesticida carbendazim (CBZ). No que se refere ao agente de contraste, foi reportado o uso de um amino-fosfonato disponível comercialmente – dietilenotriaminopentakis(ácido metil fosfônico) (DTPMP) – para funcionalizar MNPs. Estudou-se as propriedades químicas, estruturais e magnéticas das MNPs funcionalizadas com DTPMP através de diversas técnicas de caracterização. Além disso, análises de citotoxicidade e relaxividade confirmaram o potencial das nanopartículas produzidas como agentes de contraste, uma vez que apresentaram um perfil não-citotóxico e altos valores de relaxividade (357–417 mM^{-1} s^{-1}). Em um outro estudo, desenvolveu-se um sensor para o CBZ, utilizando MNPs funcionalizadas com poli-etilenodiamina (@BPEI). Adicionalmente, foi proposto um caminho reacional para eletro-oxidação do CBZ, baseando-se em medidas eletroquímicas e detecção dos produtos de oxidação por espectrometria de massa. Estes resultados sugerem que a oxidação do CBZ ocorra através da inserção de radicais hidroxila e que a reação redox tenha o mesmo número de elétrons e prótons. Os valores de limite de detecção (LOD) e de quantificação (LOQ) para o metodologia eletroanalítica foram 38,7 a 64,0 e 61,7 a 73,4 nmol L^{-1}, respectivamente, que são menores que a concentração máxima de CBZ aceita pelas agências reguladoras brasileiras. Além disso, uma metodologia eletroanalítica para o CBZ em águas naturais foi desenvolvida com sucesso. Portanto, a metodologia sonoquímica apresentou baixo custo, ser de fácil execução e economia de tempo. Além disso, se mostrou eficaz tanto para sintetizar MNPs quanto para modificar sua superfície com diferentes agentes funcionalizantes. Como resultado, foram obtidos nanosistemas capazes de atuarem como agentes para diagnóstico médico por imagem e na construção de eletrodos modificados para identificação de pesticidas.

Palavras-chave: metodologia sonoquímica; nanopartículas magnéticas; agentes de contraste; sensores eletroquímicos.

LIST OF FIGURES

LIST OF SCHEMES

LIST OF TABLES

LIST OF ABBREVIATIONS AND ACRONYMS

@BPEI	MNPs functionalized with BPEI
@CIT	MNPs functionalized with CIT
@PAANa	MNPs functionalized with PAANa
ACN	Acetonitrile
ANVISA	Brazilian National Health Surveillance Agency
AOAC	The Association of Official Analytical Collaboration
APTES	3-Aminopropyltriethoxysilane
Au^0	Gold nanoparticles
BPEI	Branched polyethylenimine
BPEI	Branched-polyethylenimine
BR	Britton-Robinson
CBZ	Carbendazim
CIT	Trisodium citrate
CL_a	Confidence limit of the intercept
CL_b	Confidence limit of the slope
CV	Cyclic voltammetry
DFT	Density functional theory
DLS	Dynamic light scattering
DMSA	Meso-2,3-Dimercaptosuccinic acid
DMSO	Dimethyl sulfoxide
DTPMP	Diethylenetriaminepenta (methylene phosphonic acid)
DTPMP-Fe^{2+}-Fe^{3+}	Complex of DTPMP and Fe cations
EDTA	Ethylenediaminetetraacetic acid
ELR	Echo-limited regime
ESI-MS	Electrospray ionization mass spectrometry
FC	Field cooling
Fe_3O_4-H	Fe_3O_4 NPs synthesized by hydrothermal approach
Fe_3O_4-U	Fe_3O_4 NPs synthesized by sonochemistry approach
FSE	Fast spin echo
FTIR	Fourier transform infrared spectroscopy

FWHM	Full-width at half maximum
GCE	Glassy-carbon electrode
GC-MS	Gas chromatography coupled with mass spectrometry
H0.5	Sample of Fe_3O_4 NPs synthesized with 0.5 g of DTPMP by hydrothermal approach
H1.0	Sample of Fe_3O_4 NPs synthesized with 1.0 g of DTPMP by hydrothermal approach
HBSS	Hanks' balanced salt solution
HPLC	High-performance liquid chromatography
HPLC-DAD	High-pressure liquid chromatography coupled with diode array detector
ICP-OES	Inductively coupled plasma-optical emission spectroscopy
IEP	Isoelectric point
LC-MS	Liquid-Chromatography coupled with mass spectrometry
LDH	Lactate dehydrogenase
LOD	Limit of detection
LOQ	Limit of quantification
MAR	Motional average regime
MEMS	Multi-echo multi-slice
MNPs	Magnetic nanoparticles
MR	Magnetic resonance
MRI	Magnetic resonance imaging
MS	Mössbauer spectroscopy
MS	Mass spectrometry
MTT	3-(-4,5-dimethyl-2-thiazolyl)-2,5-diphenyl-2H-tetrazolium bromide
NaOL	Sodium oleate
NPs	Nanoparticles
PAA	Polyacrylic acid
PAANa	Sodium polyacrylate
PEG	Polyethylene glycol
PEG	Polyethylene glycol
PEI	Polyethylenimine

QS	Hyperfine quadrupole splitting
RSD_R	Relative standard deviation of recovery
SAR	Specific adsorption rate
SDR	Static dephasing regime
SPE	Solid-phase extraction
SWV	Square wave-voltammetry
TEM	Transmission electron microscopy
U0.5	Sample of Fe_3O_4 NPs synthesized with 0.5 g of DTPMP by sonochemistry approach
U1.0	Sample of Fe_3O_4 NPs synthesized with 1.0 g of DTPMP by sonochemistry approach
US	Ultrasound
USMNPs	Ultrasmall magnetic nanoparticles
VSM	Vibrating sample magnetometer
XPS	X-ray photoelectron spectrometer
XRD	X-ray diffraction
ZFC	Zero-field cooling

LIST OF SYMBOLS

$<T_B>$	Mean T_B
$\Delta E_{P/2}$	Half-peak width in electrochemical experiments
ΔEs	Height of the potential step
$\Delta_{m/z}$	Difference of the mass charge ratio from the theoretical value
a	Cubic cell lattice parameter
A	Amplitude of SWV pulse
B_{hf}	Magnetic hyperfine field
C–$\boldsymbol{N}$R$_2$	Amine nitrogen of BPEI
C–$\boldsymbol{O}$	Oxygen from carboxylate groups in free form
C–$\boldsymbol{O}$–Fe	Oxygen from carboxylate groups bounded to Fe atoms
C–$\boldsymbol{O}$–H	Oxygen from protonated carboxylate groups
D_{SPM}	critical size for superparamagnetism
D_{TEM}	Average particle diameter from TEM analysis
D_{XRD}	Average particle diameter from XRD analysis
$\boldsymbol{E_P}$	Peak potential
f	Frequency of SWV pulse
Fe–$\boldsymbol{N}^+$R$_3$	Nitrogen bonded to Fe of Fe_3O_4
Fe–N–$\boldsymbol{C}$	Carbon atoms bonded to amine groups bonded to Fe atoms
Fe–$\boldsymbol{O}$	Oxygen atoms of Fe_3O_4 NPs
Fe–$\boldsymbol{O}$H	Oxygen of hydroxyl groups on the surface of Fe_3O_4 NPs
f_{MAX}	Critical frequency
H	Magnetic field
H_C	Coercivity
H_{EXT}	Applied magnetic field
$\boldsymbol{I_P}$	Peak current
K	Anisotropy constant
k_B	Boltzmann constant
k_S	Standard rate constant of electron transfer
M	Magnetic moment
m/z	Mass charge ratio
M_{FC}	Magnetic moment in *FC* experiment

M_R	Remnant magnetization
M_S	Saturation magnetization
M_{ZFC}	Magnetic moment in *ZFC* experiment
$–\boldsymbol{N}^{+}R_3$	Nitrogen in protonated amine groups
$N–\boldsymbol{C}$	Carbon atoms bonded to free amine groups
PDI_{DLS}	Polydispersity index for DLS experiment
PDI_{TEM}	Polydispersity index for TEM analysis
$R\%$	Recovery of a certain analyte
r_1	Longitudinal relaxivity
r_2	Transverse relaxivity
T	Temperature
T_1	Longitudinal relaxation time
T_2	Transverse relaxation time
T_B	Blocking temperature
T_{MAX}	Maximum temperature in ZFC experiment
V	Volume of the particle
Y_{BL}	Blank signal
Y_{LOD}	Instrumental signal
δ	Average isomeric shift
ζ	Zeta Potential
κ_{MAX}	Critical kinetic parameter
$\boldsymbol{\nu}$	Scan rate in CV experiment
τ	Relaxation time
τ_0	Attempt frequency
τ_{EXP}	Time scale of the magnetic measurement
χ	Magnetic susceptibility

TABLE OF CONTENTS

1 CHAPTER I – SCIENTIFIC BACKGROUND

1.1 Introduction

Magnetic nanoparticles (MNPs) have introduced new possibilities for diagnosing and treating cancer diseases, mainly when applied in drug and gene delivery, magnetic hyperthermia, and magnetic resonance imaging (MRI) as contrast agent (KANDASAMY; MAITY, 2015). Furthermore, MNPs have proved to be a promising material for analytical sensing applications (URBANOVA *et al.*, 2014). The success of the MNPs in all mentioned applications is due to their biocompatibility, high-surface-area, easy surface functionalization, and excellent magnetic properties, which includes high saturation magnetization (M_S), manipulation of the MNPs with an external magnetic field, and the superparamagnetism behavior (URBANOVA *et al.*, 2014).

The performance of the MNPs in any application is mainly affected by their size, crystallinity, and functionalization nature (LEE *et al.*, 2015). The size mainly dictates the magnetic behavior of the MNPs: superparamagnetism is accomplished when the size is smaller than a critical size. Additionally, the size and crystallinity impact M_S, which is a vital parameter for MRI contrast agent, magnetic hyperthermia, and separation science (LEE *et al.*, 2015). At the same time, the nature of the surface functionalization modulates the biocompatibility, hydrophilicity, interparticle magnetic interactions, and colloidal stability of the MNPs (HOLA *et al.*, 2015).

Size, crystallinity, and functionalization nature are strongly related to the synthetic, functionalization methodologies and the selected functionalizing agent. Moreover, implementing these MNPs in practical applications requires developing a simplified, fast and reproducible to prepare MNPs with designed physicochemical properties (STEPHEN *et al.*, 2016). The most common approach to synthesize MNPs with high crystallinity and narrow size distribution is thermal decomposition (PENG; WANG; XUE, 2015). However, the process is laborious and time-consuming and only produces hydrophobic coated MNPs, requiring additional steps to perform a ligand exchange procedure. Therefore, a methodology is desirable to directly produce hydrophilic MNPs in a simple and faster manner while simultaneously generating MNPs with excellent physical and chemical properties (STEPHEN *et al.*, 2016).

Sonochemistry has received increasing attention in materials science synthesis because of its ability to achieve unique hot spots with temperatures greater than 5000 K and pressures as high as 1000 atm (XU, Hangxun; ZEIGER; SUSLICK, 2013). These conditions

allow the synthesis of featured functionalized MNPs quickly, making sonochemistry a viable candidate to replace thermal decomposition and help a more straightforward implementation of the practical applications of MNPs.

Therefore, this chapter describes the essential aspects of the sonochemistry and application in nanomaterial synthesis, the structure and magnetic properties of the iron oxides, and the synthesis and functionalization of the MNPs. With this chapter, we aimed to provide to the reader the scientific background concerning the field of research to make the reading of chapters 2 and 3 pleasant.

1.2 Sonochemistry, cavitation and their relation to preparation of nanomaterials

Sound waves are important physical entities for communication among humans and animals. Its behavior can be described as sine waves when it passes through a particular media. These waves impose negative (rarefaction) and positive (compression) pressure on a particular media. Properties of the sound wave are specially related to its frequency and propagation media.

Sonochemistry uses sound waves of frequency greater than 20 kHz, which are beyond the human hearing range, which explains the term "ultrasound" (ASHOKKUMAR, 2018). In recent times, ultrasound has been an essential tool in many fields of science, such as medical diagnosis, food and dairy processing, and water treatment. Another application of ultrasound is in the synthesis of chemicals, in which the powerful ultrasound induces chemical reactions or even participates in some chemical process (LI, Zhanfeng *et al.*, 2021). Therefore, this unique research area is defined as "sonochemistry" (CRUM, 1984).

The energy provided by sonochemistry to chemical reactions comes from acoustic cavitation, which means that ultrasound creates a cavity in a liquid medium. This cavity comes from dissolved gases in liquids that form small gas pockets, which act as bubble nuclei (ASHOKKUMAR, 2018; LI, Zhanfeng *et al.*, 2021). When these bubble nuclei experience negative pressure of the sound waves, gas molecules are forced to diffuse in the bubble, increasing the size of the bubble, while the positive pressure forces gas molecules to diffuse in an opposite flow, decreasing the size of the bubble, as illustrated in Figure 1A. Once the acoustic cavitation occurs by a "Rectified Diffusion" process, more gas molecules diffuse in than out, which leads to an overall increase of the bubble (CRUM, 1984). More information can be found in (CRUM, 1984) . Therefore, these bubbles grow up to a critical size range (typically tens of micrometers) under ultrasonic radiation, where they efficiently absorb ultrasonic energy. This

event leads to the overgrowth of the bubble and, subsequently, catastrophic collapse, which rapidly and adiabatically releases (~3.5 μs) energy sufficiently to increase temperature and pressure up to 1000-5000 K and 100 atm (ASHOKKUMAR, 2018; LI, Zhanfeng *et al.*, 2021). Consequently, these high localized temperatures, called "hot spots", are responsible for initiating various reactions and other physical effects. Due to the facts described above, sonochemistry is one of the forms of energy that can release substantial amounts of energy in less time (Figure 1B) (BANG; SUSLICK, 2010).

Figure 1 – (A) Schematic illustration of the hotspot formation from acoustic cavitation under sonochemistry conditions. (B) Amount of energy and pressure provided by different types of energy per second.

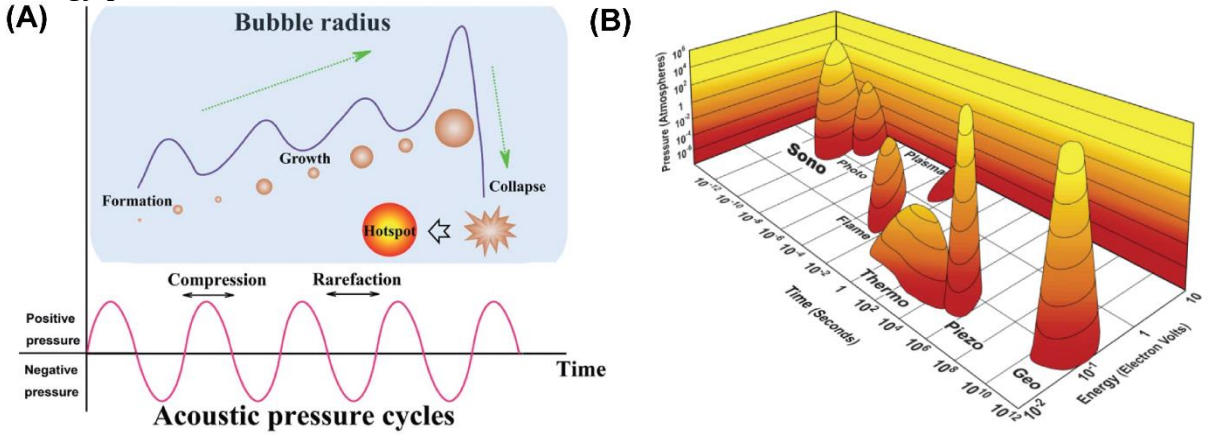

Source: (A) Reproduced from Ref. (LI, Zhanfeng *et al.*, 2021) with permission from the Royal Society of Chemistry and (B) (BANG; SUSLICK, 2010).

The high energy release from acoustic cavitation is a fascinating tool for synthesizing organic and inorganic materials. Its use can be divided into two categories:

a) Chemical reactions are initiated by high energy released from acoustic cavitation. When chemical reactions are performed in an aqueous medium, water molecules evaporate into the cavitation bubble, receiving high energy and breaking the covalent bonds, generating radicals, as presented in equation 1.1:

$$H_2O \rightarrow OH^{\bullet} + H^{\bullet} \qquad (1.1)$$

Thus, $OH^{\bullet}$ and $H^{\bullet}$ can act as an oxidizing and reducing agent for a variety of chemical reactions. For instance, gold nanoparticles (Au^0) can be synthesized by

sonochemistry in argon-saturated aqueous solution, according to the equation 1.2 (NAGATA *et al.*, 1996):

$$AuCl_4^- + 3\,H^\bullet \rightarrow Au^0 + 3\,H^+ + 4\,Cl^- \quad (1.2)$$

b) Acoustic cavitation also induces a series of physical effects that produce or facilitate chemical reactions and change the features of the nanoparticles. These effects are simple heating, shock waves, and microjets. The microjets come from the liquid that rushes to fill the collapsing bubble, which provokes shear forces on the molecules near the collapsing (MCKENZIE *et al.*, 2019). Which concerns shock waves, they propagate in an omnidirectional, causing a compression of the surrounding liquid due to the acoustic cavitation (LI, Zhanfeng *et al.*, 2021). These processes increase mass transport and interparticle collisions, inducing a narrow size distribution and more straightforward surface functionalization of the nanomaterials (LI, Zhanfeng *et al.*, 2021). Recently, MORTON *et al.* (2021) evidenced that the sono-exfoliation of graphite occurs through shock waves with a pressure magnitude up to 5 MPa and liquid-jets of 80 m s^{-1}.

Regarding the preparation of magnetic nanoparticles, we hypothesize that these physical events were responsible for the faster preparation and outstanding properties of the functionalized magnetic nanoparticles used in this Thesis.

1.3 Structure and magnetic properties

1.3.1 Structure

Magnetic spinel ferrites are a large group of materials with the same structure as the natural spinel ($Mg_2Al_2O_4$) (HARRIS, Vincent G., 2012). The most important and abundant material of this group is magnetite (Fe_3O_4). The general formula of the group is $M^{2+}Fe_2O_4$, where the divalent cation may be Mn^{2+}, Ni^{2+}, Fe^{2+}, Co^{2+}, Zn^{2+}, and Mg^{2+}. In this structure, the metallic cations are coordinated to oxygen in two forms, generating octahedral (A-site) and tetrahedral (B-site) sites. The spinel space group is *Fd3m*, and the unit cell contains eight units of AB_2O_4 with 16 cations in A-sites and 8 in B-sites, as shown in Figure 2 (SICKAFUS; WILLS; GRIMES, 1999). Three types of spinel ferrites exist, and they are classified

accordingly to the site of the divalent cation; a more detailed explanation can be found in (GALVÃO, *et al.*, 2015). Magnetite is an *inverse spinel*, in which all Fe^{2+} cations are in A-sites, while Fe^{3+} cations are distributed equally between A- and B-sites.

Figure 2 – Representative structure of Fe_3O_4.

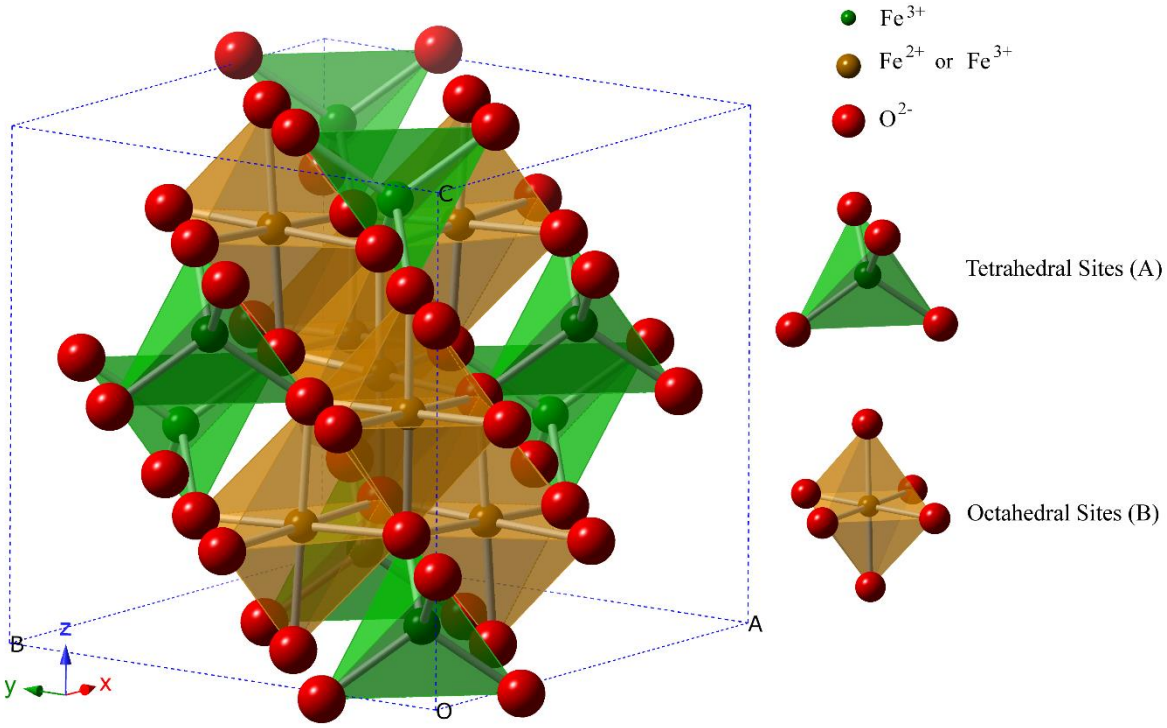

Source: Author.

The other two principal iron oxides are hematite (α-Fe_2O_3) and maghemite (γ-Fe_2O_3). The first is the most stable and is widely used in catalysis, pigments, and gas sensors primarily due to its low cost and high resistance to corrosion (WU, Wei; JIANG; ROY, 2016). However, α-Fe_2O_3 has weak ferromagnetism at room temperature, with a saturation magnetization often smaller than 1 emu g^{-1} (WU, Wei; JIANG; ROY, 2016). On the other hand, γ-Fe_2O_3 and Fe_3O_4 exhibit ferrimagnetism at room temperature, with their bulk saturation magnetizations are 76 and 92 emu g^{-1}, respectively (CAO *et al.*, 2016; KOLEN'KO *et al.*, 2014). Therefore, concerning the new applications of magnetic iron oxide nanoparticles that require strong interaction with magnetic fields, γ-Fe_2O_3 and Fe_3O_4 are often used.

In fact, γ-Fe_2O_3 and Fe_3O_4 have a similar crystal structure, as shown in Figure 3. Each unit cell of maghemite is formed by 32 O^{2-} ions, $21\frac{1}{3}$ Fe^{3+} ions and $2\frac{1}{3}$ vacancies, in which 8 cations occupy tetrahedral sites B-sites, and the remaining cations are in A-sites, along with the vacancies (WU, Wei; JIANG; ROY, 2016). Thus, when Fe^{2+} cations of Fe_3O_4 oxidizes, γ-

Fe_2O_3 is formed. There is no literature agreement for the model that describes the magnetic nanoparticles when Fe_3O_4 is partially oxidized. To the best of our knowledge, there are four models: core-shell like structure, such as Fe_3O_4@γ-Fe_2O_3 (FRISON *et al.*, 2013); Individual particles, which suppose that when the oxidation starts, it occurs throughout the entire volume of the particle (DA COSTA *et al.*, 2014); an oxidation gradient from the surface to the center of the nanoparticles (SANTOYO SALAZAR *et al.*, 2011); γ-Fe_2O_3-Fe_3O_4 solid solution with a possible enrichment of Fe^{3+} at the surface (KOLEN'KO *et al.*, 2014). Indeed, the two latter models are similar. In our opinion, the solid solution model has more consistent experimental evidence. Magnetization measurements as a function of the temperature in functionalized magnetic nanoparticles indicated that Fe^{3+} species are in excess both in the core and surface of the nanoparticle (KOLEN'KO *et al.*, 2014). Additionally, the authors evidenced that conversion of γ-Fe_2O_3 to Fe_3O_4 is limited by the temperature rather than heating time (KOLEN'KO *et al.*, 2014).

Figure 3 – The XRD peak lines from γ-Fe_2O_3 (purple), Fe_3O_4 (blue), and α-Fe_2O_3 (red).

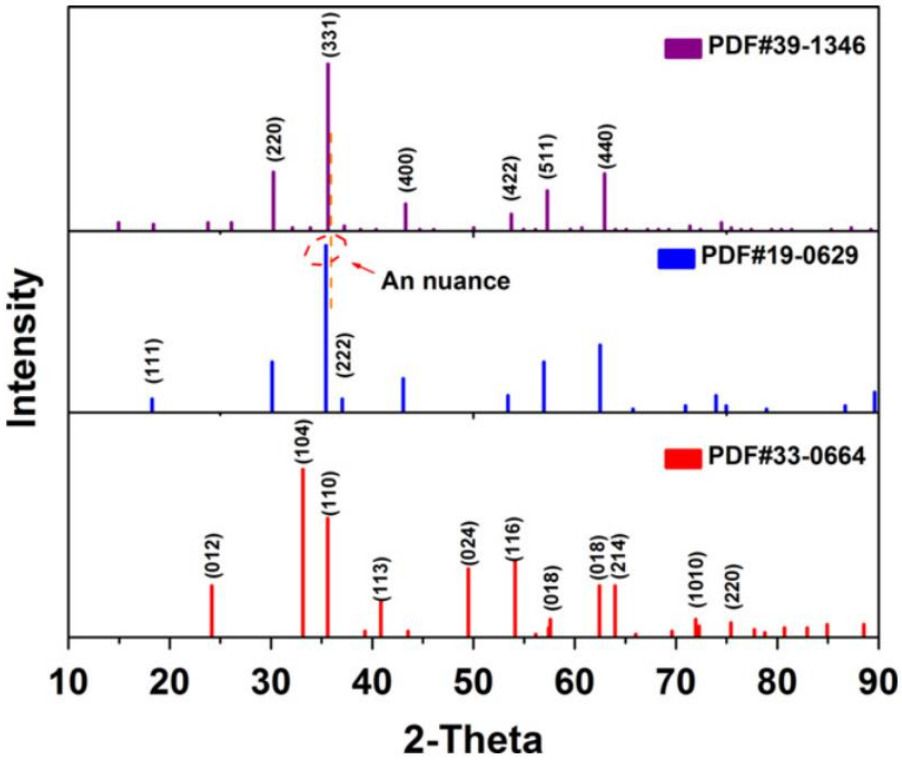

Source: (WU, Wei *et al.*, 2015)

1.3.2 Superparamagnetism

The net magnetic behavior of a particular material comes from the movement of its unpaired electrons. For this reason, most iron-containing materials interact with magnetic fields. Regarding magnetic materials, there are two main types: ferromagnetic and ferrimagnetic. Ferro- and ferrimagnetic materials exhibit a net magnetization; however, in ferromagnetic materials, all spin moments are aligned to each other. Unlike, ferrimagnetic materials have spin moments aligned anti-parallel; however, the spins are not entirely canceled. An illustration of their spin alignment is shown in Figure 4 A–B (GALVÃO, *et al.*, 2015). Magnetite can be classified as ferrimagnetic material once the electronic spin of A- and B-sites are anti-parallel to each other. The spin of 8 Fe^{3+} cations of A-site is canceled with the spin of 8 Fe^{2+} in B-site. Thus, the net magnetic moment derives from Fe^{2+} in A-sites (KOZLENKO *et al.*, 2019).

Figure 4 – Illustration of the magnetic behavior of (A) ferromagnetic and (B) ferrimagnetic materials.

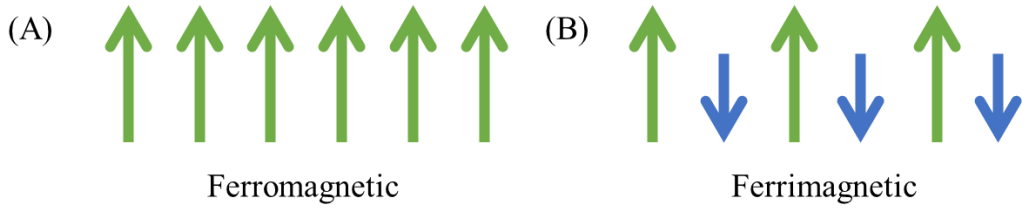

Source: author

To demagnetize a bulk ferro- or ferrimagnetic material at constant room temperature, it must apply a magnetic field in the opposite direction with a field greater than the one to magnetize. The intensity of the field to demagnetize the material is known as coercivity (H_C) (SPALDIN, 2010). Materials with high H_C values are widely applied in storage media devices once they have a "memory", which is the remnant magnetization (M_R) (GALVÃO, *et al.*, 2015). Additionally, a bulk magnetic material has a magnetic moment (M), even in the absence of an applied magnetic field (H), due to anisotropy energy, which holds M along the easy direction (SPALDIN, 2010). Anisotropy energy is given by the product of the anisotropy constant (K) and the volume of the particle (V).

When a ferro- or ferrimagnetic material has zero H_C and M_R, it exhibits the superparamagnetism behavior, which happens when thermal energy ($k_B\ T$) overcomes anisotropy energy, causing a spontaneous vanishing of M, once the magnetization is no longer

fixed in one direction, but fluctuates randomly. In thermal energy, k_B and T are Boltzmann constant and temperature, respectively (LONG *et al.*, 2016). This behavior is similar to the one observed in paramagnetic species, however, with a much higher M and magnetic susceptibility (χ).

At room temperature, superparamagnetism is only observed when the particle reaches nanometric dimensions since anisotropy energy is decreased when the particle volume decreases. Therefore, it is possible to define the critical size for superparamagnetism (D_{SPM}); if the particle reaches a size below D_{SPM}, it exhibits superparamagnetic behavior at a specific temperature. Additionally, there is a temperature that, with a particle of a specific size, thermal energy will surpass anisotropy, which is called blocking temperature (T_B). For instance, if a magnetic nanoparticle is designed for biological applications, it must exhibit superparamagnetic behavior at 37 ºC; this nanoparticle must have a size that induces a T_B below 37 ºC.

To calculate these parameters, we must consider the rate at which thermal equilibrium is reached. For example, after a M is induced in a nanoparticle, the time to reach the equilibrium (M = 0) is called relaxation time (τ) and can be calculated by equation 1.3 (GUIMARAES, 2009):

$$\tau = \tau_0 e^{\frac{KV}{k_B T}} \tag{1.3}$$

Where τ_0 is the attempt frequency usually in the range of 10^{-12} to 10^{-9} *s*. Equation 1.3 demonstrates that the observed magnetic behavior depends on the timescale of the measurement (τ_{EXP}). If $\tau < \tau_{EXP}$, superparamagnetism is observed, while if $\tau > \tau_{EXP}$ nanoparticles will be in a blocked regime (ferro- or ferrimagnetism). For the direct measurement of M, τ_{EXP}= 100 *s*, unlike Mössbauer spectroscopy or nuclear magnetic resonance that τ_{EXP}= 10^{-9} to 10^{-7} *s* (GUIMARAES, 2009). Considering $\tau = \tau_{EXP}$ = 100 *s* and $\tau_0 = 10^{-9}$ *s*, it is possible to arrange equation 1.3 to obtain equation 1.4 (GUIMARAES, 2009):

$$V_{SPM} \approx \frac{25 k_B T}{K} \tag{1.4}$$

Consequently, it is possible to obtain an expression of D_{SPM} for a spherical particle (equation 1.5) (GUIMARAES, 2009):

$$D_{SPM} \approx \left(\frac{6}{\pi} V_{SPM}\right)^{1/3} \quad (1.5)$$

The D_{SPM} for magnetite, at room temperature, was estimated to be in the range of 30 nm (DUNLOP, 1973), while the value estimated by equations 1.4 and 1.5 is 24 nm. Similarly, T_B can be estimated by the equation 1.6:

$$T_B \approx \frac{KV}{25k_B} \quad (1.6)$$

Considering a spherical Fe_3O_4 nanoparticle of 20 nm diameter and anisotropy constant of 15 kJ m^{-3} (MAMIYA *et al.*, 2020), T_B can be estimated in 182 K, using equation 1.6. Furthermore, SHIM *et al.* (2008) validated experimentally the size dependency of T_B for oleic acid-coated nickel oxide (NiO) nanoparticles, as shown in Figure 5 – red circles. The plot indicates that the higher the size of the particles, the greater T_B.

In the scope of magnetic nanoparticles characterizations, the measurement of T_B is an important step, which can be accomplished by zero-field cooling (*ZFC*) and field cooling (*FC*) procedures. First, the magnetic sample is cooled to a few Kelvin during the ZFC measurement under no external applied magnetic field (H_{EXT}). Then, the magnetic moment (M_{ZFC}) is recorded as the temperature is raised to room temperature under a small H_{EXT}. Afterward, the sample is cooled again while being exposed to $H_{EXT,}$ and again the magnetic moment is recorded (M_{FC}). Therefore, in the two curves, *M* is recorded as a dependence of *T*, as shown in Figure 6.

For *ZFC*, on cooling a non-magnetized magnetic nanoparticle below T_B, *M* of the nanoparticle are oriented along the easy magnetization axes and blocked in random directions (GUBIN *et al.*, 2005; JOY; KUMAR; DATE, 1998), which means that the thermal energy is not enough to surpass the anisotropy barrier (Figure 6 – point *a*). As *T* increases, M_{ZFC} increases once thermal energy is higher enough to unlock *M* of the particles from easy axes of magnetization. At this stage, the M_{ZFC} direction starts to be aligned to H_{EXT} (MANDEL *et al.*, 2013). When $T=T_B$, *M* of the magnetic nanoparticles are entirely blocked and oriented as H_{EXT} (MANDEL *et al.*, 2013) (Figure 6 – T_B point). At $T > T_B$, a superparamagnetic state is achieved, the small H_{EXT} is not high enough to magnetize, and M_{ZFC} decreases with increasing of *T* (MANDEL *et al.*, 2013) due to the fluctuation of *M* (Figure 6 – point *b*). When the *FC* curve is recorded, M_{FC} initially increases with decreasing of *T* once thermal energy is decreasing, which leads to the gradually blocking of spin in the H_{EXT} direction. When $T < T_B$, magnetic

nanoparticles are entirely blocked in the H_{EXT} direction, and M_{FC} is approximately constant (GUBIN *et al.*, 2005) (Figure 6 – point *c*). Although, in highly anisotropic systems, M_{FC} increases with decreasing of *T* (JOY; KUMAR; DATE, 1998).

How is it possible to extract T_B from these data? There is no standard procedure, but the three main possibilities are: *i*) T_B extracted from maximum *ZFC* magnetization temperature (T_{MAX}); *ii*) T_B as the temperature for inflection point of *ZFC* curve; *iii*) *T* derivative of the difference between *ZFC* and *FC* curves, to obtain a T_B distribution (BRUVERA *et al.*, 2015). The third method is adequate to evaluate real samples once they always present a size dispersion that implies anisotropy barrier distribution and T_B distribution. A log-normal distribution describes the size dispersion of nanoparticle systems, thus T_B as well. Therefore, briefly, the procedure is fit log-normal distributions in $\frac{d(ZFC-FC)}{dT}$ *vs.* *T* data, and extract the mean T_B ($<T_B>$) (BRUVERA *et al.*, 2015). In this Thesis, this procedure was used to calculate $<T_B>$ for the samples prepared herein.

Figure 1.5 – Plot of T_B against the volume of oleic acid-coated NiO NPs (red circles). Blue triangle and pink star are the values extracted from (32) and (33), respectively. A solid line is drawn using the variation of *K* with *V* of the nanoparticle. The inset shows an expanded view for small *V*.

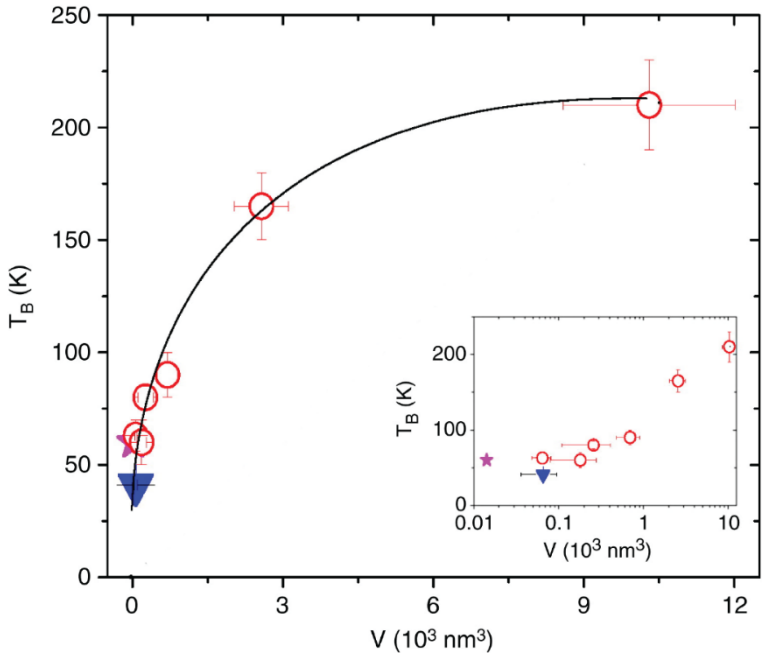

Source: adapted from (SHIM *et al.*, 2008).

Figure 6 – Illustrative example of *ZFC-FC* curve for magnetic nanoparticles such as Fe_3O_4.

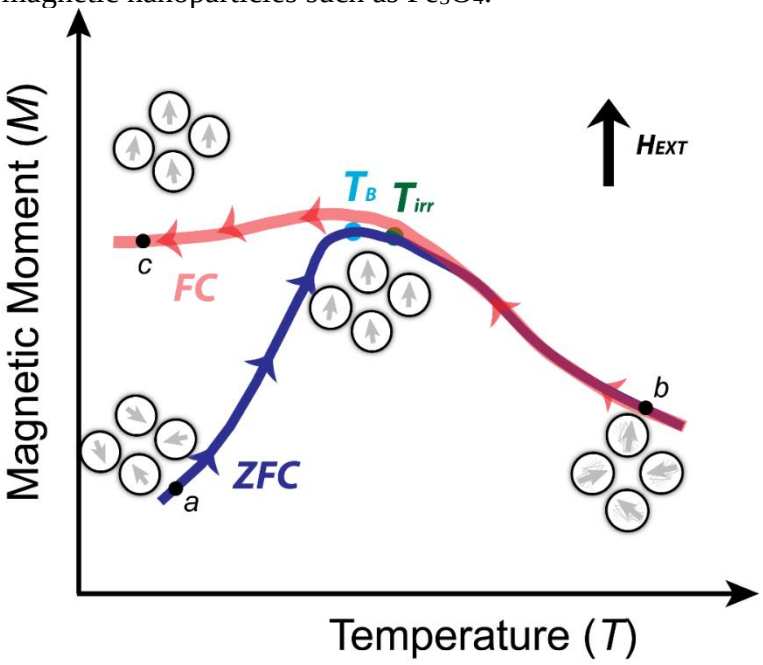

Source: author.

1.4 Synthesis and functionalization

1.4.1 Functionalization

When the size of the particles reaches nano dimensions, the fraction of atoms at the surface is remarkably increased, which makes the surface features have an essential role in the properties of the nanoparticles. Therefore, additional features can be incorporated into the nanomaterial by surface functionalization. Among many possible additional features, some examples are colloidal stabilization in aqueous or organic solvents, specific interaction to biological molecules, biocompatibility, catalytic properties, responsive properties to physical chemical stimuli (HOLA *et al.*, 2015). Thus, functionalization is the anchorage of chemical species on the nanoparticles' surface through physical or chemical interactions to give an additional feature to the nanomaterial.

Regarding the biomedical and biotechnological applications of magnetic nanoparticles, the surface of Fe_3O_4 or γ-Fe_2O_3 must be functionalized to prevent degradation in an unfriendly environment; avoid aggregation of the nanoparticles and provide functional groups for attachment of bioactive compounds (HOLA *et al.*, 2015). These aspects can be accomplished only by a hydrophilic surface once these applications require interactions in

aqueous mediums. In other words, functionalization must lead to a compatibilization to water, which means that it will provide means to maintain the nanoparticles finely dispersed in aqueous mediums (BOHARA; THORAT; PAWAR, 2016).

Two mechanisms can avoid aggregation of nanoparticles: *i)* steric repulsion – due to the increase of the repulsive osmotic forces by the biding of large molecules on the surface, such as polymers or surfactants (POLTE, 2015); *ii)* electrostatic repulsion – Coulomb repulsion forces arise from electrical double layer due to the presence of charged chemical groups, such as carboxylic acid/carboxylate, amine and phosphate groups (POLTE, 2015).

Three pathways accomplish hydrophilic functionalization of MNPs: ligand exchange (Figure 7A), encapsulation (Figure 7B), and direct or *in-situ* functionalization (Figure 7 C) (BOHARA; THORAT; PAWAR, 2016). Ligand exchange is used when the synthetic methodology of the MNPs originates hydrophobic-coated nanoparticles, which is the case for thermal decomposition. Then, more strongly binding hydrophilic ligands replace the hydrophobic, resulting in a phase transfer from organic to aqueous solution (Figure 7A) (BOHARA; THORAT; PAWAR, 2016). Encapsulation is also performed on a hydrophobic surface by adding an amphiphilic molecule, as shown in Figure 7B. This process occurs by the intercalation of the hydrophobic part of the added molecule with the initial ligand on the surface of the MNPs, which leaves the hydrophilic groups on the outer part of the surface. Direct or *in-situ* functionalization occurs mainly in two situations: *i*) magnetic nanoparticles are synthesized without any ligand, and the hydrophilic agent is directly coupled to the surface; *ii*) when magnetic nanoparticles are being formed, usually in the growth step, functionalizing agent is bound to the surface (BOHARA; THORAT; PAWAR, 2016). The second situation is preferable since the hydrophilic nanoparticle is prepared in a single step, and the quality of the functionalization is higher once ligands are added during the growth step to avoid further aggregation (BOHARA; THORAT; PAWAR, 2016). In this sense, the most used procedures are ligand exchange, once the thermal decomposition is one the most used methodology for MNPs, and direct or *in-situ* functionalization, due to convenience. Thus it is discussed in this chapter possible functionalizing agents and experimental procedures only for these pathways.

To prepare hydrophilic MNPs, the functionalizing agent molecule must have a chemical group that strongly binds to the surface and provides electrostatic and/or steric repulsions. Typically, ethoxysilane (BEZERRA *et al.*, 2017), amine (NETO *et al.*, 2017), carboxylic/carboxylate (NETO *et al.*, 2017), catechol (ZENG *et al.*, 2014), and phosphonate groups (MONTEIL *et al.*, 2014) coordinate to the iron atoms of the MNP's surface, as shown in Figure 8A. In addition, the functionalizing agent should also have a three-dimensional

structure that projects out chemical groups that provide electrostatic and/or steric repulsions. These groups dictate part of nanomaterial's chemical features, such as colloidal stability, surface charge, hydrodynamic size. They are usually carboxylic acid/carboxylate (NETO *et al.*, 2017), phosphonate (MONTEIL *et al.*, 2014), amine (BEZERRA *et al.*, 2017), hydroxyl (WANG, Yi-Xiang J, 2011), and polyethyleneglycol (PENG *et al.*, 2013) groups (Figure 8B). Figure 8C exhibits the main functionalizing agents used to coat MNPs.

Figure 7 – Main examples of the synthetic pathway to produce functionalized magnetic nanoparticles.

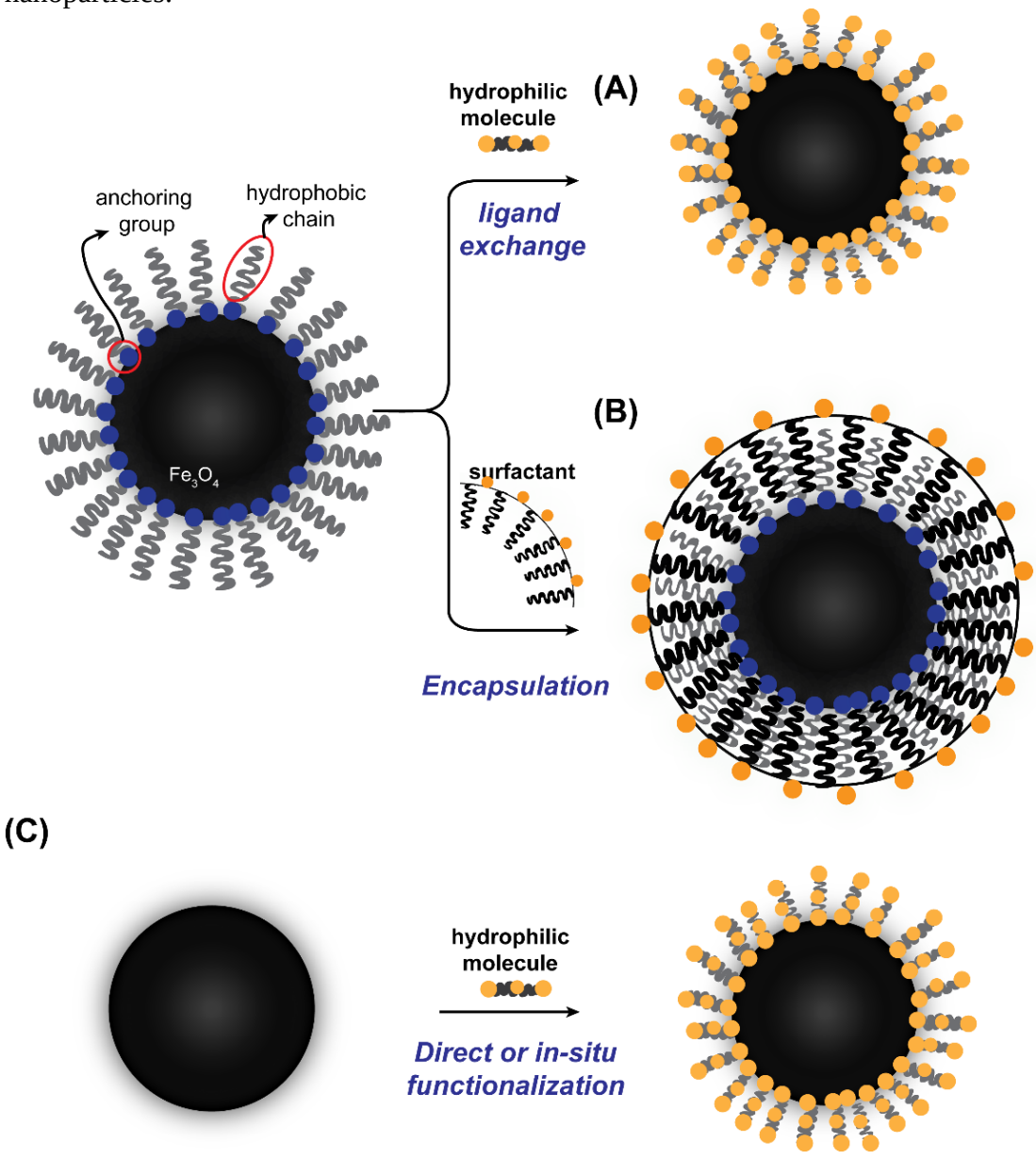

Source: author.

Figure 8 – Schematic representation of the leading chemical groups that (A) bind to the surface and (B) provide electrostatic and/or steric repulsions. (C) Most used functionalizing agents for MNPs. Abbreviation and references: APTES – 3-Aminopropyltriethoxysilane (GALVÃO *et al.*, 2018); BPEI – branched polyethylenimine (XIA *et al.*, 2014); Chitosan (SZPAK *et al.*, 2014); Citric acid (NIGAM; BARICK; BAHADUR, 2011); PAA – polyacrylic acid (KOLEN'KO *et al.*, 2014); CMC – carboxymethylcellulose (SITTHICHAI *et al.*, 2015); PEG with terminal carboxyl (NOSRATI *et al.*, 2019); DMSA – meso-2,3-Dimercaptosuccinic acid (SONG *et al.*, 2012); Dopamine (GAO, Fan *et al.*, 2014); Alendronic acid (OLEKSA *et al.*, 2021).

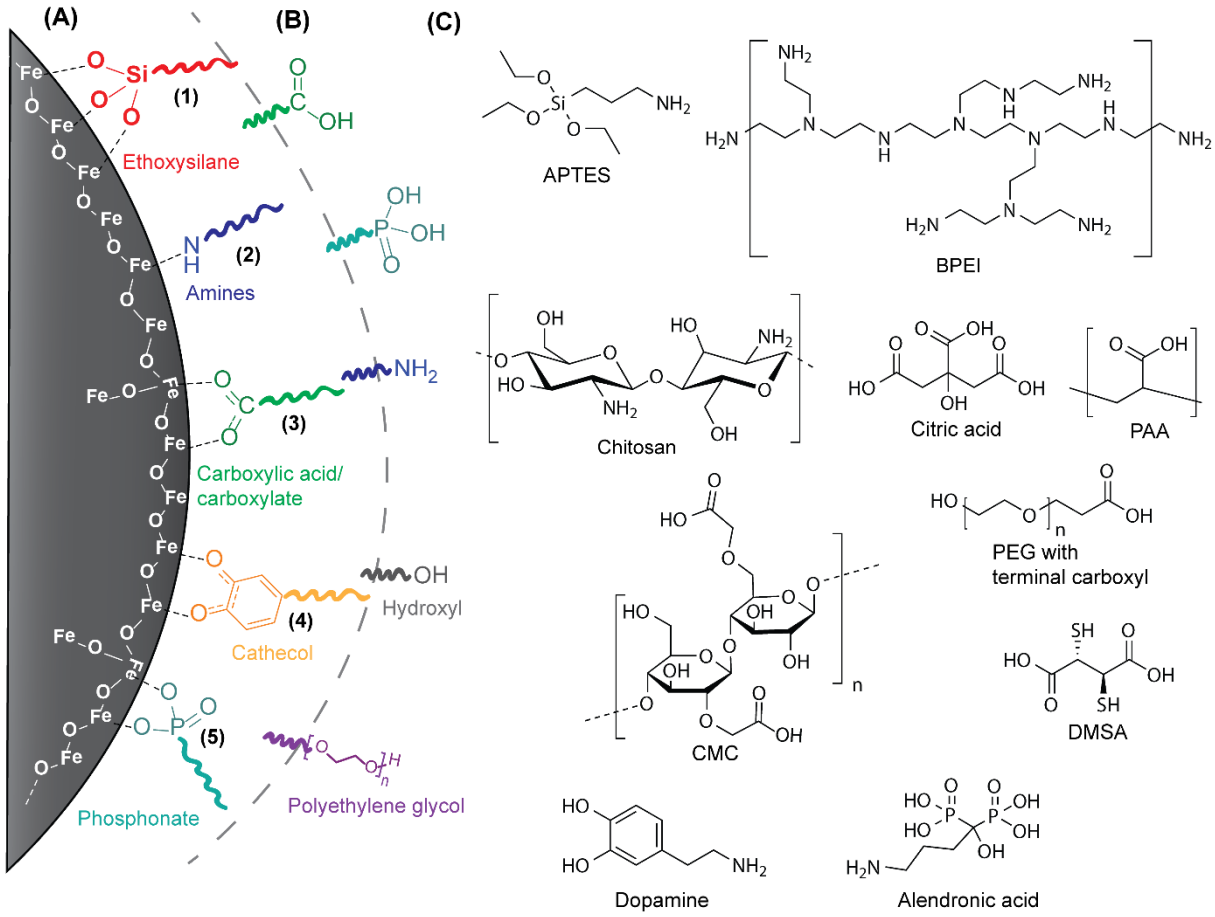

Source: author.

1.4.2 Methods to prepare MNPs

1.4.2.1 Co-precipitation

The co-precipitation method is the simplest, easiest, and most used method to prepare MNPs with average diameters below 50 nm (REDDY *et al.*, 2012). This process consists of a mixture of metallic salts aqueous solutions and a precipitant agent, a base such as NaOH or NH_4OH. Co-precipitation involves condensation reactions where the species in solution bond together through oxygenated bridges. Recently, LAGROW *et al.* (2019) revealed the reaction pathway for Fe_3O_4/γ-Fe_2O_3 under co-precipitation conditions. Authors evidenced,

though *in situ* synchrotron X-Ray diffraction, and under pH = 12 and sodium carbonate as precipitating agent, that two initial phases were formed, poorly crystalline ferrihydrite from Fe^{3+} ions and iron hydroxide carbonate from Fe^{2+}. The ferrihydrite phase acts as the seeds that grow into the Fe_3O_4/γ-Fe_2O_3, whereas iron carbonate acts as feedstock to supply Fe^{2+} ions for the nanoparticle's phase change and growing. The schematic growth mechanism is showing in Figure 9.

Figure 9 – Schematic of growth mechanism for Fe_3O_4/γ-Fe_2O_3.

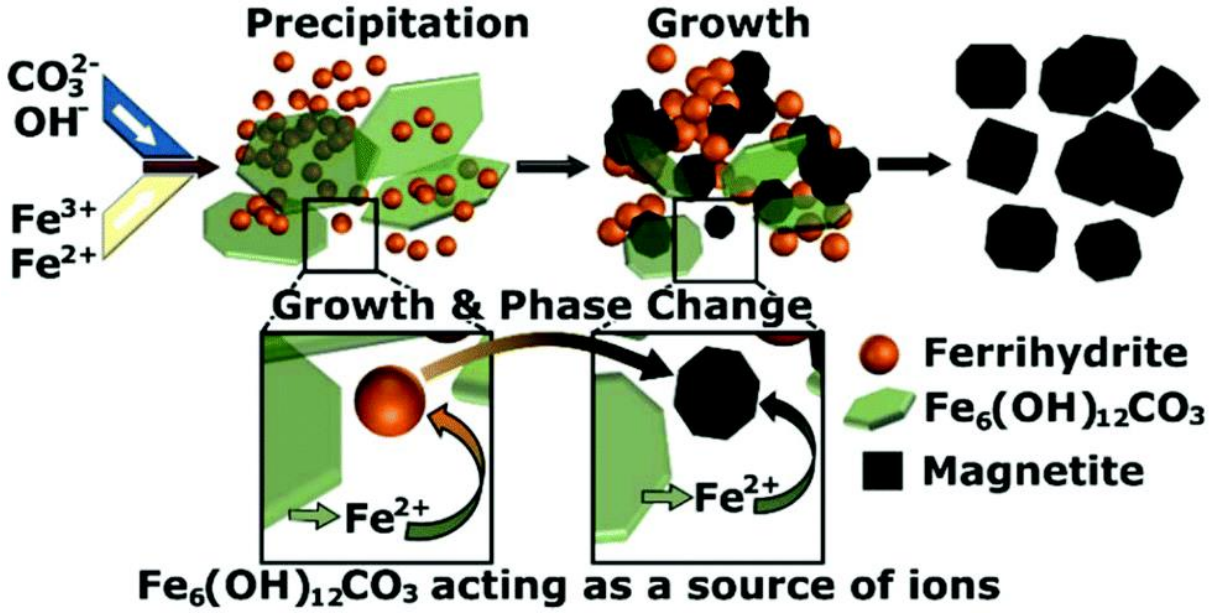

Source: Reproduced from Ref. (LAGROW *et al.*, 2019) with permission from the Royal Society of Chemistry.

The size, shape, and composition of the MNPs depend on the experimental parameters, including the types of iron salts (chlorides, perchlorates, sulfates, nitrates), concentrations of these salts, Fe(II)/Fe(III) ratio, final pH value, and ionic strength of the medium (WU, Wei *et al.*, 2015). For instance, Yazdani and co-authors concluded that increasing the size of the anion of iron precursor led to a decrease of the Fe_3O_4 NPs (YAZDANI; SEDDIGH, 2016). In addition, the authors reported that bigger anions increase the thickness of the diffuse layer around nuclei particles and increase the mass transfer resistance. These events hinder the growth of the particles and, consequently, decrease the size of the particles.

Pereira and co-authors studied the effect of isopropanolamine and diisopropanolamine, as precipitating agent, on the properties of MFe_2O_4 (M = Fe, Co, and Mn) (PEREIRA *et al.*, 2012) and compared with traditional NaOH. The use of alkanolamines decreases the size of the particles (up to 6 times) and enhances saturation magnetization (M_S)

(up to 1.3 times). Regarding the size, it decreased once the alkanolamines formed metallic complexes in solution that competed with the ferrite precipitation. Furthermore, which concerns the increase of the M_S values, interactions of the nitrogen and oxygen atoms of the alkanolamines with the iron atoms at the surface reduced the surface spin-effect.

Although co-precipitation is a successful and classic technique for synthesizing MNPs, it still has the significant drawback of poor size distribution control, which results in the generation of polydispersed NPs (RAVIKUMAR; BANDYOPADHYAYA, 2011).

1.4.2.2 Hydrothermal/Solvothermal

When geologists and analytical chemists need to dissolve substances with low aqueous solubility, they insert them in a closed reactor, usually made of Teflon, sealed with stainless steel autoclave, and heat up to a temperature higher than the boiling point of the solvent. As a result, the analyte is dissolved and analyzed. This approach later became important to synthesize several nanomaterials, including MNPs. Additionally, the difference between hydrothermal and solvothermal is the solvent; in hydrothermal, the solvent is water, while in solvothermal, the solvent can be several chemicals, including methanol, ethanol, ethylene glycol, and glycerol. High temperatures used in this method enable rapid nucleation and growth, leading to small size NPs (REDDY *et al.*, 2012). Additionally, this method has also been used to produce single-crystal particles. Hence the hydrothermally produced NPs have better crystallinity (WU, *et al.*, 2015). Thus, the achievement of small and highly crystalline NPs is the main advantage of this method.

Hydrothermal synthesis of MNPs can be performed using the same co-precipitation procedure, except that the heating stage is performed in a stainless steel autoclave. For instance, Kolen'ko and co-authors proposed a large-scale co-precipitation and hydrothermal approach to synthesize sodium poly-acrylate functionalized MNPs (KOLEN'KO *et al.*, 2014). The hydrothermally prepared sample exhibited exceptional M_S and specific adsorption rate (SAR) values. The values of M_S and SAR were 84.01 emu g^{-1} and 86.87 W g^{-1}, respectively, while the NPs prepared by co-precipitation exhibited 72.38 emu g^{-1} and 46.4 W g^{-1}, respectively. The authors attributed the enhancement in the magnetic properties due to the large particle diameter and elevated synthesis temperature.

Another possibility to synthesize MNPs is to use only one iron source (usually $FeCl_3 \bullet 6H_2O$), a poly-alcohol as a solvent and reducing agent (ethylene glycol and PEG), and a precipitating agent such as NH_4OH, NaOH, $NH_4(CH_3CH_2COO)$ (KOZAKOVA *et al.*, 2015).

In this case, the reducing agent and/or solvent can also act as a functionalizing agent. For example, considering using NH_4OH as a precipitating agent and ethylene glycol as a solvent, the mechanism towards Fe_3O_4 NPs is shown in the following equations (KOZAKOVA *et al.*, 2015). The first step is the dissociation of the base:

$$NH_4OH \rightarrow NH_4^+ + Cl^- \quad (1.7)$$

The second step is the formation of iron(III) hydroxide and γ-Fe_2O_3:

$$Fe^{3+} + 3\ OH^- \rightarrow Fe(OH)_3 \quad (1.8)$$

$$2\ Fe(OH)_3 \rightarrow \gamma Fe_2O_3 + 3H_2O \quad (1.9)$$

Ethylene glycol can undergo dehydration, and the so-formed acetaldehyde reduces Fe^{3+} to Fe^{2+}. Then ferrous hydroxide is formed by reaction with hydroxyl ions:

$$2\ HOCH_2CH_2OH \rightarrow 2\ CH_3CHO + 2\ H_2O \quad (1.10)$$

$$2\ CH_3CHO + 2\ Fe^{3+} \rightarrow CH_3COCOCH_3 + 2\ Fe^{2+} + 2\ H^+ \quad (1.11)$$

$$Fe^{2+} + 2\ OH^- \rightarrow Fe(OH)_2 \quad (1.12)$$

Then Fe_3O_4 is formed by the reaction between ferrous and ferric hydroxides:

$$2\ Fe(OH)_3 + Fe(OH)_2 \rightarrow Fe_3O_4 + 4\ H_2O \quad (1.13)$$

Furthermore, ultrasmall magnetic nanoparticles (USMNPs) can be prepared by hydrothermal method using only $FeCl_3 \cdot 6H_2O$ as the iron precursor, ascorbic acid as reducing agent, and $NaHCO_3$ as precipitating agent (XIAO *et al.*, 2011)(63). The USMNPs synthesized in this work exhibited 5.1 nm of crystallite size and exceptional colloidal stability and biocompatibility, mainly due to the presence of ascorbic acid. These properties enable the prepared USMNPs as a promising candidate to be applied as a contrast agent for magnetic resonance imaging (MRI).

The main disadvantage of hydrothermal/solvothermal methodology is still the time of reaction, which is usually between 2 and 8 h (JI *et al.*, 2021; KOLEN'KO *et al.*, 2014).

1.4.2.3 Thermal decomposition

The obtaining of polydispersed MNPs is the main disadvantage of co-precipitation and hydrothermal/solvothermal approaches. For this reason, thermal decomposition has become the most popular methodology to prepare monodisperse and highly crystalline MNPs. For this approach, synthesis of MNPs occurs through thermal decomposition of an iron precursor in an organic solvent with a high boiling point, with a functionalizing agent. Iron precursors are usually $Fe(CO)_5$, $Fe(acac)_3$ (acac = acetylacetonate), and iron(III) oleate (WU, Wei; JIANG; ROY, 2016), while the organic solvents are oleic acid, oleyamine, 1-octadecene, and dioctyl ether (GAVILÁN *et al.*, 2021). Furthermore, when long-chain carboxylic acids or amines are used as the solvent, they also act as a functionalizing agent. For this reason, thermal decomposition always originates hydrophobic functionalized MNPs. Besides oleic acid and oleyamine, other commonly used functionalizing agents are trioctylphosphine oxide, trimethylamine oxide, hexadecylamine (GAVILÁN *et al.*, 2021).

The main factor for the production of monodispersed nanoparticles in thermal decomposition is the clear separation between nucleation and growth steps, according to Lamer Concept (Figure 10) (SCHLADT *et al.*, 2011). Lassenberger and co-authors evidenced the Lamer Concept and provided increased detail in the particle formation (LASSENBERGER *et al.*, 2017) by using *in situ* small-angle X-ray scattering techniques to analyze all the phases of the iron oxide formation. The iron precursor was $Fe(CO)_5$, dioctyl ether was the solvent, and oleic acid was used as functionalizing agent. The authors proposed the following steps for the synthesis, as shown in Figure 11: *i*) heat-up lag phase; *ii*) decomposition of $Fe(CO)_5$ to form iron(III)-oleate complex; *iii*) formation of the cluster that are precursors to the nuclei; *iv*) a second heating lag phase; *v*) burst nucleation; *vi*) growth phase. Furthermore, it was evidenced that the number of nuclei can be controlled by $Fe(CO)_5$/olecid acid ratio, besides the heating rate, controlling the final size of the nanoparticles.

Figure 10 – LaMer plot illustrating the separation of nucleation and growth of the NPs during their synthesis. C_S is critical supersaturation level; C_{min}^{nu} is the minimum concentration for nucleation; C_{max}^{nu} is the maximum concentration for nucleation.

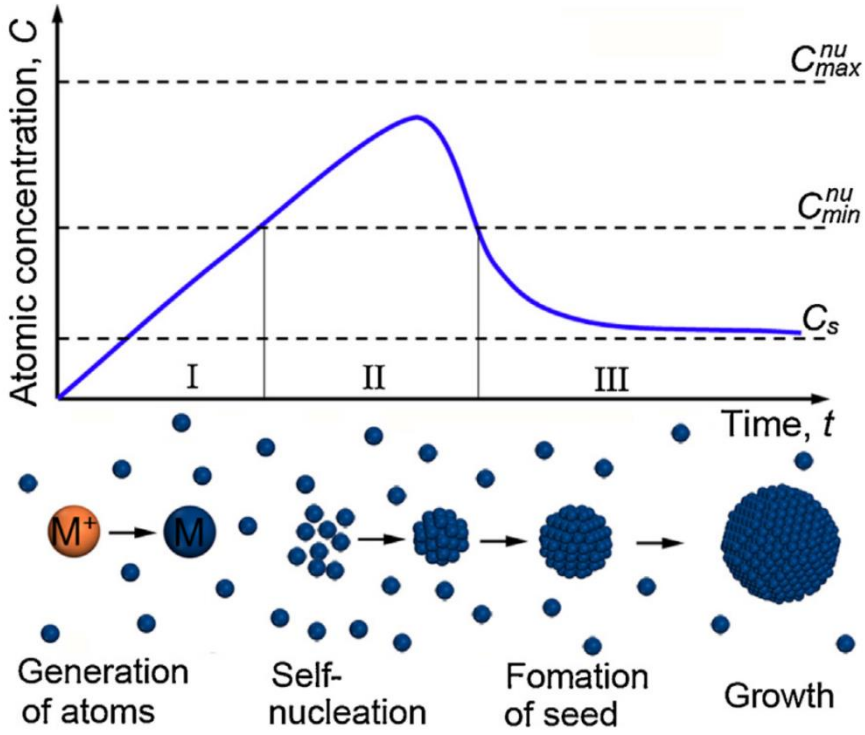

Source:(YOU; FANG, 2016).

Figure 11 – Distinct phases in the thermal decomposition of $Fe(CO)_5$ in the presence of oleic acid. Each phase is described in the text.

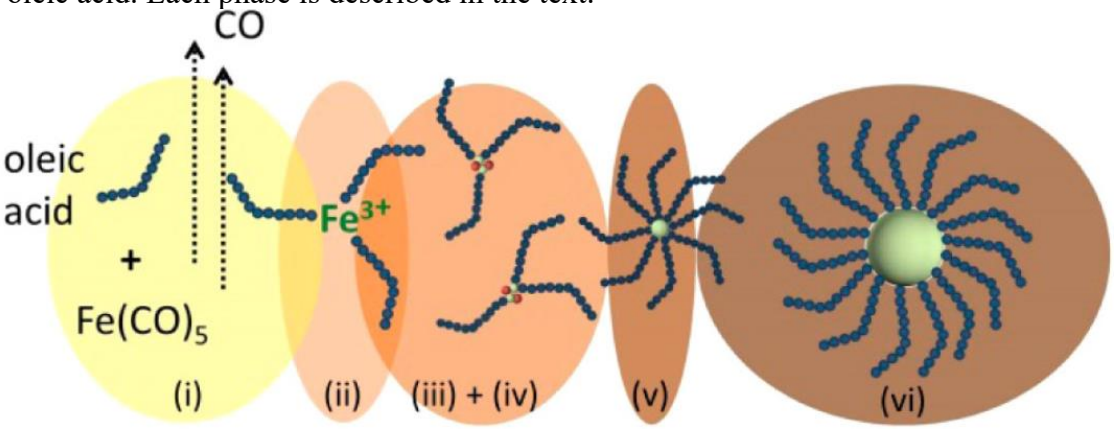

Source: Used with permission from (LASSENBERGER *et al.*, 2017). Copyright 2017 American Chemical Society.

Kemp and co-authors revealed the chemical reactions involved during the thermal decomposition synthesis of Fe_3O_4/γ-Fe_2O_3 (KEMP *et al.*, 2016). The synthesis was performed using iron(III) oleate as iron precursor and 1-octadecene as solvent. The authors proposed that Fe^{3+} reduction occurred by decarboxylation of iron oleate and oxidation of 1-octadecene.

Additionally, this study clarified the role of O_2 by evidencing that without this oxidation step, Wüstite (FeO) is found as a relevant secondary phase.

Furthermore, adjusting the synthetical parameters of thermal decomposition modulates the nucleation and growth process, leading to MNPs with various shapes and surfaces structures. Zhou and co-authors performed thermal decomposition of iron(III) oleate in the presence of sodium oleate (NaOL), and they evidenced that using 1-octadecene as a solvent, NaOL preferentially bound to Fe_3O_4 {111} facets to lead to the formation of Fe_3O_4 {111} facet exposed plates, truncated octahedrons and tetrahedrons (Figure 12 A–D). While in a high-boiling temperature tri-*n*-octylamine solvent, they obtained Fe_3O_4 {100} facets exposed cubes, concaves, assembled, and multi-branched structures by varying the NaOL/iron(III) oleate molar ratio (Figure 12 E–H).

Figure 12 – Transmission electron micrographs of iron oxides A) plates, B) truncated octahedrons, C)-D) tetrahedrons, E) cubes, F) concaves, G) assembled, and H) multi-branched structures.

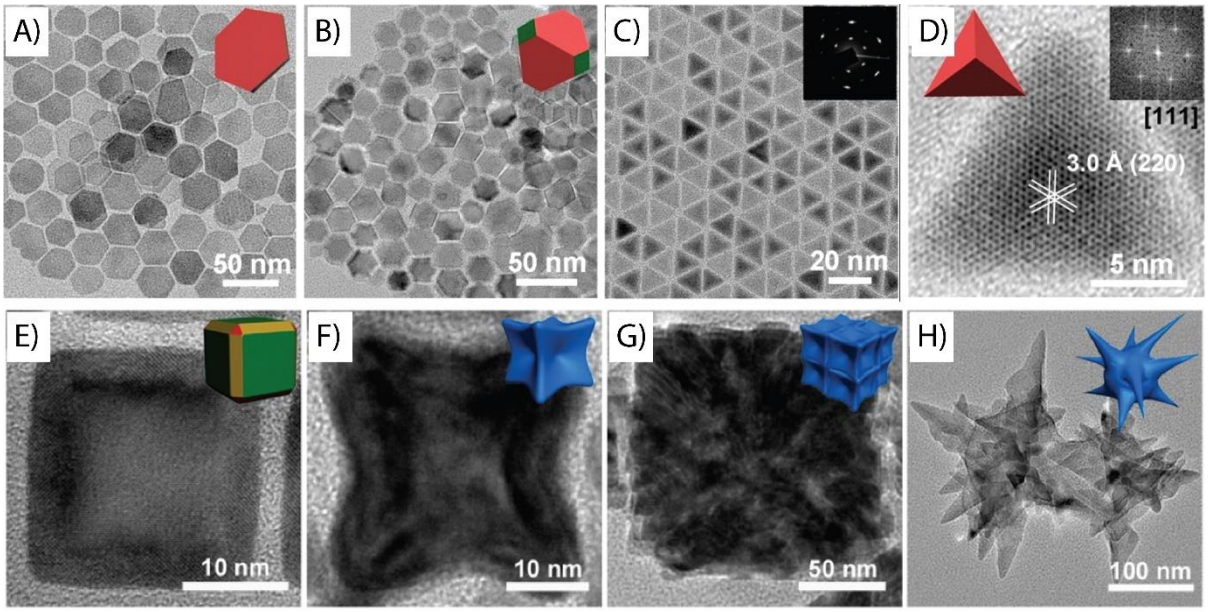

Source: Adapted with permission from (ZHOU, Zijian *et al.*, 2015). Copyright 2015 American Chemical Society.

However, thermal decomposition is a laborious process. One day is required to produce the iron(III) oleate, the most used iron precursor, followed by a second day to perform the thermal decomposition of the complex and purification of the MNPs (STEPHEN *et al.*, 2016). Moreover, once the thermal decomposition directly produces only hydrophobic MNPs, an additional ligand exchange process is necessary to infer hydrophilicity to the surface (Figure 7 A), which is necessary for most modern applications of the MNPs (STEPHEN *et al.*, 2016). However, the translation from bench to practical applications requires a simplified approach to

synthesize high-quality and reproducible MNPs. For this reason, we developed a rapid sonochemical approach to directly produce hydrophilic functionalized MNPs with excellent magnetic and colloidal properties, which was the topic of our master thesis (ANDRADE NETO, 2016), and it is already published (NETO *et al.*, 2017). Herein, we expanded the potential of the sonochemical approach by preparing a novel amino-phosphonate functionalized MNPs and demonstrated that these sonochemically synthesized MNPs have a great potential to be applied as electrochemical sensors for pesticides.

2 CHAPTER II – A NOVEL AMINO PHOSPHONATE-COATED MAGNETIC NANOPARTICLE AS MRI CONTRAST AGENT

2.1 Introduction

Magnetic resonance imaging (MRI) is a noninvasive, nonionizing, and radiation-free imaging technique, which has been applied in diagnosis and prognosis of several diseases (ZHELTOVA *et al.*, 2020). MRI image obtention is based on the contrast generated between health and diseased tissues, promoted by a chemical-based contrast agent that the shortening relaxation times of water protons leads to an enhancement of the tissues contrast (ZHAO *et al.*, 2020). Magnetic nanoparticles (MNPs) have been emerged as a great MRI contrast agents, which introduce new possibilities into biomedical research and clinical diagnosis (GAUGER; HERSHBERGER; BRONSTEIN, 2020; NI *et al.*, 2017; PENG; WANG; XUE, 2015; WAHSNER *et al.*, 2019).

For this proposal, MNPs must follow some additional requisites, such as good colloidal stability at physiological salt concentrations and at different pH levels to enable intravenously administration (AMSTAD; TEXTOR; REIMHULT, 2011; LI, Yanan; ZHANG, 2019). Therefore, MNPs have been surface-modified with capping agents in order to prevent their aggregation into human body, and also decrease overall cytotoxicity. Indeed, surface modification can modulate the behavior of MNPs in physiological medium, improving biocompatibility and hydrophilicity (FARZIN *et al.*, 2020; HOLA *et al.*, 2015). For instance, functionalizing agents can rearrange the atoms on MNPs surface, affecting the magnetic field inhomogeneity and playing an essential role regarding water molecules interactions (ZHANG, Weizhong *et al.*, 2018). Therefore, the performance of MNPs as MRI contrast agent is also tailored by the chosen of an excellent capping agent.

According to literature, several functionalizing agents can be found for MRI applications, which these compounds promote hydroxyl, carboxylic acids or amine groups in order to interact with external working environment (HOLA *et al.*, 2015; NI *et al.*, 2017; ZHANG, Weizhong *et al.*, 2018). Generally, capping agents are based on polyethylene glycol (PEG) (DU *et al.*, 2018; JEON *et al.*, 2020) and dextran (UNTERWEGER *et al.*, 2018); polyacrylic acid (WANG, Guannan *et al.*, 2014); carboxymethyl cellulose (LEONEL *et al.*, 2019), carboxyl-functionalized PEG (HU *et al.*, 2010) and citrate (XU, Fenghua *et al.*, 2009); and chitosan (AMINI-FAZL; MOHAMMADI; KHEIRI, 2019) and polyethylenimine (PEI) (KIM *et al.*, 2020). Catechol-based capping agents are also used, however they do not interact

directly to the working environment (GALLI *et al.*, 2019; ZENG *et al.*, 2014).

Another class of functionalizing agent is based on phosphonate molecules, mainly due to the strong affinity of phosphate/phosphoric acid groups to Fe atoms on MNPs surface (DEMIN; PERSHINA; *et al.*, 2018), where phosphonate derivatives can promote better chemical stability against hydrolysis, pH variations, dilutions and oxidation (MONTEIL *et al.*, 2014). Therefore, phosphonate-based functionalizing agents have been used in surface post-modification of MNPs, once phosphonate groups can act as a crosslinking between MNPs surface and functionalizing agent molecule (BORDEIANU *et al.*, 2017; LAM *et al.*, 2016; TORRISI *et al.*, 2014; WALTER *et al.*, 2017). For instance, TORRISI *et al.* (2014) synthesized phosphonic acid poly(ethylene glycol) copolymers to coat MNPs, in which the phosphonate groups are attached to Fe atoms on inner MNPs surface, whereas polyethylene glycol lengths is on the outer of surface boundary. However, external phosphonate surface groups provide interesting features, such as: a) interaction with rare earth elements, which could generate a more versatile profile to MNPs application (BORDEIANU *et al.*, 2017; LAM *et al.*, 2016; TORRISI *et al.*, 2014; WALTER *et al.*, 2017); b) bone affinity property for diagnostic of bone-related pathologies (NGUYEN *et al.*, 2018); c) concerning application as contrast agent for MRI, phosphonate groups promote an enhancement in relaxivity through second sphere effects due to strong hydrogen bonding interaction with water molecules (JACQUES *et al.*, 2010; LEBDUŠKOVÁ *et al.*, 2007). Besides outstanding versatility of phosphonate-based molecules application, their use as functionalizing agents on magnetic nanoparticles still limited.

Therefore, in this work, we propose an amino phosphonate-functionalized Fe_3O_4 NPs, using diethylenetriaminepenta (methylene phosphonic acid) (DTPMP) (Scheme 1A) as capping agent. Recently, DTPMP has been used to study sodium sulfate crystallization (RUIZ-AGUDO; RODRIGUEZ-NAVARRO; SEBASTIÁN-PARDO, 2006), preparing hollow Co-DTPMP complexes to be used as Fenton catalysts (ZHU, Yun-Pei; REN; YUAN, 2014), radioanalytical separation (LV *et al.*, 2016) and corrosion inhibitor (SELVAKUMAR; BALANAGA KARTHIK; THANGAVELU, 2014). DTPMP has also been used as chelating agent for gadolinium (Gd^{3+}) to be applied as contrast agent in calcified tissues (BLIGH *et al.*, 1994). The authors reported that the complex DTPMP-Gd^{3+} exhibited high bone affinity and renal clearance (BLIGH *et al.*, 1994). Herein, we truly believe that this molecule is a good candidate as functionalizing agent due to the following reasons: a) it is a commercially available compound with a relative low price; b) its molecular arrangement allows both attached and free-form phosphoric acid groups on MNPs surface, offering an enhanced chemical and colloidal stability, hydrophilic surface, as well as a tunable post-modification profile; c) the presence of

both amine and phosphoric acid groups can generate a amphoteric surface, where, depending on the pH of the medium, gives a positive or negative surface charge. Therefore, the proposed phosphonate-based nanomaterial presents a versatile profile for MRI and other technological applications, such as sensing formulations, catalysis, separation science and biological areas (MA *et al.*, 2011). Although, to the best of our knowledge, no study has been reporting functionalization process on MNPs using DTPMP.

Scheme 1 – (A) Structure of DTPMP. (B) Chemical routes to synthesize DTPMP-coated MNPs.

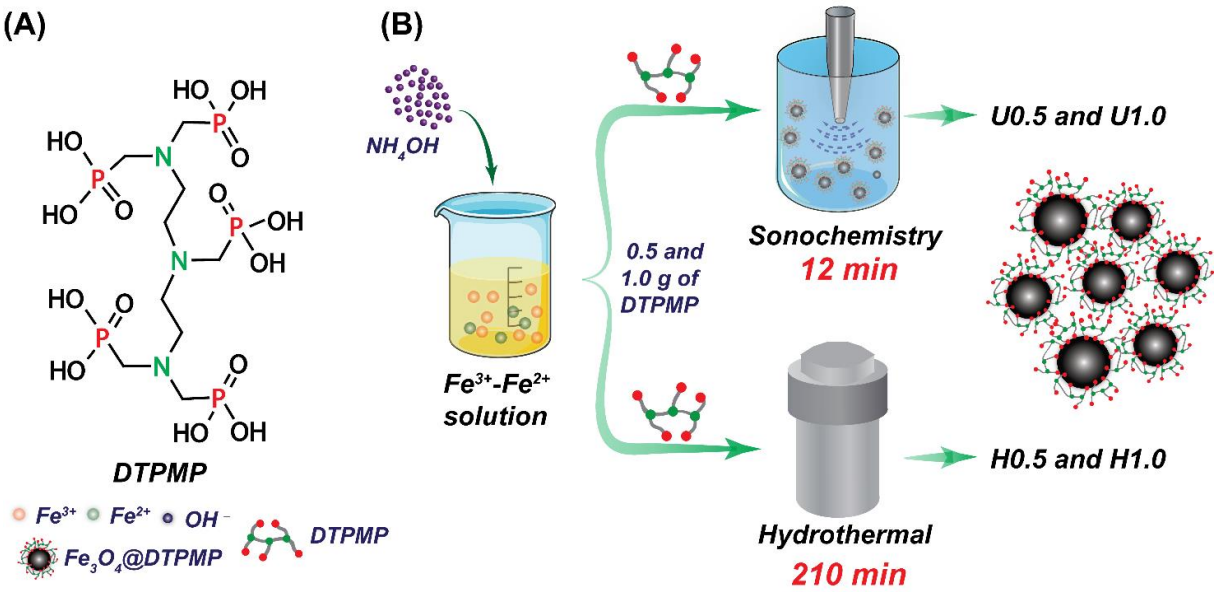

Source: author

Concerning performance of functionalized MNPs, the synthetic methodology plays a key role regarding material properties and structure (WU, Wei; JIANG; ROY, 2016), which it can be modulated according to final application. Herein, sonochemistry has drawn much attention of the scientific community mainly due to cavitation phenomenon, which provides a unique environment reaction with hot spots in the range of 5000 K and pressures higher than 1000 atm (XU, Hangxun; ZEIGER; SUSLICK, 2013). Remarkably, our group has been developed advanced nanomaterials by sonochemistry approach for different applications, such as electrochemical sensor (FREIRE, T.M. M. *et al.*, 2016), sunscreen formulation (BARBOSA *et al.*, 2018) and MRI contrast agent (NETO *et al.*, 2017). Recently, we developed a fast ultrasound-assisted method, around 12 min, to prepare MNPs functionalized with sodium polyacrylate, trisodium citrate, branched polyethylenimine and sodium oleate, which exhibited excellent magnetic, colloidal, and relaxivity properties for MRI application.

Therefore, the main propose of this study was to synthesize a novel ultrasound-

assisted hybrid nanomaterial with great performance as MRI contrast agent, and also compare sonochemical and hydrothermal methods regarding time reaction and final material properties. Herein, the overall DTPMP-functionalized Fe_3O_4 NPs characterization was achieved through a combination of techniques to precisely describe structure, morphology and magnetic properties of MNPs, as well as particles colloidal stability in aqueous medium and cytotoxicity. Finally, the MNPs were evaluated as MRI contrast agent, which also showed great potential to be applied in other biological and technological applications.

2.2 Materials and methods

2.2.1 Materials

Iron chloride (III) hexahydrate ($FeCl_3$•$6H_2O$) and iron sulfate heptahydrate ($FeSO_4$•$7H_2O$) were purchased from Vetec Química, Brazil. Diethylenetriaminepenta (methylene phosphonic acid) – (DTPMP, Scheme 1A) 50% (T) was purchased from Sigma–Aldrich and used as received. Ammonium hydroxide (29%) (NH_4OH) was purchased from Dinâmica Química, Brazil. All other reagents were used as received without any further purification.

2.2.2 Synthesis of DTPMP-functionalized Fe_3O_4 NPs

The DTPMP-coated NPs were synthesized by two methodologies, sonochemistry and hydrothermal approach. For each pathway, two stoichiometries of functionalizing agent, 0.5 g and 1.0 g of DTPMP, were tested (Scheme 1B).

2.2.2.1 Sonochemistry procedure

DTPMP-based MNPs were synthesized according to ultrasound-assisted method developed in our group (NETO *et al.*, 2017), using an ultrasound equipment (Q500 Sonicator - Qsonica) with a microtip probe of 3.2 mm under sonication conditions of 200 W and pulse-regime of *3s on* and *1s off*. Briefly, 1.0 g (3.60 mmol) of $FeSO_4 \cdot 7H_2O$ and 1.9 g (7.03 mmol) of $FeCl_3 \cdot 6H_2O$ were dissolved in 15 mL of deionized water. This obtained solution was heated up until reached 60 °C (~3 min) and further sonicated during 1 min under already described sonication conditions. Subsequently, 10 mL of concentrated NH_4OH solution were added under sonication for 4 min. Then, 4 mL of a solution containing a certain amount of DTPMP (see

below) was added into reaction mixture, allowing sonication in the last 4 min.

For sample containing 0.5 g of DTPMP, the solution of DTPMP was prepared by adding 0.6 mL of DTPMP in 3.4 mL of deionized water. For sample with 1.0 g of DTPMP, 1.2 mL of concentrated DTPMP were added in 2.8 mL of deionized water. Additionally, in order to remove the excess of NH_4OH and unbounded DTPMP molecules, the obtained particles were washed with 30 mL deionized water followed by magnetic decantation (3 times). Furthermore, the NPs were dialyzed until neutral pH. Finally, the samples were centrifuged for 10 min at 3000 rpm to remove large aggregates.

This procedure generated two samples labeled as U0.5 and U1.0, which correspond to ultrasound-assisted Fe_3O_4 NPs with 0.5g and 1.0g of DTPMP, respectively, as shown in Scheme 1B. It was also prepared uncoated Fe_3O_4 NPs by the same methodology, which was labeled as Fe_3O_4-U.

2.2.2.2 Hydrothermal

For hydrothermal approach, an adapted methodology was followed according to KOLEN'KO *et al.*, 2014. Firstly, 3.80 g (14 mmol) of $FeCl_3 \cdot 6H_2O$ and 2.05 g (7 mmol) of $FeSO_4 \cdot 7H_2O$ were dissolved in 38 mL of deionized water, and further added into a 90 mL of poly(tetrafluoroethylene) (PTFE) vessel. Then, 20 mL of NH_4OH were added to the obtained solution, followed by addition of a certain amount (see below) of concentrated DTPMP. Then, the PTFE reactor was closed and sealed in a stainless-steel autoclave, which was kept at 150 ºC for 3.5 h (See Scheme 1B). For sample with 0.5 g and 1.0 g of DTPMP, 0.6 mL and 1.2 mL of concentrated DTPMP was used, respectively.

For hydrothermal particles, the purification step was similar to one described for sonochemistry approach. Hydrothermal procedure generated two samples labeled as H0.5 and H1.0, which correspond to Fe_3O_4 NPs prepared by hydrothermal method with addition of 0.5g and 1.0g of DTPMP, respectively (Scheme 1B). Uncoated Fe_3O_4 NPs obtained by hydrothermal methodology were labeled as Fe_3O_4-H.

2.2.2.3 Complex DTPMP-Fe^{2+}-Fe^{3+}

In order to evaluate the interactions between DTPMP molecules and Fe atoms on the surface of Fe_3O_4 NPs, a complex of DTPMP and Fe^{2+}–Fe^{3+} cations was synthesized. Briefly, 1.34 g (4.9 mmol) of $FeCl_3 \cdot 6H_2O$ and 1.35 g (4.9 mmol) of $FeSO_4 \cdot 7H_2O$ were dissolved in 8 mL of deionized water. Then, 1.0 mL of concentrated DTPMP was added, which it was observed

the formation of a light yellowish precipitate. The mixture remained under magnetic stirring for 30 min. To remove the unbounded iron cations, the precipitate was washed with 30 mL of deionized water followed by centrifugation (2000 rpm for 5 min). The precipitate was dried under vacuum for further characterizations.

2.2.3 Characterization of DTPMP-functionalized Fe_3O_4 NPs

X-ray diffraction (XRD) analysis were performed using an X'Pert MPD X-ray powder diffractometer (PANalytical, Westborough, United States) with 40 kV and 30 mA in a scanning range of 2θ = 20-80° equipped with a Co Kα tube. The diffraction patterns were obtained using a Bragg–Brentano geometry in the continuous mode with a speed of 0.5 °/min and step size of 0.02° (2θ). The Rietveld structure refinement was used to interpret and analyze the diffraction data using the program DBWstools (BLEICHER; SASAKI; PAIVA SANTOS, 2000). The full-width at half maximum (FWHM) of the instrument was calculated with the standard hexaboride lanthanum. The crystallite size of each sample was calculated using Scherrer's equation.

Transmission electron microscopy (TEM) images were obtained with a MSC JEOL TEM-2100 200 kV microscope, equipped with a CCD (TVip–16 MP) and TV (Gatan ES500W) available from LNNano, Campinas, Brazil. TEM samples were dispersed in isopropyl alcohol and deposited in a drop onto carbon-coated copper grids. Subsequently, the deposited samples were allowed to dry completely overnight before analysis. The size distribution curves were obtained by manually size measuring of 150 particles (JIN *et al.*, 2015), using the software ImageJ (U.S. National Institutes of Health, Bethesda, MD). The polydispersity index for TEM analysis (PDI_{TEM}) was calculated as reported in literature (TIUNOV *et al.*, 2016). The coating thickness distribution curves were obtained by manually thickness measuring of 25 particles using ImageJ software. The data were determined measuring the distance from an imaginary plane, perpendicular to nanoparticle surface, to the end of the coating in the core-shell interface of the nanoparticle.

Mössbauer spectroscopy (MS) data were recorded at room temperature (300 K) with a FAST (ConTec) Mössbauer system spectrometer using the transmission geometry. A ^{57}Co radioactive source was used. The data analysis was performed using the NORMOS program written by R. A. Brand (distributed by Wissenschaftliche Elektronik GmbH, Germany). The isomer shifts (δ) relative to α-Fe were found at room temperature.

Vibrating sample magnetometer (VSM) measurements at 300 K were recorded on

a superconducting quantum interference device SQUID-VSM magnetometer from Quantum Design. Prior to the measurements, the particles were dried overnight in vacuum at room temperature, ground using an agate mortar, and finally placed in gelatin capsules for the measurements. Hysteresis loops were obtained at 300 K by applying a magnetic field up to ±20 kOe. Zero-field-cooling (ZFC) and field-cooling (FC) curves were obtained also in dried samples using the Vibrating Sample Magnetometer Mini 5 T from Cryogenic Ltd, with an applied magnetic field of 100 Oe. In order to obtain additional information concerning the blocking temperature (T_B) distribution of the NPs, it was applied the methodology of BRUVERA *et al.* (2015) on our ZFC-FC data.

The presence of DTPMP molecules on the surface of the NPs was studied by Fourier transform infrared spectroscopy (FTIR). The spectra were recorded using a Shimadzu model 8300 spectrophotometer. The samples were grounded in an agate mortar and pressed into KBr discs. The range used was 4000-400 cm^{-1}, with a resolution of 2 $cm^{-1}$and 128 scans.

Chemical surface analyses of the nanoparticles were carried out in a K-Alpha X-ray photoelectron spectrometer (XPS) (Thermo Fisher Scientific, United Kingdom) equipped with a hemispherical electron analyzer and an aluminum anode ($K\alpha$ = 1486.6 eV) as X-ray source. Measurements of the DTPMP-coated NPs were carried out by using charge compensation during the analyses, and the pressure of the chamber was kept below 2×10^{-8} mbar. Survey (i.e., full-range) and high-resolution spectra were recorded using pass energies of 1 and 0.1 eV, respectively. The spectrum fitting was performed by assuming a mixed Gaussian/Lorentzian peak shape (the ratio of the Gaussian to Lorentzian form was 0.4). For the fitting of the samples U0.5, U1.0, H0.5 and H1.0 the same FWHM values as the values obtained for the samples Fe_3O_4-U and DTPMP-Fe^{2+}-Fe^{3+} were used. The X-ray photoelectron spectra presented here are the result of the average of three spectra collected at three different regions for each sample.

The hydrodynamic size of the NPs in colloidal dispersion was measured in dynamic light scattering (DLS) experiments using a Malvern Zetasizer NS 3601 at 25 °C. The DLS measurements were performed on a diluted dispersion of the NPs (~0.066 mg mL^{-1}), with a single scattering angle of 173°. The hydrodynamic size of the synthesized samples was further analyzed using phosphate buffers at pH=7.4 (PB 7.4) and PB at different salt concentration (PBS 7.4). The size estimated by DLS was expressed as Z-average values, and the polydispersity index (PDI_{DLS}) values were calculated using the cumulate method. Five measurements were performed for each sample. The zeta potential (ζ) of each sample was measured using the same instrument at 25 °C. Furthermore, measurements of hydrodynamic

size and ζ at different pH values were performed using the MPT-2 Titrator device (Malvern Instruments). For the adjustment of the pH during the experiments the following solutions were used: 0.25, 0.01 mol L^{-1} NaOH and 0.25 mol L^{-1} HCl.

2.2.4 Toxic evaluation of the DTPMP-functionalized NPs on human neutrophils

2.2.4.1 Isolation of human neutrophils

Human leucocyte-rich blood from healthy adults was obtained from HEMOCE (blood bank), Fortaleza, Brazil. Polymorphonuclear cells were isolated by the Lucisano and Mantovani's method (LUCISANO; MANTOVANI, 1984) with slight modifications (KABEYA *et al.*, 2002), and the obtained cells suspension (80–90% neutrophils) showed 90 ± 2.0% of viability, stablished by the exclusion with Trypan blue method. The methods were carried out in accordance with the approved guidelines and Ethics Committee on Human Research (CAAE no. 18398819.2.0000.5054).

2.2.4.2 LDH activity test

The neutrophils suspension was incubated at 37˚C for 15 minutes with Hanks' solution (the medium, non-treated group), water (vehicle, control group), Triton X-100 (0.2%, cytotoxic standard) and samples U0.5; U1.0; H0.5 and H1.0 (100, 50 and 10 μg/mL). After incubation, the tubes were placed in a centrifuge at 4˚C for 10 minutes. Then, the supernatant of each sample was collected and maintained at low temperature to perform the absorbance measurement. The LDH activity was determined according to the LDH Liquiform kit Labtest (LDH Liquiform of Labtest Diagnostica, Lagoa Santa, MG, Brazil), where it was calculated using the following equation:

$$A = [(A_1 - A_2)/2] \times 1746.03 \quad (2.1)$$

Where: A = LDH enzymatic activity (U/L); A_1 = absorbance at 1 min; A_2 = absorbance at 3 min and 1746.03 is the current factor calculated by the manufacturer.

2.2.4.3 MTT test

Human neutrophils were exposed to the sample U1.0 (10, 50 and 100 μg/mL), water (vehicle, control), Hanks' balanced salt solution (HBSS) (culture medium, negative control) or Triton X-100 (0.2%, cytotoxic standard) for 15 minutes at 37°C, followed by addition of 200

μL of 3-(-4,5-dimethyl-2-thiazolyl)-2,5-diphenyl-2H-tetrazolium bromide (MTT). After 3h of incubation with MTT, the cells were washed with phosphate buffer solution, and the dimethyl sulfoxide (DMSO) (100 μL) was added for the solubilization of the formazan products. The absorbance was measured at 540 nm (MOSMANN, 1983).

For both tests, the results are expressed as mean ± standard error of the mean (S.E.M.). The statistical significance of differences between groups was determined by One-Way anova, followed by Tukey for multiple comparisons as a post hoc test. The significance level was set at $p < 0.05$.

2.2.5 Relaxivity measurements and MRI-weighted images

Five aqueous dilutions with different nanoparticle concentrations (between 0 and 0.16 mM Fe) were prepared for each sample, using an aqueous solution of agar 0.5 % (w/v) as solvent aiming to simulate MRI signals from human tissues. 200 μL aliquots of each dilution were measured in a mini spec mq60 contrast agent analyzer from Bruker at 37 °C and under 1.41 T magnetic field, using Carr Purcell Meiboom Gill (CPMG) sequence for transverse relaxation time (T_2) calculations. The transverse relaxivity constant (r_2) were calculated as the slope of the curve obtained by fitting the T_2^{-1} values versus the Fe concentration (mM). The Fe concentrations of the solutions were calculated using an inductively coupled plasma-optical emission spectroscopy (ICP-OES) analyzer (Shimadzu ICPE-9000).

MR phantom imaging was performed in a 3 T horizontal bore MR Solutions Benchtop (Guildford, U.K.) equipped with 48 G cm^{-1}actively shielded gradients. For imaging the samples, a 56 mm diameter quadrature bird-cage coil was used in transmit/receive mode. For the phantom measurements, the samples at different concentrations (between 25 and 150 μM in Fe) were dissolved in 200 μL of Milli-Q water a placed in custom-printed PLA holders. All MR images of the phantoms were acquired with an image matrix 256 × 252, field of view (FOV) 60 × 60 mm, three slices with a slice thickness of 1 mm, and 1 mm slice gap. For T_2-weighted imaging, a fast spin echo (FSE) sequence with the following parameters was used: T_E= 14ms, T_R= 3000 ms, N_A= 15, A_T = 47m 25s. T_2 maps were acquired using multi-echo multi-slice (MEMS) sequences with the following parameters: T_E= 15 ms, T_R= 1400 ms, N_A= 10, A_T = 44m 55s. Post-processing was performed using ImageJ software. T_2 maps were reconstructed using following the standard equation: $S_n = S_0$ [1 – exp ($TE \times n/T_2$)], where S is the signal intensity, TE is the echo time and T_2 is relaxation time.

2.3 Results

After DTPMP-coated MNPs synthesis, a full characterization analysis was performed in order to evaluate the success of the DTPMP functionalization and its impact on the structural (XRD and MS), magnetic (VSM and ZFC-FC) and colloidal (DLS) properties of the MNPs. Furthermore, FT-IR and XPS chemically showed how DTPMP molecules are binding on MNPs surface. In addition, we evaluated its potential to be applied as contrast agent in MRI through cytotoxicity experiments, relaxivity measurements and weighted MR images.

2.3.1 Structure and magnetic properties

2.3.1.1 XRD

XRD patterns for the synthesized MNPs are shown in Figure 2.1A. Data from the Rietvield structural refinement are shown in Table 1. Both the percentage of errors (R_{WP}) and goodness of fitting (S) values were found to be in agreement with those of a high-quality refinement (data not shown) (FREIRE, R. M. *et al.*, 2013). The analysis of the position and intensity of the diffraction peaks confirmed that all synthesized MNPs samples are composed of a single crystalline phase with a spinel structure *Fd3m* (ICSD code: 84611) (IYENGAR *et al.*, 2014), which is characteristic of Fe_3O_4 and γ-Fe_2O_3 oxidative like-form, being classified as isostructural phases.

Cubic cell lattice parameter (a) of the samples were 8.357, 8.357, 8.359, 8.369, 8.358 and 8.369 Å for U1.0, U0.5, Fe_3O_4-U, H1.0, H0.5, and Fe_3O_4-H, respectively, as shown in Table 1. Regarding the profile of the XRD peaks, all samples exhibited narrow and well-defined peaks, evidencing high crystallinity, unless for samples H1.0 and H0.5, which presented broader FWHM values (data not shown). Furthermore, crystallite size of the samples was calculated by Scherrer equation (See Table 1) using the data extracted from Rietveld refinement. The corresponding values for the samples U1.0, U0.5, Fe_3O_4-U, H1.0, H0.5, and Fe_3O_4-H were 10.9 ± 0.2, 10.7 ± 0.2, 12.0 ± 0.2, 7.2 ± 0.1, 7.8 ± 0.1 and 14.8 ± 0.3 nm, respectively.

Figure 13 – XRD patterns of the as-synthesized NPs. Red lines are the diffractogram adjusted according to Rietvield refinement and green lines are subtraction between observed and adjusted data.

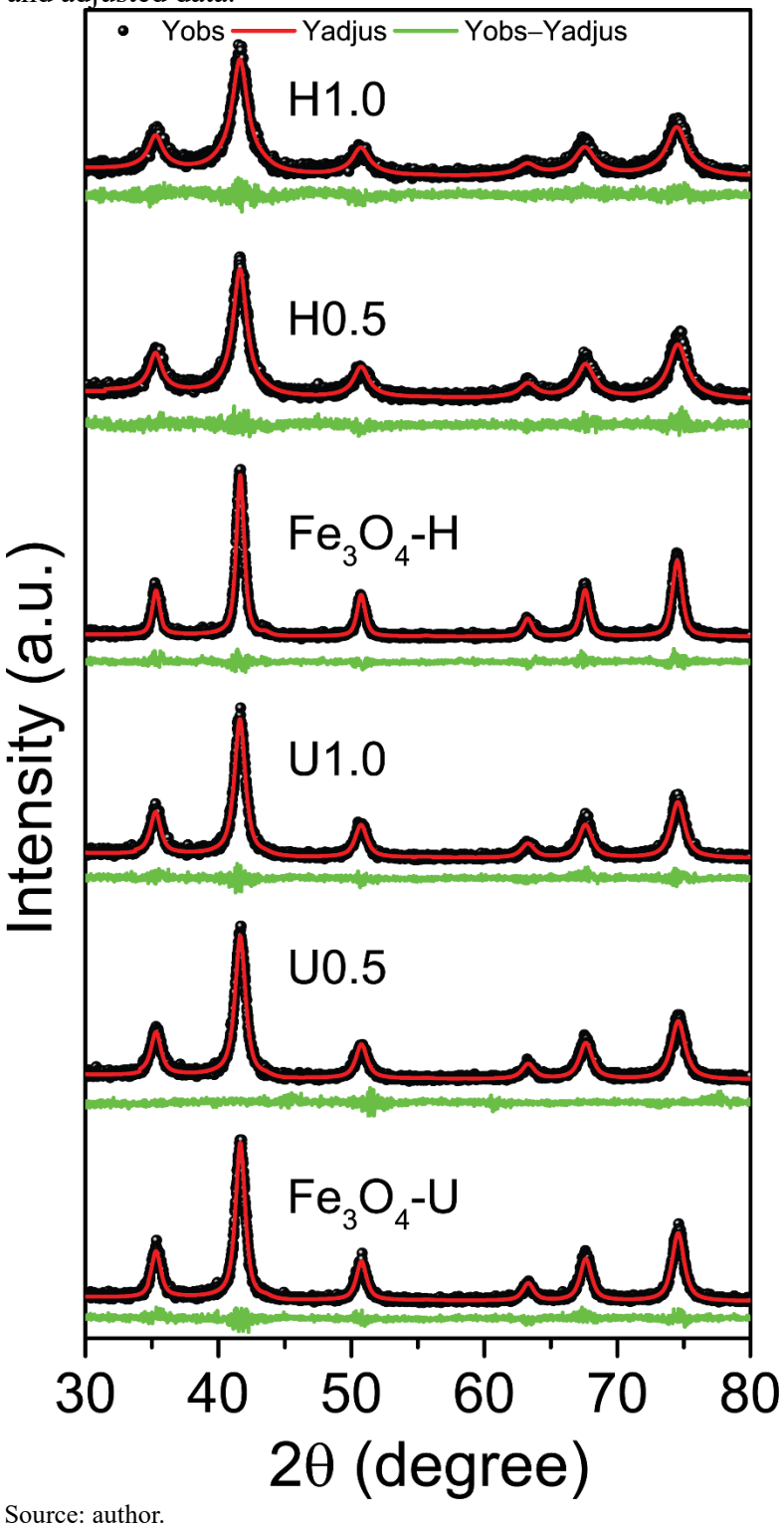

Source: author.

Table 1 – Structural and magnetic parameters from XRD Patterns (through Rietveld Refinement), TEM, VSM (300 K) and ZFC-FC analysis.

Sample	XRD		TEM		VSM (300 K)			ZFC/FC				
	a (Å)	D_{XRD} (nm)	D_{TEM} (nm)	PDI_{TEM}	M_S (emu/g)	H_C (Oe)	M_r (emu/g)	T_{MAX} (K)	$<T_B>$ (K)		% Area	
									P1[a]	P2[b]	P1	P2
U1.0	8.357	10.9 ± 0.2	10.4 ± 3.1	0.30	60.8	0.39	0.024	196.7	30.5	63.3	47.6	52.4
U0.5	8.357	10.7 ± 0.2	10.2 ± 3.9	0.38	65.0	0.40	0.015	-	71.1	106.9	49.5	50.4
Fe_3O_4-U	8.359	12.0 ± 0.2	-	-	-	-	-	-	-	-	-	-
H1.0	8.369	7.2 ± 0.1	8.7 ± 2.3	0.26	64.3	10.3	0.19	131.5	12.1	59.8	19.0	81.0
H0.5	8.358	7.8 ± 0.1	8.2 ± 2.6	0.31	64.2	10.6	0.14	171.6	62.2	89.5	71.2	24.9
Fe_3O_4-H	8.369	14.8 ± 0.3	-	-	-	-	-	-	-	-	-	-

[a] and [b]: particles population1 and 2, respectively.

Source: author

2.3.1.2 Mössbauer Spectroscopy

Mössbauer spectroscopy (MS) is a key technique in the study of magnetic materials, once MS spectrum shows information regarding their structure, electronic and magnetic properties (WITTE *et al.*, 2016). MS spectra for all samples synthesized by sonochemistry approach (Figure 14A) showed broadened ferrimagnetic sextets. Herein, a magnetic hyperfine field distribution was used to fit measured spectra. In the spectra profile of the samples U0.5 and U1.0 were observed a significant change in comparison to Fe_3O_4-U sample, where the sextets were broader for functionalized samples (See Figure 14A). Indeed, a considerable change was also evidenced in the magnetic hyperfine field (B_{hf}) distribution as a consequence of the functionalization with DTPMP (Figure 14B). For Fe_3O_4-U sample, the peak with highest intensity is centered at 47 T, whereas it appears at 45 and 44 T for U1.0 and U0.5, respectively. Moreover, the samples U1.0 and U0.5 exhibited peaks centered in 3 and 14 T, which may be observed in low intensity or absent in the distribution of the uncoated Fe_3O_4 NP sample. Additionally, the average isomeric shift (δ) was calculated for samples prepared by sonochemistry, showing values around 0.34 ± 0.02, 0.33 ± 0.02 and 0.33 ± 0.02 mm s^{-1} for U1.0, U0.5 and Fe_3O_4-U, respectively.

Interestingly, for samples prepared *via* hydrothermal method, it was observed a completely different MS spectra profile, as seen in Figure 14C, in comparison to those synthesized by sonochemistry. A broader adsorption line composed by a quadrupole doublet was evidenced for the samples H0.5 and H1.0. In this sense, a hyperfine quadrupole splitting

(*QS*) distribution was used to fit measured spectra (Figure 14D). For the samples H1.0 and H0.5, the peaks of the *QS* distribution are centered in 0.6 and 0.5 mm/s, respectively.

In contrast, the uncoated Fe_3O_4-H sample exhibits two ferrimagnetic sextets, which are assigned to the Fe atoms at the octahedral (green sub-spectrum) and tetrahedral (blue sub-spectrum) environments of Fe_3O_4 (Figure 14C – bottom spectrum). The hyperfine parameters calculated from the site distribution fit are shown in Figure 14D , and the obtained values are in agreement to other Fe_3O_4 NPs synthesized by hydrothermal method (DAOU *et al.*, 2006).

2.3.1.3 TEM

We performed a TEM analysis aiming to acquire information concerning morphology, size and structure of the DTPMP-coated NPs. TEM micrographs are shown in Figure 15A–D. The average particle diameter (D_{TEM}) and the calculated polydispersity index (PDI_{TEM}) values obtained by TEM images are listed in Table 1. Size distribution curves are presented as insets in Figure 15. The D_{TEM} values of all samples were similar to those found through XRD data analysis (D_{XRD}). For the samples U1.0, U0.5, H1.0 and H0.5 the average diameter values were 10.4 ± 3.1, 10.2 ± 3.9, 8.7 ± 2.3 and 8.2 ± 2.6 nm, respectively, whereas, the PDI_{TEM} values were 0.30, 0.38, 0.26 and 0.31, respectively.

In general, for all synthesized NPs, TEM micrographs showed a core-type structure of a pseudo spherical morphology, which is expected when the synthesis of Fe_3O_4 NPs is performed through coprecipitation reaction of Fe^{2+} and Fe^{3+} ions using ammonium hydroxide (KOLEN'KO *et al.* , 2014; LU *et al.*, 2013).

For the samples U1.0 and H1.0, a core-shell like structure was observed, as signed by the red arrows in Figure 15B and D, which can be attributed to the DTPMP coating. The average thickness values of the coating were 3.3 ± 1.7 and 14.9 ± 5.1 nm for samples U1.0 and H1.0, respectively. In Figure 16A is shown the thickness distribution curves for samples U1.0 and H1.0. In contrast, none core-shell structure was found for samples prepared with 0.5g of DTPMP. The representative image with higher magnification of the sample U0.5 confirmed an absence of a core-shell structure, i.e. a DTPMP coating was not observed. However, magnetite crystalline planes were well-defined, indicating a good crystallinity (See Figure 16B).

Figure 14 – (A) MS spectra of the DTPMP-coated NPs synthesized by the sonochemistry approach. (B) Hyperfine field distribution curves of each sonochemistry synthesized sample. (C) MS spectra of the DTPMP-coated NPs synthesized by the hydrothermal approach. For the sample H-Fe_3O_4 the green and blue lines are the site distributions for the populations of Fe atoms at octahedral and tetrahedral sites, respectively. (D) Data extracted from the site distribution of the sample: OCT, octahedral site; TETRA, tetrahedral site; IS, isomer shift; B, magnetic hyperfine field; wid, line width.

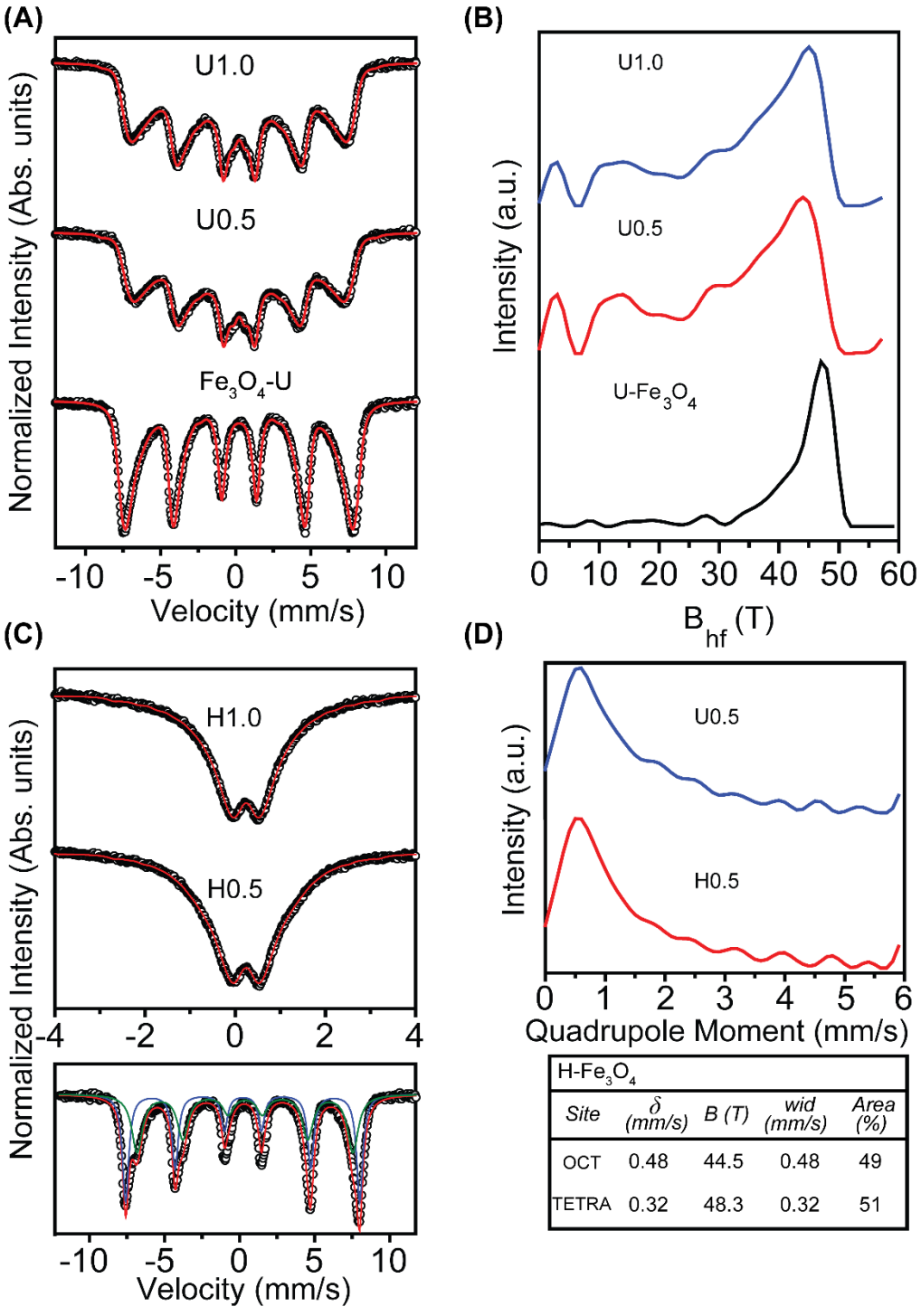

H-Fe_3O_4

Site	δ (mm/s)	B (T)	wid (mm/s)	Area (%)
OCT	0.48	44.5	0.48	49
TETRA	0.32	48.3	0.32	51

Source: Author.

Figure 15 – TEM micrographs of the samples (A) U0.5, (B) U1.0, (C) H0.5, and (D) H1.0. Red arrows indicate the presence of a shell-like structure. Inset: Size distribution curve obtained from TEM analysis for each sample. The average diameter value for each sample is shown in Table 1.

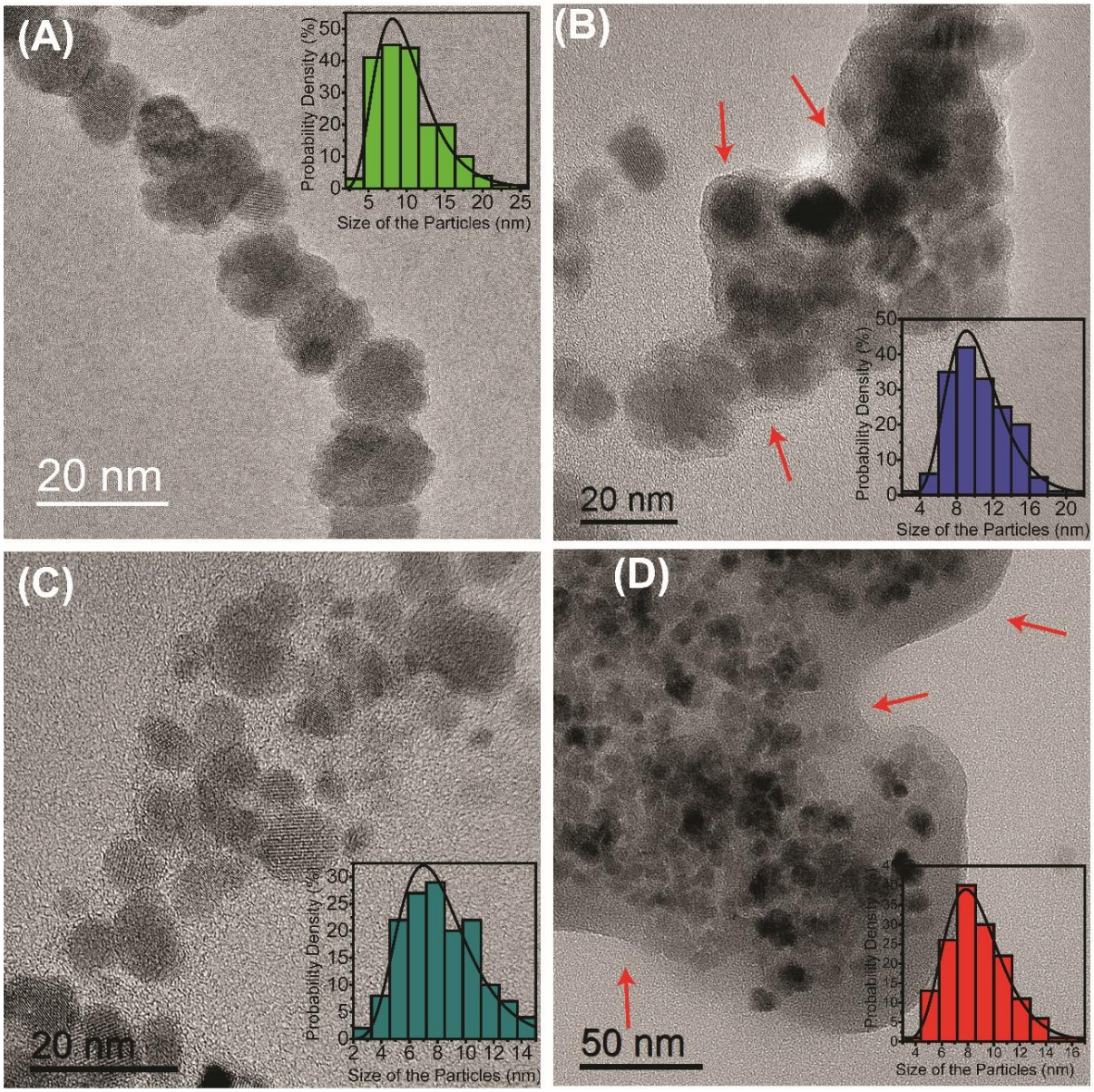

Source: author.

Figure 16 – (A) Coating thickness distribution curves of samples U1.0 and H1.0. Numbers in red and blue are the average ± SD of the samples U1.0 and H1.0, respectively. (B) TEM image with higher magnification of the sample U0.5.

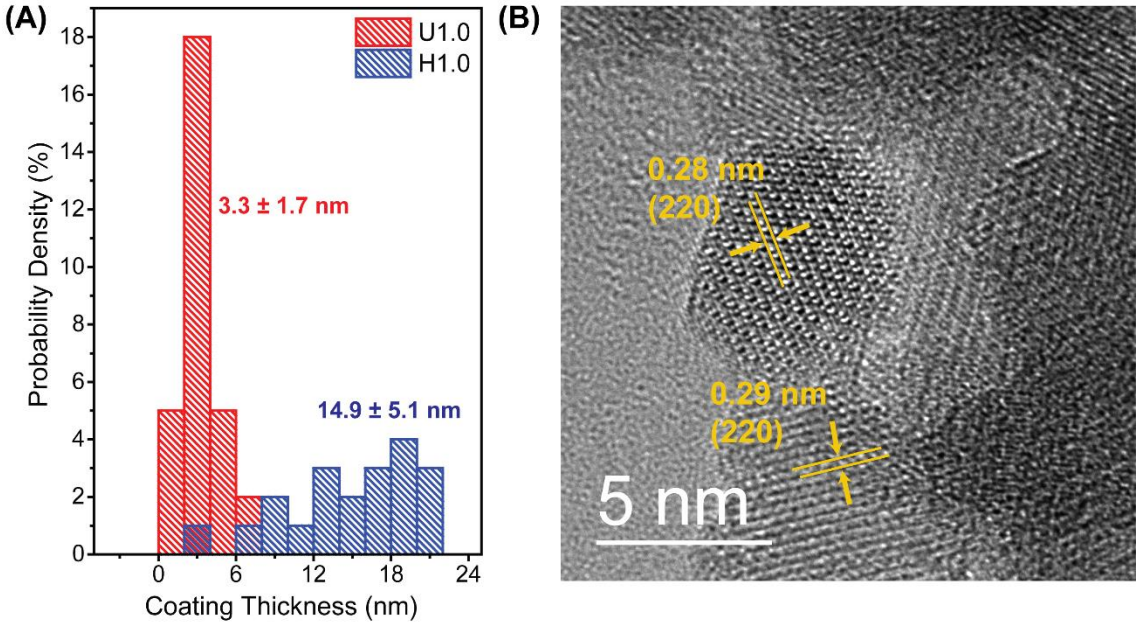

Source: author.

2.3.1.4 Magnetic measurements

The hysteresis loops of DTPMP-coated NPs at 300 K are shown in Figure 17, where low field curves are exhibited inset, evidencing small hysteresis loop for all analyzed samples. From these measurements, magnetization saturation (M_S) values were calculated, as well as remnant magnetization (M_R) and coercivity (H_C). All values are summarized in Table 1. It was observed small numerical variation for M_S and H_C parameters, comparing NPs synthesized by sonochemistry and hydrothermal methods. For example, the samples H1.0, H0.5, U1.0 and U0.5 showed M_S around 64.3, 64.2, 60.8 and 65.0 emu/g, respectively.

Magnetization curves as a function of temperature were measured under ZFC-FC conditions (Figure 18A). All samples showed FC curve with a flat profile at low temperatures, as a consequence of the presence of dipolar interactions (KOLEN'KO *et al.*, 2014). The blocking temperature (T_B) of magnetic NPs is defined as the crossover between superparamagnetic and ferrimagnetic states. Therefore, at T_B, sufficient energy is provided to the system and the spin is found to surpass the barrier energy, in order to perform the relaxation process towards another equilibrium position (GALVÃO *et al.*, 2015). In this sense, T_B may be estimated by the maximum of the ZFC curve (T_{MAX}) (DE LA PRESA *et al.*, 2015). Except for U0.5 sample, all other samples exhibited a maximum in ZFC, as can be seen in Table 1 for

obtained T_B values.

Figure 17 – Hysteresis loops of DTPMP-coated samples at 300 K.

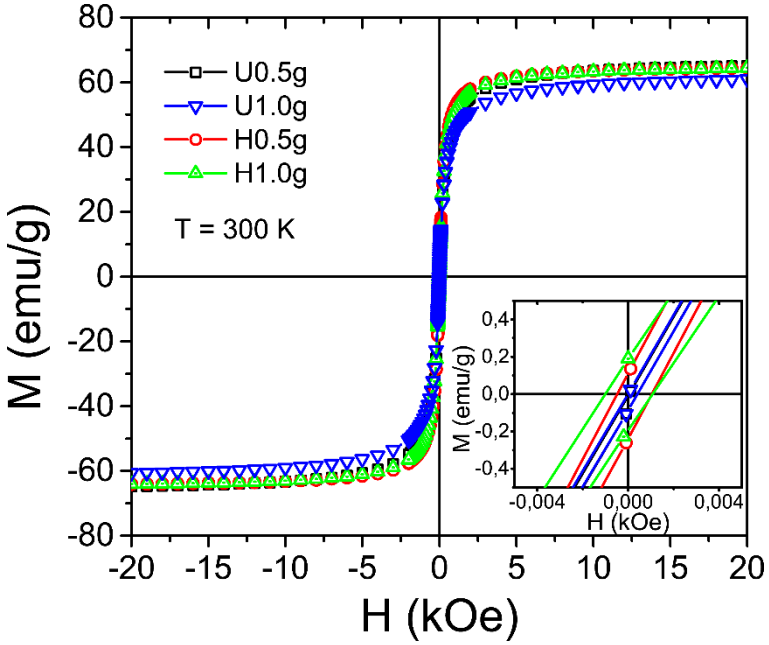

Source: author.

Figure 18 – (A). ZFC and FC magnetization curves Solid dots represent FC curves and open dots represent ZFC curves. (B) Log-normal fit of the d(ZFC–FC)/dT derivative for the DTPMP coated NPs. Population 1: green distribution; Population 2: blue distribution. Magnetic field used in the experiment: H = 100 Oe.

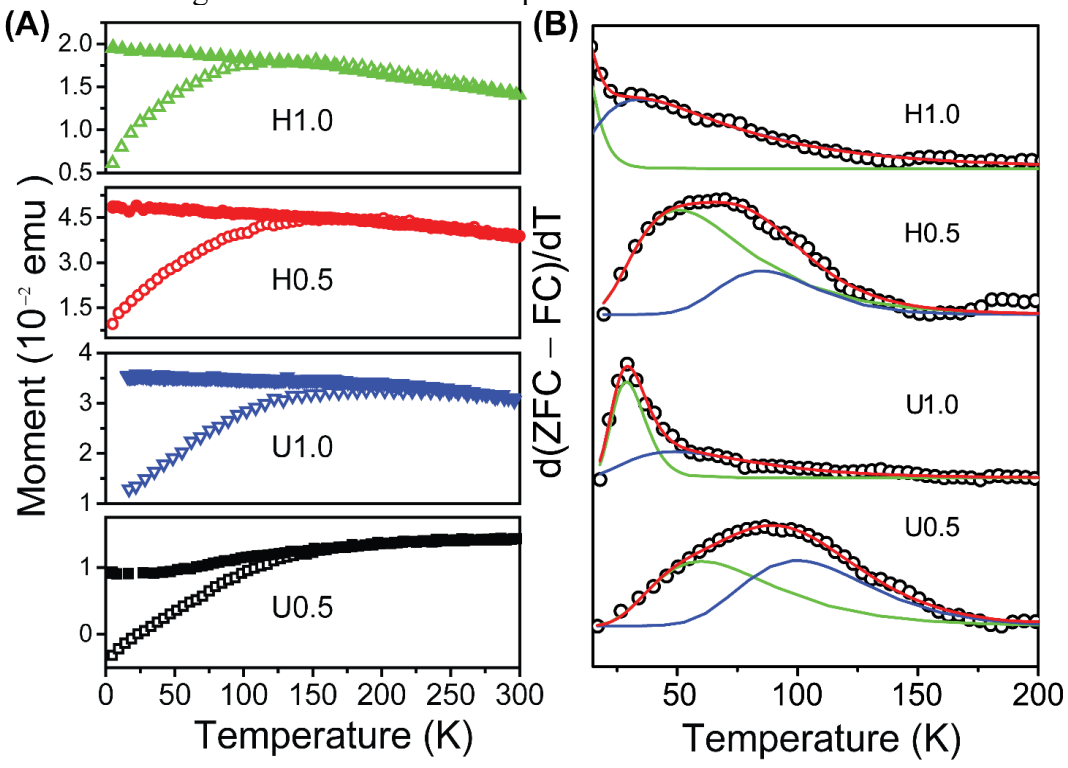

Source: author.

It was observed small numerical variation for M_S and H_C parameters, comparing NPs synthesized by sonochemistry and hydrothermal methods. For example, the samples H1.0, H0.5, U1.0 and U0.5 showed M_S around 64.3, 64.2, 60.8 and 65.0 emu/g, respectively.

However, it is worth to mention that this method is not completely suitable for estimate T_B, since T_{MAX} is affected by experimental parameters and size dispersion (BRUVERA *et al.*, 2015). Indeed, as T_B is proportional to volume of the NPs, and, in real systems, this parameter is reasonably described by a log-normal distribution. Therefore, a more appropriate methodology would be considered T_B as a distribution in order to calculate the values closer to the real ones (BRUVERA *et al.*, 2015) . Thus, firstly we used the temperature derivative of the ZFC–FC difference to extract a distribution of T_B values. Then, the data could be described using a log-normal distribution. The maximum of the simulated curve was assumed to be a T_B mean ($<T_B>$), and area of a log-normal distribution was also investigated (Figure 18B and Table 1). Furthermore, T_B distributions of synthesized DTPMP-coated NPs were better fit to two log-normal distributions, which physically means two populations of particles, as shown in the Table 1 (P1 and P2). Efforts to fit those using just one distribution were unsuccessful. As a consequence, the coefficients of determination (R^2) were not suitable. Table 2 shows the mean $<T_B>$, standard deviation of $<T_B>$, area for each distribution and R^2 for each fit.

Table 2 – Parameters extracted from the lognormal fitting of the d(ZFC-FC)/dT derivative curves.

Sample	T_{MAX}(K)	$<T_B>$ (K)		Standard Deviation of T_B		% Area		R^2
		Population 1	Population 2	Population 1	Population 2	Population 1	Population 2	
U1.0	196.7	30.53	63.34	0.24	0.51	47.6	52.4	0.9883
U0.5	-	71.08	106.92	0.42	0.26	49.5	50.4	0.9952
H1.0	131.5	12.10	59.80	0.40	0.74	19.0	81.0	0.9923
H0.5	171.6	62.16	89.55	0.45	0.23	71.2	24.9	0.9748

Source: author.

2.3.2 DTPMP-coating properties

FT-IR and XPS analyses were performed in order to confirm the functionalization of DTPMP with magnetite NPs, and also evaluate coating properties regarding final material applications.

For XPS and FTIR measurements, a complex of DTPMP and Fe^{2+} and Fe^{3+} was prepared in order to observe the peak and bands relative to the chemical interaction between Fe and DTPMP molecules, labeled as DTPMP-Fe^{2+}-$Fe3^{+}$. Indeed, the regions of the spectrum of

DTPMP-Fe^{2+}-$Fe3^{+}$ were then compared to DTPMP-coated MNPs spectra. In this regard, we assumed that the Fe ions complex was coordinated to phosphonate and/or amine groups.

2.3.2.1 XPS

The functionalized NPs were investigated regarding Fe, O, N and P atoms by XPS, since it is well-known as a suitable and sensitive surface technique. The survey spectra for all samples are presented in the Figure A1A-F, exhibited in Appendix A. In Figure 19A and B is shown the deconvoluted high-resolution XPS spectra for (A) O 1s and (B) N1s. The high-resolution spectra for Fe $2p_{3/2}$ and P2p are shown in Figure A2 A-C. Moreover, the atomic concentration at the surface (AC %), data extracted by the deconvolution, and the attributions to each sub-spectrum are shown in Table A2.

The O1s absorption showed valuable information concerning to DTPMP and Fe_3O_4 NPs interactions (Figure 19A). For non-functionalized Fe_3O_4 NPs, three peaks were observed, 529.98, 531.42 and 533.40 eV, which are related to Fe–O from Fe_3O_4(Fe–O_{Fe3O4}), Fe–OH (Fe–OH_{Fe3O4}) and absorbed H_2O, respectively (CHENG *et al.*, 2005). In contrast, the DTPMP-Fe^{2+}-Fe^{3+} complex exhibited two peaks centered in 531.28 and 532.84 eV, where the first one can be assigned to P–O–Fe, P=O and/or P=O•••Fe (labeled P–$O_{DTPMP-Fe}$) (DAOU *et al.*, 2007; PARAMONOV *et al.*, 2008). Moreover, it was not attempt to differentiate the peak of Fe–OH of Fe_3O_4 from the P–$O_{DTPMP-Fe}$, for the samples functionalized with DTPMP (Figure 19A). Thus, the spectra of the DTPMP-coated NPs were assigned with three peaks centered in 530.08, 531.39 and 533.94 eV. The peak of highest intensity shifted to values slightly smaller than those of the DTPMP complex. Additionally, the ratio between the area of the peaks P–$O_{DTPMP-Fe}$ (Fe–OH_{Fe3O4} for uncoated Fe_3O_4) and Fe–O_{Fe3O4} were 0.34, 0.49, 0.47, 0.66 and 0.76 for the samples Fe_3O_4-U, U0.5, U1.0, H0.5 and H1.0, respectively (Table A1).

Figure 19 – Deconvoluted high-resolution XPS spectra for (A) O1s and (B) N1s of all synthesized samples. The most important attributions for each sub-spectrum are shown in this Figure. The attributions for all sub-spectra are shown in Table A2.

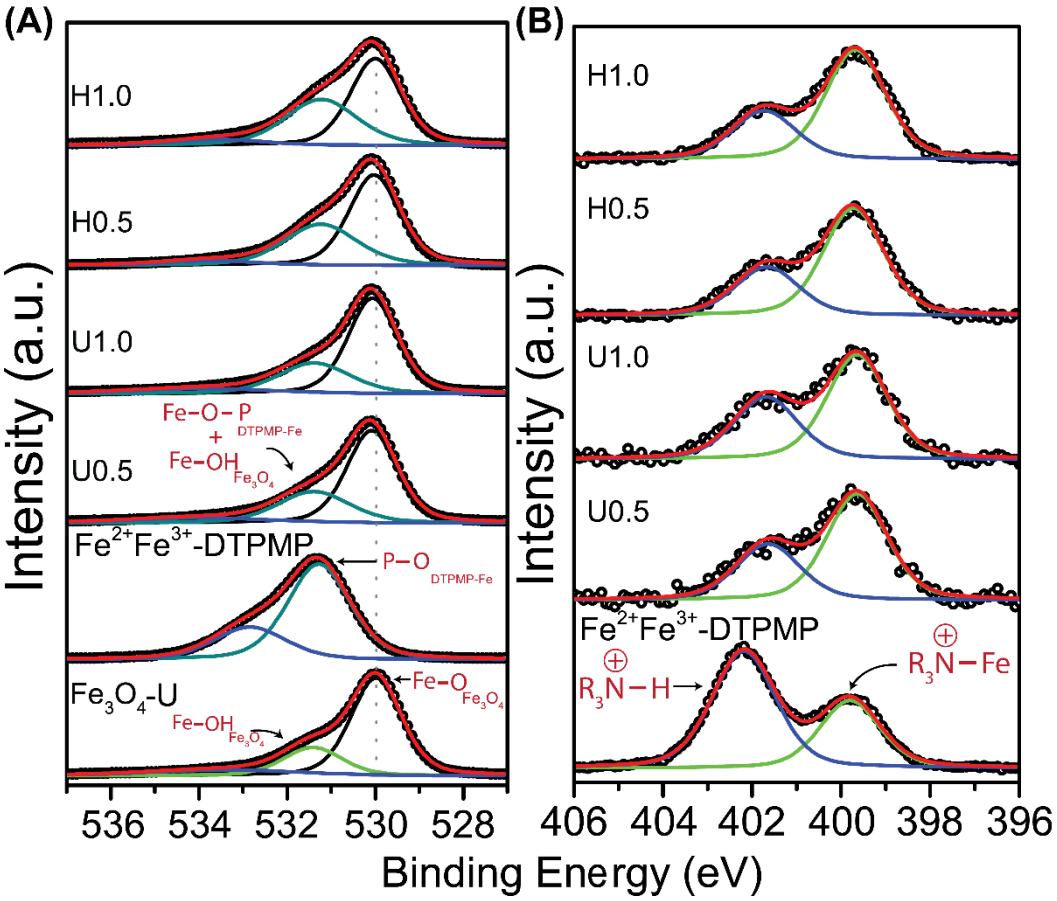

Source: author.

Relevant information concerning to DTPMP and Fe_3O_4 surface interactions can also be extracted from the high-resolution N1s spectra (Figure 19B). A broad peak was detected for all samples, fitted into two components, 399.7 and 401.7 eV, where the first peak is attributed to amine groups from DTPMP bonded to Fe atoms from Fe_3O_4 (R_3N^+–Fe), and the second was assigned to protonated amine groups from DTPMP (R_3N^+–H) (Figure 19B and Table A1) (INCORVIO; CONTARINI, 1989; JUNG; JACOBS, 1995; WANG, Yongliang *et al.*, 2011). The peak at 399.7 eV is mainly attributed to the amine groups bonded to Fe atoms due to the presence of this peak in the complex sample DTPMP-Fe^{2+}-Fe^{3+}, and according to the literature, nitrogen atoms from DTPMP participate in the coordination to iron atoms in DTPMP-Fe complex (OAKES; VAN KRALINGEN, 1984). Interestingly, the R_3N^+–Fe peak was more intense for functionalized NPs in comparison to R_3N^+–Fe for DTPMP-Fe^{2+}-Fe^{3+} complex (Figure 19B).

Information concerning the number of amine groups bonded to the surface can be extracted from the ratio between the area of R_3N^+–Fe ($A_{R3N+–Fe}$) and R_3N^+–H ($A_{R3N+–H}$). The ratio ($A_{R3N+–Fe}/A_{R3N+–H}$) values were 0.55, 1.80, 1.59, 2.10 and 2.14 for the samples DTPMP-Fe^{2+}-$Fe3^+$, U0.5, U1.0, H0.5 and H1.0, respectively. In regard to the absorption of P2p, the spectra were adjusted with two peaks, $P2p_{3/2}$ (lowest binding energy) and $P2p_{1/2}$ (highest binding energy). Additional peaks were not evidenced for DTPMP-coated NPs, in comparison to DTPMP-Fe^{2+}-$Fe3^+$ complex (Figure A2C). However, spectra of functionalized NPs presented a shift towards small binding energies (Figure A2C). The AC values of P on the surface of the NPs were 3.57, 3.86, 4.41 and 4.79 % for the samples U0.5, U1.0, H0.5 and H1.0, respectively (Table A2).

2.3.2.2 FT-IR

Regarding FT-IR vibrational modes relative to the core material, all samples presented two bands between 400 and 800 cm^{-1} (Figure A3) (IYENGAR *et al.*, 2014), attributed to stretching vibrations of Fe−O bond ($\nu_{Fe–O}$) in tetrahedral and octahedral sites. The samples Fe_3O_4-U, U0.5, U1.0, H0.5 and H1.0 presented $\nu_{Fe–O}$ bands centered in 561, 584, 588, 588 and 584 cm^{-1}, respectively.

Concerning the bonding mechanism between Fe_3O_4 NP surface and DTPMP, FT-IR has been shown to be a suitable technique, specifically for phosphonate groups, through the analysis of a set of vibrational modes located between 850 and 1210 cm^{-1} (BARJA; TEJEDOR-TEJEDOR; ANDERSON, 1999; DEMIN; MEKHAEV; *et al.*, 2018; THOMAS *et al.*, 2016;

TUDISCO *et al.*, 2012), as shown in Figure 20A. Regarding the binding of phosphate groups and iron oxides, Barja *et al.* (1999) reported three possibilities through the systematic study of the complexation of methylphosphonic acid with goethite particles, such as protonated monodentate complex [R–PO(OH)(O–Fe)], bridging bidentate complex [R–PO(O–Fe)$_2$] and deprotonated monodentate complex [R–P(PO$_2$)(O–Fe)]. Additionally, Demin *et al.* (2018) also considered a tridentate complex form [R–P(O–Fe)$_3$].

Figure 20 – (A) Deconvoluted FTIR spectra of the region of interest for the elucidation of the mechanism of bonding between Fe_3O_4 NPs and DTPMP. (B) Schematic illustration for main vibrational modes, considering deconvolution spectral. (C) The proposal of bonding between Fe_3O_4 NPs and DTPMP molecule. Attributions of each sub-spectrum are shown in Table 3. Small letters (*a'*, *a"*, *b* and *c*) represent the sub-spectrum relative to each chemical group presents in DTPMP-coated MNPs.

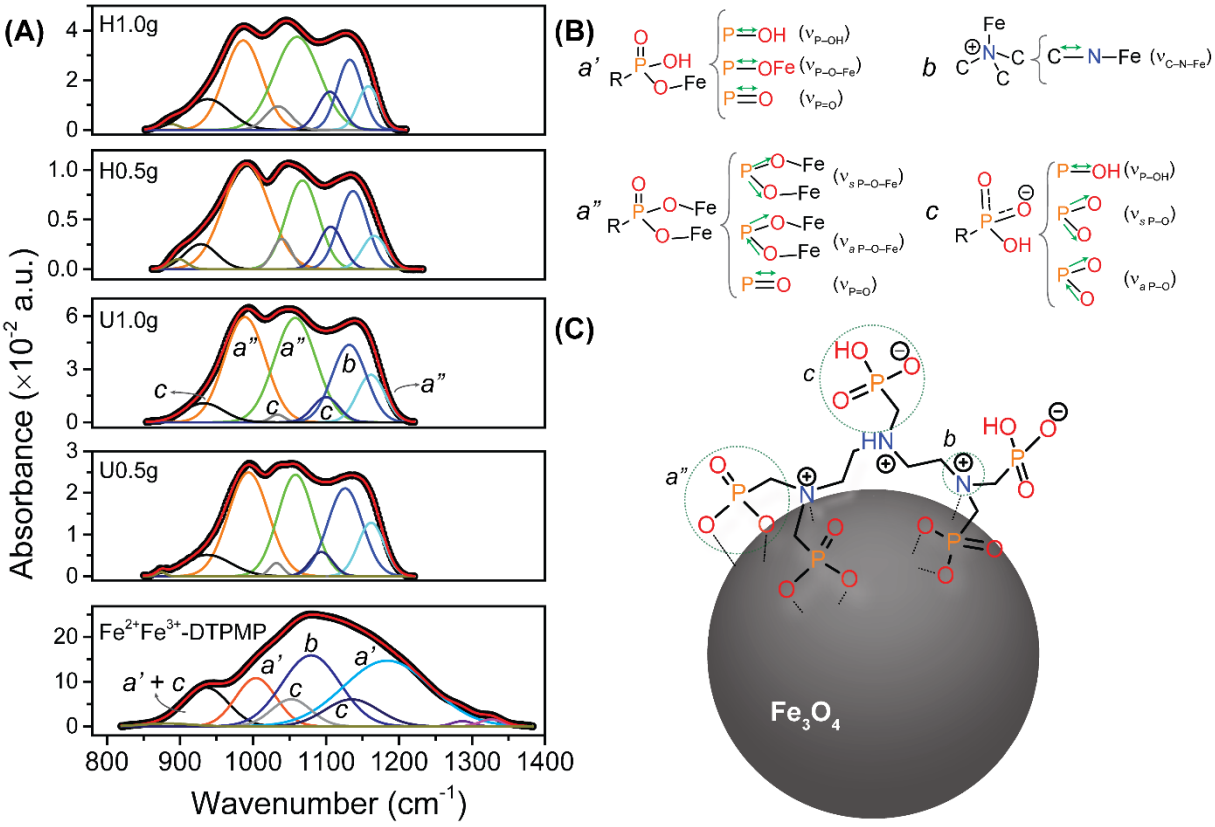

Source: author

In this work, the bonded mechanism is proposed considering all above complex-form possibilities, in which we performed a spectral deconvolution of FT-IR spectra for the region of interest, as shown in Figure 20A. The attribution to each sub-spectrum is in Table 3. It was considered, in the spectral deconvolution, vibrational modes relative to four chemical

groups, as shown in Figure 20B. The main chemical groups considered into discussion were: phosphoric acid groups anchored to the Fe atoms as protonated monodentate complex (*a'*), presenting stretching of the groups P–OH, P–OFe and P=O ($\nu_{P–OH}$, $\nu_{P–O–Fe}$ and $\nu_{P=O}$ – Figure 20B *a'*); phosphoric acid groups anchored to the Fe atoms as bridging bidentate complex (*a''*), presenting symmetrical and asymmetrical stretching of the groups P–OFe ($\nu_{s\ P–O–Fe}$ and $\nu_{a\ P–O–Fe}$) and P=O ($\nu_{P=O}$), as shown in Figure 20B *a''*; tertiary amine groups bonded to Fe atoms (*b*) with stretching of C–N ($\nu_{C–N}$) (Figure 20B *b*); free phosphoric acid groups (*c*) presenting $\nu_{P–OH}$ as well as symmetrical and asymmetrical stretching of P–O ($\nu_{s\ P–O}$ and $\nu_{a\ P–O}$). All above mentioned groups are inserted in the spectral deconvolution vibrational modes in Figure 20A.

For DTPMP-Fe^{2+}-$Fe3^{+}$ sample, the bond between phosphoric acid groups and Fe atom are characterized by the presence of the following stretching vibrational modes: $\nu_{P–OH}$ (936 cm^{-1}), $\nu_{P–O–Fe}$ (1004 cm^{-1}) and $\nu_{P=O}$ (1183 cm^{-1}) (Figure 20A *a'*), which can be related to a protonated monodentate complex (BARJA; TEJEDOR-TEJEDOR; ANDERSON, 1999). It was also evidenced in 1079 cm^{-1} stretching vibrations for C–N–Fe groups, which is supported by XPS results (Figure 20A *b*) (LANIGAN; PIDSOSNY, 2007). Regarding free phosphoric acid groups, which were in the form of $R–PO_3H^-$, we detected three vibrational modes: $\nu_{P–OH}$ (883 and 936 cm^{-1}), $\nu_{a\ PO2}$ and $\nu_{s\ PO2}$ (1052 and 1135 cm^{-1}, respectively) (Figure 20A *c*) (BARJA; TEJEDOR-TEJEDOR; ANDERSON, 1999).

For DTPMP-functionalized MNPs, we evidenced the same bands observed in the complex for the bonding between nitrogen and iron as well as free phosphoric acid groups (Figure 20A-B *b* and *c*). However, phosphoric acid groups were anchored onto the surface through bridging bidentate form, due to the presence of the following vibrational modes: $\nu_{s\ P–O–Fe}$, $\nu_{a\ P–O–Fe}$ (989 and 1100 cm^{-1}, respectively) and $\nu_{P=O}$ (1161 cm^{-1}) (Figure 20A-B *a''*) (BARJA; TEJEDOR-TEJEDOR; ANDERSON, 1999; BASLY *et al.*, 2013; ZENOBI *et al.*, 2008). Based on these results, we proposed the model of interaction between DTPMP and Fe_3O_4 NPs as shown in Figure 20C.

Table 3 – Data from the deconvolution of FT-IR spectra in 850-1350 cm^{-1}. References in the Table: (1) (PERSSON; NILSSON; SJÖBERG, 1996); (2) (BARJA; TEJEDOR-TEJEDOR; ANDERSON, 1999); (3) (CÎRCU *et al.*, 2018); (4) (ZENOBI *et al.*, 2008); (5) (LANIGAN; PIDSOSNY, 2007); (6) (AHMED *et al.*, 2019); (7) (PARAMONOV *et al.*, 2008) (8) (GROSVENOR *et al.*, 2004) (9) (CHENG *et al.*, 2005).

Sample (R^2)	Peak center (cm^{-1})	Height (a.u.)	Area (a.u.)	FWHM (a.u.)	Attribution	Ref.
DTPMP-Fe^{2+}-Fe^{3+} (0.9999)	882.7	0.007	0.57	80.4	ν_{P-OH} free R–PO_3H^-	(1)
	936.1[a' + c]	0.087	6.54	70.9	ν_{P-OH} of R–PO(OH)(O–Fe) + ν_{P-OH} of R–PO_3H^-	(2)
	1004.0[a']	0.108	7.48	65.1	ν_{P-O-Fe} R–PO(OH)(O–Fe)	(2)
	1052.3[c]	0.061	4.14	64.0	$\nu_{s\ PO2}$ free R–PO_3H^-	(2)
	1079.5[b]	0.159	15.85	93.8	ν_{C-N-Fe}	(2,3)
	1135.1[c]	0.061	5.60	86.8	$\nu_{a\ PO2}$ free R–PO_3H^-	(2)
	1183.6[a']	0.147	22.02	140.7	$\nu_{P=O}$	(2)
	1286.8	0.012	0.42	33.6	δ_{P-OH} free R–PO_3H^-	(4)
	1326.1	0.016	0.62	37.4	δ_{N-H} of protonated R_3–N^+	(5)
U0.5 (0.9999)	874.3	0.001	0.01	14.1	δ_{Fe-O-H}	(6)
	937.0[c]	0.005	0.42	77.2	ν_{P-OH} free R–PO_3H^-	(2)
	993.8[a"]	0.025	1.72	64.9	$\nu_{s\ P-O-Fe}$	(7,8)
	1032.1[c]	0.003	0.07	22.1	$\nu_{s\ PO2}$ free R–PO_3H^-	(2)
	1058.3[a"]	0.024	1.49	57.3	$\nu_{a\ P-O-Fe}$	(7,8)
	1093.5[c]	0.006	0.23	36.7	$\nu_{a\ PO2}$ free R–PO_3H^-	(2)
	1126.2[b]	0.021	1.26	56.2	ν_{C-N-Fe}	(9,3)
	1161.7[a"]	0.013	0.57	42.0	$\nu_{P=O}$	(9,8)
U1.0 (0.9999)	932.5[c]	0.011	0.74	64.5	ν_{P-OH} free R–PO_3H^-	(2)
	988.8[a"]	0.059	4.19	66.2	$\nu_{s\ P-O-Fe}$	(2)
	1033.5[c]	0.004	0.11	23.4	$\nu_{s\ PO2}$ free R–PO_3H^-	(2)
	1057.8[a"]	0.059	4.22	67.2	$\nu_{a\ P-O-Fe}$	(2)
	1100.0[c]	0.014	0.64	42.3	$\nu_{a\ PO2}$ free R–PO_3H^-	(2)
	1131.7[b]	0.044	2.58	55.3	ν_{C-N-Fe}	(9,3)
	1161.5[a"]	0.027	1.27	44.6	$\nu_{P=O}$	(9,8)
H0.5 (0.9999)	898.0	0.001	0.03	28.1	δ_{Fe-O-H}	(6)
	928.5[c]	0.003	0.14	52.5	ν_{P-OH} free R–PO_3H^-	(2)
	990.9[a"]	0.011	0.84	74.6	$\nu_{s\ P-O-Fe}$	(7,8)
	1039.5[c]	0.003	0.10	30.1	$\nu_{s\ PO2}$ free R–PO_3H^-	(2)
	1067.6[a"]	0.009	0.50	52.7	$\nu_{a\ P-O-Fe}$	(7,8)
	1106.4[c]	0.004	0.18	39.1	$\nu_{a\ PO2}$ free R–PO_3H^-	(2)
	1136.9[b]	0.008	0.39	46.1	ν_{C-N-Fe}	(9,3)
	1166.1[a"]	0.003	0.14	39.3	$\nu_{P=O}$	(9,8)
H1.0 (0.9999)	886.8	0.002	0.07	29.0	δ_{Fe-O-H}	(6)
	937.9[c]	0.012	0.93	70.3	ν_{P-OH} free R–PO_3H^-	(2)
	986.5[a"]	0.036	2.34	61.1	$\nu_{s\ P-O-Fe}$	(7,8)
	1034.6[c]	0.009	0.42	41.3	$\nu_{s\ PO2}$ free R–PO_3H^-	(2)
	1060.3[a"]	0.037	2.92	73.2	$\nu_{a\ P-O-Fe}$	(7,8)
	1105.2[c]	0.015	0.64	39.4	$\nu_{a\ PO2}$ free R–PO_3H^-	(2)
	1132.5[b]	0.028	1.21	40.4	ν_{C-N-Fe}	(9,3)
	1158.0[a"]	0.018	0.65	34.5	$\nu_{P=O}$	(9,8)

[a', a", b, c] Indicate the chemical group in the sub-spectrum of each DTPMP-functionalized sample illustrated in Figure 20.

Source: author.

2.3.3 Colloidal properties

The nanoparticles exhibited a magneto-fluid response in water after DTPMP functionalization, i.e. if a magnet bar is placed close to the colloidal dispersion, the fluid is attracted to the magnet as whole, and no separation between dispersed nanoparticles and liquid phase is observed. Actually, this behavior is an additional evidence of the success of the functionalization step, as well as the good colloidal stability.

In-depth, the hydrodynamic properties of the aqueous dispersions of the coated-MNPs were evaluated by DLS in three different solvents: deionized water, phosphate buffer 7.4 (PB 7.4) and phosphate buffer saline 7.4 (PBS 7.4). They were selected due to their biological relevance. All samples were measured in terms of hydrodynamic size, polydispersity index (PDI_{DLS}) and zeta potential (ζ), as shown in Table 4. In both buffer dispersions, the hydrodynamic size for all samples did not increase in comparison to deionized water NPs dispersion. All size distributions curves exhibited unimodal behavior (Figure A8-11). Interestingly, for the NPs synthesized by sonochemistry, the PDI_{DLS} values increased when the samples were dispersed in physiological solutions, whereas the opposite behavior occurred for samples obtained by hydrothermal route. It is worth mentioning that the Z-average size values were around 15 times bigger than the average particles diameter calculated by XRD and TEM, potentially indicating cluster formation in aqueous environment.

Table 4 – Hydrodynamic particle size, surface charge and PDI obtained by DLS in different aqueous solvents.

Sample	Solvent	Hydrodynamic diameter (nm)	PDI_{DLS}	ζ (mV)[a]
U1.0	H_2O	149.1 ± 0.7	0.101 ± 0.020	–31.3 ± 0.51
	PB 7.4	124.1± 0.7	0.140 ± 0.012	
	PBS 7.4	133.5 ± 2.4	0.310 ± 0.031	
U0.5	H_2O	151.4 ± 1.3	0.086 ± 0.026	–36.0 ± 1.10
	PB 7.4	127.3 ± 1.3	0.149 ± 0.007	
	PBS 7.4	123.1 ± 1.0	0.201 ± 0.020	
H1.0	H_2O	142.9 ± 0.8	0.247 ± 0.006	–28.0 ± 1.99
	PB 7.4	131.0 ± 0.9	0.205 ± 0.009	
	PBS 7.4	125.5 ± 0.5	0.199 ± 0.010	
H0.5	H_2O	125.3 ± 1.0	0.212 ± 0.007	–33.2 ± 0.88
	PB 7.4	135.7 ± 1.2	0.275 ± 0.006	
	PBS 7.4	117.0 ± 1.0	0.214 ± 0.006	

[a] pH around 6.5

Source: author

The ζ is an important parameter to be analyzed regarding colloidal suspensions, once it gives a clear magnitude and nature of the surface electric charge. All evaluated samples showed surface charge values between –28.0 ± 1.99 and –36.0 ± 1.10 mV (Table 4), mainly related to the de protonation of the phosphonic acid groups from DTPMP.

In order to have a deeper understanding of the surface properties of DTPMP-coated NPs, ζ and Z-average size were measured as a function of pH (Figure 21A and B). The sample U1.0 was selected as a model once this sample exhibited a greater performance as MRI contrast agent. In acid medium (pH in the range of 3–4), the ζ showed positive values due to the protonation of the tertiary amine groups from DTPMP on particles surface. At pH values higher than 4.08, which is the isoelectric point (IEP) of DTPMP, it was observed negative values of surface charge. At pH 10, the ζ reached a minimum of –32.5 mV.

Hydrodynamic size followed similar profile, where values close to IEP, the samples exhibited highest size values. It is known that the absence of electric charge on the surface causes the attractive forces of Wander-Walls, in order to overcome the repulsive electrostatic force, leading to aggregation of the particles and higher hydrodynamic size values. This behavior is confirmed through the macroscopic colloidal stability, as shown in Figure 21B. For instance, in Figure 21B – point II, when the colloidal suspension of DTPMP-coated MNPs reaches pH 4, the NPs precipitate, and as the pH increases, the NPs become dispersed (Figure 21B – Point III and IV).

Figure 21 – (A) Influence of the pH medium in zeta potential and hydrodynamic size of the sample U1.0. (B) Images of the U1.0 suspension at different pH levels. All image samples are in equal dilution factor.

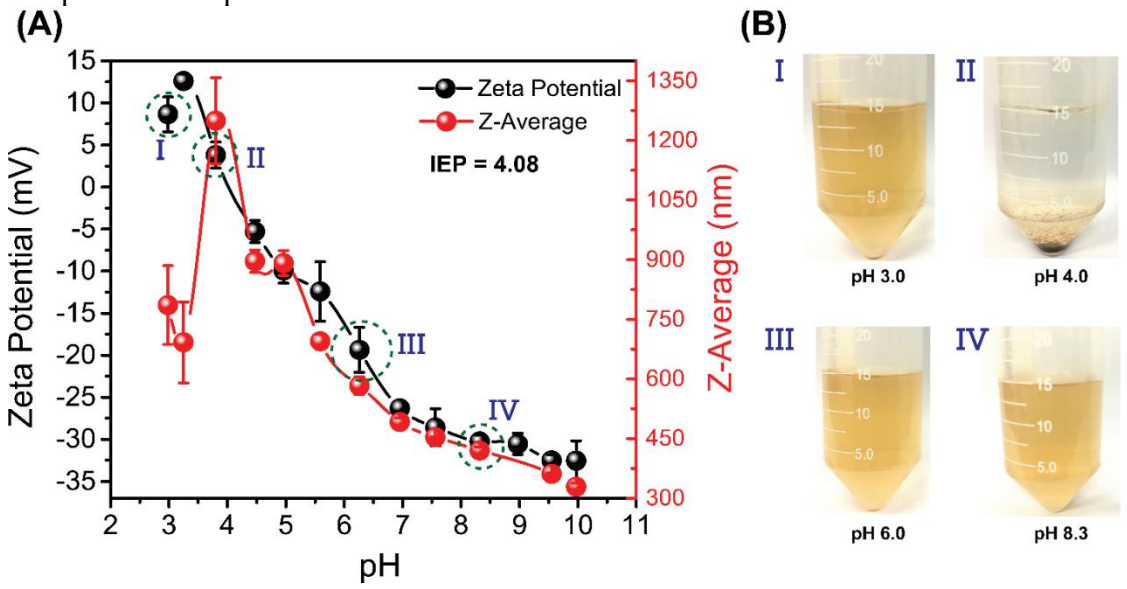

Source: author

2.3.4 Cytotoxicity evaluation

For MRI contrast agent application, a preliminary evaluation of the DTPMP-coated NPs on human neutrophils viability must be performed. In this work, two cytotoxicity tests were used, LDH activity and MTT assay.

In LDH assay, none of coated samples showed significant increase in the enzymatic activity in comparison to control group (Figure 22A). However, the addition of Triton X-100 0.2% (w/v) (positive control) significantly increased the LDH activity in the extracellular medium. Within this context, and considering greater relaxivity properties, cell viability by MTT test was performed for the sample U1.0, in order to evaluate other cell function effects (Figure 22B). The addition of U1.0 sample at 10, 50 and 100 μg/mL on human neutrophils suspension did not present a significant reduction in cellular viability (97-116 % of viable cells) when compared to vehicle group/control group (100 % of viable cells). Indeed, the percentage of viable cells in the HBSS group (medium cell culture) was similar to vehicle group (data not shown).

Figure 22 – Toxic evaluation of the as-synthesized NPs measured by (A) lactate dehydrogenase (LDH) activity and (B) MTT test on human neutrophils. No significant difference was found when related to the control group. ($p < 0.05$; ANOVA and Tukey's post hoc test). The results represent mean ± SEM of three separate experiments.

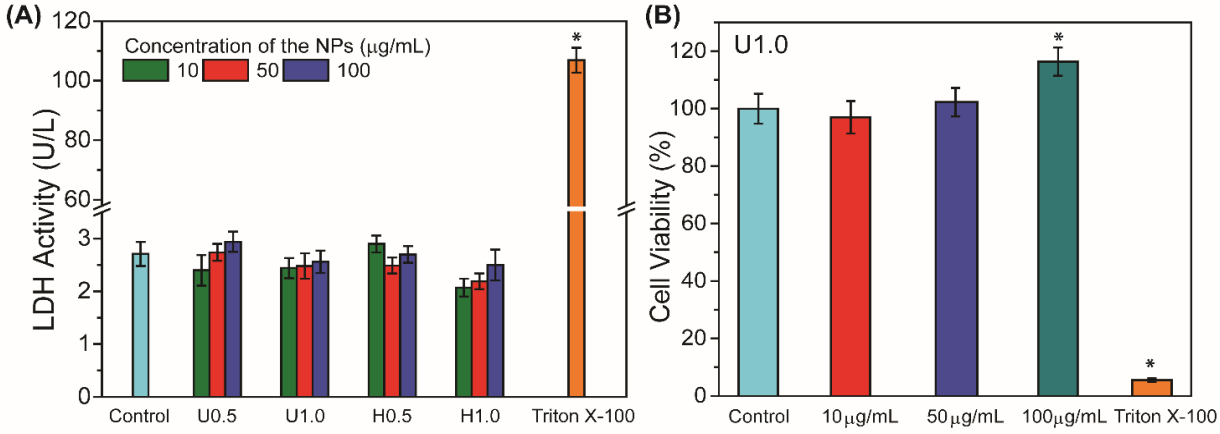

Source: author

2.3.5 Magnetic resonance imaging properties

MNPs with average diameter around 7–20 nm are traditionally considered as T_2 contrast agents in MRI, as can provide a dark contrast when MR images are acquired under T_2-weighted sequences (5). For magnetic nanoparticles, the dark (hypointense) contrast generated by T_2-contrast agents is a result of the interaction between microscopic magnetic field inhomogeneities caused by the NPs and hydrogen atoms. This interaction shortens the T_2 of the protons in their vicinities (LIN; LIU; GAO, 2019). Agar 0.5% (w/v) was selected as solvent for the phantom imaging experiments instead of deionized water (HUANG *et al.*, 2014), in order to better simulate the T_2 signal of living tissues, since relaxivity properties of this gel are well-described and frequently used as MRI phantoms reference (HELLERBACH *et al.*, 2013).

The efficiency of a nanomaterial dispersion as a T_2-contrast agent for MRI is evaluated in terms of transverse relaxivity (r_2) and the ration between r_2 and longitudinal relaxivity (r_1) – r_2 / r_1. These parameters can be evaluated by preparing MNPs dispersions at different dilutions, and further measuring the relaxation time (T_2 and T_1) for each dispersion. Finally, the slope of the plot between relaxation rate (T_2^{-1} or R_2; T_1^{-1} or R_1) versus concentration of Fe (mmol L^{-1}) can be calculated (SHIN *et al.*, 2015). The r_2, r_1 and r_2 / r_1 values for the samples U0.5, U1.0, H0.5 and H1.0 are presented in the Table 5. Linear fitting between the inverse of T_1 and T_2 versus Fe concentration, are shown in Figure A8 (A–D) and Figure 23A and B, respectively.

Figure 23C and D show a T_2-weighted MR image of the phantom and a T_2 map for all prepared dispersions containing functionalized NPs. In both images, as the Fe concentration increases in the dispersion, a greater contrast is observed, e.g. as dark the contrast in T_2-weighted image as short the relaxation time in T_2 map. Additionally, in T_2-weighted image, no apparent difference was evidenced among analyzed samples. However, samples U1.0 and U0.5 induced a slightly greater shortening in T_2 in comparison to H0.5 and H1.0, as shown in T_2 map (Figure 23D).

Table 5 – Longitudinal (r_1), transversal (r_2) relaxivities and ratio r_2 / r_1 for DTPMP-coated MNPs prepared in this work.

Sample	r_1 (mM s^{-1})	r_2 (mM s^{-1})	r_2 / r_1
U0.5	7.39 ± 0.01	375.0 ± 0,24	50.78 ± 0.01
U1.0	8.65 ± 0.01	417.4 ± 0.3	48.25 ± 0.05
H0.5	7.98 ± 0.04	357.6 ± 0.4	44.83 ± 0.02
H1.0	9.51 ± 0.05	416.7 ± 0.2	43.81 ± 0.01

Source: author

Figure 23 – Linear fittings of the inverse transversal relaxation time versus Fe concentration and r_2 relaxivity values of the samples: (A) U0.5 and U1.0 and (B) H0.5 and H1.0. (C)T_2-weighted images (fast spin echo sequence) for the DTPMP-coated magnetic nanoparticles. (D) T_2 map (multi-echo multi-slice, MEMS) sequence for the DTPMP-coated magnetic nanoparticles.

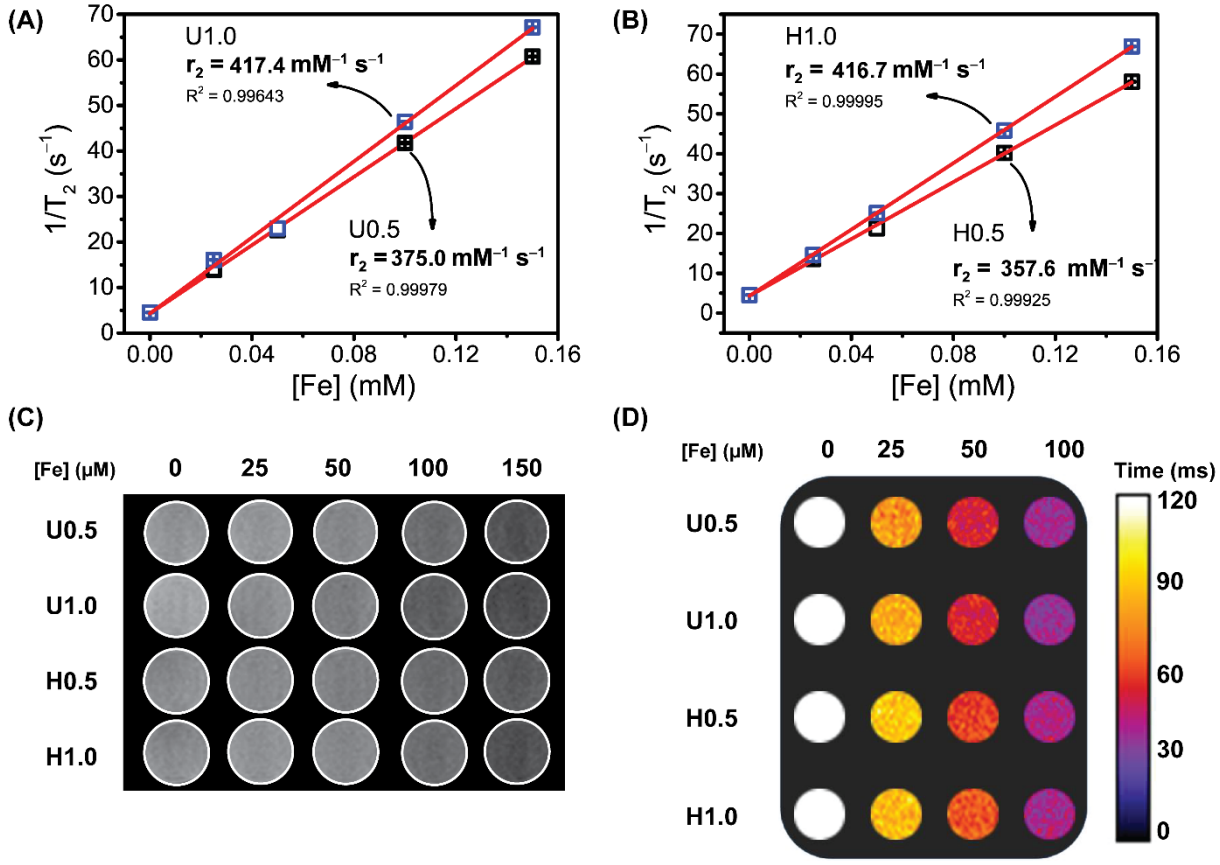

Source: author

2.4 Discussion

2.4.1 Effect of DTPMP in the structural and magnetic properties of MNPs

In this work, the commercial DTPMP was presented as a new functionalizing agent for Fe_3O_4 NPs. For this purpose, DTPMP-coated NPs were synthesized using two different stoichiometries of capping agent (0.5 and 1.0 g), as well as two different well-established methodologies: sonochemistry and hydrothermal synthesis. Therefore, in order to evaluate the changes induced by DTPMP functionalization itself, a complete structural and magnetic characterization of synthesized NPs was performed aiming to understand both the effect of the amount of DTPMP on particles surface and the adopted methodologies.

XRD results indicate that NPs are composed of a single structural phase, which is related to an inverse spinal structure. This phase is characteristic of Fe_3O_4 and γ-Fe_2O_3. Additionally, cubic cell lattice parameters for our samples present values characteristic of NPs,

and also intermediate values between obtained iron oxide phases (8.396 Å for Fe_3O_4 and 8.346 Å for γ-Fe_2O_3) (BAAZIZ *et al.*, 2014; DAOU *et al.*, 2006). Besides these values have been related to partial oxidation of Fe^{2+}, this behavior is not so far discussed herein, in-depth it is already reported in our previous work (NETO *et al.*, 2017).

Samples U0.5 and U1.0 exhibited narrow and well-defined peaks in XRD patterns, which evidence a high crystallinity and small crystallite size for these samples. In comparison, hydrothermally coated NPs showed significant lower average crystallite size. This behavior can be related to time-addition of DTPMP, which in hydrothermal method the functionalizing agent is added in the reaction medium just after NH_4OH addition. The presence of DTPMP molecules, may hinder the growth of the MNPs and lead to smaller and poorly crystallized nanoparticles (OROZCO-HENAO *et al.*, 2016) (Figure 2.1), as shown through crystallite size values obtained by Scherrer's equation and average particle diameter by TEM (Table 1).

TEM micrographs showed a core–shell structure for samples U1.0 and H1.0 (Figure 15B and D), where the core is composed by iron oxide, as already described, and the shell mainly by organic matter. This structure-type was also evidenced for phosphonated polyethylenimine-coated magnetic nanoparticles (MONTEIL *et al.*, 2014). For samples U0.5 and H0.5, the images did not show similar structure profile. Interesting, these samples also presented a thin shell since smaller quantity of DTPMP was used. In this case, during analysis, the high energy of the electron beam of TEM may have degraded the shell of these coated NPs, herein a core-shell structure was not evidencing. Additionally, for U1.0 and H1.0 samples, the organic matter-formed shell may be composed of a complex of DTPMP and Fe ions, which this hypothesis is based on the significant changes observed in the structural and magnetic properties caused by DTPMP functionalization, especially in the interparticle dipolar interactions.

MS spectra profiles and T_B values for the samples could also give a support about shell composition (Figure 14A and C; Figure 14B and D; Figure 18B and Table 1). Regarding to MS analysis, it is important to remember that MS spectrum of bulk Fe_3O_4 is composed by two well-defined ferri- or ferromagnetic sextets, related to Fe^{3+} in tetrahedral sites and Fe^{3+} and Fe^{2+} in octahedral sites. As the size of particles decreases, the sextets exhibit broadened lines as a result of the presence of superparamagnetic fluctuations (DAOU *et al.*, 2009). When size decrease over the superparamagnetic critical size (25–30 nm for Fe_3O_4) leads to a broadened ferrimagnetic sextet, becoming a paramagnetic doublet (KOLEN'KO *et al.*, 2014). However, in real systems, as MNPs interact among themselves mainly through coupling of magnetic dipole, these interactions can affect relaxation processes of the spins in MNPs. Therefore, dipole

interactions can actually change the profile of MS spectra of Fe_3O_4 NPs (GERBER *et al.*, 2015).

Thus, for samples U0.5, U1.0 and uncoated-Fe_3O_4, the expected MS spectra would exhibit a paramagnetic doublet due to MNPs average size values below superparamagnetic critical size. However, when the particles exhibit dipolar interactions, broadened sextets are evidenced even for MNPs below superparamagnetic critical size (GERBER *et al.*, 2015; LEÓN-FÉLIX *et al.*, 2014). Interestingly, for the samples U0.5 and U1.0, the spectra showed broader sextets with respect to uncoated-Fe_3O_4 (Figure 14A), clearly indicating a decrease of dipolar interactions induced by DTPMP functionalization. Additionally, the DTPMP coating provided a significant down shift of B_{hf} of the peak of higher intensity in the B_{hf} distribution, and also induced the appearance of peaks with lower B_{hf} values (Figure 14B). This behavior can be attributed to the increase of NPs population with smaller average diameter, where according to Witte *et al.*, the decrease in B_{hf} value can be induced by a reduction of particles size (WITTE *et al.*, 2016). On the other hand, the presence of paramagnetic quadrupole doublet in MS spectra of the samples H0.5 and H1.0 clearly indicates a lower magnitude of dipolar interactions when compared to samples U0.5 and U1.0 (Figure 14A and C), also supported by the decrease of particle size (WITTE *et al.*, 2016).

Concerning VSM measurements, both applied methodology of synthesis and amount of DTPMP addition did not significantly affect magnetic parameters of the MNPs (Figure 17 and Table 1). Moreover, M_S values for all samples are similar or slightly higher than those reported for functionalized Fe_3O_4 NPs synthesized by hydrothermal, sonochemistry or co-precipitation reaction route (DOLORES; RAQUEL; ADIANEZ, 2015; LU *et al.*, 2013; SRIVASTAVA *et al.*, 2011; WU, Longyun *et al.*, 2015). The H_C values for all samples were very similar, even for the samples H0.5 and H1.0, which showed a duplet in the MS spectra and smaller mean particle diameter when compared to the other samples. Nevertheless, small values of H_C can be related to electric currents trapped in the superconducting coil of the squid magnetometer, which induce artificial broadenings of the hysteresis loops up to 20 Oe for all samples (*inset* in Figure 17).

The amount of DTPMP effect in the dipolar interactions of DTPMP-coated Fe_3O_4 NPs was also investigated through T_B distributions (Figure 18B). As MNPs have great potential to be applied *in vivo*, a deeply evaluation of magnetic dipolar interactions must be performed. In general, cellular uptake assays have shown aggregates formation of MNPs in cell medium (MARTINEZ-BOUBETA *et al.*, 2012; SALAS *et al.*, 2014), consequently influencing their magnetic properties governed by interparticle interactions (LÉVY *et al.*, 2011)(90), as well as their signal generation (LÉVY *et al.*, 2012) and heating efficiency (DI CORATO *et al.*, 2014).

In this regard, it is possible to correlate T_B with dipolar interactions of MNPs, considering that the increase of the strength of the dipole interaction would lead to higher T_B values (SRIVASTAVA *et al.*, 2011). This relation can be performed since the dipole interactions arise from the spin–spin coupling of different nanoparticles, and that the higher this interaction, the greater the barrier energy to occur spin relaxation. In this sense, T_B values by the maximum of ZFC curve (T_{MAX}) and temperature derivative method of the ZFC–FC difference have been measured (Figure 18B and Table 1). These two methods generated different values of T_B, but the trend observed was the same for both. Once temperature derivative method considers aspects present in real systems, it will be consider just their values for now on.

Since the T_B distributions were adjusted by bimodal log-normal distribution, two distributions in the size distribution curves obtained by TEM would also be expected (Figure 15A–D). However, TEM size distributions were not well adjusted with two log-normal distributions. The non-agreement in this respect between TEM size and the T_B distributions occurs because, in TEM, just a fraction of particles have their size measured (150 particles) in contrast to ZFC–FC measurements that consider a bigger population of particles. However, TEM results and T_B distributions converged for the width of the distributions. Samples U1.0 and H1.0 showed narrower T_B distributions and smaller PDI_{TEM} values, in comparison to samples U0.5 and H0.5 (Table 1 and Figure 18B).

In Figure 18B, it is possible to notice that the T_B distributions were significantly affected by the amount of DTPMP added during syntheses, although they exhibited the same average particle diameter, profile of MS spectra, hyperfine parameter distribution, and M_S values, as shown in Figure 13 and 14, Table 1, Figure 17). As whole, we also evidenced that the increasing of the amount of DTPMP leads to a narrower T_B distribution and smaller $<T_B>$ values, indicating that increasing the amount DTPMP a decrease of dipolar interactions is achieved. These results can be supported by TEM micrographs that indicate the presence of core shell-like structure only for U1.0 and H1.0 samples, as shown the red arrows in Figure 15B and D. The shell of DTPMP increases the interparticle distance, which decreases spin–spin coupling and, consenquently, diminishes the dipolar interactions (FLEUTOT *et al.*, 2013; PAULY *et al.*, 2012). This explanation also covers the fact that H1.0 showed lower $<T_B>$values than U1.0, once H1.0 exhibited a thicker shell-like structure (Figure 15B and D).

2.4.2 Mechanism of DTPMP bonding

FTIR and XPS analyses were performed in order to confirm the functionalization, evaluating the nature of interaction between DTPMP and Fe_3O_4 surface and assigning the mechanism of bonding.

XPS spectra for all DTPMP-coated MNPs showed peaks relative to electrons of 2p orbitals of P and 1s orbital of N. In this case, the results evidence the presence of atoms only from DTPMP molecules on the surface of Fe_3O_4 (Table A1), confirming the success of the functionalization of the particles. Additionally, it is also important to notice that as the amount of added DTPMP increases, higher concentration of P and N are evidenced on the surface of Fe_3O_4, as seen in Table A1. This fact is also supported by TEM results, which showed a core-shell structure only for samples U1.0 and H1.0. Indeed, it confirms the proposed hypothesis that samples with larger amount of DTPMP have less interparticle interactions (Table 1, Figure 18 and Table A1).

In high–resolution XPS, the spectra for N1s and O1s showed peaks with similar binding energies for complex DTPMP–Fe sample (Figure 19AB). Concerning to O1s peak, we evidenced that the samples coated with DTPMP exhibited an increase in the ratio between the area of the peaks centered in 531.30 and 530.08 eV, as a result of the contribution of the O atom in the bonds P–O–Fe, P=O and P=O•••Fe (DAOU *et al.*, 2007; DEMIN; MEKHAEV; *et al.*, 2018; PARAMONOV *et al.*, 2008), as seen in Figure 19A. It is also important to notice that the peak in 531.3 eV was also evidenced in the spectrum of DTPMP–Fe complex. For N1s analysis, the spectra indicate that amine groups from DTPMP molecules have considerable contributions to surface functionalization of Fe_3O_4, once the N1s peak centered in 399.7 eV can be attributed to amine groups anchored to iron oxide surface (INCORVIO; CONTARINI, 1989; JUNG; JACOBS, 1995; WANG, Yongliang *et al.*, 2011). Additionally, the same peak is also observed in the spectrum of DTPMP–Fe complex. Furthermore, our results indicate that a higher number of nitrogen atoms from DTPMP molecules interacts with Fe_3O_4 NP surface in comparison to complex sample. This behavior can be evidenced regarding to the higher relative intensity of the peak in 399.7 eV (R_3N^+–Fe) in comparison to 401.7 eV (R_3N^+–H), for all coated samples (Figure 19B). Herein, we could relate the interaction through two nitrogen atoms from DTPMP molecule bonded to Fe atoms on Fe_3O_4 NP surface. Indeed, it also supported by the ratio, approximately ~2, of relative areas of R_3N^+–Fe and R_3N^+–H peaks ($A_{R3N+–Fe}/A_{R3N+–H}$), indicating that the double of R_3N^+–Fe-form nitrogen are bonded to Fe atoms when compared to nitrogen atoms in their protonated form (R_3N^+–H) (Table A1).

To strongly validate our model of interaction between DTPMP and Fe_3O_4, we performed a FTIR spectral deconvolution in the region between 850 and 1220 cm^{-1} for DTPMP-functionalized MNPs. The proposed model was well-fitted to experimental data, giving R^2 values for all deconvolution spectra around 0.9999 (Table 3).

For the DTPMP functionalized MNPs, we inserted bands relative to three chemical groups presented in our model (Figure 20A-C): phosphoric acid groups anchored to Fe atoms (*a"*), amine groups coordinated to Fe (*b*) atoms and free phosphoric acid groups (*c*). Concerning *a"* group, the band ~1166 cm^{-1} can be attributed to P=O, which it is not evidenced for tridentate and monodentate complex forms. Additionally, according to previous works, bands at ~1060 and 990 cm^{-1} are attributed to P–O–Fe groups (DEMIN; MEKHAEV; *et al.*, 2018; THOMAS *et al.*, 2016; TUDISCO *et al.*, 2012; WALTER *et al.*, 2017), which can be assigned to asymmetrical and symmetrical vibrational modes for bidentate form, respectively. These facts indicate a bridging bidentate bonding between phosphoric acid groups from DTPMP molecules and Fe atoms from Fe_3O_4 NPs (Figure 20C *a"*).

Still considering the interaction between amine groups and Fe atoms (Figure 20A-C *b*), we detected a vibrational mode centered at ~1100 cm^{-1} that was assigned to stretching of C–N–Fe. This attribution is considered based on the study of Lanigan *et al*. (2007), which performed FTIR measurements of EDTA-transition metals complexes and observed a vibrational mode, ν_{C-N}, at ~1100 cm^{-1} for the coordination of tertiary amine groups to these metals. Furthermore, we already evidenced ν_{C-N} at ~1100 cm^{-1} for polyethylenimine-functionalized MNPs in a previous work (NETO *et al.*, 2017).

Vibrational modes relative to free phosphoric acid groups were also evidenced in the proposed bonding model. Indeed, after purification procedure, the pH level is around 6 – 7, then the phosphoric acid groups are in the form of $R–PO_3H^-$ (Figure 20C *c*). Thereby, three vibrational modes were detected: symmetrical-asymmetrical PO_2 stretching and P–OH stretching. It is also important to mention that PO_2 stretching for free phosphoric acid must appear in higher wavenumber values in comparison to P–O–Fe stretching, according to Hook's law for vibration springs applied to vibrational spectroscopy (BARJA; TEJEDOR-TEJEDOR; ANDERSON, 1999). Therefore, the proposal of mechanism of bonding was well-adjusted considering Hook's law (See Table 3).

After this whole discussion regarding mechanism of DTPMP bonding, it is also relevant to consider other variations of those bonding possibilities, since the exactly structure of DTPMP-functionalized Fe_3O_4 NPs could be just evaluated by aid of quantum theoretical calculations, which are beyond the scope of this work. However, it has been proved by FT-IR

and XPS that the interaction between DTPMP and Fe_3O_4 NP surface occurs through both phosphate and amine groups from DTPMP molecule, providing an activated surface profile with surface-linked phosphate groups through bidentate bridges and outer free-phosphoric acid groups onto the surface of MNPs, as shown in Figure 20C.

2.4.3 Surface properties of DTPMP-functionalized MNPs

Zeta potential is the electrostatic potential at the shear plane that separates stationary layer and a mobile layer of charges in a surface charged nanoparticle (LUXBACHER, 2014). One of factors which affects ζ value, in functionalized NPs, is the coating thickness. According to Lowry *et al.*, (2016) for nanoparticles with larger coating thickness the imaginary shear plane, which defines ζ, is pushed outward, decreasing the overall magnitude of the zeta potential, even if the nanoparticles have greater amount of charged molecules. Therefore, the smaller magnitude of ζ for the samples U1.0 and H1.0 can be related to the larger coating thickness, evidenced in TEM analysis (Figure 15A–D) (LOWRY *et al.*, 2016).

As the main proposal application of MNPs is to be used in biomedicine, i.e. the site of action is inside human body, the colloidal stability in biological environment is a crucial requirement. Herein, the functionalization agent must be covalently bonding on the surface of the MNPs, and also through specific mechanisms in order to prevent particle aggregation (AMSTAD; TEXTOR; REIMHULT, 2011). Therefore, light-scattering measurements are a key technique in the development of this novel functionalized MNPs, since can better evaluate the behavior MNPs in aqueous suspensions.

Considering DLS results, there is a significant difference among all prepared samples for PDI_{DLS} values. Samples H0.5 and H1.0 present higher *PDI* values than U0.5 and U1.0, which indicates that hydrothermal methodology produced MNPs more polydisperse particles, in agreement with results reported by our group and CAI *et al.*, 2013 (See Table 4).

Furthermore, the synthesized samples exhibited good colloidal stability in physiological solvents, once hydrodynamic size value did not increase upon solvents dispersion. However, a significant increase in PDI_{DLS} values were observed when the samples U0.5 and U1.0 were suspended in PB 7.4 and PBS7.4, although no signal of macroscopic aggregation or precipitation of the particles was evidenced during experiments performance. Moreover, diluted samples of DTPMP-coated MNPs have shown good colloidal stability in water for more than six months.

As DTPMP molecule have both phosphoric acid and tertiary amines, it is expected

that the DTPMP-coated Fe_3O_4 NPs exhibit positive and negative ζ values, depending on pH of the medium. Then, sample U1.0 was selected as a representative sample and its hydrodynamic size and ζ values were evaluated as a function of pH (See Figure 21). At low pH values, positive ζ values were found, due to protonation of amine groups. Above pH of 4.08 (DTPMP IEP), deprotonation of phosphoric acid groups induced negative ζ values. Interestingly, the greater value of hydrodynamic size of the curve was evidenced at pH near IEP, as expected from the electrostatic stabilization mechanism of colloidal NPs. This amphoteric behavior promotes good colloidal stability at different pH, providing a versatility profile of DTPMP- covered MNPs application, principally in biosensing, catalysis, and separation media and biochemistry (MA *et al.*, 2011).

2.4.4 Influence of structural, magnetic and colloidal properties on the performance of the DTPMP-functionalized MNPs as MRI contrast agent

According to the r_2 / r_1 ratio value, MNPs can be classified as T_1-, T_2- and dual-type MRI contrast agent. T_1-type contrast agent has a r_2 / r_1 value lower than 5, whereas r_2 / r_1 values higher than 10 are classified as T_2-type, and values between 5 and 10 can be considered as dual-type contrast agent (ZHANG, Weizhong *et al.*, 2018). Herein, we can consider the MNPs synthesized in this work as T_2 MRI contrast agent, once we determined r_2 / r_1 values of 50.78, 48.25, 44.83 and 43.81 mM^{-1} s^{-1} for the samples U0.5, U1.0, H0.5 and H1.0, respectively (Table 5).

Regarding the transverse relaxivity, our results highlighted the best performance in T_2 weighted MRI for the samples synthesized with 1.0g of DTPMP as seen in Figure 23A–B and Table 5. After extensive structural, magnetic and colloidal characterizations, we could certainly support this behavior.

MRI contrast agents produce contrast in the MRI exams through a shortening (T_2 or T_1) of the relaxation time of protons from water molecules in the surroundings of the contrast agent. The interaction between the contrast agent and water molecules can happen in three different levels, with respect to the contrast agent-water molecule interface: a) inner sphere – portion, where hydrogen atoms from water (or another molecule) bind directly to the paramagnetic metal center; b) second sphere – intermediate sphere of contrast, where the contrast agent interacts with boundary hydrogen nuclei, i.e. not directly to metal center (e.g. diffusing water molecules, exchangeable protons from water molecules in the nearby environment affect the outer sphere relaxation); c) outer sphere – surrounding bulk water

molecules. These portions contribute to the final relaxivity value (r_1 or r_2) (NI *et al.*, 2017; ZHANG, Weizhong *et al.*, 2018). For T_2 contrast agents, second and outer sphere are regions that promote more significantly to relaxivity values (NI *et al.*, 2017; ZHANG, Weizhong *et al.*, 2018). As a consequence, and well-reported, the T_2 relaxivity is principally affected by the size of the magnetic core and the hydrodynamic diameter and surface coating of MNPs (LEE; HYEON, 2012; NI *et al.*, 2017; ZHANG, Weizhong *et al.*, 2018). The size of the magnetic core influences the relaxivity mainly through M_S value, since higher is the M_S more efficiently MNPs can induce field inhomogeneity and can influence a greater volume of surrounding hydrogen atoms (ZHANG, Weizhong *et al.*, 2018).

On the other hand, when functionalized MNPs are dispersed in water, they can interact with themselves to form clusters which may have different hydrodynamic size. This parameter affects r_2 values regarding three distinctive regimes, motional average regime (MAR), static dephasing regime (SDR) and echo-limited regime (ELR). In MAR, r_2 increases with the increasing of the hydrodynamic size value, then reaches a plateau in SDR, which in this stage r_2 is independent of the hydrodynamic size. Furthermore, an increase in the hydrodynamic size leads to a decrease in r_2 (ELR) (PÖSELT *et al.*, 2012).

Regarding to the boundary hydrodynamic size for each regime, PÖSELT et al., 2012 evidence these three regimes for polyethylenglycol-coated MNPs, and according to reported results, DTPMP-coating MNPs can be fitted between SDR and ELR regimes, core and hydrodynamic size values around 8.2–10.4 and 125–151 nm, respectively, where r_2 is maximized. However, the exactly dependency of r_2 to hydrodynamic size is characteristic of each sample, and it can be mainly affected by core-size distribution and dipolar interactions.

Actually, the surface functionalization of MNPs can in-depth affects r_2. For the best of our knowledge, there is no publication reporting a systematic evaluation of the influence of the surface coating properties of MNPs considering these three cited regimes. In general, surface properties of MNPs can affect r_2 through following four manners: a) arrangement of the surface atoms – the capping agent can induce a reduction of surface spin canting, which increases M_S and consequently r_2 values (ZHANG, Weizhong *et al.*, 2018); b) magnetic field inhomogeneity – capping ligands rich in π-electrons can generate small local magnetic fields to an opposite direction, contributing to enhance field inhomogeneity (NI *et al.*, 2017); c) interactions with water molecules – the capping agent plays an important role making water molecules diffuse closer to the magnetic core, which they can be more efficiently influenced by induced magnetic field of magnetic nanoparticles. Thus, it is desirable that the coating layer interacts with water molecules in order to increase their residence time around the magnetic

core (LEE; HYEON, 2012). Therefore, it is expected that the hydrophilicity of the capping agent attached to the nanoparticles' surface plays a key role in their relaxivity properties, where more hydrophilic is the coating higher is r_2 value (DUAN *et al.*, 2008); d) thickness – an increase in the thickness of the coating layer leads to a longer distance between hydrogen atoms and magnetic core, which decreases r_2 (ZHANG, Weizhong *et al.*, 2018). However, Tong *et al.* (2010) suggests that there is an optimal core-to-coating ratio which a higher content of hydrophilic coating compensates the larger distance between protons and core of the MNPs. After synthesizing PEG-coated MNPs, the authors observed that different molecular weights of PEG produced MNPs with different coating thickness, and highest value of r_2 was achieved for – MNPs coated with intermediate value of PEG molecular weight (TONG *et al.*, 2010).

Considering our results, as well as discussed hypothesis, samples U1.0 and H1.0 have a higher relaxivity rate due to their higher hydrophilicity surface in comparison to U0.5 and H0.5 samples. The higher hydrophilic profile of U1.0 and H1.0 are evidenced due to higher content of DTPMP on MNPs surface, which was observed by XPS and TEM analysis as seen in Figure 15 and Table A1. Indeed, these results are in agreement with our previously work that evidenced a higher relaxivity for sodium polyacrylate-coated MNPs in comparison to branched polyethylenimine (NETO *et al.*, 2017), once carboxylate groups promoted a higher hydrophilicity surface when compared to amine groups (ZHENG *et al.*, 2017).

2.4.5 DTPMP-coated NPs are non-toxic for human neutrophils

Though development of new materials for medical applications the non-toxicity profile against human cells must be a crucial requirement. Within this context, cytotoxicity model tests are an important tool to select these materials with acceptable toxic effects. Herein, in this work, freshly isolated cells were used to easier evaluate the biochemical dynamics of the *in vivo* cells in the presence of DTPMP-coated MNPs (TERESA *et al.*, 2013).

Neutrophils are the most abundant leukocytes in human blood and constitute the first line of innate host defense against pathogens and associated acute inflammations (COUTO *et al.*, 2014). Therefore, these cells are highly adequate to evaluate the safety of certain under-evaluated materials to be used through intravenous administration. According to our LDH activity assay results, DTPMP-coated NPs obtained by both sonochemistry and hydrothermal route presented as non-toxic for neutrophil plasma membrane. Additionally, since U1.0 sample showed greater medical-applied characteristics, it was investigated regarding to mitochondrial metabolic activity of human neutrophils by MTT assay (WANG, Piwen; HENNING; HEBER,

2010). As expected, no difference was observed between control group and cells treated with U1.0 at all tested concentrations, proving in-depth that magnetic nanoparticles are non-toxic for plasma membrane and/or metabolism of human neutrophils.

2.4.6 DTPMP-coated NPs as an alternative MRI contrast agent

As already herein reported, this work successfully shows the usage of commercial and costless compound DTPMP as a capping agent of Fe_3O_4 NPs, evaluating the potential application of this novel MNP as MRI contrast agent. Our results greatly support this intended application based on following reasons: a) high colloidal stability in physiological buffers, evidenced by dynamic light scattering experiments; b) good biocompatibility highlighted by the cytotoxicity tests, where none of the samples presented any harmful effect against neutrophils membrane or metabolic activity; c) High r_2 values confirm the potential of DTPMP-MNPs as MRI contrast agents. Indeed, r_2 values of all synthesized samples are 4 to 6 times higher than those of commercial T_2 contrast agents (References: Resovist, Feridex, and Combidex) (WANG, 2011; WANG; HUSSAIN; KRESTIN, 2001). Additionally, our nanoparticles have shown a better performance than other MNPs reported with similar physical-chemical properties and conventional coating agents (CAI *et al.*, 2013; JEDLOVSZKY-HAJDÚ *et al.*, 2012; SANTRA *et al.*, 2009; XU *et al.*, 2009).

Nevertheless, it is important to mention that the sample U1.0 was synthesized in just 12 min, following the sonochemistry methodology developed by our group (NETO *et al.*, 2017), and using only water as solvent. Actually, the ultrasound technique has been shown as a versatile synthetic route methodology which was already suitable for synthesis of amine- and carboxylic acids/carboxylate-functionalized NPs, and now for amino-phosphonate MNPs.

2.4.7 Sonochemistry vs. hydrothermal

Sonochemistry has become a remarkable synthetic route for a wide range of advanced nanomaterials, representing an ecofriendly alternative for time and energy-consuming techniques. (XU; ZEIGER; SUSLICK, 2013; YAO; PAN; LIU, 2020). In this study, we used the chemical power of ultrasound irradiation itself though the well-known cavitation phenomenon, where the high energy induced by implosive collapse of cavitation bubbles could generate localized hot-spots in the liquid. Considering co-precipitation reaction under acoustic cavitation, energy enough is released in a short reaction-time, providing ultrafast synthesis and also increasing crystallinity of nanoparticles (XU; ZEIGER; SUSLICK, 2013). For instance,

ultrasound-assisted surface-functionalized MNPs have been reported with higher M_S values, consequently, leading to a better performance in MRI and hyperthermia applications (LEE *et al.*, 2015; WU, Wei *et al.*, 2015). In our previous work, we synthesized MNPs functionalized with carboxylate and amine groups using sonochemistry approach, which exhibited enhanced magnetic and relaxivity properties in comparison to other conventional methodologies (NETO *et al.*, 2017). As expected, in this currently work, we successfully obtained a novel amino-phosphonate MNP under US irradiation in just 12 min, providing a high-quality material with a potential to be applied as MRI contrast.

For comparison, we also used hydrothermal approach to prepare DTPMP-coated MNPs, which is a conventional synthetic methodology, taking the advantage of performing the synthesis of nanomaterials at temperatures well above the boiling point of the solvent (150 ºC-220ºC). It is possible to achieve these temperatures once the reaction is performed under high pressurized environment, by using a sealed high-pressure reaction vessel. The relatively high temperature should provide nanomaterials with higher crystalline (WU, 2015), in comparison to those synthetic methodologies performed at smaller temperatures (25-100 ºC). In this sense, it is expected that hydrothermally obtained MNPs would have higher M_S values and consequently better performance as T_2 MRI contrast agent (LEE *et al.*, 2015). However, we did not evidence that profile in MNPs synthesized by hydrothermal approach. Indeed, considering MRI performance, all tested samples presented similar behavior. Additionally, the samples U1.0 and H1.0 also showed other similar properties, which exhibited good colloidal stability in physiological fluids (Table 4), non-cytotoxicity to human neutrophilis (Figure 22) and the difference in their transversal relaxivity was just 1 mM^{-1} s^{-1} (Figure 23). The main difference was the layer thickness of the DTPMP coating (Figure 16A), where U1.0 exhibited smaller and more homogeneous thickness of DTPMP coating.

Herein, by using sonochemistry approach, we could achieve a great performance as T_2 MRI contrast agent in a shorter reaction-time, around 17x faster than hydrothermal methodology. Therefore, we truly believe that the sonochemistry is a powerful synthetic approach to obtain amino-phosphonate-functionalized MNPs for MRI contrast agent, principally due to be an easy, fast and low energy cost strategy. Moreover, the novelty of this study may overcome some challenges regarding magnetic nanoparticles in clinical usage.

2.5 Conclusions

In summary, we successfully developed a novel phosphonate-coated material, with outstanding properties, using a commercial capping agent with affordable cost that has been underutilized in the literature. The DTPMP-coated Fe_3O_4 material was prepared through two synthetic methodologies, sonochemistry and hydrothermal approaches. Furthermore, we performed a full characterization of structural, magnetic and colloidal properties of the DTPMP-coated MNPs, which allowed us to conclude: a) increasing of the amount of functionalized DTPMP decreases the dipolar magnetic interactions in Fe_3O_4 NPs, regarding to a formation of shell-like structure for samples with more DTPMP; b) XPS and FTIR analysis confirmed that DTPMP molecule and Fe_3O_4 NPs have a chemical interaction through both amino and phosphate groups from DTPMP; c) DTPMP-coated MNPs have a magneto-fluid response characteristic of a ferrofluid; d) dynamic light scattering experiments confirmed that the surface of synthesized MNPs presents amphoteric properties. Moreover, our results also supported that this novel material has a great potential to be applied as MRI contrast agent, once exhibited colloidal stability in physiological fluids, non-cytotoxicity to human neutrophils and high value of transverse relaxivity.

It is also important to highlight that sonochemistry proved to be a more effective synthetic methodology, considering 17x faster reaction-time. Actually, ultrasound-assisted samples showed greater performance once exhibited similar or even better transversal relaxivity values in comparison to hydrothermal samples. Although we have only tested DTPMP-coated MNPs as MRI contrast agent, and considering their outstanding reported properties, we believe that these versatile nanoparticles could be applied in other technological applications, such as magnetic hyperthermia, separation science, catalysis and sensing.

3 CHAPTER III – FUNCTIONALIZED Fe_3O_4 NANOPARTICLES AS A HIGLY EFFICIENT ELECTROCHEMICAL SENSOR FOR CARBENDAZIM

3.1 Introduction

Pesticides are essential for protecting crops against harmful pests. About 2 million tons of pesticides are used around the world each year. As one of the top food-producing countries, Brazil has a large share of pesticide application (DE *et al.*, 2014; SYAFRUDIN *et al.*, 2021). Excessive use of pesticides can leave residues at unwanted sites and harm non-target species including humans (LAURA *et al.*, 2013). An important place of pesticide contamination is water resource such as streams, lakes, and groundwater, mainly due to the close connection between soil and water bodies (SYAFRUDIN *et al.*, 2021). To avoid human uptake of pesticides through contaminated water and food, it is necessary to monitor them with analytical tools in a precise and timely manner (KUMAR *et al.*, 2020).

Chromatographic techniques are the most commonly methodology for pesticide analysis (GRIMALT; DEHOUCK, 2016), including high-pressure liquid chromatography coupled with diode array detector (HPLC-DAD), mass spectrometry (MS), and gas chromatography coupled with mass spectrometry (GC-MS). These techniques allow the determination of multiple residues with high reproducibility and low limit of detection (LOD) and limit of quantification (LOQ). However, they require not only expensive instruments and supplies (KUMAR *et al.*, 2020) but also specific protocols of sample preparation, such as solid-phase extraction (SPE) frequently used for pesticide analysis in water. These procedures used to clean up, extract, and preconcentrate the analytes also means additional steps and longer time requirement (BONES *et al.*, 2006).

Electroanalytical methodologies have been shown as suitable alternatives to traditional chromatographic techniques, mainly because of their ease of operation, sensitivity, portability, and low instrument cost (ZHU, Chengzhou *et al.*, 2015). Furthermore, the electroanalytical techniques are faster and easier for analyzing pesticides in water because pre-treatment is not required (GOMES *et al.*, 2019). In this context, incorporating nanomaterials onto the surface of the working electrode could increase the efficiency of these devices. Magnetic nanoparticles (MNPs) are popular materials to incorporate into electrodes to enhance the sensor features. Besides ease of preparation, a large surface area, ready availability, and low costs (RAMU *et al.*, 2020), MNPs have an easily functionalizable surface because the Fe atoms there readily interact with carboxylate, amine, phosphonate, and catechol groups (HOLA *et al.*,

2015). Thus, the electrode surface may be efficiently modulated by incorporating MNPs functionalized with different chemical groups. These materials can tailor the electrode-analyte interaction, affecting the electrochemical signal and adsorption of the analyte.

The analyte considered in this study is carbendazim (CBZ), a broad-spectrum fungicide used to prevent pathogen infection in fruits and vegetables (Figure 24A) (FENG *et al.*, 2019). The benzimidazole ring of CBZ provides long-term stability against natural degradation, which contributes to the wide distribution of its residual in water and soil environments (TIAN *et al.*, 2019). Studies in animals indicate that even at low dosages, CBZ affects the liver and causes specific changes in hematological and biochemical parameters (MUTHUVIVEGANANDAVEL *et al.*, 2008). Another animal study concluded that CBZ at sufficiently high doses induces embryo lethality, retarded fetal development, and congenital malformations (SITAREK, 2001). The Brazilian National Health Surveillance Agency (ANVISA) reported that CBZ was one of the most detected pesticides in fruits (PROGRAMA DE ANÁLISE DE RESÍDUOS DE AGROTÓXICOS EM ALIMENTOS 2016-2018, [*s. d.*]). CBZ was also detected in water samples (superficial, river, or tap waters) from several Brazilian states such as São Paulo (MONTAGNER *et al.*, 2014), Mato Grosso (RIBEIRO, A C A *et al.*, 2013), Maranhão (GASPAR *et al.*, 2005), Santa Catarina (DE SOUZA *et al.*, 2016), and Tocantins(GUARDA *et al.*, 2020). In this context, it is necessary to develop new analytical methodologies for the detection and quantification of CBZ.

Several electrochemical sensors using nanomaterials have been developed to detect and quantify CBZ (ILAGER *et al.*, 2021; ÖZCAN; HAMID; ÖZCAN, 2021; SANT'ANNA *et al.*, 2020; ZHANG, Xue *et al.*, 2021). However, the exact mechanism of the redox reactions remains controversial. Four mechanisms have been proposed: *a*) CBZ is oxidized to form a benzimidazole *N*-oxide on the nitrogen atom of the benzimidazole ring (SANT'ANNA *et al.*, 2020)(24); *b*) oxidation reaction to form a benzimidazole-2-ylidene carbamate (ZHOU, Yuanzhen; LI; *et al.*, 2019); *c*) oxidation reaction to generate the 2-hydroxybenzimidazole radical, followed by a dimerization reaction and reduction of ketone groups to alcohols (MAXIMIANO *et al.*, 2016) and *d*) oxidation reaction to form the nitrenium ion on CBZ; The hydroxylation reaction of the benzene ring through an oxidation reaction is followed by additional oxidation to generate quinone imine (TEMGOUA *et al.*, 2021). Liao *et al.* (2019) proposed mechanism *a* based on density functional theory (DFT) calculations; however the corresponding oxidation products were not directly detected. Recently, Temgoua *et al.* (2021) combined electrochemistry with high-resolution MS for product detection to study the

simulated environmental degradation of CBZ, and proposed new possible oxidation products and *d* mechanism.

In this work, we applied three MNPs functionalized with branched polyethylenimine (@BPEI), sodium polyacrylate (@PAANa), and trisodium citrate (@CIT) to modify the surface of glassy carbon electrodes (GCEs). Figure 24B is a schematic representation of the MNPs. First, the MNPs were synthesized by a rapid sonochemical approach developed by our group (NETO *et al.*, 2017) (Figure 24C*a*). Subsequently, $K_4[Fe(CN)_6]$ was used as a probe to measure the electroactive area of the modified working electrodes, and the MNPs causing the most enhancement were selected for the electroanalytical determination of CBZ (Figure 24C*b*). Next, we proposed an electrochemical reaction pathway for CBZ based on LC-MS detection of the oxidized products of CBZ and electrochemical experiments (Figure 24C*c*). Finally, an electrochemical methodology was developed to detect and quantify CBZ in natural waters samples using the selected MNPs (Figure 24C*d*). Overall, this work used a rapid method to prepare nanomaterials for sensor applications, proposed an electrochemical pathway for CBZ oxidation, and developed an electroanalytical methodology for quantifying CBZ in natural waters.

Figure 24 – (A) Molecular structure of CBZ. (B) Schematic representation of functionalized MNPs used in this work. (C) Experimental steps performed in this work.

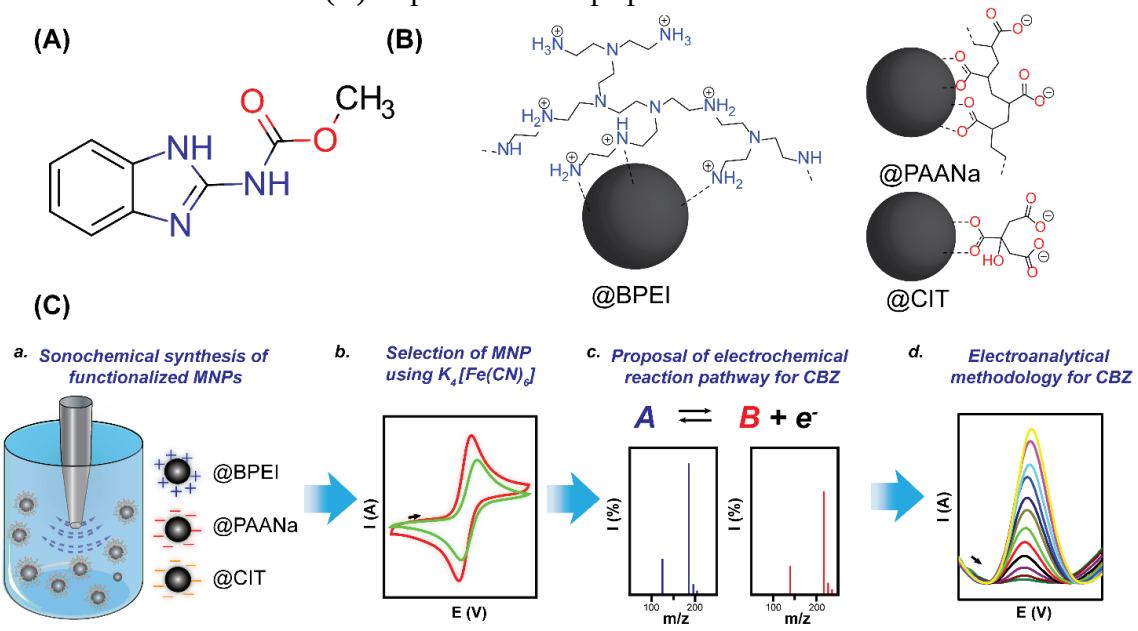

Source: author

3.2 Materials and methods

3.2.1 Materials

$FeCl_3.6H_2O$, $FeSO_4.7H_2O$ and $K_4[Fe(CN)_6]$ were purchased from Vetec Química. PAANa (Mw = 5100), BPEI (Mw = 10000), CIT, CBZ (97%) were purchased from Sigma-Aldrich. Ammonium hydroxide (NH_4OH) (29%) was purchased from Dinâmica Química. All of them were used without further purification. All solutions were prepared with water purified by a Milli-Q system (Millipore Corp.).

3.2.2 Synthesis of functionalized MNPs

Functionalized MNPs were synthesized by the sonochemistry approach developed in our group (NETO *et al.*, 2017), using ultrasound equipment of 20 kHz and a microtip probe of 3.2 mm, under 200 W of power and *3s on* and *1s off* pulse-regime. The samples @BPEI, @PAANa, and @CIT were prepared under the same protocol.

In brief, two aqueous solutions were prepared, an iron salts solution and coating agent (CA) solution. The iron solution contained 1.16 g (4.17 mmol) of $FeSO_4.7H_2O$ and 1.85 g (6.84 mmol) of $FeCl_3.6H_2O$ dissolved in 15 mL of water, while the CA solution contained 1.0 g of CA in 4.0 mL of water. The solution of iron salts was heated until 60 ºC and sonicated for 1 min. Afterward, NH_4OH was added under sonication for 4 min. Finally, the CA solution was also added under sonication for 4 min.

Several washes with water removed the excess of NH_4OH and unbounded CA molecules. Finally, the samples were dispersed in water and centrifuged for 10 min at 3000 rpm to remove large aggregates. Thus, the samples were de-aerated with nitrogen to remove the dissolved oxygen and stored in deionized water under 10 ºC.

3.2.3 Characterization of MNPs

Transmission electron microscopy (TEM) images were obtained with an MSC JEOL TEM-2100 200 kV microscope, equipped with a CCD (TVip–16 MP) and TV (Gatan ES500W) available from LNNano, Campinas, Brazil. TEM samples were dispersed in isopropyl alcohol and deposited in a drop onto carbon-coated copper grids. Subsequently, the deposited samples were allowed to dry completely overnight before analysis. The size distribution curves were obtained by manually measuring 150 particles (JIN *et al.*, 2015), using

ImageJ (U.S. National Institutes of Health, Bethesda, MD). The polydispersity index for TEM analysis (PDI_{TEM}) was calculated as reported in literature (TIUNOV *et al.*, 2016).

Chemical surface analyses of the nanoparticles were carried out in a K-alpha X-ray photoelectron spectrometer (XPS) (Thermo Fisher Scientific, United Kingdom) equipped with a hemispherical electron analyzer and an aluminum anode ($K\alpha$ = 1486.6 eV) as X-ray source. Measurements were carried out using charge compensation during the analyses, and the chamber's pressure was kept below 2×10^{-8} mbar. Survey (i.e., full-range) and high-resolution spectra were recorded using pass energies of 1 and 0.1 eV, respectively. The spectrum fitting was performed by assuming a mixed Gaussian/Lorentzian peak shape (the ratio of the Gaussian to Lorentzian form was 0.4). The X-ray photoelectron spectra presented here result from the average of three spectra collected at three different regions for each sample.

3.2.4 Sensor preparation

Electrochemical sensors were prepared by modifying the surface of the glassy carbon electrode (GCE – Ø 3 mm) with @BPEI, @PAANa, and @CIT suspensions, in a concentration of 1 mg mL^{-1} for all MNPs. Before modification, the GCE electrode was polished with 3 µm diamond paste and sonicated in absolute ethanol and water for 3 min. Afterward, 5 µL of MNPs suspensions were drop-casted onto the GCE surface. Finally, the solvent was evaporated at 40 ºC for 20 min. When the sensor was not in use, it was stored in a desiccator.

3.2.5 Electrochemical experiments

All electrochemical experiments were carried out at room temperature, using Autolab PGSTAT 101 Metrohm- Eco Chemie controlled by a personal computer, using Nova version 1.11 or 2.00 software. Furthermore, we employed a three-electrode system consisting of modified GCE as working electrode, a Pt sheet as the auxiliary electrode, and $Ag_{(s)}/AgCl_{(s)}/Cl^-_{(aq)}$ (saturated KCl) as the reference electrode. For these experiments, a cell containing 10 mL of supporting electrode was used.

We used Cyclic voltammetry (CV) in $K_4[Fe(CN)_6]$ to select the magnetic nanoparticle to be used in CBZ determination by measuring the electroactive area of each modified GCE. For this study, successive voltammograms were registered with a window potential of –0.2-0.7 V, varying scan rate from 0.01 to 0.150 V s^{-1}. Electrochemical active areas were calculated using the Randles-Sevcik equation (PERIYASAMY *et al.*, 2019).

CV and square wave-voltammetry (SWV) experiments, using CBZ as an analyte, were performed in a window potential of 0.3-1.5 V. Before any measurement of SWV in CBZ, we performed three SWV measurements in Britton-Robinson (BR) buffer 0.04 mol L^{-1}. Both CV and SWV were used to characterize the electrochemical behavior of CBZ, while only SWV was the electrochemical technique to propose analytical methodology. To regenerate the working electrode surface area between SWV measurements and ensure the experiment's reproducibility, we performed a SWV measurement in the cell containing only the supporting electrolyte.

3.2.6 Electroanalytical methodology

Before analytical development, we optimized pH, supporting electrolyte, accumulation potential and time, potential pulse frequency (*f*), pulse amplitude (*A*), and height of the potential step (ΔEs), towards maximum values of sensibility and selectively (peak current and half peak width). Afterward, analytical curves were constructed from the correlation between peak current ($\boldsymbol{I_P}$) and CBZ concentration ([CBZ]). Linear regression was performed by the method of least squares. Finally, the confidence limit of the slope (CL_b) and intercept (CL_a) were calculated according to Miller and Miller (34).

Limit of detection (LOD) was calculated according to instrumental signal (Y_{LOD}), which is significantly different from the blank signal (Y_{BL}), as proposed by Miller and Miller (MILLER; MILLER, 2018), once this method is more suitable for our system. The instrumental signal was calculated by equation 3.1:

$$Y_{LOD} = Y_{BL} + 3 \times S_{BL} \quad (3.1)$$

Where S_{BL} is the standard deviation from ten measurements of Y_{BL}. Then, the concentration related to Y_{LOD} was calculated using linear regression. Finally, the limit of quantification (LOQ) was calculated similarly, according to equation 3.2:

$$Y_{LOQ} = Y_{BL} + 10 \times S_{BL} \quad (3.2)$$

Likewise, the concentration related to Y_{LOQ} was calculated by equation from linear regression.

The precision of the proposed method was evaluated based on the reproducibility of $\boldsymbol{I_P}$ values of the standard solution of CBZ using five modified electrodes. Moreover, the method's repeatability was assessed by measuring seven consecutive $\boldsymbol{I_P}$ values of the same CBZ solution.

For comparison, we used the method developed by PALMA *et al.* (2004) to perform a calibration curve for CBZ, using HPLC-DAD (model Shimadzu 20A prominence and detector SPD-M20A). Standard solutions of CBZ, ranging from $1.05 \times 10^{-7} – 1.26 \times 10^{-6}$ mol L^{-1}, were prepared in acetonitrile (ACN) and injected in HPLC using isocratic elution of the mixture ACN/ammonium acetate 1 mmol L^{-1} 1:3, on the C18 reversed-phase column (30 cm 4.0 mm D.I and 0,45 µm particle diameter), a column temperature of 35 ºC and injection volume of 25 µL

3.2.7 Electrochemical analysis of CBZ in natural waters

To confirm the applicability of the electrochemical sensor developed herein, we performed CBZ recovery measurements in natural waters from two locations in the state of Ceará, Brazil. One sample was collected in Acarape do Meio reservoir, located in Redenção, characterized by high pollution due to domestic sewerage and agricultural practices, such as bananas, beans, and corn. Another sample was collected in the city of Pacatuba, which is responsible for the water supply to Fortaleza, the capital of the state of Ceará (Gavião reservoir) (OLIVEIRA *et al.*, 2013).

The sample preparation was performed according to França *et al.* (2012). First, the sample was strained in a 0.5 µm filter to remove particulate components. Then supporting electrolyte was prepared by dissolving BR buffer salts in the natural waters, and the pH of the solution was adjusted to 3.0, and SWV measurements were performed without further treatment. The exaction was studied based on recovery (*R%*) of CBZ, which was performed in the doped samples adding known amounts of the pesticide. The CBZ recovery was calculated using equation 3.3:

$$R(\%) = 100 \times \frac{[\mathrm{CBZ}]_{\mathrm{found}}}{[\mathrm{CBZ}]_{\mathrm{added}}} \qquad (3.3)$$

The uncertainty of the measurement was performed according to the equations described in (HARRIS, Daniel C., 2010; MILLER; MILLER, 2018), and the method's precision was evaluated from the BIAS parameter.

3.2.8 Elucidation of electrochemical oxidation mechanism of CBZ

We proposed a possible pathway for electrochemical reactions of CBZ with the aid of electrochemical experiments and the detection of the products generated by exhaustive electrolysis and identified by mass spectrometry analysis.

Exhaustive electrolysis was performed by chronoamperometry under a potential of 1.3 V for 9 h in acetic acid/acetate buffer (0.04 mol L^{-1}) at pH 3.3. For this experiment, CBZ concentration was 9.90 μmol L^{-1}, and GCE was modified with @BPEI suspension. For an electrode area of 321.84 mm^2, 117 μL of 1.0 mg mL^{-1} @BPEI suspension was used. A volume of the solution (reaction medium) was immediately injected into a HPLC-DAD system under the same conditions described in section 3.2.6.

The reaction medium from electrolysis was also analyzed by electrospray ionization mass spectrometry (ESI-MS). ESI-MS spectra were obtained for mass structural characterization using an LTQ Orbitrap XL (Thermo Fisher Scientific, Bremen, Germany). The LTQ-Orbitrap XL was equipped with electrospray ionization (ESI) source, which was operated in positive ion mode. Positive ion source settings were: Capillary temperature 300 °C, sheath gas flow 25, auxiliary gas flow 17, sweep gas flow 5, source voltage 3.5 kV, source current 100.0 μA, capillary voltage 18 V, and tube lens 75.0 V. Full scan MS data were obtained over the mass range of 100 to 400 Da. The samples were injected using the direct infusion method. Mass spectrometric data were collected using Xcalibur version 2.1 (Thermo Fisher Scientific, Bremen, Germany).

3.2.9 Theoretical calculation of UV absorption spectra of possible oxidation products

All molecules were optimized in density functional theory (DFT)(PARR; WEITAO, 1994) level using B3LYP (TIRADO-RIVES; JORGENSEN, 2008) hybrid functional and 6-311G* basis set without symmetry constraint. The calculation of positive frequencies confirmed the ground state of each molecule. Solvent effects were considered in the simulations using CPCM continuum solvation model (TAKANO; HOUK, 2005) implemented in ORCA Version 4.1.2 package (NEESE *et al.*, 2020). The TD-DFT (ADAMO; JACQUEMIN, 2013) calculations of transition energies were performed on optimized geometries with the same functional, basis set, and solvation model. The creation of ORCA inputs and the theoretical UV absorption spectra analysis were performed in the Avogadro (HANWELL *et al.*, 2012) and Gabedit (ALLOUCHE, 2011) software, respectively.

3.3 Results and discussion

3.3.1 Characterization of MNPs

The performance of MNP-based electrochemical sensors is affected by properties of the MNPs, such as their size, morphology, and surface chemistry. Therefore, we performed TEM and XPS analysis of the MNPs in order to understand the electrochemical results (LUO *et al.*, 2014).

In terms of morphology, all the MNPs were pseudo-spherical (Figure 25A–C), which is expected when the Fe_3O_4 NPs were synthesized through the coprecipitation of Fe^{2+} and Fe^{3+} ions by ammonium hydroxide (LU *et al.*, 2013). The particle size distribution curves are provided as insets in Figure 25A–C, and these data were used to calculate the average particle diameter (D_{TEM}) and polydispersity index (PDI_{TEM}). The samples @BPEI, @PAANa, and @CIT had D_{TEM} values of 8.74 ± 2.35, 9.28 ± 4.78, and 8.49 ± 2.66 nm, and their PDI_{TEM} values are 0.269, 0.516, and 0.313, respectively. One-way ANOVA and Tukey's test ($p < 0.05$) did not show a significant difference in the average diameter for all MNPs, although @PAANa had a higher degree of polydispersity. The TEM micrographs in Figure 25D–F have sufficiently high magnification to show well-defined exposed crystallographic facets and crystalline planes, indicating good crystallinity in the samples. Furthermore, the HRTEM images revealed the interplanar distances of 0.470, 0.284, and 0.240 nm, which agree well with the (111), (220), and (222) planes for the crystalline phase of the inverse spinel of magnetite (Fe_3O_4). However, our results did not support the assumption that the exposed planes in Figure 25D–F are the main exposed planes.

XPS is a surface-sensitive technique suitable for characterizing surface functional groups. The XPS survey spectra and the deconvoluted subcomponents are presented in Figure B1 and Table B1, exhibited in Appendix B, respectively. All samples evidenced the $Fe2p_{3/2}$ (709.98–710.78 eV) and $Fe2p_{1/2}$ (723.68–724.38 eV) signals due to the Fe atoms of Fe_3O_4 (Table B1). On the functionalized Fe_3O_4 nanoparticle surface, there were N1s and C1s signals from the BPEI, PAANa, and CIT molecules (Figure 26A–F and Table B1).

Figure 25 – TEM micrographs of functionalized MNPs. (A) and (B): @BPEI; (C) and (D): @PAANa; (E) and (F): @CIT. The crystal planes and their interplanar distances are labeled in yellow. Insets: size distribution curves of the MNPs.

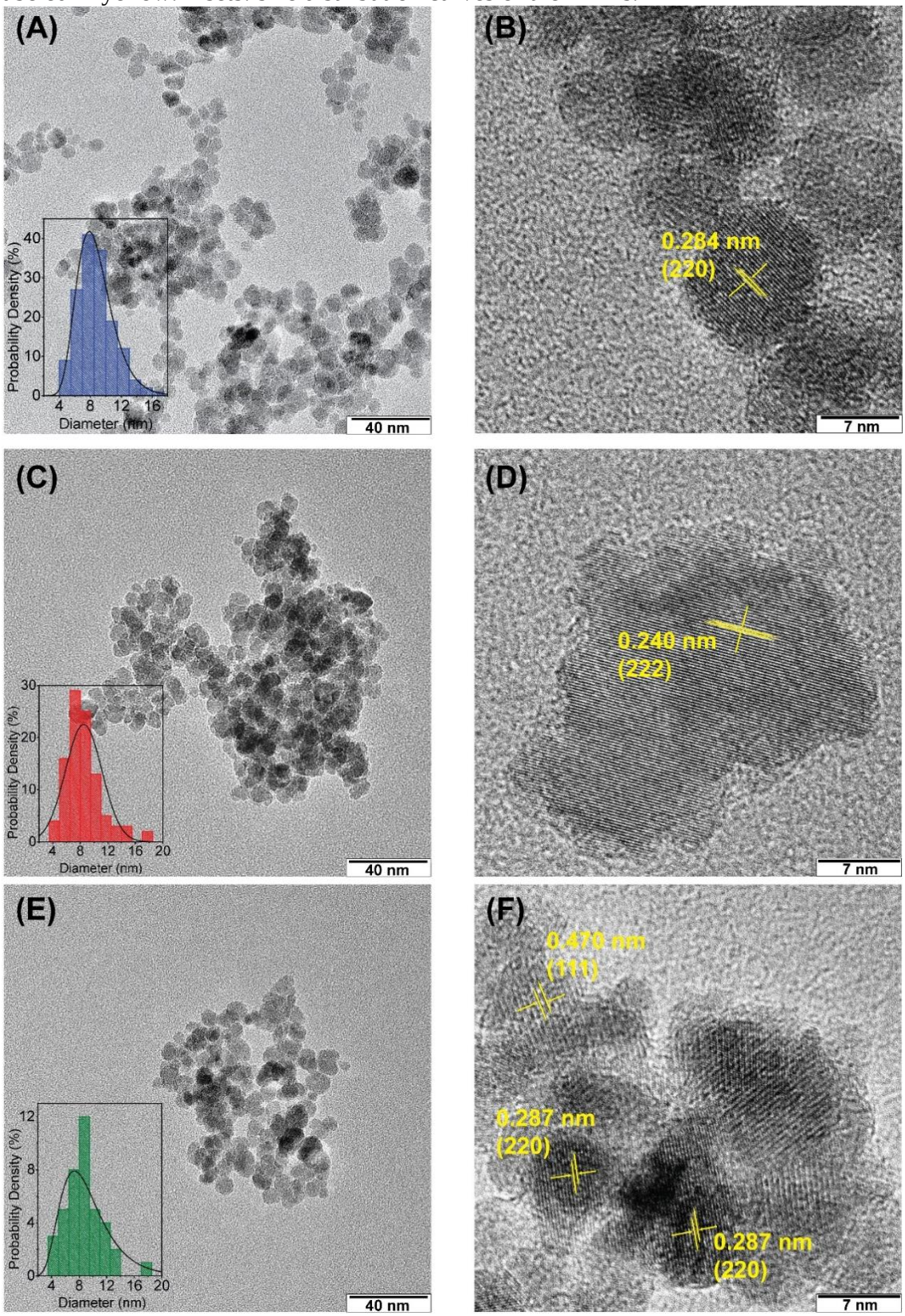

Source: author

The N1s spectra of @BPEI included three components centered at 399.02, 400.63, and 404.20 eV, as shown in Figure 26A and Table B1. The amine nitrogen of BPEI (C–***N***R_2) has the lowest binding energy (ARTYUSHKOVA *et al.*, 2017; CONRADIE; CONRADIE; ERASMUS, 2014; INCORVIO; CONTARINI, 1989; WANG, Yongliang *et al.*, 2011). Moreover, the binding energy of nitrogen bonded to Fe of Fe_3O_4 (Fe–***N***$^+R_3$) is also within this region (GRAF *et al.*, 2009). Thus, this observed peak may contain contributions from both groups. The component at 400.63 eV was assigned to nitrogen in protonated amine groups (–***N***$^+R_3$), while that with the highest binding energy is related to the N1s shake-up satellite (EVANGELISTA *et al.*, 2009). The C1s spectrum also presents three components at 285.35, 288.00, and 291.82 eV (Figure 26B). The first component can be attributed to carbon atoms bonded to free amine groups (N–***C***) and amine groups bonded to Fe atoms (Fe–N–***C***) (LOUETTE; BODINO; PIREAUX, 2005b). Interestingly, the relative area of this component in C1s is close to those of the C–***N***R_2 and Fe–***N***$^+R_3$ components in N1s (Figure 26A–B and Table B1). The component at 288.00 eV is related to carbon atoms bonded to protonated amine groups (***C***–N^+R_3), and its percentage area is close to the related N1s component of –***N***$^+R_3$ (Figure 26A–B and Table B1) (LOUETTE; BODINO; PIREAUX, 2005b). The component with the highest energy (291.82 eV) is a C1s shake-up satellite (EVANGELISTA *et al.*, 2009).

For @PAANa and @CIT, Figure 26C–F shows their high-resolution spectra in the O1s and C1s regions. These two samples have similar spectral profiles, because of the proximate chemical composition of the functionalized agents. Thus, @PAANa and @CIT share the same spectral assignments. The high-resolution spectra of O1s reveals four components at 530.06, 531.31, 533.55, and 236.47 eV (Figures 2C and E). The signal at the lowest energy can be assigned to the oxygen atoms of Fe_3O_4 NPs (Fe–***O***) (POULIN *et al.*, 2010). That at 531.31 eV comes from hydroxyl groups on the surface of Fe_3O_4 NPs (Fe–***O***H), (POULIN *et al.*, 2010) although there are also minor contributions from carboxylate groups in free form (C–***O***) and coordinated to Fe atoms (C–***O***–Fe) (DEMIN *et al.*, 2018; LOUETTE; BODINO; PIREAUX, 2005). Moreover, the signal at 533.55 eV is attributed to absorbed water molecules and protonated carboxylate groups (C–***O***–H) (LOUETTE; BODINO; PIREAUX, 2005a; POULIN *et al.*, 2010). The signal at the highest energy is due to the O1s shake-up satellite (GROSVENOR *et al.*, 2004). Furthermore, high-resolution C1s spectra for @CIT and @PAANa exhibited four signals at 284.77, 286.45, 288.49, and 290.83 eV (Figures 2D and F). The signal at the highest energy is due to the shake-up satellite (EVANGELISTA *et al.*, 2009), while the first three can be respectively assigned to the ***C***–***C*** (284.77 eV), ***C***–O (286.45 eV), and O=***C***–O (288.49 eV) groups of PAANa and CIT (LOUETTE; BODINO; PIREAUX,

2005b).

Figure 26 – High-resolution XPS spectra of functionalized MNPs. (A) N1s spectrum of @BPEI, (B) C1s spectrum of @BPEI, (C) O1s spectrum of @PAANa, (D) C1s spectrum of @PAANa, (E) O1s spectrum of @CIT, and (F) C1s spectrum of @CIT.

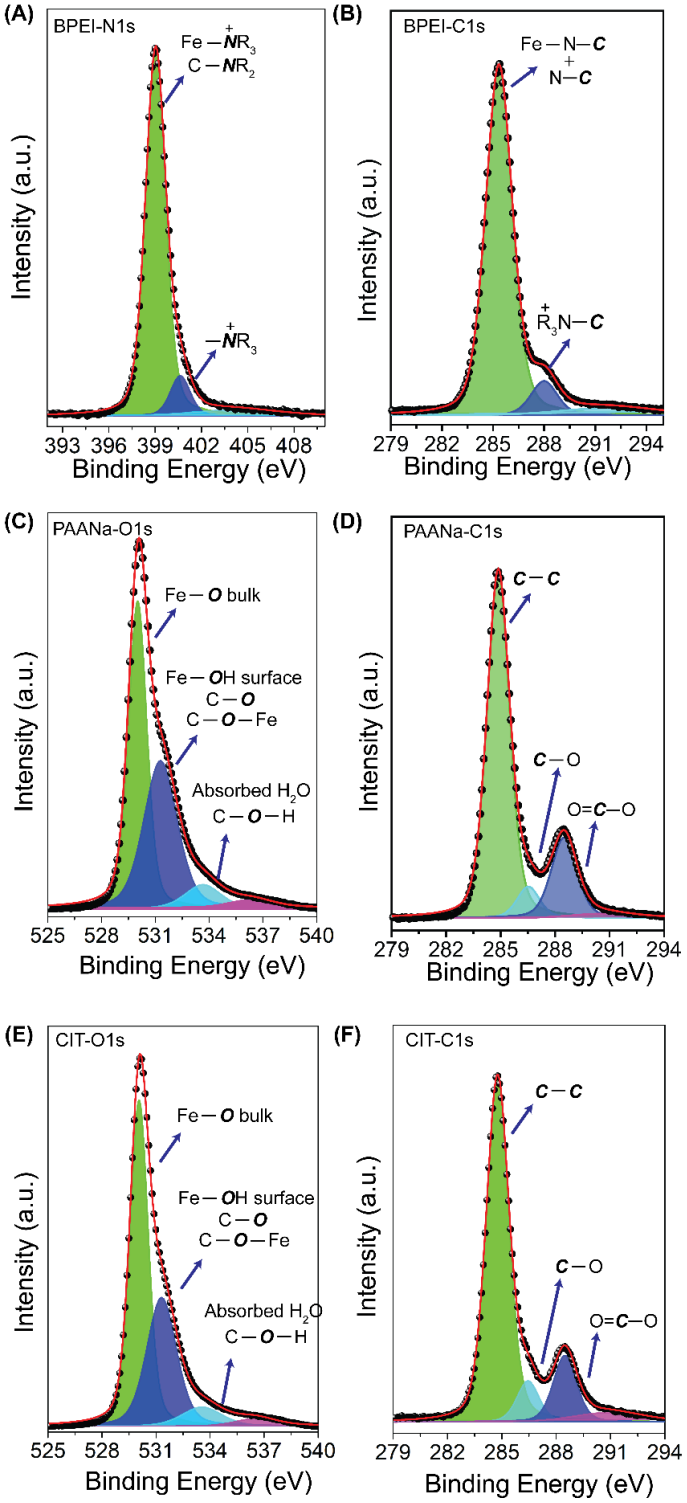

Source: author

3.3.2 Electrochemical performance of MNPs-modified GCE in the ferrocyanide/ferricyanide system

To evaluate the effects of GCE functionalization by different MNPs, CV measurements (2×10^{-3} mol L^{-1} $K_4[Fe(CN)_6]$ in 0.1 mol L^{-1} KCl, scan rates of 10–150 mV s^{-1}) were carried out for GCE modified with @BPEI, @PAANa, and @CIT (Figure 27A). The electroactive areas for the bare and modified GCEs were calculated using the Randles–Ševčík equation and shown in Figure 27B. @BPEI, @PAANa, and @CIT all increased the electroactive area compared to bare GCE by 18.5%, 12.2%, and 12.7%, respectively. This enhanced electroactive area can be explained by the magnetic nanoparticles creating a magnetic field in specific direction due to the electric field, thereby facilitating the electron flow (KAUSHIK *et al.*, 2009). In addition, modifying the electrode surface with any nanomaterial tends to increase the surface area and facilitate electron transfer (RAMU *et al.*, 2020). The difference between the anodic and cathodic peak potentials ($\boldsymbol{E_{pa} - E_{pc}}$) was 74.9 ± 1.1, 90.3 ± 1.6, 98.9 ± 4.7, and 74.9 ± 1.3 mV for @BPEI, @PAANa, @CIT, and bare GCE, respectively. Among the functionalized electrodes, @BPEI produced a larger surface area than @PAANa or @CIT (Figure 27B). Our characterizations indicated that the main difference between these MNPs was the functional surface groups (see Section 3.3.1). @BPEI contains free amine groups on the surface, which are protonated at pH < 6.5 (NETO *et al.*, 2017) to generate positive charges that further facilitate electron transfer of $K_4[Fe(CN)_6]$ and enhance the electroactive area (RAMU *et al.*, 2020; SOUSA *et al.*, 2017). Based on these results, we selected GCE modified with @BPEI as the working electrode for CBZ detection.

3.3.3 Electrochemical behavior of CBZ on @BPEI/GCE

3.3.3.1 Cyclic and square-wave voltammetry conditions

During the first CV cycle, the response to CBZ included one anodic ($P2_a$) and two cathodic processes ($P2_c$ and $P1_c$), as shown in Figure 28A. Interestingly, the second CV scan revealed an anodic process ($P1_a$) as a reversible process of $P1_c$. An explanation for this behavior will be given later in Section 3.3.4. First, the anodic ($P1_a$) and cathodic ($P1_c$) potential peaks ($\boldsymbol{E_P}$) were around 0.70 and 0.68 V, while the second anodic ($P2_a$) and cathodic ($P2_c$) processes appeared at 1.08 and 1.03 V, respectively. The influence of scan rate ($\boldsymbol{v}$) on $P2_a$ was studied for v = 0.1–1.5 V s^{-1} (see Figure B2A–B). The value of $\boldsymbol{I_P}$ varied nonlinearly with $\boldsymbol{v^{0.5}}$ (Figure B2B), whereas $\boldsymbol{I_P}$ was linear to $\boldsymbol{v}$ with a correlation coefficient (R^2) of 0.9962, indicating an

adsorption-controlled process (COMPTON; BANKS, 2007) (Figure B2A). Furthermore, these CV experiments are essential for proposing the mechanism of CBZ oxidation, and the related results will be discussed in Section 3.3.4. Because of the low response to the analyte under these CV conditions, SWV was chosen instead for the electrochemical detection of CBZ.

Figure 27 – (A) CV curves of $K_4[Fe(CN)_6]$ (2×10^{-3} mol L^{-1} in 0.1 mol L^{-1} KCl) at a scan rate of 75 mV s^{-1}. Working electrode: GCE modified with @BPEI, @CIT, and @PAANa, and non-modified GCE. (B) Electroactive area of MNP-modified GCEs and non-modified GCE. The areas were calculated using the CV data and the Randles-Ševčík equation.

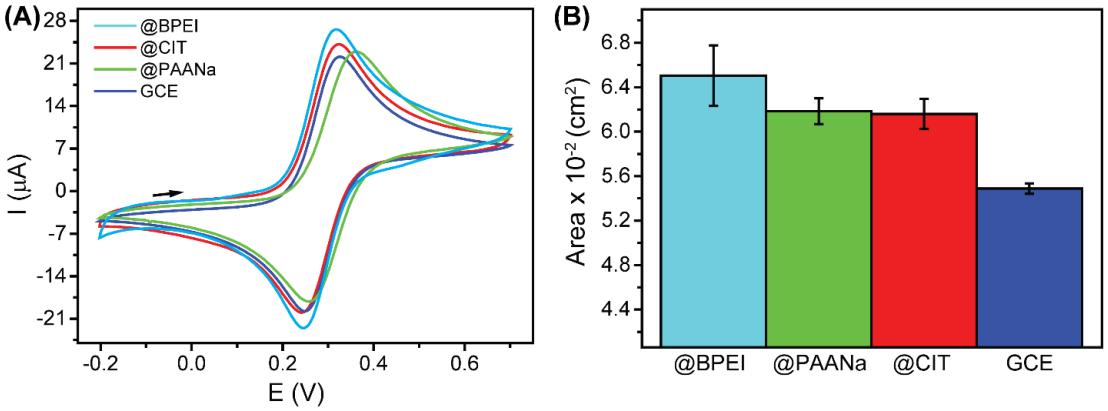

Source: author

The SWV characterization data of CBZ (Figure 28B) revealed two anodic ($P1_a$ and $P2_a$) and two cathodic processes ($P1_c$ and $P2_c$) in the forward and backward components, respectively, similar to the behavior observed in the CV results (Figure 28A). The peak potentials in the first process were 0.70 ($P1_a$) and 0.73 V ($P1_c$), while the second anodic and cathodic processes ($P2_a$ and $P2_c$) had the same peak potential of 1.09 V. These processes are only related to CBZ, as the blank voltammogram did not show any redox reaction (Figure B3). Because of the higher peak values, we selected $P2_a$ as the signal for developing the electroanalytical methodology. Thus, the values of $\boldsymbol{I_P}$ and the half-peak width ($\Delta E_{P/2}$) of $P2_a$ were optimized to increase the sensitivity and selectivity of the electroanalytical method.

Figure 28 – Electrochemical behavior of CBZ during (A) CV and (B) SWV. Electrolyte: 0.04 mol L^{-1} BR buffer , pH = 3.0, [CBZ] = 9.90 µmol L^{-1}; CV scan rate: 0.6 V s^{-1}. Optimization of electrolyte pH: (C) SWV of CBZ at different electrolyte pH values and (D) dependence of the forward peak current (I_P) and the potential (E_P) as a function of electrolyte pH. @BPEI concentration: 1 mg mL^{-1}; SWV parameters: f = 100 s^{-1}; a = 50 mV; ΔEs = 2 mV. Inset in (A): CV curves for the regions of $P1_a$ and $P1_c$.

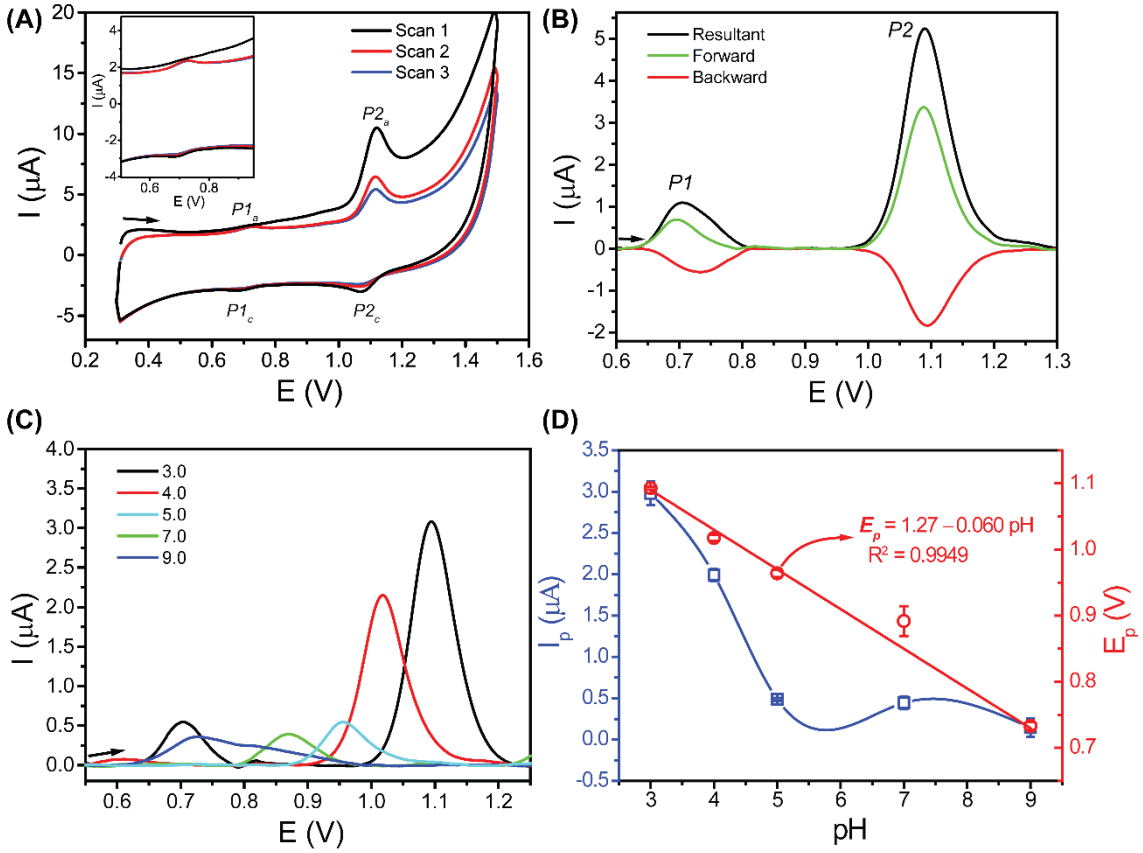

Source: author

To reveal the role of BPEI in the electroanalytical determination of CBZ, SWV experiments were also performed under the same conditions with bare GCE, GCE modified with uncoated Fe_3O_4 NPs, and free BPEI. Figure 29 shows the $P2_a$ data for all electrodes. The average values of I_P (n = 5) were 4.45 ± 1.26, 3.38 ± 0.88, 2.71 ± 0.74, and 3.05 ± 0.13 µA; and their average E_P values (n = 3) were 1.068 ± 0.001, 1.072 ± 0.005, 1.069 ± 0.002, and 1.093 ± 0.002 V for bare GCE, uncoated Fe_3O_4, free BPEI, and @BPEI, respectively. Thus, @BPEI induced a smaller I_P value compared to the uncoated Fe_3O_4 and a higher E_P value compared to all other electrodes. Subsequently, the electrodes were compared in terms of their ability to regenerate after measurements and maintain similar I_P values. Figure 30A–D show five successive SWV measurements of CBZ. The variance in the obtained I_P values is 28.3%, 25.9%, 27.2%, and 4.3% for bare GCE, uncoated Fe_3O_4, free BPEI, and @BPEI, respectively. These results indicate that @BPEI has enhanced the capacity to regenerate working electrode

at least several times.

These results can be explained by the following factors. *i*) At pH = 3, the amine groups of BPEI are protonated, leading to a positively charged surface. *ii*) Because CBZ has pKa = 4.3, the benzimidazole nitrogen is protonated at pH = 3 with an overall positive charge on the CBZ molecule. *iii*) Therefore, the presence of @BPEI decreases CBZ adsorption through electrostatic repulsion. RAMU *et al.* (2020) reported an increase in $\boldsymbol{I_P}$ by modifying carbon electrodes with @BPEI. However, their target analyte was bisphenol A, which under the studied conditions carry the opposite electrostatic charge to that of BPEI. The increase in $\boldsymbol{E_P}$ values also corroborates this hypothesis, as a higher energy is required to drive the redox reaction.

3.3.3.2 Optimization of electrochemical parameters for CBZ determination

The first parameter to optimize was pH of the supporting electrolyte (BR buffer), which was varied from 3.0–9.0. Figure 28C shows the SWV data under different pH values, and the $\boldsymbol{I_P}$ and $\boldsymbol{E_P}$ values for $P2_a$ are shown in Figure 28D. Figure B4 shows the $\boldsymbol{I_P}$ and $\boldsymbol{E_P}$ values for $P2_c$. For both processes, we observed a decrease in $\boldsymbol{I_P}$ upon increasing the pH (Figure 28D and Figure B4). Therefore, the optimal pH is 3.0. Likewise, $\boldsymbol{E_P}$ shifted to lower values as pH increased (Figure 28D and Figure B4), as predicted by the Nernst Equation (WALCZAK *et al.*, 1997). For $P2_a$, the relationship between $\boldsymbol{E_P}$ and pH can be described by $\boldsymbol{E_P}(P2_a) = 1.27 - 0.060\ pH$ (Figure 28D). The calculated slope (60 mV) was close to the theoretical value for an electrochemical reaction with the same number of protons and electrons (BARD; FAULKNER, 2000; HO *et al.*, 2015). $P2_c$ showed the same results (Figure B4).

Subsequently, the supporting electrolyte, the accumulating time and potential, and the SWV parameters were optimized, and the results are shown in Figures B5, B6, and B7, respectively. The optimized conditions are: *a*) BR buffer as supporting electrolyte; *b*) accumulating time of 60 s and accumulating potential of 0.95 V; *c*) SWV parameters: $f = 70\ s^{-1}$, a = 50 mV, and ΔEs = 2 mV. These conditions were used for the electroanalytical determination of CBZ.

Figure 29 – Square-Wave Voltammetry (SWV) of carbendazim (CBZ) 9.90 µmol L^{-1} in Britton-Robinson buffer (BRB) 0.04 mol L^{-1} pH = 3.0 using as working electrodes: unmodified Glassy carbon electrode (GCE), and modified GCE with branched polyethylenimine (Free BPEI), Magnetite NPs (Fe_3O_4), and @BPEI. Concentration of modifying agents: 1mg mL^{-1}. SWV parameters: frequency (*f*) = 100 s^{-1}; amplitude (*a*) = 50 mV; step potential (ΔEs) = 2 mV.

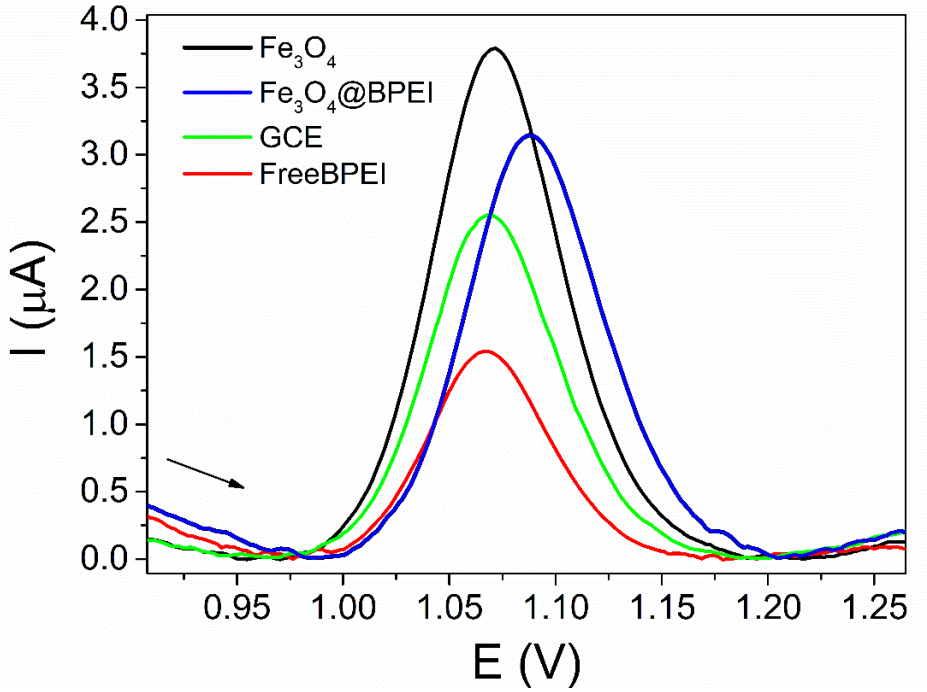

Source: author

Figure 30 – Comparison of the capability to regenerate the working electrode for SWV in CBZ 9.90 µmol L^{-1} of the followed working electrodes: (A) GCE, (B) Free BPEI, (C) Fe_3O_4, (D) @BPEI. Regeneration methodology: SWV measurement in the BRB 0.04 mol L^{-1} without CBZ. Electrolyte: BRB 0.04 mol L^{-1} pH = 3.0. Concentration of modifying agents: 1mg mL^{-1}. SWV parameters: f = 100 s^{-1};A = 50 mV; ΔEs = 2 mV.

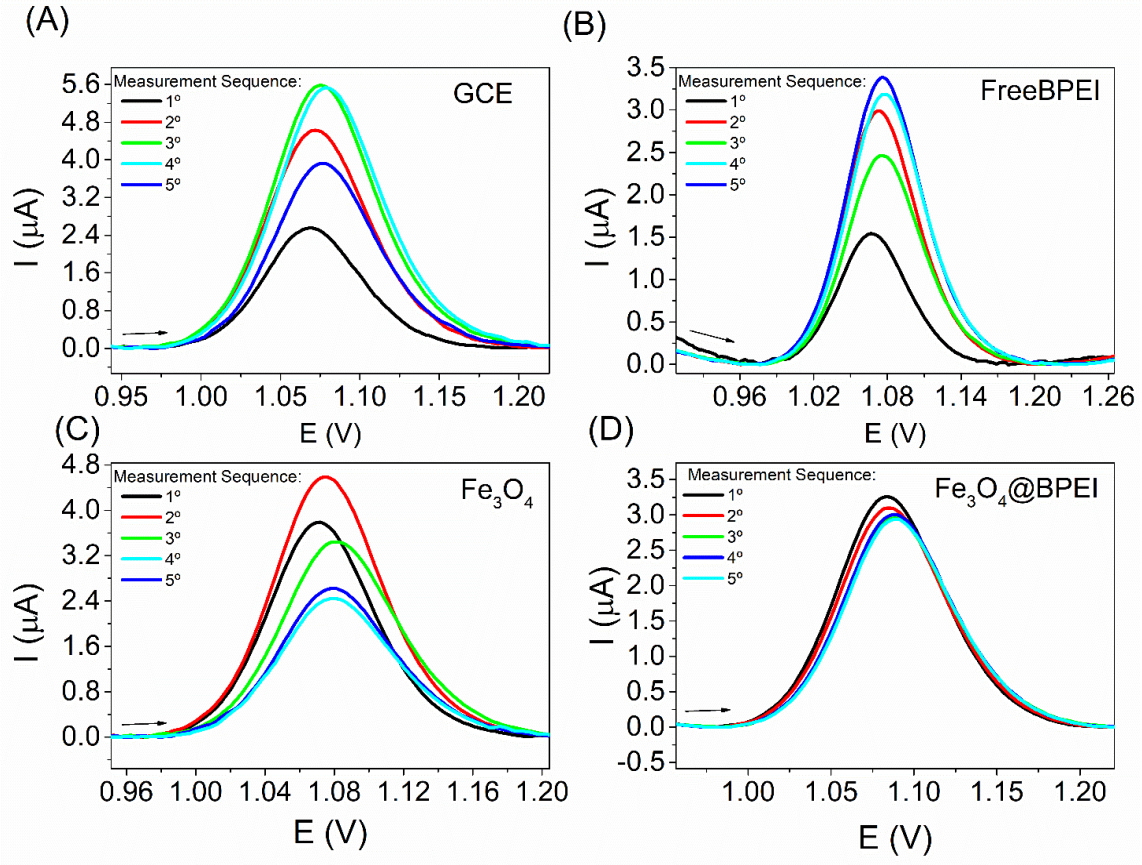

Source: author

3.3.4 Elucidation of electrochemical oxidation mechanism of CBZ

One of the goals in this work is obtaining new insights into the mechanism of CBZ oxidation. For instance, we could detect the oxidation products of CBZ and clarify the origin of hydroxyl radicals (•OH) that insert into the CBZ structure. Our proposed mechanism is shown in Figures 3.8A–B.

During the electrochemical oxidation of CBZ, water is oxidized first to generate •OH (Figure 31A*I*), which reacts with the CBZ radical formed by the direct loss of one electro and H^+ from CBZ (Figure 31A*II*). Our results also suggest that •OH can insert into the CBZ structure at three sites to generate three possible products shown in Figure 31B. In Sections 3.3.4.1 and 3.3.4.2 below, we present the experimental results that support these assumptions.

Figure 31 – Proposed mechanism for the electrochemical reactions of CBZ in BR buffer at pH 3.0. (A) Oxidation in two steps: *I.* generation of hydroxyl radicals by water oxidation, *II.* oxidation of CBZ molecule. (B) Three possible products of electrochemical oxidation of CBZ. The positions of hydroxyl radical are in accordance with the three possible locations of the CBZ radical.

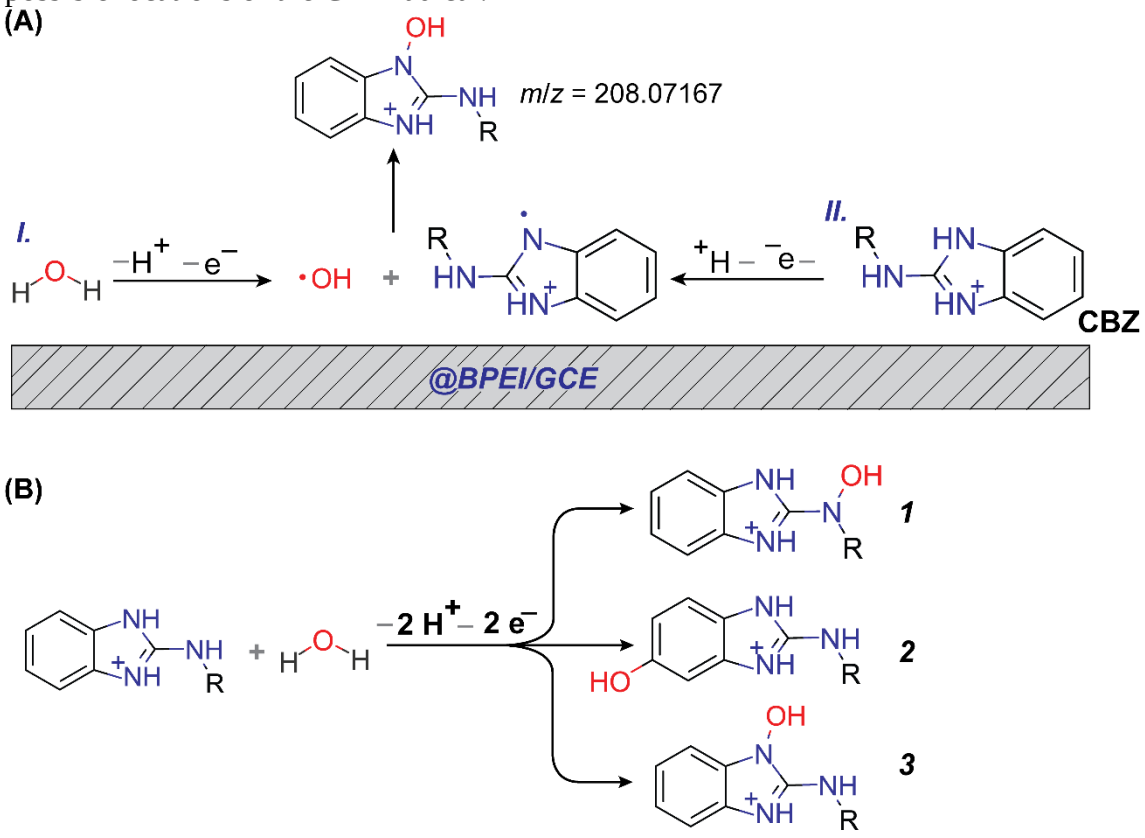

Source: author

3.3.4.1 Detection of oxidation products

To detect the oxidation products of CBZ, we performed exhaustive electrolysis under an applied potential of 1.3 V for 9 h. Immediately afterward, the reaction mixture was injected into an HPLC-DAD system for product analysis. The obtained chromatogram is shown in Figure 32A. Peak 1 at around 8.2 min is due to unoxidized CBZ. Peak 2 at 9.3 min is due to the CBZ oxidation products and contains three components centered at 8.8, 9.2, and 9.5 min, which we attribute to three possible oxidation products (compounds ***1***, ***2,*** and ***3*** in Figure 31B). This is supported by the following reasoning:

a) Compounds ***1***, ***2,*** and ***3*** are positional isomers and therefore expected to have similar retention times, as shown in Figure 32A. According to DFT calculation, the dipole moments of ***1***, ***2***, ***3***, and CBZ in the H_2O/ACN mixture are 5.1, 5.2, 4.7, and 8.4 a.u., respectively. Assignment of each component was performed based on the expected interaction strength of these molecules in the apolar

stationary phase.

b) All the components in peak 2 have similar experimental UV spectra, as shown by the blue lines in Figure 32. All components present a most intense signal at 196 nm, and a second most intense one at 219–225 nm. The spectra differ from each other in the region of 240–280 nm. Part 1 contains two smaller bands at 243 and 275 nm, whereas parts 2 and 3 have only one at 272 nm. Furthermore, the experimental spectra were compared to the theoretical ones of ***1***, ***2,*** and ***3*** calculated by DFT (Figure 33B–D, red lines). All compounds showed good agreement in intensity and wavenumber to the first two signals (196 and 221 nm). Compounds ***2*** and ***3*** differ in their intensity for the third signal, which could be attributed to errors in the DFT/B3LYP method relative to the experimental data (HOMEM-DE-MELLO *et al.*, 2005; LUCAS *et al.*, 2014). On the other hand, the experimental spectrum of part 1 agrees well with the theoretical spectrum for all compounds (Figure 32B). The agreement in wavenumber and signal intensity between our experimental and theoretical spectra of CBZ support the validity of our approach (Figure 32E). Additionally, the theoretical spectra for ***1***, ***2,*** and ***3*** are similar to each other, and so are the experimental spectra for peak 2.

c) TEMGOUA *et al.* (2021) performed a spin density calculation of the CBZ molecule minus one electron and one proton. They demonstrated that the probability of finding an unpaired electron is higher at the carbamate nitrogen, benzimidazole nitrogen, and two aromatic carbons. However, one of the aromatic carbons is bonded to the nitrogen of the five-membered ring and cannot form another bond. Therefore, these three sites allowing the unpaired electron represent the three possibilities to couple with •OH.

The reaction medium after electrolysis was analyzed by high-resolution MS to further confirm the oxidation products. Figure 33A shows the mass spectrum obtained from direct infusion of the reaction medium. The most intense signal comes from CBZ+H, with a mass charge ratio (*m*/*z*) of 192.07653 that differs from the theoretical value by $\Delta_{m/z}$ = –1.266 ppm. We identified a signal of *m*/*z* 208.07136, which can be attributed to compounds ***1***, ***2,*** or ***3*** ($\Delta_{m/z}$ = –1.239 ppm) (see Figure 32A, inset) and corroborate the mechanism proposed in Figure 31. Furthermore, the MS^2 spectrum for the fragment of *m*/*z* 208.07136 confirms compounds ***1***, ***2,*** and ***3*** (Figure 32B). Figure 32B depicts the proposed fragmentation pathway for compound ***3*** based on the observed ions *m/z* 176.04545, 148,05054, and 80.04947, even though the

presence of this molecule was not yet confirmed because this MS^2 spectrum is also suitable for ***1*** and ***2***.

Therefore, our HPLC-DAD experiments, theoretical calculation, and MS data all support the mechanism presented in Figure 31. The following subsection presents the electrochemical data corroborating the proposed electrochemical pathway for CBZ.

Figure 32 – (A) HPLC chromatogram for standard solution of CBZ and products from electrochemical oxidation of CBZ. Number ***1***, ***2*** and ***3*** indicates are relative to the three possible oxidation products, as shown in Figure 34 (B) of the main text. In (B) to (E) are shown experimental and theoretical UV absorption spectra for, compounds ***1***, ***2*** and ***3*** and CBZ. Important to mention that the experimental spectra were extracted from HPLC-UV run of the Figure 32 (A). Experimental spectra in (C) to (E) are relative to each part of the peak 2 in chromatogram in (A).

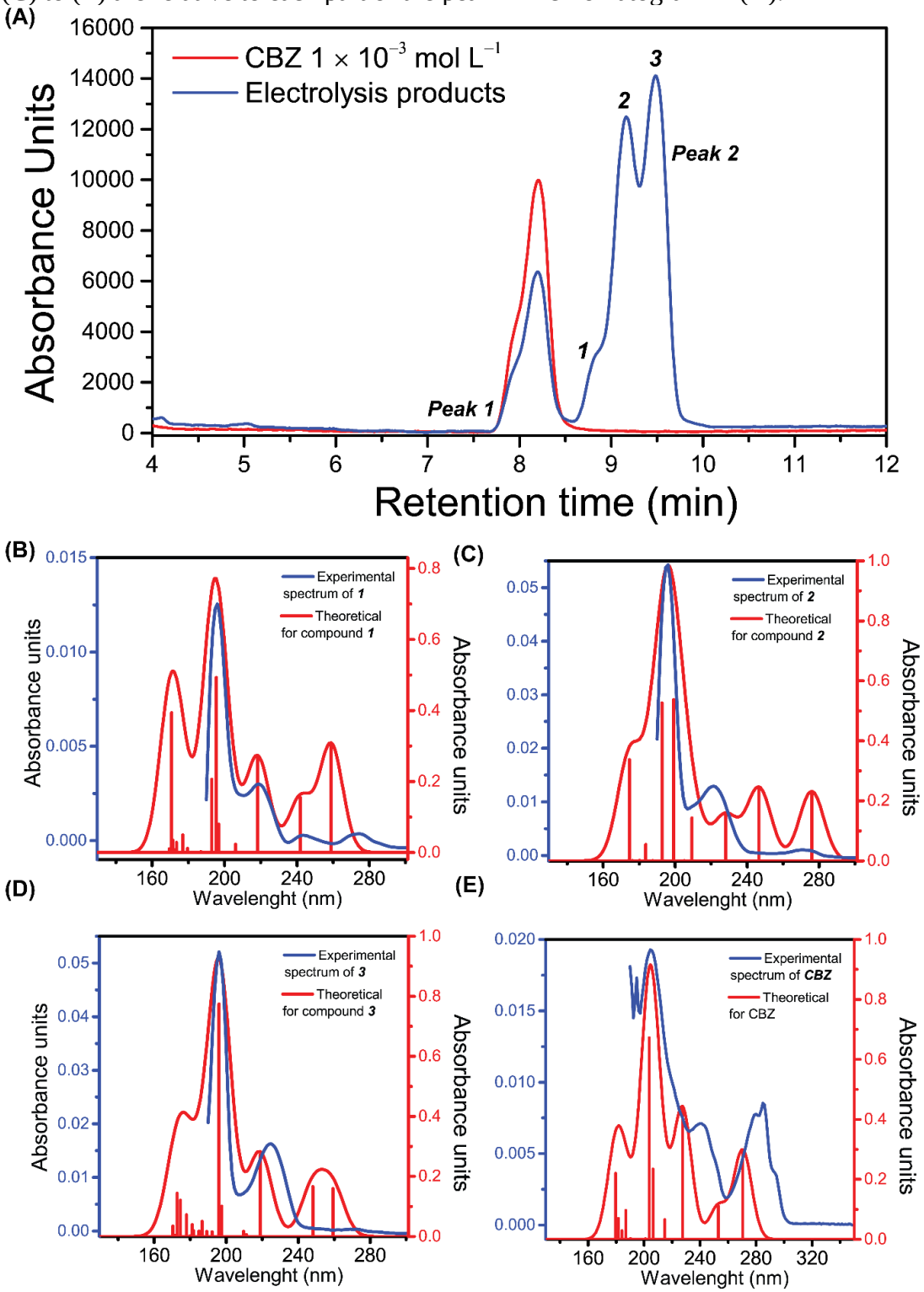

Source: author.

Figure 33 – (A) Direct infusion MS analysis of the oxidation products of CBZ. Inset: Mass range for compounds ***1***, ***2*** and ***3*.** (B) MS^2 analysis of the *m*/z = 208.07167. The chemical reactions are suggested fragmentation of compound ***3***. Important to mention that this spectrum could be assigned to ***1*** and ***2***, as well.

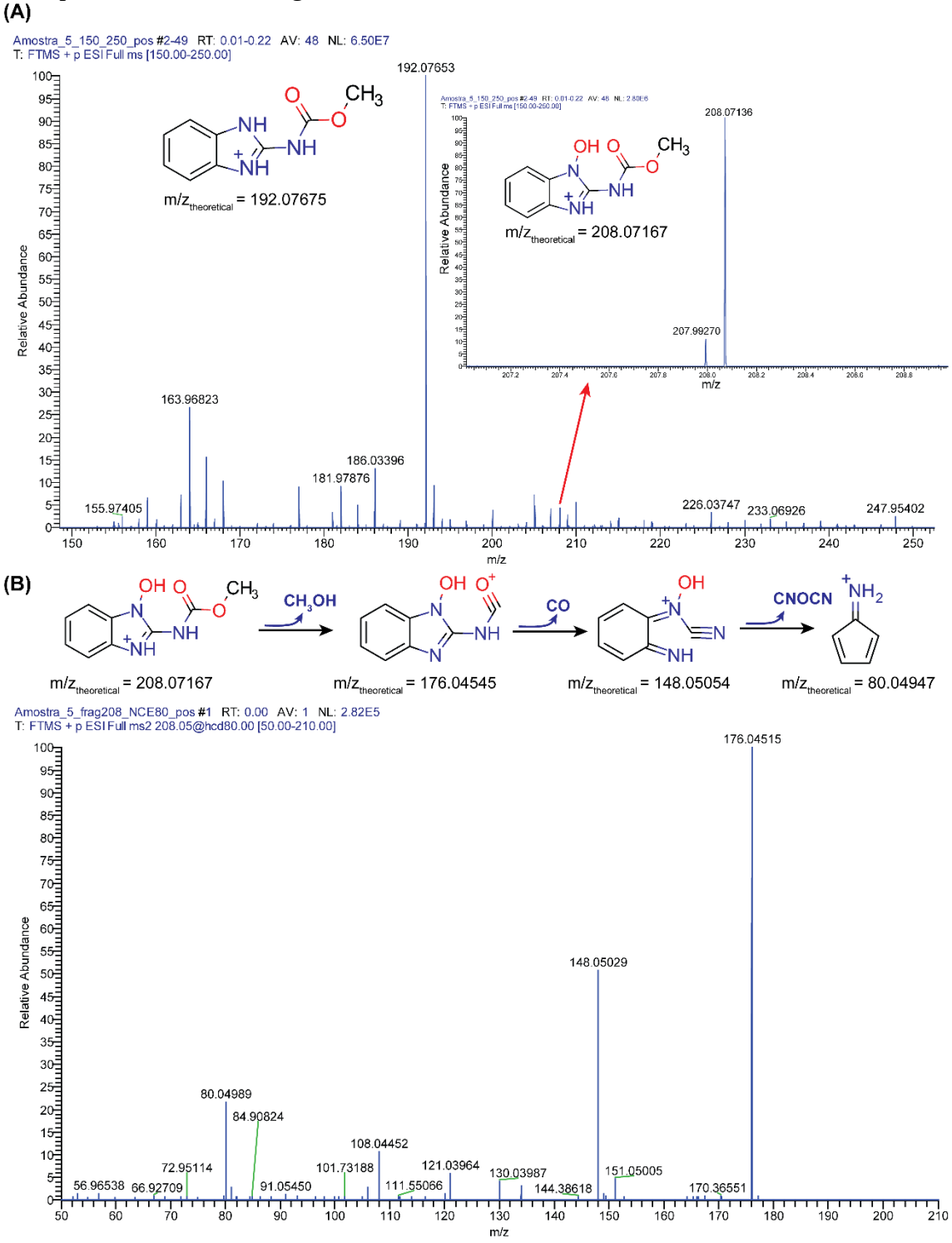

Source: author.

3.3.4.2 Electrochemical evidence for the electrochemical pathway of CBZ

Any proposed reaction mechanism must agree with the observed data. When protons participate in electrochemical reactions, the effects of pH on the E_P values are crucial for revealing the ratio between protons and electrons involved. The Nernst equation (3.4) predicts that, for an oxidation reaction involving equal numbers of protons and electrons, the E_P value is reduced by 59 mV per pH unit (WALCZAK *et al.*, 1997):

$$\frac{dE}{dpH} = -\frac{2{,}303\ RT}{F}\frac{m}{n} = -59\ (mV)\frac{m}{n} \tag{3.4}$$

Where *R*, *T,* and *F* have their usual meanings, and *m* and *n* are the numbers of protons and electrons, respectively. In Figure 28D and Figure B4, $P2_a$ and $P2_c$ exhibited a slope of – 60 mV, which is close to the theoretical value for an electrochemical reaction with $m = n$, in accordance with the mechanism proposed in Figure 31.

The variation of CV profile with scan rate also provides critical information about the electrochemical mechanisms. The linear dependence of I_P with ν shows that CBZ oxidation is a surface reaction (Figure B2A). For a surface reaction with EC, EC with second-order reaction, or ECE mechanisms, the theoretical Laviron's approach predicts that the E_P value for an oxidation reaction varies by 59.2/*n* (mV) per unit of log ν, according to equation (3.5)(DEVAUD; GULA, 1978; LAVIRON, 1972; LAVIRON; MEUNIER-PREST, 1994):

$$\frac{dE}{d\log\nu} = \frac{2{,}303\ RT}{nF} = \frac{59.2\ (mV)}{n} \tag{3.5}$$

Our study demonstrated a slope of 28.62 mV from the relation between E_P value of $P2_a$ and log ν (Figure 34A), which gives $n = 2.1 \approx 2$ electrons. Thus, the electrochemical reaction of CBZ in *P2* involves two electrons and two protons, as proposed in our mechanism.

We suggest that the process at a lower potential (*P1*) is due to the oxidation of unprotonated CBZ, while *P2* is attributed to that of protonated CBZ. The same attribution was made by HUA *et al.* (2011) in their study of poly(*N*-butyl benzimidazole) oxidation. This proposition agrees with the E_P values of *P1* and *P2*, in that a higher potential is required to remove an electron from an already positive species.

Another point that needs to be clarified is the origin of •OH incorporated into the CBZ structure. Previous studies reported that oxygen transfer reactions of organic compounds

involve •OH species that are generated in the water discharge reaction and adsorbed on the electrode surface (HOU *et al.*, 2009; PANIZZA; CERISOLA, 2009; VITT; JOHNSON, 1992). Equations (3.6) and (3.7) show the general mechanisms. A competition reaction for the O-transfer reaction is the oxygen evolution, which is shown in Equation (3.8) (PANIZZA; CERISOLA, 2009):

$$\equiv \mathrm{S}[\quad] + \mathrm{H_2O} \rightarrow \equiv \mathrm{S}[\bullet\,\mathrm{OH}] + \mathrm{H^+} + \mathrm{e^-} \tag{3.6}$$

$$\equiv \mathrm{S}[\bullet\,\mathrm{OH}] + \mathrm{R} \rightarrow \equiv \mathrm{S}[\quad] + \mathrm{RO} + \mathrm{H^+} + \mathrm{e^-} \tag{3.7}$$

$$\equiv \mathrm{S}[\bullet\,\mathrm{OH}] + \mathrm{H_2O} \rightarrow \equiv \mathrm{S}[\quad] + \mathrm{O_2} + 3\mathrm{H^+} + 3\mathrm{e^-} \tag{3.8}$$

where $\equiv S[\quad]$ is the electrode surface site for adsorption, and R and RO are the organic compound and its hydroxylated product, respectively. Our results corroborate the mechanism of O-transfer though •OH (Figure 31A*I*), since we observed a product with *m*/*z* matching compounds ***1***, ***2,*** and ***3***. Additionally, $P1_a$ was absent in the first CV scan of Figure 28A, because the electrode must be under a higher positive potential to generate •OH in order to oxidize the unprotonated CBZ. In the first scan, the electrode did not adsorb •OH to oxidize the unprotonated CBZ. NISHA *et al.* (2020) found similar behavior in the electrochemical oxidation of benzo(a)pyrene. Those authors observed a specific role of high anodic potential (1.2 V *vs*. Ag/AgCl) for the redox electrochemical reactions of benzo(a)pyrene at around 0.0 V *vs*. Ag/AgCl, and they attributed this high anodic potential was necessary to generate •OH and initiate the surface-confined hydroxylation of benzo(a)pyrene.

The nature of the electrochemical process of CBZ under SWV conditions was studied by analyzing the influence of *f* on $\boldsymbol{I_P}$ (Figure 34B) and the profile of the voltammograms (Figure 34C). The ratio $\boldsymbol{i_P}/f$ for the forward and backward components of *P2* had a parabolic dependence on *f*, as shown in Figure 34B. This behavior is predicted by the theory of quasi-reversible surface redox reactions (KOMORSKY-LOVRIĆ; LOVRIĆ, 1995). The critical frequency (f_{MAX}) is the frequency where this ratio reaches maximum, and it is related to the standard rate constant of electron transfer (k_S) and the critical kinetic parameter (κ_{MAX}) though Equation (3.9):

$$k_S = f_{MAX} \times \kappa_{MAX} \tag{3.9}$$

To calculate κ_{MAX}, one must know the electron transfer coefficient (α), which can be obtained when the peak width at half height ($\Delta E_{1/2}$) is independent of *f* (KOMORSKY-LOVRIĆ; LOVRIĆ, 1995):

$$\Delta E_{1/2} = \frac{63.5}{\alpha n} \quad (3.10)$$

In our case at f = 200 s^{-1}, $\Delta E_{1/2}$ = 77.9 ± 1.0 mV, which gives α = 0.4. Thus, κ_{MAX} can be calculated using Equation (3.11) (KOMORSKY-LOVRIĆ; LOVRIĆ, 1995):

$$\kappa_{MAX} = 1.13 + 1.13(\alpha - 0.55)^2 \quad (3.11)$$

Therefore, κ_{MAX} = 1.10 under these experimental conditions. The critical frequencies for the forward and backward components are 40 and 50 s^{-1}, which gives k_S = 44 and 55 s^{-1} for both components, respectively. To the best of our knowledge, this is the first time that this constant has been calculated under SWV conditions.

Figure 34 – (A) Dependence of $\boldsymbol{E_p}$ values of $P2_a$ on log $\boldsymbol{\nu}$ in the CV data of CBZ (9.90 µmol L^{-1}). Red line: linear regression. (B) Dependence of the ratio $\boldsymbol{i_P/f}$ on f in the SWV data. (C) Profile of the forward and backward currents of $P2$ at different f values. General conditions: [CBZ] = 9.90 µmol L^{-1}, 0.04 mol L^{-1} BR buffer at pH = 3.0 as the electrolyte, and modifying agent (@BPEI) concentration of 1 mg mL^{-1}. SWV conditions: accumulating time of 60 s, potential of 0.95 V.A = 50 mV; ΔEs = 2 mV.

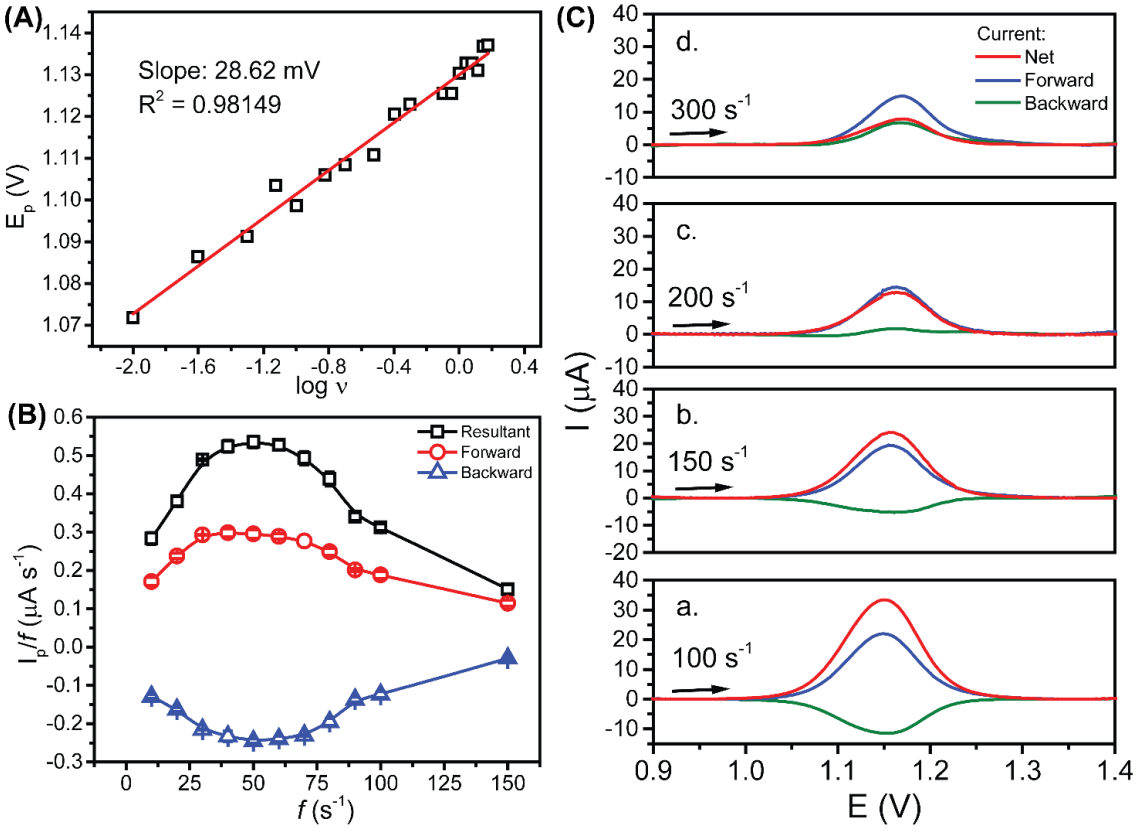

Source: author

The quasi-reversible character of CBZ can be confirmed by analyzing the SWV profiles at relatively high frequencies, as shown in Figure 34C. The characteristic of a quasi-reversible process is that the electrode reaction is affected by the interfacial electron transfer kinetics, which includes SWV, the rate of electron transfer (k_S), and f (MIRCESKI; SKRZYPEK; STOJANOV, 2018). For example, when the duration of the SWV pulse is considerably long (low f) in comparison to k_S, the redox equilibrium is established during the potential pulse, and a cathodic current is observed in the backward component (Figure 34Ca). However, when the SWV pulse is rapid (high f) in comparison to k_S, the amount of oxidized product is small at the moment of current sampling, and the backward component is absent (Figures 3.11Cb and c) or even positive (Figure 34Cd), which is characteristic of an irreversible process (MIRCESKI; SKRZYPEK; STOJANOV, 2018). Therefore, the change in the reversibility shown in Figure 34C further confirms the quasi-reversible character of CBZ.

3.3.5 Electroanalytical methodology for CBZ using @BPEI/GCE

3.3.5.1 Analytical curve

After optimizing the parameters, we obtained an analytical curve for CBZ concentrations from 39.8 to 157 nmol L^{-1} under SWV conditions in BR buffer (pH 3.0). This curve was based on measurement using three individual @BPEI/GCE electrodes and three CBZ solutions at each concentration. Figure 35 shows the relationship between the $\boldsymbol{I_P}$ values of $P2_a$ and CBZ concentration ([CBZ]), as well as representative SWV curves for different [CBZ] (inset). Some figures of merit are listed in Table 6. The repeatability of the method was evaluated by measuring the signal in SWV for seven replicates of the same CBZ solution and electrode. Meanwhile, the reproducibility was obtained using five electrodes and CBZ solutions. The repeatability and reproducibility were 1.31 and 2.84%, respectively (Table 6), indicating that the electrodes are suitable for practical applications.

There are two linear regions in the correlation between $\boldsymbol{I_P}$ and [CBZ] in Figure 35, one in the range of 39.8 to 79.4 nmol L^{-1} ($\mathbf{R_1}$) and another in the range of 79.4 to 157 nmol L^{-1} ($\mathbf{R_2}$). The LOD and LOQ values are 38.7 and 61.7 nmol L^{-1} for $\mathbf{R_1}$ and 64.0 and 73.4 nmol L^{-1} for $\mathbf{R_2}$, respectively (Table 6). These values are below the maximum permitted limit by Brazilian regulations for CBZ in natural waters (630 nmol L^{-1}) (BRASIL, 2011), confirming the potential applicability of this sensor for quantifying CBZ in natural waters. These values are also comparable to or lower than those of other electrochemical sensors based on nanomaterial-modified electrodes, as shown in Table 7. Furthermore, the LOD and LOQ

calculated in this work are in the same range as other analytical methodologies for CBZ in natural waters, such as liquid-liquid microextraction UV-VIS spectroscopy (LOD = 11 nmol L^{-1}) (POURREZA; RASTEGARZADEH; LARKI, 2015) and liquid-liquid microextraction HPLC-FD (LOD = 17 nmol L^{-1}) (FARHADI; FARAJZADEH; MATIN, 2009). We additionally constructed an analytical curve for CBZ using HPLC-DAD. The corresponding LOD and LOQ values (88.0 and 293 nmol L^{-1}, respectively; Table 6) are higher than those obtained by SWV. These facts indicate satisfactory performance of the proposed sensor.

Figure 35 – Analytical curve for the quantification of CBZ using the SWV electrochemical technique. Inset: SWV data at different [CBZ]. Electrolyte: BR buffer (0.04 mol L^{-1}, pH 3.0). Concentration of modifying agent: 1 mg mL^{-1}. Accumulating time: 60 s, potential: 0.95 V. SWV parameters: f = 70 s^{-1};A = 50 mV; ΔEs = 2 mV.

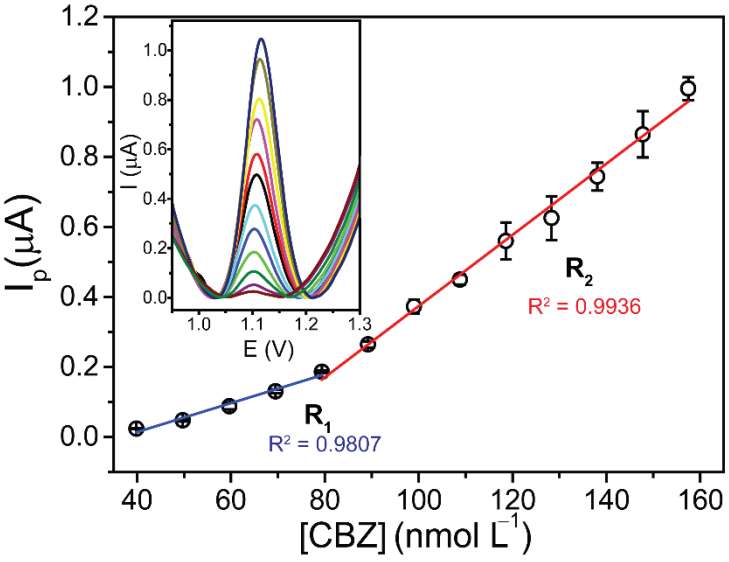

Source: author.

Table 6 – Parameters of the analytical curve obtained for CBZ detection using @BPEI/GCE and HPLC.

Parameter	**SWV**		**HPLC**
	R_1	**R_2**	
Linearity Range (nmol L^{-1})	39.8– 79.4	79.4 – 157	105 – 1260
Intercept (A)	-1.51×10^{-7}	-6.42×10^{-7}	1998.25
Slope (A mol^{-1} L^{-1})	4.12	10.02	2.00×10^{10}
CL_a (A)	$4.80 \pm \times 10^{-8}$	$\pm 7.04 \times 10^{-8}$	652.77
CL_b (A mol^{-1} L^{-1})	± 0.78	± 0.58	8.48×10^{8}
R^2	0.9808	0.9937	0.9945
S_a (A)	2.041×10^{-8}	3.72×10^{-8}	360.25
LOD (nmol L^{-1})	38.7	64.0	8.80×10^{-8}
LOQ (nmol L^{-1})	61.7	73.4	2.93×10^{-7}
%RSD Repeatability (n = 7)	1.31		
%RSD Reproducibility (n = 5)	2.84		

Source: author.

3.3.5.2 Determination of CBZ in natural waters samples

An efficient analytical methodology for detecting pesticide residues in natural waters can help minimize the uptake of these hazardous compounds (KUMAR *et al.*, 2020). Therefore, we studied the applicability of the proposed sensor for CBZ detection and quantification in natural waters. The physicochemical parameters of the water samples are listed in Table B2. According to our results, the collected water samples did not contain CBZ.

Next, the natural waters samples were spiked with CBZ at three levels of 66.9, 89.2, and 119.0 nmol L^{-1}. These spiked samples were prepared in triplicates and analyzed using three individual electrodes. The recovery percentage [*R(%)*], confidence limit, relative standard deviation of recovery (RSD_R), and BIAS were calculated. The obtained values are listed in Table 8. The *R(%)* values for water samples collected in Acarape do Meio ranged from 61.8% to 83.4%, and RSD_R ranged from 1.7% to 5.3%. In contrast, for the sampled collected in Gavião, *R(%)* ranged from 80.2% to 94.4% and RSD_R ranged from 1.8% to 2.9%. The Association of Official Analytical Collaboration (AOAC) expects different levels of *R(%)* and RSD_R according to the mass fraction of the analyte. For the level studied in this work, AOAC expects *R(%)* between 60% and 115% and RSD_R of 21% (APPENDIX F: GUIDELINES FOR STANDARD METHOD PERFORMANCE REQUIREMENTS, 2016). Therefore, our values indicate the suitability of the proposed methodology.

Table 7 – Comparison of the proposed electrode to other modified electrodes for the determination of CBZ.

Electrode	**Technique**	**Linear range (mol L^{-1})**	**LOD (nmol L^{-1})**	**REF**
GCE[a]-$ZnFe_2O_4$-SWCNTs[b]	DPV	$5.00 \times 10^{-7} – 1.00 \times 10^{-4}$	90	(DONG *et al.* 2017)
GCE-MC[c]	DPV	$9.50 \times 10^{-7} – 9.55 \times 10^{-5}$	9.5×10^{5}	(MANISANKAR *et al.* 2005)
GCE-SiO_2-MWCNTs[d]	SWV	$2.00 \times 10^{-7} – 4.00 \times 10^{-6}$	56	(RAZZINO *et al.*, 2015)
GCE-MWCNTs	SWV	$2.56 \times 10^{-7} – 3.11 \times 10^{-6}$	55	(RIBEIRO, W. F. *et al.*, 2011)
GCE-MWCNTs	SWV	$4.00 \times 10^{-8} – 4.01 \times 10^{-7}$	14	(PETRONI *et al.*, 2016)
GCE-P-HCNFs[e]	DPV	$1.00 \times 10^{-7} – 3.50 \times 10^{-5}$	38	(CUI *et al.*, 2017)
CPE[f]-PIL[g]-OMC[h]	DPV	$6.53 \times 10^{-9} – 4.18 \times 10^{-6}$	2.1	(YA *et al.*, 2015)
BDD[i]	SWV	$5.00 \times 10^{-7} – 1.50 \times 10^{-5}$	120	(FRANÇA *et al.*, 2012)
SPCE[j] Micellar CTAB[l]-RGO[m]	SWV	$1.31 \times 10^{-7} – 2.61 \times 10^{-5}$	26	(AKKARACHANCHAINON *et al.*, 2017)
CPE-OMM[n]	SWV	$1.00 \times 10^{-6} – 7.00 \times 10^{-6}$	30	(YANKE *et al.*, 2017)
GCE- β-CD[o]–RGO	DPV	$1.00 \times 10^{-7} – 4.00 \times 10^{-5}$	19	(PHAM *et al.*, 2016)
CPE-Ce-doped $ZnWO_4$	DPV	$1.00 \times 10^{-8} – 5.50 \times 10^{-6}$	3.3	(ZHOU, Yuanzhen; CUI; *et al.*, 2019)
GCE-nanoporous Au^0	DPV	$3.00 \times 10^{-6} – 1.20 \times 10^{-4}$	240	(GAO, Xinyu *et al.*, 2019)
GCE-nanoporous Cu^0-RGO	DPV	$5.00 \times 10^{-7} – 3.00 \times 10^{-5}$	90	(TIAN *et al.*, 2019)
GCE-CMC-CNTs[p]	DPV	$3.00 \times 10^{-8} – 1.00 \times 10^{-5}$	15	(GAN *et al.*, 2019)
GCE-AuNRs@ZIF@GO[q]	DPV	$2.80 \times 10^{-8} – 3.5 \times 10^{-5}$	4.1	(ILAGER *et al.*, 2021)
CPE-La-doped Nd_2O_3[r]	DPV	$8.00 \times 10^{-8} – 5.0 \times 10^{-5}$	27	(ZHOU et al., 2019)
GCE-WO_3[s]	SWV	$1.00 \times 10^{-7} – 2.5 \times 10^{-4}$	22	(ILAGER *et al.*, 2021)
@BPEI/GCE	SWV	R_1: $3.98 \times 10^{-8} – 7.94 \times 10^{-8}$ R_2: $7.94 \times 10^{-8} – 1.57 \times 10^{-7}$	R_1: 39 R_2: 64	**This Work**

[a] glassy carbon electrode; [b] single-walled carbon nanotubes; [c] sodium montmorillonite clay; [d] multi-walled carbon nanotubes; [e] phosphorus-doped helical carbon nanofibers;[f] carbon paste electrode; [g] pyrrolidinium ionic liquid; [h] ordered mesoporous carbon; [i] boron-doped diamond electrode; [j] screen-printed carbon electrode; [l] cetyltrimethylammonium bromide; [m] reduced graphene oxide; [n] octyltriethoxisilane modified montmorillonite; [o] β-cyclodextrin; [p] Carboxymethyl cellulose functionalized carbon nanotubes; [q] Au nanorods (AuNRs) encapsulated by zeolitic imidazolate framework (ZIF-8) and graphene oxide (GO); [r] La-doped neodymium (III) oxide; [s] tungsten oxide.

Source: author.

Table 8 – Results of the recovery of CBZ in natural waters using SWV.

Reservoir	$[CBZ]_{added}$ (nmol L^{-1})	$[CBZ]_{found}$ (nmol L^{-1})	Confidence limit (nmol L^{-1})	R (%)	RSD_R (%)	BIAS (%)
Acarape do Meio	66.9	43.0	± 5.4	61.8	5.3	–38.2
	89.2	74.3	± 4.8	83.4	2.7	–16.6
	119	96.9	± 3.9	81.7	1.7	–18.3
Gavião	66.9	65.6	4.48	94.4	2.9	–5.6
	89.2	81.7	4.44	91.5	2.3	–8.5
	119	95.1	3.95	80.2	1.8	–19.8

Source: author.

To evaluate the matrix effect in natural waters samples, Student's *t*-test was employed to compare the slopes of the analytical curves obtained in BR buffer with those in Acarape do Meio and Gavião. The slopes in the two regions of linearity ($\mathbf{R_1}$ and $\mathbf{R_2}$) were compared. The values of t_{R1} for Acarape do Meio and Gavião are 1.70 and 0.016, respectively, which are lower than the critical *t* value of 2.92 ($n = 2$; 95% confidence level). However, the t_{R2} values for Acarape do Meio and Gavião (4.12 and 7.92, respectively) are higher than the critical *t* value of 1.86 ($n = 8$; 95% confidence level). Thus, there was a matrix effect only at higher CBZ concentrations, which indicates that the BIAS found in our recovery experiments is due to the interaction of CBZ with the organic components in natural waters.

The selectivity of the method was evaluated by monitoring the CBZ signal when the electrolyte was added with different interfering compounds. Some of the added species are frequently found in natural waters, such as $NaNO_3$, $CaCl_2$, $MgCl_2$, KH_2PO_4, $Al_2(SO_4)_3$, citric acid, and ascorbic acid. Difenoconazole, imidacloprid, and chlorpyrifos were also tested as possible interfering agents because they are frequently found together with CBZ in crops. The concentration of each interfering species was approximately 100-fold that of CBZ (7.996×10^{-8} mol L^{-1}). Figure B8 shows the percentage change in the CBZ signal after adding each interfering agent. In most cases the change was less than 5%, except for $Al_2(SO_4)$ and ascorbic acid. Using Student's *t*-test, we compared the average $\boldsymbol{I_P}$ signals with and without the interfering species. The *t* values for $NaNO_3$, $CaCl_2$, $MgCl_2$, KH_2PO_4, $Al_2(SO_4)_3$, citric acid, ascorbic acid, difenoconazole, imidacloprid, and chlorpyrifos are 0.24, 1.99, 0.21, 0.19, 1.55, 0.51, 1.07, 0.43, 0.46, and 0.19, respectively. These values are smaller than the critical *t* value of 2.132 ($n – 2 = 4$; 95% confidence), indicating that the CBZ signal was not significantly affected by the interfering species.

3.4 Conclusions

In summary, we applied MNPs to enhance the performance of electrochemical sensors. An electroanalytical methodology for quantifying CBZ in natural waters was developed using an MNP-modified GCE, and an oxidation pathway for CBZ was also proposed. The functionalized MNPs were prepared by a rapid sonochemistry approach. Their modification on the GCEs enhanced the electroactive area by 12%–18%. MNPs functionalized with BPEI were selected to develop the electroanalytical methodology, since its incorporation onto GCE increased the electrode's regeneration capability and efficiency. After optimization of the electrochemical parameters for CBZ detection, an oxidation pathway for CBZ was proposed based on analyzing the products of exhaustive electrolysis by HPLC-DAD, high-resolution MS, and MS^2 to confirm the number of product species and their identity. Electrochemical measurements also corroborated the proposed mechanism, identified the number of protons and electrons involved, and clarified the origin of hydroxyl radical added to the CBZ structure. SWV study under variable pulse frequencies confirmed the quasi-reversible character of the CBZ redox process. The electroanalytical methodology gave LOD and LOQ values of 38.7 to 64.0 and 61.7 to 73.4 nmol L^{-1}, respectively, which are lower than the maximum permitted limit for CBZ by Brazilian regulation. The proposed sensor exhibited good stability (%RSD = 1.31), reproducibility (%RSD = 2.84), and anti-interference ability. Additionally, an electroanalytical methodology was successfully developed for CBZ detection in natural waters. In summary, this work made progresses in the fields of nanomaterials (by rapidly preparing nanoparticles as potential sensor components), electrochemistry (by proposing the reaction pathway for CBZ oxidation), and analytical chemistry (by developing an electroanalytical methodology for CBZ as an alternative to traditional chromatographic techniques).

4 CHAPTER IV – GENERAL CONCLUSIONS

This work has engaged in two front lines: the proposition of a novel amino-phosphonate functionalized MNPs that exhibited great potential as a contrast agent for MRI; and the elaboration of electrochemical sensor for detection and quantification of the pesticide carbendazim in natural waters. However, these two fronts have a connection bridge: the sonochemistry approach. This methodology proposed by our group acted as the feedstock of high-quality MNPs for both front, consolidating the sonochemistry approach as an essential tool to rapidly prepare functionalized MNPs. Furthermore, the samples produced in this work were used in other applications through cooperation with partner groups, such as enzyme immobilization (BEZERRA *et al.*, 2020, 2017), antenna devices (DE MENEZES *et al.*, 2020), and arsenic speciation (DA SILVA *et al.*, 2021). Therefore, we can firmly affirm that this work contributed to different research fields, but connected by materials science, from analytical chemistry to medical imaging diagnosis.

REFERENCES

ADAMO, Carlo; JACQUEMIN, Denis. The calculations of excited-state properties with Time-Dependent Density Functional Theory. **Chemical Society Reviews**, vol. 42, nº 3, p. 845–856, 2013.

AHMED, Ashour A.; GYPSER, Stella; LEINWEBER, Peter; FREESE, Dirk; KÜHN, Oliver. Infrared spectroscopic characterization of phosphate binding at the goethite-water interface. **Physical Chemistry Chemical Physics**, 2019.

AKKARACHANCHAINON, Nontapol; RATTANAWALEEDIROJN, Pranee; CHAILAPAKUL, Orawon; RODTHONGKUM, Nadnudda. Hydrophilic graphene surface prepared by electrochemically reduced micellar graphene oxide as a platform for electrochemical sensor. **Talanta**, vol. 165, nº Supplement C, p. 692–701, 2017. DOI

ALLOUCHE, Abdul-Rahman. Gabedit—A graphical user interface for computational chemistry softwares. **Journal of Computational Chemistry**, vol. 32, nº 1, p. 174–182, 15 jan. 2011.

AMINI-FAZL, Mohammad Sadegh; MOHAMMADI, Reza; KHEIRI, Karim. 5-Fluorouracil loaded chitosan/polyacrylic acid/Fe_3O_4 magnetic nanocomposite hydrogel as a potential anticancer drug delivery system. **International Journal of Biological Macromolecules**, vol. 132, p. 506–513, 2019.

AMSTAD, Esther; TEXTOR, Marcus; REIMHULT, Erik. Stabilization and functionalization of iron oxide nanoparticles for biomedical applications. **Nanoscale**, vol. 3, nº 7, p. 2819–2843, 2011.

ANDRADE NETO, D. A. **Magnetic ressonance imaging contrast agents obtained by fast sonochemistry approach**. 2016. 84 f. Federal University of Ceará, 2016.

APPENDIX F: GUIDELINES FOR STANDARD METHOD PERFORMANCE REQUIREMENTS. **Official Methods of Analysis**. 20th ed. Rockville, MD, USA, MD, USA: AOAC INTERNATIONAL, 2016.

ARTYUSHKOVA, Kateryna; MATANOVIC, Ivana; HALEVI, Barr; ATANASSOV, Plamen. Oxygen Binding to Active Sites of Fe-N-C ORR Electrocatalysts Observed by Ambient-Pressure XPS. **Journal of Physical Chemistry C**, vol. 121, n° 5, p. 2836–2843, 2017.

ASHOKKUMAR, Muthupandian. Introductory text to sonochemistry. **ChemTexts**, vol. 4, nº 2, p. 7, 2018.

BAAZIZ, Walid; PICHON, Benoit P; FLEUTOT, Solenne; LIU, Yu; LEFEVRE, Christophe; GRENECHE, Jean-Marc; TOUMI, Mohamed; MHIRI, Tahar; BEGIN-COLIN, Sylvie. Magnetic Iron Oxide Nanoparticles: Reproducible Tuning of the Size and Nanosized-Dependent Composition, Defects, and Spin Canting. **The Journal of Physical Chemistry C**, vol. 118, nº 7, p. 3795–3810, 2014.

BANG, Jin H.; SUSLICK, Kenneth S. Applications of ultrasound to the synthesis of nanostructured materials. **Advanced Materials**, vol. 22, nº 10, p. 1039–1059, 2010.

BARBOSA, J. S.; NETO, D. M.A.; FREIRE, R. M.; ROCHA, J. S.; FECHINE, L. M.U.D.; DENARDIN, J. C.; VALENTINI, A.; DE ARAÚJO, T. G.; MAZZETTO, S. E.; FECHINE, P. B.A. Ultrafast sonochemistry-based approach to coat TiO_2 commercial particles for sunscreen formulation. **Ultrasonics Sonochemistry**, vol. 48, p. 340–348, 2018.

BARD, A J; FAULKNER, L R. **Electrochemical Methods: Fundamentals and Applications**. [*S. l.*]: Wiley, 2000.

BARJA, Beatriz C.; TEJEDOR-TEJEDOR, M. Isabel; ANDERSON, Marc A. Complexation of methylphosphonic acid with the surface of goethite particles in aqueous solution. **Langmuir**, vol. 15, nº 7, p. 2316–2321, 1999.

BASLY, Brice; POPA, Gabriela; FLEUTOT, Solenne; PICHON, Benoit P; GAROFALO, Antonio; GHOBRIL, Cynthia; BILLOTEY, Claire; BERNIARD, Aurélie; BONAZZA, Pauline; MARTINEZ, Hervé; FELDER-FLESCH, Delphine; BEGIN-COLIN, Sylvie. Effect of the nanoparticle synthesis method on dendronized iron oxides as MRI contrast agents. **Dalton Transactions**, vol. 42, nº 6, p. 2146–2157, 2013.

BEZERRA, Rayanne M; MONTEIRO, Rodolpho R C; NETO, Davino M Andrade; DA SILVA, Francisco F M; DE PAULA, Regina C M; DE LEMOS, Telma L G; FECHINE, Pierre B A; CORREA, Marcio A; BOHN, Felipe; GONÇALVES, Luciana R B; DOS SANTOS, José C S. A new heterofunctional support for enzyme immobilization: PEI functionalized Fe_3O_4 MNPs activated with divinyl sulfone. Application in the immobilization of lipase from Thermomyces lanuginosus. **Enzyme and Microbial Technology**, vol. 138, p. 109560, 2020.

BEZERRA, Rayanne M.; NETO, Davino M.Andrade; GALVÃO, Wesley S.; RIOS, Nathalia S.; CARVALHO, Ana Caroline L.de M.; CORREA, Marcio A.; BOHN, Felipe; FERNANDEZ-LAFUENTE, Roberto; FECHINE, Pierre B.A.; DE MATTOS, Marcos C.; DOS SANTOS, José C.S.; GONÇALVES, Luciana R.B. Design of a lipase-nano particle biocatalysts and its use in the kinetic resolution of medicament precursors. **Biochemical Engineering Journal**, vol. 125, p. 104-115, 2017.

BLEICHER, Lucas; SASAKI, José Marcos; PAIVA SANTOS, Carlos Oliveira. Development of a graphical interface for the Rietveld refinement program DBWS. **Journal of Applied Crystallography**, vol. 33, nº 4, p. 1189–1189, 2000.

BLIGH, S.W.Annie; HARDING, Charles T; MCEWEN, Andrew B; SADLER, Peter J; KELLY, J.Duncan; MARRIOTT, Janet A. Synthesis, characterization and comparative study of aminophosphonate chelates of gadolinium(III) ions as magnetic resonance imaging contrast agents. **Polyhedron**, vol. 13, nº 12, p. 1937–1943, 1994.

BOHARA, Raghvendra A; THORAT, Nanasaheb D; PAWAR, Shivaji H. Role of functionalization: strategies to explore potential nano-bio applications of magnetic nanoparticles. **RSC Advances**, vol. 6, nº 50, p. 43989–44012, 2016.

BONES, Jonathan; THOMAS, Kevin; NESTERENKO, Pavel N.; PAULL, Brett. On-line preconcentration of pharmaceutical residues from large volume water samples using short reversed-phase monolithic cartridges coupled to LC-UV-ESI-MS. **Talanta**, vol. 70, n° 5, p. 1117–1128, 2006.

BORDEIANU, C; PARAT, A; AFFOLTER-ZBARASZCZUK, C; MULLER, R N; BOUTRY, S; BEGIN-COLIN, S; MEYER, F; LAURENT, S; FELDER-FLESCH, D. How a grafting

anchor tailors the cellular uptake and in vivo fate of dendronized iron oxide nanoparticles. **Journal of Materials Chemistry B**, vol. 5, nº 26, p. 5152–5164, 2017.

BRUVERA, I J; MENDOZA ZÉLIS, P; PILAR CALATAYUD, M; GOYA, G F; SÁNCHEZ, F H. Determination of the blocking temperature of magnetic nanoparticles: The good, the bad, and the ugly. **Journal of Applied Physics**, vol. 118, nº 18, p. 184304, 2015.

CAI, Hongdong; AN, Xiao; CUI, Jun; LI, Jingchao; WEN, Shihui; LI, Kangan; SHEN, Mingwu; ZHENG, Linfeng; ZHANG, Guixiang; SHI, Xiangyang. Facile hydrothermal synthesis and surface functionalization of polyethyleneimine-coated iron oxide nanoparticles for biomedical applications. **ACS applied materials & interfaces**, vol. 5, nº 5, p. 1722–1731, 2013.

CAO, Derang; LI, Hao; PAN, Lining; LI, Jianan; WANG, Xicheng; JING, Panpan; CHENG, Xiaohong; WANG, Wenjie; WANG, Jianbo; LIU, Qingfang. High saturation magnetization of γ-Fe_2O_3 nano-particles by a facile one-step synthesis approach. **Scientific Reports**, vol. 6, nº 1, p. 32360, 2016.

CHENG, Fong-Yu; SU, Chia-Hao; YANG, Yu-Sheng; YEH, Chen-Sheng; TSAI, Chiau-Yuang; WU, Chao-Liang; WU, Ming-Ting; SHIEH, Dar-Bin. Characterization of aqueous dispersions of Fe_3O_4 nanoparticles and their biomedical applications. **Biomaterials**, vol. 26, nº 7, p. 729–738, 2005.

CÎRCU, M; RADU, T; PORAV, A S; TURCU, R. Surface functionalization of Fe_3O_4@SiO_2 core-shell nanoparticles with vinylimidazole-rare earth complexes: Synthesis, physico-chemical properties and protein interaction effects. **Applied Surface Science**, vol. 453, p. 457–463, 2018.

COMPTON, Richard G; BANKS, Craig E. **Understanding voltammetry**. [*S. l.*]: World Scientific, 2007.

CONRADIE, M M; CONRADIE, J; ERASMUS, E. Immobilisation of iron tris(β-diketonates) on a two-dimensional flat amine functionalised silicon wafer: A catalytic study of the formation of urethane, from ethanol and a diisocyanate derivative. **Polyhedron**, vol. 79, p. 52–59, 2014.

COUTO, Diana; FREITAS, Marisa; VILAS-BOAS, Vânia; DIAS, Irene; PORTO, Graça; LOPEZ-QUINTELA, M Arturo; RIVAS, José; FREITAS, Paulo; CARVALHO, Félix; FERNANDES, Eduarda. Interaction of polyacrylic acid coated and non-coated iron oxide nanoparticles with human neutrophils. **Toxicology Letters**, vol. 225, nº 1, p. 57–65, 2014.

CRUM, L A. Acoustic cavitation series: part five rectified diffusion. **Ultrasonics**, vol. 22, nº 5, p. 215–223, 1984. DOI

CUI, Rongjing; XU, Dong; XIE, Xiaohan; YI, Yuyang; QUAN, Ying; ZHOU, Maixi; GONG, Jinjian; HAN, Zhida; ZHANG, Genhua. Phosphorus-doped helical carbon nanofibers as enhanced sensing platform for electrochemical detection of carbendazim. **Food Chemistry**, vol. 221, p. 457–463, 2017.

DA COSTA, Geraldo Magela; BLANCO-ANDUJAR, Cristina; DE GRAVE, Eddy; PANKHURST, Quentin A. Magnetic Nanoparticles for in Vivo Use: A Critical Assessment of Their Composition. **The Journal of Physical Chemistry B**, vol. 118, nº 40, p. 11738–11746,

2014.

DA SILVA, Francisco L F; NETO, Davino M Andrade; DE MENEZES, Fernando L; SA, Ivero P; DE HIGUERA, Julymar M; FECHINE, Pierre B A; DA COSTA, Luelc S; NOGUEIRA, Ana R A; LOPES, Gisele S; MATOS, Wladiana O. Non-chromatographic arsenic speciation analyses in wild shrimp (Farfantepenaeus brasiliensis) using functionalized magnetic iron-nanoparticles. **Food Chemistry**, vol. 345, p. 128781, 2021.

DAOU, T J; BEGIN-COLIN, S; GRENÈCHE, J M; THOMAS, F; DERORY, A; BERNHARDT, P; LEGARÉ, P; POURROY, G. Phosphate Adsorption Properties of Magnetite-Based Nanoparticles. **Chemistry of Materials**, vol. 19, nº 18, p. 4494–4505, 2007.

DAOU, T J; POURROY, G; BEGIN-COLIN, S; GRENECHE, J M; ULHAQ-BOUILLET, C; LEGARE, P; BERNHARDT, P; LEUVREY, C; ROGEZ, G. Hydrothermal Synthesis of Monodisperse Magnetite Nanoparticles. **Chem. Mater.**, vol. 18, nº 18, p. 4399–4404, 2006.

DAOU, T J; POURROY, G; GRENECHE, J M; BERTIN, A; FELDER-FLESCH, D; BEGIN-COLIN, S. Water soluble dendronized iron oxide nanoparticles. **Dalton transactions**, nº 23, p. 4442–4449, 2009.

DE, Arnab; BOSE, Rituparna; KUMAR, Ajeet; MOZUMDAR, Subho. **Targeted delivery of pesticides using biodegradable polymeric nanoparticles**. [*S. l.*]: Springer, 2014.

DE LA PRESA, P; LUENGO, Y; VELASCO, V; MORALES, M P; IGLESIAS, M; VEINTEMILLAS-VERDAGUER, S; CRESPO, P; HERNANDO, A. Particle Interactions in Liquid Magnetic Colloids by Zero Field Cooled Measurements: Effects on Heating Efficiency. **The Journal of Physical Chemistry C**, vol. 119, nº 20, p. 11022–11030, 2015.

DE MENEZES, Fernando L; ANDRADE NETO, Davino M; RODRIGUES, Maria D; LIMA, Helder L; PAIVA, Denis v; DA SILVA, Marcelo A; FECHINE, Lillian M; SOMBRA, Antônio S; FREIRE, Rafael M; DENARDIN, Juliano C; ROSA, Morsyleide D; DE SOUZA FILHO, Men D; MAZZETTO, Selma E; FECHINE, Pierre B. From Magneto-Dielectric Biocomposite Films to Microstrip Antenna Devices. **Journal of Composites Science** , vol. 4, nº 4, 2020.

DE SOUZA, R v; GARBOSSA, L H P; CAMPOS, C J A; VIANNA, L F de N; VANZ, A; RUPP, G S. Metals and pesticides in commercial bivalve mollusc production areas in the North and South Bays, Santa Catarina (Brazil). **Marine Pollution Bulletin**, vol. 105, nº 1, p. 377–384, 2016.

DEMIN, Alexander M; MEKHAEV, Alexander v; ESIN, Alexander A; KUZNETSOV, Dmitry K; ZELENOVSKIY, Pavel S; SHUR, Vladimir Ya.; KRASNOV, Victor P. Immobilization of PMIDA on Fe_3O_4 magnetic nanoparticles surface: Mechanism of bonding. **Applied Surface Science**, vol. 440, p. 1196–1203, 2018.

DEMIN, Alexander M; PERSHINA, Alexandra G; MININ, Artem S; MEKHAEV, Alexander v; IVANOV, Vladimir v; LEZHAVA, Sofiya P; ZAKHAROVA, Alexandra A; BYZOV, Iliya v; UIMIN, Mikhail A; KRASNOV, Victor P; OGORODOVA, Ludmila M. PMIDA-Modified Fe3O4 Magnetic Nanoparticles: Synthesis and Application for Liver MRI. **Langmuir**, vol. 34, nº 11, p. 3449–3458, 2018.

DEVAUD, M; GULA, D. Comportement électrochimique des chlorures de di et trinéophylétain dans divers milieux. **Electrochimica Acta**, vol. 23, nº 6, p. 565–569, 1978.

DI CORATO, Riccardo; ESPINOSA, Ana; LARTIGUE, Lenaic; THARAUD, Mickael; CHAT, Sophie; PELLEGRINO, Teresa; MÉNAGER, Christine; GAZEAU, Florence; WILHELM, Claire. Magnetic hyperthermia efficiency in the cellular environment for different nanoparticle designs. **Biomaterials**, vol. 35, nº 24, p. 6400–6411, ago. 2014.

DOLORES, Reyman; RAQUEL, Serrano; ADIANEZ, Garcia-Leis. Sonochemical synthesis of iron oxide nanoparticles loaded with folate and cisplatin: Effect of ultrasonic frequency. **Ultrasonics Sonochemistry**, vol. 23, p. 391–398, 2015.

DONG, Yuanyuan; YANG, Lijun; ZHANG, Lei. Simultaneous Electrochemical Detection of Benzimidazole Fungicides Carbendazim and Thiabendazole Using a Novel Nanohybrid Material-Modified Electrode. **Journal of Agricultural and Food Chemistry**, vol. 65, nº 4, p. 727–736, 2017.

DU, Liang; WANG, Wentao; ZHANG, Chengqi; JIN, Zhicheng; PALUI, Goutam; MATTOUSSI, Hedi. A Versatile Coordinating Ligand for Coating Semiconductor, Metal, and Metal Oxide Nanocrystals. **Chemistry of Materials**, vol. 30, nº 20, p. 7269–7279, 2018.

DUAN, Hongwei; KUANG, Min; WANG, Xiaoxia; WANG, Y Andrew; MAO, Hui; NIE, Shuming. Reexamining the effects of particle size and surface chemistry on the magnetic properties of iron oxide nanocrystals: New insights into spin disorder and proton relaxivity. **Journal of Physical Chemistry C**, vol. 112, p. 8127–8131, 2008.

DUNLOP, D J. Superparamagnetic and single-domain threshold sizes in magnetite. **Journal of Geophysical Research**, vol. 78, nº 11, p. 1780–1793, 1973.

EVANGELISTA, F.; RUOCCO, A.; GOTTER, R.; COSSARO, A.; FLOREANO, L.; MORGANTE, A.; CRISPOLDI, F.; BETTI, M. G.; MARIANI, C. Electronic states of CuPc chains on the Au(110) surface. **Journal of Chemical Physics**, vol. 131, p. 174710, 2009.

FARHADI, Khalil; FARAJZADEH, Mir Ali; MATIN, Amir Abbas. Liquid chromatographic determination of benomyl in water samples after dispersive liquid-liquid microextraction. **Journal of Separation Science**, vol. 32, n° 14, 2009.

FARZIN, Ali; ETESAMI, Seyed Alireza; QUINT, Jacob; MEMIC, Adnan; TAMAYOL, Ali. Magnetic Nanoparticles in Cancer Therapy and Diagnosis. **Advanced Healthcare Materials**, vol. 9, nº 9, p. 1901058, 2020.

FENG, Shuxiao; LI, Yangguang Yingchun; ZHANG, Ruyue; LI, Yangguang Yingchun. A novel electrochemical sensor based on molecularly imprinted polymer modified hollow N, S-Mo_2C/C spheres for highly sensitive and selective carbendazim determination. **Biosensors and Bioelectronics**, vol. 142, p. 111491, 2019.

FLEUTOT, S; NEALON, G L; PAULY, M; PICHON, B P; LEUVREY, C; DRILLON, M; GALLANI, J.-L.; GUILLON, D; DONNIO, B; BEGIN-COLIN, S. Spacing-dependent dipolar interactions in dendronized magnetic iron oxide nanoparticle 2D arrays and powders. **Nanoscale**, vol. 5, nº 4, p. 1507–1516, 2013.

FRANÇA, Rafaela F.; DE OLIVEIRA, Hueder Paulo M; PEDROSA, Valber A.; CODOGNOTO, Lucia. Electroanalytical determination of carbendazim and fenamiphos in natural waters using a diamond electrode. **Diamond and Related Materials**, vol. 27–28, p. 54–59, 2012.

FREIRE, R. M.; RIBEIRO, T. S.; VASCONCELOS, I. F.; DENARDIN, J. C.; BARROS, E. B.; MELE, Giuseppe; CARBONE, L.; MAZZETTO, S. E.; FECHINE, P. B. A. $MZnFe_2O_4$ (M = Ni, Mn) cubic superparamagnetic nanoparticles obtained by hydrothermal synthesis. **Journal of Nanoparticle Research**, vol. 15, nº 5, p. 1616, 2013.

FREIRE, T.M. M.; DUTRA, L.M.U. M.U.; QUEIROZ, D.C. C.; RICARDO, N.M.P.S. M.P.S.; BARRETO, K.; DENARDIN, J.C. C.; WURM, Frederik R.; SOUSA, C.P. P.; CORREIA, A.N. N.; DE LIMA-NETO, P.; FECHINE, P.B.A. B.A. Fast ultrasound assisted synthesis of chitosan-based magnetite nanocomposites as a modified electrode sensor. **Carbohydrate Polymers**, vol. 151, p. 760–769, 2016.

FRISON, Ruggero; CERNUTO, Giuseppe; CERVELLINO, Antonio; ZAHARKO, Oksana; COLONNA, Gian Maria; GUAGLIARDI, Antonietta; MASCIOCCHI, Norberto. Magnetite–Maghemite Nanoparticles in the 5–15 nm Range: Correlating the Core–Shell Composition and the Surface Structure to the Magnetic Properties. A Total Scattering Study. **Chemistry of Materials**, vol. 25, nº 23, p. 4820–4827, 2013.

GALLI, Marco; ROSSOTTI, Beatrice; AROSIO, Paolo; FERRETTI, Anna Maria; PANIGATI, Monica; RANUCCI, Elisabetta; FERRUTI, Paolo; SALVATI, Anna; MAGGIONI, Daniela. A new catechol-functionalized polyamidoamine as an effective SPION stabilizer. **Colloids and Surfaces B: Biointerfaces**, vol. 174, p. 260–269, 2019.

GALVÃO, W S; PINHEIRO, B B; GOLÇALVES, L R B; DE MATTOS, M C; FONSECA, T S; REGIS, T; ZAMPIERI, D; DOS SANTOS, J C S; COSTA, L S; CORREA, M A; BOHN, F; FECHINE, P B A. Novel nanohybrid biocatalyst: application in the kinetic resolution of secondary alcohols. **Journal of Materials Science**, vol. 53, nº 20, p. 14121–14137, 2018.

GALVÃO, Wesley S.; NETO, Davino M.A.; FREIRE, Rafael M.; FECHINE, P.B.A. Super-Paramagnetic Nanoparticles with Spinel Structure: A Review of Synthesis and Biomedical Applications. **Solid State Phenomena**, vol. 241, p. 139–176, 2015.

GAN, Tian; LI, Jiebin; LI, Hanxiao; LIU, Yangxiao; XU, Zhihong. Synthesis of Au nanorod-embedded and graphene oxide-wrapped microporous ZIF-8 with high electrocatalytic activity for the sensing of pesticides. **Nanoscale**, vol. 11, nº 16, p. 7839–7849, 2019.

GAO, Fan; QU, Hua; DUAN, Yangyang; WANG, Jing; SONG, Xiao; JI, Tianjiao; CAO, Lixin; NIE, Guangjun; SUN, Shuqing. Dopamine coating as a general and facile route to biofunctionalization of superparamagnetic Fe_3O_4 nanoparticles for magnetic separation of proteins. **RSC Advances**, vol. 4, nº 13, p. 6657–6663, 2014.

GAO, Xinyu; GAO, Yan; BIAN, Congcong; MA, Hanyue; LIU, Honglei. Electroactive nanoporous gold driven electrochemical sensor for the simultaneous detection of carbendazim and methyl parathion. **Electrochimica Acta**, vol. 310, p. 78–85, 2019.

GASPAR, Simone Maria F. S.; NUNES, Gilvanda Silva; PINHEIRO, Cláudio Urbano B.; DO AMARANTE JÚNIOR, Ozelito Possidônio. Avaliação de risco de pesticidas aplicados no município de Arari, Maranhão, Brasil: base para programa de controle ambiental do Rio Mearim. **Revista de Ecotoxicologia e Meio Ambiente,** vol. 15, 2005.

GAUGER, Andrew J; HERSHBERGER, Kian K; BRONSTEIN, Lyudmila M. Theranostics Based on Magnetic Nanoparticles and Polymers: Intelligent Design for Efficient Diagnostics and Therapy . **Frontiers in Chemistry** , vol. 8, p. 561, 2020.

GAVILÁN, Helena; AVUGADDA, Sahitya Kumar; FERNÁNDEZ-CABADA, Tamara; SONI, Nisarg; CASSANI, Marco; MAI, Binh T; CHANTRELL, Roy; PELLEGRINO, Teresa. Magnetic nanoparticles and clusters for magnetic hyperthermia: optimizing their heat performance and developing combinatorial therapies to tackle cancer. **Chemical Society Reviews**, vol. 50, p. 11614–11667, 2021.

GERBER, Olivier; PICHON, Benoit P; ULHAQ, Corinne; GRENÈCHE, Jean-Marc; LEFEVRE, Christophe; FLOREA, Ileana; ERSEN, Ovidiu; BEGIN, Dominique; LEMONNIER, Sebastien; BARRAUD, Elodie; BEGIN-COLIN, Sylvie. Low Oxidation State and Enhanced Magnetic Properties Induced by Raspberry Shaped Nanostructures of Iron Oxide. **The Journal of Physical Chemistry C**, vol. 119, nº 43, p. 24665–24673, 29 out. 2015.

GOMES, Rayane N; BEZERRA-NETO, João R; SOUSA, Camila P; MEDEIROS, Samuel L S; BECKER, Helena; SOARES, Janete Eliza S; DE LIMA-NETO, Pedro; CORREIA, Adriana N. Understanding the dipyrone oxidation allying electrochemical and computational approaches. **Analytica Chimica Acta**, vol. 1051, p. 49–57, 2019.

GRAF, Nora; YEGEN, Eda; GROSS, Thomas; LIPPITZ, Andreas; WEIGEL, Wilfried; KRAKERT, Simone; TERFORT, Andreas; UNGER, Wolfgang E.S. XPS and NEXAFS studies of aliphatic and aromatic amine species on functionalized surfaces. **Surface Science**, vol. 603, n° 18, p. 2849–2860, 2009.

GRIMALT, Susana; DEHOUCK, Pieter. Review of analytical methods for the determination of pesticide residues in grapes. **Journal of Chromatography A**, vol. 1433, p. 1–23, 2016.

GROSVENOR, A P; KOBE, B A; BIESINGER, M C; MCINTYRE, N S. Investigation of multiplet splitting of Fe2p XPS spectra and bonding in iron compounds. **Surface and Interface Analysis**, vol. 36, nº 12, p. 1564–1574, 2004.

GUARDA, P M; GUALBERTO, L D S; MENDES, D B; GUARDA, E A; DA SILVA, J E C. Analysis of triazines, triazoles, and benzimidazoles used as pesticides in different environmental compartments of the Formoso River and their influence on biodiversity in Tocantins. **Journal of Environmental Science and Health - Part B Pesticides**, vol. 55, nº 9, p. 783–793, 2020.

GUBIN, Sergei P; KOKSHAROV, Yurii A; KHOMUTOV, G B; YURKOV, Gleb Yu. Magnetic nanoparticles: preparation, structure and properties. **Russian Chemical Reviews**, vol. 74, nº 6, p. 489–520, 2005.

GUIMARAES, Alberto Passos. **Principles of nanomagnetism**. [*S. l.*]: Springer, 2009.

HANWELL, Marcus D; CURTIS, Donald E; LONIE, David C; VANDERMEERSCH, Tim; ZUREK, Eva; HUTCHISON, Geoffrey R. Avogadro: an advanced semantic chemical editor, visualization, and analysis platform. **Journal of Cheminformatics**, vol. 4, nº 1, p. 17, 2012.

HARRIS, Daniel C. **Quantitative Chemical Analysis**. Eighth. New York: Clancy Marshall, 2010.

HARRIS, Vincent G. Modern Microwave Ferrites. **IEEE Transactions on Magnetics**, vol. 48, nº 3, p. 1075–1104, mar. 2012.

HELLERBACH, Alexandra; SCHUSTER, Verena; JANSEN, Andreas; SOMMER, Jens. MRI Phantoms – Are There Alternatives to Agar? **PLOS ONE**, vol. 8, nº 8, p. e70343, 2013.

HO, Junming; COOTE L., Michelle; CRAMER J., Christopher; TRYHLAR G., Donald. Theoretical Calculation of Reduction Potentials. **Techniques For Studies Of Electrochemical Reactions In Solution**. [*S. l.*: *s. n.*], 2015.

HOLA, Katerina; MARKOVA, Zdenka; ZOPPELLARO, Giorgio; TUCEK, Jiri; ZBORIL, Radek. Tailored functionalization of iron oxide nanoparticles for MRI, drug delivery, magnetic separation and immobilization of biosubstances. **Biotechnology Advances**, vol. 33, nº 6, Part 2, p. 1162–1176, 2015.

HOMEM-DE-MELLO, P; MENNUCCI, B; TOMASI, J; DA SILVA, A B F. The effects of solvation in the theoretical spectra of cationic dyes. **Theoretical Chemistry Accounts**, vol. 113, nº 5, p. 274–280, 2005..

HOU, Yining; QU, Jiuhui; ZHAO, Xu; LIU, Huijuan. Electrochemical incineration of dimethyl phthalate by anodic oxidation with boron-doped diamond electrode. **Journal of Environmental Sciences**, vol. 21, nº 10, p. 1321–1328, 2009.

HU, Fengqin; MACRENARIS, Keith W; A. WATERS, Emily; SCHULTZ-SIKMA, Elise A; ECKERMANN, Amanda L; MEADE, Thomas J. Highly dispersible, superparamagnetic magnetite nanoflowers for magnetic resonance imaging. **Chemical Communications**, vol. 46, nº 1, p. 73–75, 2010.

HUA, Mu-Yi; CHEN, Hsiao-Chien; TSAI, Rung-Ywan; LIN, Yu-Chen; WANG, Leeyih. A novel biosensing mechanism based on a poly(N-butyl benzimidazole)-modified gold electrode for the detection of hydrogen peroxide. **Analytica Chimica Acta**, vol. 693, nº 1, p. 114–120, 2011.

HUANG, Guoming; LI, Hui; CHEN, Jiahe; ZHAO, Zhenghuan; YANG, Lijiao; CHI, Xiaoqin; CHEN, Zhong; WANG, Xiaomin; GAO, Jinhao. Tunable T_1 and T_2 contrast abilities of manganese-engineered iron oxide nanoparticles through size control. **Nanoscale**, vol. 6, nº 17, p. 10404–10412, 2014.

ILAGER, Davalasab; SEO, Hyungtak; KALANUR, Shankara S; SHETTI, Nagaraj P; AMINABHAVI, Tejraj M. A novel sensor based on $WO_3 \cdot 0.33H_2O$ nanorods modified electrode for the detection and degradation of herbicide, carbendazim. **Journal of Environmental Management**, vol. 279, p. 111611, 2021.

INCORVIO, Michael John; CONTARINI, Salvatore. X-Ray Photoelectron Spectroscopic Studies of Metal/Inhibitor Systems: Structure and Bonding at the Iron/Amine Interface. **Journal of The Electrochemical Society** , vol. 136, nº 9, p. 2493–2498, 1989.

IYENGAR, Srividhya J.; JOY, Mathew; GHOSH, Chandan Kumar; DEY, Subhrajyoti; KOTNALA, Ravinder K.; GHOSH, Swapankumar. Magnetic, X-ray and Mössbauer studies on magnetite/maghemite core–shell nanostructures fabricated through an aqueous route. **RSC Advances**, vol. 4, nº 110, p. 64919–64929, 2014.

JACQUES, Vincent; DUMAS, Stéphane; SUN, Wei-Chuan; TROUGHTON, Jeffrey S; GREENFIELD, Matthew T; CARAVAN, Peter. High-relaxivity magnetic resonance imaging contrast agents. Part 2. Optimization of inner- and second-sphere relaxivity. **Investigative**

radiology, vol. 45, nº 10, p. 613–624, 2010.

JEDLOVSZKY-HAJDÚ, Angéla; TOMBÁCZ, Etelka; BÁNYAI, István; BABOS, Magor; PALKÓ, András. Carboxylated magnetic nanoparticles as MRI contrast agents: Relaxation measurements at different field strengths. **Journal of Magnetism and Magnetic Materials**, vol. 324, nº 19, p. 3173–3180, 2012.

JEON, Sangmin; PARK, Bum Chul; LIM, Seungho; YOON, Hong Yeol; JEON, Yoo Sang; KIM, Byung-Soo; KIM, Young Keun; KIM, Kwangmeyung. Heat-Generating Iron Oxide Multigranule Nanoclusters for Enhancing Hyperthermic Efficacy in Tumor Treatment. **ACS Applied Materials & Interfaces**, vol. 12, nº 30, p. 33483–33491, 2020.

JI, Yanjing; HAN, Zeyu; DING, Han; XU, Xinkai; WANG, Danyang; ZHU, Yanli; AN, Fei; TANG, Shang; ZHANG, Hui; DENG, Jing; ZHOU, Qihui. Enhanced Eradication of Bacterial/Fungi Biofilms by Glucose Oxidase-Modified Magnetic Nanoparticles as a Potential Treatment for Persistent Endodontic Infections. **ACS Applied Materials & Interfaces**, vol. 13, nº 15, p. 17289–17299, 2021.

JIN, Xiaoying; CHEN, Xiaohu; CHENG, Yute; WANG, Longshen; HU, Bing; TAN, Junjun. Effects of hydrothermal temperature and time on hydrothermal synthesis of colloidal hydroxyapatite nanorods in the presence of sodium citrate. **Journal of colloid and interface science**, vol. 450, p. 151–158, 2015.

JOY, P A; KUMAR, P S Anil; DATE, S K. The relationship between field-cooled and zero-field-cooled susceptibilities of some ordered magnetic systems. **Journal of Physics: Condensed Matter**, vol. 10, nº 48, p. 11049–11054, 1998.

JUNG, Chu W.; JACOBS, Paula. Physical and chemical properties of superparamagnetic iron oxide MR contrast agents: ferumoxides, ferumoxtran, ferumoxsil. **Magnetic Resonance Imaging**, vol. 13, nº 5, p. 661–674, 1995.

KABEYA, Luciana M; KANASHIRO, Alexandre; AZZOLINI, A E; SORIANI, Frederico M; LOPES, J L; LUCISANO-VALIM, Yara M. Inhibitory effect of eight simple coumarins on the lucigenin enhanced chemiluminescence of rabbit neutrophils. **Research communications in molecular pathology and pharmacology**, vol. 111, nº 1–4, p. 103–113, 2002.

KANDASAMY, Ganeshlenin; MAITY, Dipak. Recent advances in superparamagnetic iron oxide nanoparticles (SPIONs) for in vitro and in vivo cancer nanotheranostics. **International Journal of Pharmaceutics**, vol. 496, nº 2, p. 191–218, 2015.

KAUSHIK, Ajeet; SOLANKI, Pratima R.; ANSARI, Anees A.; SUMANA, G.; AHMAD, Sharif; MALHOTRA, Bansi D. Iron oxide-chitosan nanobiocomposite for urea sensor. **Sensors and Actuators B-Chemical**, vol. 138, nº 2, p. 572–580, 2009. D

KEMP, Scott J; FERGUSON, R Matthew; KHANDHAR, Amit P; KRISHNAN, Kannan M. Monodisperse magnetite nanoparticles with nearly ideal saturation magnetization. **RSC Advances**, vol. 6, nº 81, p. 77452–77464, 2016.

KIM, June-Hyun; KIM, Sung-Man; YOON, In-Ho; KIM, Ilgook. Application of polyethylenimine-coated magnetic nanocomposites for the selective separation of Cs-enriched clay particles from radioactive soil. **RSC Advances**, vol. 10, nº 37, p. 21822–21829, 2020.

KOLEN'KO, Yury v; BAÑOBRE-LÓPEZ, Manuel; RODRÍGUEZ-ABREU, Carlos; CARBÓ-ARGIBAY, Enrique; DEEPAK, Francis Leonard; PETROVYKH, Dmitri Y; CERQUEIRA, M Fátima; KAMALI, Saeed; KOVNIR, Kirill; SHTANSKY, Dmitry v; LEBEDEV, Oleg I; RIVAS, Jose. High-Temperature Magnetism as a Probe for Structural and Compositional Uniformity in Ligand-Capped Magnetite Nanoparticles. **The Journal of Physical Chemistry C**, vol. 118, nº 48, p. 28322–28329, 2014.

KOLEN'KO, Yury v.; BAÑOBRE-LÓPEZ, Manuel; RODRÍGUEZ-ABREU, Carlos; CARBÓ-ARGIBAY, Enrique; SAILSMAN, Alexandra; PIÑEIRO-REDONDO, Yolanda; CERQUEIRA, M. Fátima; PETROVYKH, Dmitri Y.; KOVNIR, Kirill; LEBEDEV, Oleg I.; RIVAS, José. Large-Scale Synthesis of Colloidal Fe_3O_4 Nanoparticles Exhibiting High Heating Efficiency in Magnetic Hyperthermia. **The Journal of Physical Chemistry C**, vol. 118, nº 16, p. 8691–8701, 2014.

KOMORSKY-LOVRIĆ, Šebojka; LOVRIĆ, Milivoj. Square-wave voltammetry of quasi-reversible surface redox reactions. **Journal of Electroanalytical Chemistry**, vol. 384, nº 1, p. 115–122, 1995.

KOZAKOVA, Z; KURITKA, I; KAZANTSEVA, N E; BABAYAN, V; PASTOREK, M; MACHOVSKY, M; BAZANT, P; SAHA, P. The formation mechanism of iron oxide nanoparticles within the microwave-assisted solvothermal synthesis and its correlation with the structural and magnetic properties. **Dalton Transactions**, vol. 44, nº 48, p. 21099–21108, 2015.

KOZLENKO, D P; DUBROVINSKY, L S; KICHANOV, S E; LUKIN, E v; CERANTOLA, V; CHUMAKOV, A I; SAVENKO, B N. Magnetic and electronic properties of magnetite across the high pressure anomaly. **Scientific Reports**, vol. 9, nº 1, p. 4464, 2019.

KUMAR, Vanish; VAID, Kalyan; BANSAL, Suneev Anil; KIM, Ki-Hyun. Nanomaterial-based immunosensors for ultrasensitive detection of pesticides/herbicides: Current status and perspectives. **Biosensors and Bioelectronics**, vol. 165, p. 112382, 2020.

LAGROW, Alec P; BESENHARD, Maximilian O; HODZIC, Aden; SERGIDES, Andreas; BOGART, Lara K; GAVRIILIDIS, Asterios; THANH, Nguyen Thi Kim. Unravelling the growth mechanism of the co-precipitation of iron oxide nanoparticles with the aid of synchrotron X-Ray diffraction in solution. **Nanoscale**, vol. 11, nº 14, p. 6620–6628, 2019.

LAM, T; AVTI, P K; POULIOT, P; MAAFI, F; TARDIF, J.-C.; RHÉAUME, É; LESAGE, F; KAKKAR, A. Fabricating water dispersible superparamagnetic iron oxide nanoparticles for biomedical applications through Ligand exchange and direct conjugation. **Nanomaterials**, vol. 6, nº 6, p. 1, 2016.

LANIGAN, Katherine C.; PIDSOSNY, Katie. Reflectance FTIR spectroscopic analysis of metal complexation to EDTA and EDDS. **Vibrational Spectroscopy**, vol. 45, n° 1, p. 2–9, 2007.

LASSENBERGER, A; GRÜNEWALD, T A; VAN OOSTRUM, P D J; RENNHOFER, H; AMENITSCH, H; ZIRBS, R; LICHTENEGGER, H C; REIMHULT, E. Monodisperse Iron Oxide Nanoparticles by Thermal Decomposition: Elucidating Particle Formation by Second-Resolved in Situ Small-Angle X-ray Scattering. **Chemistry of Materials**, vol. 29, nº 10, p. 4511–4522, 2017.

LAURA, Ma.; SNCHEZ-SALINAS, Enrique; DANTN GONZLEZ, Edgar; LUISA, Mara. Pesticide Biodegradation: Mechanisms, Genetics and Strategies to Enhance the Process. **Biodegradation - Life of Science**. [*S. l.*: *s. n.*], 2013.

LAVIRON, E. Influence of the adsorption of the depolarizer or of a product of the electrochemical reaction on polarographic currents: XVII. Theoretical study of a reversible surface reaction followed by a first order chemical reaction in linear potential sweep voltam. **Journal of Electroanalytical Chemistry and Interfacial Electrochemistry**, vol. 35, nº 1, p. 333–342, 1972.

LAVIRON, E; MEUNIER-PREST, R. Theory of EC1, EC2, EC1E, EEC1 and irreversible surface reactions in polarography. **Journal of Electroanalytical Chemistry**, vol. 375, nº 1, p. 79–87, 1994.

LEBDUŠKOVÁ, Petra; HERMANN, Petr; HELM, Lothar; TÓTH, Éva; KOTEK, Jan; BINNEMANS, Koen; RUDOVSKÝ, Jakub; LUKEŠ, Ivan; MERBACH, André E. Gadolinium(iii) complexes of mono- and diethyl esters of monophosphonic acid analogue of DOTA as potential MRI contrast agents: solution structures and relaxometric studies. **Dalton Transactions**, nº 4, p. 493–501, 2007.

LEE, Nohyun; HYEON, Taeghwan. Designed synthesis of uniformly sized iron oxide nanoparticles for efficient magnetic resonance imaging contrast agents. **Chemical Society Reviews**, vol. 41, nº 7, p. 2575–2589, 2012.

LEE, Nohyun; YOO, Dongwon; LING, Daishun; CHO, Mi Hyeon; HYEON, Taeghwan; CHEON, Jinwoo. Iron Oxide Based Nanoparticles for Multimodal Imaging and Magnetoresponsive Therapy. **Chemical Reviews**, vol. 115, nº 19, p. 10637–10689, 2015.

LEONEL, Alice G; MANSUR, Herman S; MANSUR, Alexandra A P; CAIRES, Anderson; CARVALHO, Sandhra M; KRAMBROCK, Klaus; OUTON, Luis Eugenio F; ARDISSON, José Domingos. Synthesis and characterization of iron oxide nanoparticles/carboxymethyl cellulose core-shell nanohybrids for killing cancer cells in vitro. **International Journal of Biological Macromolecules**, vol. 132, p. 677–691, 2019.

LEÓN-FÉLIX, L.; CHAKER, J.; PARISE, M.; COAQUIRA, J. A H; DE LOS SANTOS VALLADARES, L.; BUSTAMANTE, A.; GARG, V. K.; OLIVEIRA, A. C.; MORAIS, P. C. Synthesis and characterization of uncoated and gold-coated magnetite nanoparticles. **Hyperfine Interactions**, vol. 224, nº 1–3, p. 179–188, 2014.

LÉVY, Michael; GAZEAU, Florence; BACRI, Jean-Claude; WILHELM, Claire; DEVAUD, Martin. Modeling magnetic nanoparticle dipole-dipole interactions inside living cells. **Physical Review B**, vol. 84, nº 7, p. 75480, 16 ago. 2011.

LÉVY, Michael; WILHELM, Claire; DEVAUD, Martin; LEVITZ, Pierre; GAZEAU, Florence. How cellular processing of superparamagnetic nanoparticles affects their magnetic behavior and NMR relaxivity. **Contrast Media and Molecular Imaging**, vol. 7, nº 4, p. 373–383, 2012.

LI, Yanan; ZHANG, Hui. Fe_3O_4-based nanotheranostics for magnetic resonance imaging-synergized multifunctional cancer management. **Nanomedicine**, vol. 14, nº 11, p. 1493–1512, 2019.

LI, Zhanfeng; DONG, Jun; WANG, Lun; ZHANG, Yongqiang; ZHUANG, Tingting; WANG, Huiqi; CUI, Xuejun; WANG, Zonghua. A power-triggered preparation strategy of nano-structured inorganics: sonosynthesis. **Nanoscale Advances**, vol. 3, nº 9, p. 2423–2447, 2021.

LIAO, Xiaoning; HUANG, Zhiwen; HUANG, Kai; QIU, Mei; CHEN, Fuliang; ZHANG, Yongfan; WEN, Yangping; CHEN, Jinyin. Highly Sensitive Detection of Carbendazim and Its Electrochemical Oxidation Mechanism at a Nanohybrid Sensor. **Journal of The Electrochemical Society**, vol. 166, nº 6, p. B322–B327, 2019.

LIN, Hongyu; LIU, Kun; GAO, Jinhao. Surface Engineering to Boost the Performance of Nanoparticle-Based T1 Contrast Agents. **European Journal of Inorganic Chemistry**, vol. 2019, nº 34, p. 3801–3809, 2019.

LONG, Le Quoc; HUE, Tran Thi Bich; HOAN, Nguyen Xuan; CUONG, Le Viet; THANG, Pham Duc; HOANG, Thai; TRUC, Trinh Anh. Growth Mechanism and Stability of Magnetite Nanoparticles Synthesized by the Hydrothermal Method. **Journal of Nanoscience and Nanotechnology**, vol. 16, nº 7, p. 7373–7379, 2016.

LOUETTE, Pierre; BODINO, Frederic; PIREAUX, Jean-Jacques. Poly(acrylic acid) (PAA) XPS Reference Core Level and Energy Loss Spectra. **Surface Science Spectra**, vol. 12, nº 1, p. 22–26, 2005a.

LOUETTE, Pierre; BODINO, Frederic; PIREAUX, Jean-Jacques. Poly(ethylene oxide) (PEO) XPS Reference Core Level and Energy Loss Spectra. **Surface Science Spectra**, vol. 12, n° 1, p. 59, 2005b.

LOWRY, Gregory v; HILL, Reghan J; HARPER, Stacey; RAWLE, Alan F; HENDREN, Christine Ogilvie; KLAESSIG, Fred; NOBBMANN, Ulf; SAYRE, Philip; RUMBLE, John. Guidance to improve the scientific value of zeta-potential measurements in nanoEHS. **Environmental Science: Nano**, vol. 3, nº 5, p. 953–965, 2016.

LU, Ting; WANG, Junhu; YIN, Jie; WANG, Aiqin; WANG, Xiaodong; ZHANG, Tao. Surfactant effects on the microstructures of Fe_3O_4 nanoparticles synthesized by microemulsion method. **Colloids and Surfaces A: Physicochemical and Engineering Aspects**, vol. 436, p. 675–683, 2013.

LUCAS, Francisco Willian De S; MASCARO, Lucia H; FILL, Taicia P; RODRIGUES-FILHO, Edson; FRANCO-JUNIOR, Edison; HOMEM-DE-MELLO, Paula; LIMA-NETO, Pedro de; CORREIA, Adriana N. Diclofenac on Boron-Doped Diamond Electrode: From Electroanalytical Determination to Prediction of the Electrooxidation Mechanism with HPLC-ESI / HRMS and Computational Simulations. **Langmuir**, vol. 30, n° 19, p. 5645–5654, 2014.

LUCISANO, Y M; MANTOVANI, B. Lysosomal enzyme release from polymorphonuclear leukocytes induced by immune complexes of IgM and of IgG. **The Journal of Immunology**, vol. 132, nº 4, p. 2015–2020, 1984.

LUO, Tao; MENG, Qiang Qiang; GAO, Chao; YU, Xin Yao; JIA, Yong; SUN, Bai; JIN, Zhen; LI, Qun Xiang; LIU, Jin Huai; HUANG, Xing Jiu. Sub-20 nm-Fe_3O_4 square and circular nanoplates: Synthesis and facet-dependent magnetic and electrochemical properties. **Chemical Communications**, vol. 50, n° 100, p. 15952–15955, 2014.

LUXBACHER, Thomas. The ZETA guide: Principles of the streaming potential technique.

Anton Paar GmbH: Graz, Austria, 2014.

LV, Kai; HAN, Jun; YANG, Chu-Ting; CHENG, Chang-Ming; LUO, Yang-Ming; WANG, Xiao-Lin. A category of hierarchically porous tin (IV) phosphonate backbone with the implication for radioanalytical separation. **Chemical Engineering Journal**, vol. 302, p. 368–376, 2016.

MA, Yanhang; XING, Lei; ZHENG, Haoquan; CHE, Shunai. Anionic−Cationic Switchable Amphoteric Monodisperse Mesoporous Silica Nanoparticles. **Langmuir**, vol. 27, nº 2, p. 517–520, 2011.

MAMIYA, Hiroaki; FUKUMOTO, Hiroya; CUYA HUAMAN, Jhon L; SUZUKI, Kazumasa; MIYAMURA, Hiroshi; BALACHANDRAN, Jeyadevan. Estimation of Magnetic Anisotropy of Individual Magnetite Nanoparticles for Magnetic Hyperthermia. **ACS Nano**, vol. 14, nº 7, p. 8421–8432, 2020.

MANDEL, K.; HUTTER, F.; GELLERMANN, C.; SEXTL, G. Stabilisation effects of superparamagnetic nanoparticles on clustering in nanocomposite microparticles and on magnetic behaviour. **Journal of Magnetism and Magnetic Materials**, vol. 331, p. 269–275, 2013.

MANISANKAR, P; SELVANATHAN, G; VEDHI, C. Utilization of sodium montmorillonite clay-modified electrode for the determination of isoproturon and carbendazim in soil and water samples. **Applied Clay Science**, vol. 29, nº 3, p. 249–257, 2005.

MARTINEZ-BOUBETA, Carlos; SIMEONIDIS, Konstantinos; SERANTES, David; CONDE-LEBORÁN, Iván; KAZAKIS, Ioannis; STEFANOU, George; PEÑA, Luis; GALCERAN, Regina; BALCELLS, Lluis; MONTY, Claude; BALDOMIR, Daniel; MITRAKAS, Manassis; ANGELAKERIS, Makis. Adjustable Hyperthermia Response of Self-Assembled Ferromagnetic Fe-MgO Core–Shell Nanoparticles by Tuning Dipole–Dipole Interactions. **Advanced Functional Materials**, vol. 22, nº 17, p. 3737–3744, 2012.

MAXIMIANO, Elizabete Maria; DE LIMA, Fábio; CARDOSO, Claudia Andrea Lima; ARRUDA, Gilberto José Incorporation of thermally activated zeolite into carbon paste electrodes for voltammetric detection of carbendazim traces in milk samples. **Journal of Applied Electrochemistry**, vol. 46, nº 6, p. 713–723, 2016.

MCKENZIE, Thomas G; KARIMI, Fatemeh; ASHOKKUMAR, Muthupandian; QIAO, Greg G. Ultrasound and Sonochemistry for Radical Polymerization: Sound Synthesis. **Chemistry – A European Journal**, vol. 25, nº 21, p. 5372–5388, 11 abr. 2019.

MILLER, James Jane C; MILLER, James Jane C. **Statistics and chemometrics for analytical chemistry**. Sixth. [*S. l.*]: Pearson education, 2018.

MIRCESKI, Valentin; SKRZYPEK, Sławomira; STOJANOV, Leon. Square-wave voltammetry. **ChemTexts**, vol. 4, n° 17, 2018.

MONTAGNER, Cassiana C.; VIDAL, Cristiane; ACAYABA, Raphael D.; JARDIM, Wilson F.; JARDIM, Isabel C.S.F.; UMBUZEIRO, Gisela A. Trace analysis of pesticides and an assessment of their occurrence in surface and drinking waters from the State of São Paulo (Brazil). **Analytical Methods**, vol. 6, n° 14, p. 6668–6677, 2014.

MONTEIL, Clément; BAR, Nathalie; MOREAU, Bernard; RETOUX, Richard; BEE, Agnès; TALBOT, Delphine; VILLEMIN, Didier. Phosphonated polyethylenimine-coated nanoparticles: Size- and zeta-potential-adjustable nanomaterials. **Particle and Particle Systems Characterization**, vol. 31, nº 2, p. 219–227, 2014.

MORTON, Justin A; KHAVARI, Mohammad; QIN, Ling; MACIEJEWSKA, Barbara M; TYURNINA, Anastasia v; GROBERT, Nicole; ESKIN, Dmitry G; MI, Jiawei; PORFYRAKIS, Kyriakos; PRENTICE, Paul; TZANAKIS, Iakovos. New insights into sono-exfoliation mechanisms of graphite: In situ high-speed imaging studies and acoustic measurements. **Materials Today**, vol. 49, p. 10–22, 2021.

MOSMANN, Tim. Rapid colorimetric assay for cellular growth and survival: Application to proliferation and cytotoxicity assays. **Journal of Immunological Methods**, vol. 65, p. 55–63, 1983.

MUTHUVIVEGANANDAVEL, V; MUTHURAMAN, P; MUTHU, S; SRIKUMAR, K. Toxic effects of carbendazim at low dose levels in male rats. **The Journal of Toxicological Sciences**, vol. 33, nº 1, p. 25–30, 2008.

NAGATA, Yoshio; MIZUKOSHI, Yoshiteru; OKITSU, Kenji; MAEDA, Yasuaki. Sonochemical Formation of Gold Particles in Aqueous Solution. **Radiation Research**, vol. 146, nº 3, p. 333–338, 1996.

NEESE, Frank; WENNMOHS, Frank; BECKER, Ute; RIPLINGER, Christoph. The ORCA quantum chemistry program package. **The Journal of Chemical Physics**, vol. 152, nº 22, p. 224108, 2020.

NETO, Davino M A; FREIRE, Rafael M; GALLO, Juan; FREIRE, Tiago M; QUEIROZ, Danilo C; RICARDO, Nágila M P S; VASCONCELOS, Igor F; MELE, Giuseppe; CARBONE, Luigi; MAZZETTO, Selma E; BAÑOBRE-LÓPEZ, Manuel; FECHINE, Pierre B A. Rapid Sonochemical Approach Produces Functionalized Fe_3O_4 Nanoparticles with Excellent Magnetic, Colloidal, and Relaxivity Properties for MRI Application. **The Journal of Physical Chemistry C**, vol. 121, nº 43, p. 24206–24222, 2017.

NGUYEN, Tuyen Duong Thanh; PITCHAIMANI, Arunkumar; FERREL, Colin; THAKKAR, Ravindra; ARYAL, Santosh. Nano-confinement-driven enhanced magnetic relaxivity of SPIONs for targeted tumor bioimaging. **Nanoscale**, vol. 10, nº 1, p. 284–294, 2018.

NI, Dalong; BU, Wenbo; EHLERDING, Emily B; CAI, Weibo; SHI, Jianlin. Engineering of inorganic nanoparticles as magnetic resonance imaging contrast agents. **Chemical Society Reviews**, vol. 46, nº 23, p. 7438–7468, 2017.

NIGAM, Saumya; BARICK, K. C.; BAHADUR, D. Development of citrate-stabilized Fe_3O_4 nanoparticles: Conjugation and release of doxorubicin for therapeutic applications. **Journal of Magnetism and Magnetic Materials**, vol. 323, nº 2, p. 237–243, 2011.

NISHA, Sivakumar; SENTHIL KUMAR, Annamalai. Biomimetic oxidation of benzo[a]pyrene to a quinone metabolite as a cysteine-oxidation mediator on MWCNT-modified electrode surface. **Electrochimica Acta**, vol. 350, p. 136367, 2020.

NOSRATI, Hamed; SALEHIABAR, Marziyeh; FRIDONI, Mohammadjavad;

ABDOLLAHIFAR, Mohammad-Amin; KHEIRI MANJILI, Hamidreza; DAVARAN, Soodabeh; DANAFAR, Hossein. New Insight about Biocompatibility and Biodegradability of Iron Oxide Magnetic Nanoparticles: Stereological and In Vivo MRI Monitor. **Scientific Reports**, vol. 9, nº 1, p. 7173, 2019.

OAKES, John; VAN KRALINGEN, Cornelis G. Spectroscopic studies of transition-metal ion complexes of diethylenetriaminepenta-acetic acid and diethylenetriaminepenta-methylphosphonic acid. **Journal of the Chemical Society, Dalton Transactions**, nº 6, p. 1133–1137, 1984.

OLEKSA, Viktoriia; BERNÁTOVÁ, Iveta; PATSULA, Vitalii; LÍŠKOVÁ, Silvia; BALIŠ, Peter; RADOŠINSKÁ, Jana; MIČUROVÁ, Andrea; KLUKNAVSKÝ, Michal; JASENOVEC, Tomáš; RADOŠINSKÁ, Dominika; MACKOVÁ, Hana; HORÁK, Daniel. Poly(ethylene glycol)-Alendronate-Coated Magnetite Nanoparticles Do Not Alter Cardiovascular Functions and Red Blood Cells' Properties in Hypertensive Rats. **Nanomaterials** , vol. 11, nº 5, 2021.

OLIVEIRA, Thiago M B F; BECKER, Helena; LONGHINOTTI, Elisane; DE SOUZA, Djenaine; DE LIMA-NETO, Pedro; CORREIA, Adriana N. Carbon-fibre microelectrodes coupled with square-wave voltammetry for the direct analysis of dimethomorph fungicide in natural waters. **Microchemical Journal**, vol. 109, p. 84–92, 2013.

OROZCO-HENAO, J M; CORAL, D F; MURACA, D; MOSCOSO-LONDOÑO, O; MENDOZA ZÉLIS, P; FERNANDEZ VAN RAAP, M B; SHARMA, S K; PIROTA, K R; KNOBEL, M. Effects of Nanostructure and Dipolar Interactions on Magnetohyperthermia in Iron Oxide Nanoparticles. **The Journal of Physical Chemistry C**, vol. 120, nº 23, p. 12796–12809, 2016.

ÖZCAN, Ali Ayça Atılır; HAMID, Fayha; ÖZCAN, Ali Ayça Atılır. Synthesizing of a nanocomposite based on the formation of silver nanoparticles on fumed silica to develop an electrochemical sensor for carbendazim detection. **Talanta**, vol. 222, p. 121591, 2021.

PALMA, Graciela; ŚNCHEZ, Alejandra; OLAVE, Yohana; ENCINA, Francisco; PALMA, Rodrigo; BARRA, Ricardo. Pesticide levels in surface waters in an agricultural-forestry basin in Southern Chile. **Chemosphere**, vol. 7, n° 8, p. 763–770, 2004.

PANIZZA, Marco; CERISOLA, Giacomo. Direct And Mediated Anodic Oxidation of Organic Pollutants. **Chemical Reviews**, vol. 109, nº 12, p. 6541–6569, 2009.

PARAMONOV, Pavel B; PANIAGUA, Sergio A; HOTCHKISS, Peter J; JONES, Simon C; ARMSTRONG, Neal R; MARDER, Seth R; BRÉDAS, Jean-Luc. Theoretical Characterization of the Indium Tin Oxide Surface and of Its Binding Sites for Adsorption of Phosphonic Acid Monolayers. **Chemistry of Materials**, vol. 20, nº 16, p. 5131–5133,. 2008.

PARR, R G; WEITAO, Y. **Density-Functional Theory of Atoms and Molecules**. [*S. l.*]: Oxford University Press, 1994.

PAULY, M; PICHON, B P; PANISSOD, P; FLEUTOT, S; RODRIGUEZ, P; DRILLON, M; BEGIN-COLIN, S. Size dependent dipolar interactions in iron oxide nanoparticle monolayer and multilayer Langmuir-Blodgett films. **Journal of Materials Chemistry**, vol. 22, nº 13, p. 6343–6350, 2012.

PENG, Erwin; CHOO, Eugene Shi Guang; TAN, Cherie Shi Hua; TANG, Xiaosheng; SHENG, Yang; XUE, Junmin. Multifunctional PEGylated nanoclusters for biomedical applications. **Nanoscale**, vol. 5, nº 13, p. 5994–6005, 2013.

PENG, Erwin; WANG, Fenghe; XUE, Jun Min. Nanostructured magnetic nanocomposites as MRI contrast agents. **J. Mater. Chem. B**, vol. 3, nº 11, p. 2241–2276, 2015.

PEREIRA, Clara; PEREIRA, André M; FERNANDES, Carlos; ROCHA, Mariana; MENDES, Ricardo; FERNÁNDEZ-GARCÍA, María Paz; GUEDES, Alexandra; TAVARES, Pedro B; GRENÈCHE, Jean-Marc; ARAÚJO, João P; FREIRE, Cristina. Superparamagnetic MFe_2O_4 (M = Fe, Co, Mn) Nanoparticles: Tuning the Particle Size and Magnetic Properties through a Novel One-Step Coprecipitation Route. **Chemistry of Materials**, vol. 24, nº 8, p. 1496–1504, 2012.

PERIYASAMY, Sundaresan; VINOTH KUMAR, Jeyaraj; CHEN, Shen Ming; ANNAMALAI, Yamuna; KARTHIK, Raj; ERUMAIPATTY RAJAGOUNDER, Nagarajan. Structural Insights on 2D Gadolinium Tungstate Nanoflake: A Promising Electrocatalyst for Sensor and Photocatalyst for the Degradation of Postharvest Fungicide (Carbendazim). **ACS Applied Materials and Interfaces**, vol. 11, nº 40, p. 37172–37183, 2019.

PERSSON, Per; NILSSON, Nils; SJÖBERG, Staffan. Structure and Bonding of Orthophosphate Ions at the Iron Oxide–Aqueous Interface. **Journal of Colloid and Interface Science**, vol. 177, nº 1, p. 263–275, 1996.

PETRONI, Jacqueline Marques; LUCCA, Bruno Gabriel; FOGLIATO, Daniela Kárin; FERREIRA, Valdir Souza. Sensitive Approach for Voltammetric Determination of Carbendazim Based on the Use of an Anionic Surfactant. **Electroanalysis**, vol. 28, nº 6, p. 1362–1369, 2016.

PHAM, Tien Song Hiep; FU, Li; MAHON, Peter; LAI, Guosong; YU, Aimin. Fabrication of β-Cyclodextrin-Functionalized Reduced Graphene Oxide and Its Application for Electrocatalytic Detection of Carbendazim. **Electrocatalysis**, vol. 7, nº 5, p. 411–419, 2016.

POLTE, Jörg. Fundamental growth principles of colloidal metal nanoparticles – a new perspective. **CrystEngComm**, vol. 17, nº 36, p. 6809–6830, 2015.

PORTARIA Nº 2.914, DE 12 DE DEZEMBRO DE 2011. 2011.

PÖSELT, Elmar; KLOUST, Hauke; TROMSDORF, Ulrich; JANSCHEL, Marcus; HAHN, Christoph; MASSLO, Christoph; WELLER, Horst. Relaxivity Optimization of a PEGylated Iron-Oxide-Based Negative Magnetic Resonance Contrast Agent for T_2-Weighted Spin–Echo Imaging. **ACS Nano**, vol. 6, nº 2, p. 1619–1624, 2012.

POULIN, S; FRANÇA, R; MOREAU-BÉLANGER, L; SACHER, E. Confirmation of X-ray Photoelectron Spectroscopy Peak Attributions of Nanoparticulate Iron Oxides, Using Symmetric Peak Component Line Shapes. **The Journal of Physical Chemistry C**, vol. 114, nº 24, p. 10711–10718, 2010.

POURREZA, Nahid; RASTEGARZADEH, Saadat; LARKI, Arash. Determination of fungicide carbendazim in water and soil samples using dispersive liquid-liquid microextraction and microvolume UV–vis spectrophotometry. **Talanta**, vol. 134, p. 24–29, 2015.

PROGRAMA DE ANÁLISE DE RESÍDUOS DE AGROTÓXICOS EM ALIMENTOS 2016-2018. Brasília: [*s. n.*], [*s. d.*].

RAMU, A. G.; TELMENBAYAR, L.; THEERTHAGIRI, J.; YANG, D.; SONG, M.; CHOI, Dongjin. Synthesis of a hierarchically structured Fe_3O_4-PEI nanocomposite for the highly sensitive electrochemical determination of bisphenol A in real samples. **New Journal of Chemistry**, vol. 44, n° 43, p. 18633–18645, 2020.

RAVIKUMAR, C; BANDYOPADHYAYA, Rajdip. Mechanistic Study on Magnetite Nanoparticle Formation by Thermal Decomposition and Coprecipitation Routes. **The Journal of Physical Chemistry C**, vol. 115, nº 5, p. 1380–1387, 2011.

RAZZINO, Claudia A.; SGOBBI, Lívia F.; CANEVARI, Thiago C.; CANCINO, Juliana; MACHADO, Sergio A S. Sensitive determination of carbendazim in orange juice by electrode modified with hybrid material. **Food Chemistry**, vol. 170, p. 360–365, 2015.

REDDY, L Harivardhan; ARIAS, José L; NICOLAS, Julien; COUVREUR, Patrick. Magnetic Nanoparticles: Design and Characterization, Toxicity and Biocompatibility, Pharmaceutical and Biomedical Applications. **Chemical Reviews**, vol. 112, nº 11, p. 5818–5878, 2012.

RIBEIRO, A C A; DE CARVALHO DORES, E F G; AMORIM, R S S; LOURENCETTI, C. Pesticide residues in surface waters at the headwaters of São Lourenço River-MT, Brazil: Validation of a method using solid-phase extraction and liquid chromatography. **Quimica Nova**, vol. 36, nº 2, p. 284–290, 2013.

RIBEIRO, W. F.; SELVA, T. M. G.; LOPES, I. C.; COELHO, E. C. S.; LEMOS, S. G.; CAXICO DE ABREU, F.; BERNARDO DO NASCIMENTO, V.; UGULINO DE ARAÚJO, M. C. Electroanalytical determination of carbendazim by square wave adsorptive stripping voltammetry with a multiwalled carbon nanotubes modified electrode. **Analytical Methods**, vol. 3, nº 5, p. 1202, 2011.

RUIZ-AGUDO, Encarnación; RODRIGUEZ-NAVARRO, Carlos; SEBASTIÁN-PARDO, Eduardo. Sodium Sulfate Crystallization in the Presence of Phosphonates: Implications in Ornamental Stone Conservation. **Crystal Growth & Design**, vol. 6, nº 7, p. 1575–1583, 2006.

SALAS, Gorka; CAMARERO, Julio; CABRERA, David; TAKACS, Hélène; VARELA, María; LUDWIG, Robert; DÄHRING, Heidi; HILGER, Ingrid; MIRANDA, Rodolfo; MORALES, María del Puerto; TERAN, Francisco José. Modulation of Magnetic Heating via Dipolar Magnetic Interactions in Monodisperse and Crystalline Iron Oxide Nanoparticles. **The Journal of Physical Chemistry C**, vol. 118, nº 34, p. 19985–19994, 2014.

SANT'ANNA, M V S; CARVALHO, S.W.M.M.; GEVAERD, A; SILVA, J O S; SANTOS, E; CARREGOSA, I S C; WISNIEWSKI, A; MARCOLINO-JUNIOR, L H; BERGAMINI, M F; SUSSUCHI, E M. Electrochemical sensor based on biochar and reduced graphene oxide nanocomposite for carbendazim determination. **Talanta**, vol. 220, 2020.

SANT'ANNA, M V S; CARVALHO, S.W.M.M.; GEVAERD, A; SILVA, J O S; SANTOS, E; CARREGOSA, I S C; WISNIEWSKI, A; MARCOLINO-JUNIOR, L H; BERGAMINI, M F; SUSSUCHI, E M; KOKULNATHAN, Thangavelu; CHEN, S.-M. Shen-Ming. Design and Construction of the Gadolinium Oxide Nanorod-Embedded Graphene Aerogel: A Potential Application for Electrochemical Detection of Postharvest Fungicide. **ACS Applied Materials**

and Interfaces, vol. 220, nº 14, p. 16216–16226, 2020.

SANTOYO SALAZAR, Jaime; PEREZ, Lucas; DE ABRIL, Oscar; TRUONG PHUOC, Lai; IHIAWAKRIM, Dris; VAZQUEZ, Manuel; GRENECHE, Jean-Marc; BEGIN-COLIN, Sylvie; POURROY, Genevieve. Magnetic Iron Oxide Nanoparticles in 10−40 nm Range: Composition in Terms of Magnetite/Maghemite Ratio and Effect on the Magnetic Properties. **Chemistry of Materials**, vol. 23, nº 6, p. 1379–1386, 2011.

SANTRA, Santimukul; KAITTANIS, Charalambos; GRIMM, Jan; PEREZ, J Manuel. Drug/dye-loaded, multifunctional iron oxide nanoparticles for combined targeted cancer therapy and dual optical/magnetic resonance imaging. **Small**, vol. 5, nº 16, p. 1862–8, 2009.

SCHLADT, Thomas D; SCHNEIDER, Kerstin; SCHILD, Hansjörg; TREMEL, Wolfgang. Synthesis and bio-functionalization of magnetic nanoparticles for medical diagnosis and treatment. **Dalton transactions**, vol. 40, nº 24, p. 6315–6343, 2011.

SELVAKUMAR, P; BALANAGA KARTHIK, B; THANGAVELU, C. Surface and electrochemical characterization of corrosion inhibition of stainless steel in acid medium. **Journal of Materials and Environmental Science**, vol. 5, nº 6, p. 1750–1757, 2014.

SHIM, H; DUTTA, P; SEEHRA, M S; BONEVICH, J. Size dependence of the blocking temperatures and electron magnetic resonance spectra in NiO nanoparticles. **Solid State Communications**, vol. 145, nº 4, p. 192–196, 2008.

SHIN, Tae-hyun; CHOI, Youngseon; KIM, Soojin; CHEON, Jinwoo. Recent advances in magnetic nanoparticle-based multi-modal imaging. **Chemical Society Reviews**, vol. 44, p. 4501–4516, 2015.

SICKAFUS, Kurt E; WILLS, John M; GRIMES, Norman W. Structure of Spinel. **Journal of the American Ceramic Society**, vol. 82, nº 12, p. 3279–3292, 1999.

SITAREK, Krystyna. Embryolethal and teratogenic effects of carbendazim in rats. **Teratogenesis Carcinogenesis and Mutagenesis**, vol. 21, n° 5, p. 335–340, 2001.

SITTHICHAI, Sudarat; PILAPONG, Chalermchai; THONGTEM, Titipun; THONGTEM, Somchai. CMC-coated Fe_3O_4 nanoparticles as new MRI probes for hepatocellular carcinoma. **Applied Surface Science**, vol. 356, p. 972–977, 2015.

SONG, Mengjie; ZHANG, Yu; HU, Sunling; SONG, Lina; DONG, Jinlai; CHEN, Zhongping; GU, Ning. Influence of morphology and surface exchange reaction on magnetic properties of monodisperse magnetite nanoparticles. **Colloids and Surfaces A: Physicochemical and Engineering Aspects**, vol. 408, p. 114–121, 2012.

SOUSA, Camila P; DE OLIVEIRA, Raissa C; FREIRE, Tiago. M; FECHINE, Pierre B A; SALVADOR, Michele A; HOMEM-DE-MELLO, Paula; MORAIS, Simone; DE LIMA-NETO, Pedro; CORREIA, Adriana N. Chlorhexidine digluconate on chitosan-magnetic iron oxide nanoparticles modified electrode: Electroanalysis and mechanistic insights by computational simulations. **Sensors and Actuators B: Chemical**, vol. 240, p. 417–425, 2017.

SPALDIN, Nicola A. **Magnetic Materials: Fundamentals and Applications**. [*S. l.*]: Cambridge University Press, 2010.

SRIVASTAVA, S.; AWASTHI, Rishi; GAJBHIYE, Namdeo S.; AGARWAL, Vikas; SINGH, Amit; YADAV, Abhishek; GUPTA, Rakesh K. Innovative synthesis of citrate-coated superparamagnetic Fe_3O_4 nanoparticles and its preliminary applications. **Journal of Colloid and Interface Science**, vol. 359, nº 1, p. 104–111, 2011.

STEPHEN, Zachary R; DAYRINGER, Christopher J; LIM, Josh J; REVIA, Richard A; HALBERT, Mackenzie v; JEON, Mike; BAKTHAVATSALAM, Arvind; ELLENBOGEN, Richard G; ZHANG, Miqin. Approach to Rapid Synthesis and Functionalization of Iron Oxide Nanoparticles for High Gene Transfection. **ACS Applied Materials & Interfaces**, vol. 8, nº 10, p. 6320–6328, 2016.

SYAFRUDIN, Muhammad; KRISTANTI, Risky A; YUNIARTO, Adhi; HADIBARATA, Tony; RHEE, Jongtae; AL-ONAZI, Wedad A; ALGARNI, Tahani S; ALMARRI, Abdulhadi H; AL-MOHAIMEED, Amal M. Pesticides in Drinking Water—A Review. **International Journal of Environmental Research and Public Health**, vol. 18, nº 2, 2021.

AGNIESZKA, Szpak; SYLWIA, Fiejdasz; WITOLD, Prendota; TOMASZ, Strączek; CZESŁAW, Kapusta; JANUSZ, Szmyd; MARIA, Nowakowska; SZCZEPAN, Zapotoczny. T_1-T_2 Dual-modal MRI contrast agents based on superparamagnetic iron oxide nanoparticles with surface attached gadolinium complexes. **Journal of Nanoparticle Research**, vol. 16, nº 11, p. 2678, 2014.

TAKANO, Yu; HOUK, K N. Benchmarking the Conductor-like Polarizable Continuum Model (CPCM) for Aqueous Solvation Free Energies of Neutral and Ionic Organic Molecules. **Journal of Chemical Theory and Computation**, vol. 1, nº 1, p. 70–77, 2005.

TEMGOUA, Ranil C T; BUSSY, Ugo; ALVAREZ-DORTA, Dimitri; GALLAND, Nicolas; HÉMEZ, Julie; THOBIE-GAUTIER, Christine; TONLÉ, Ignas Kenfack; BOUJTITA, Mohammed. Using electrochemistry coupled to high resolution mass spectrometry for the simulation of the environmental degradation of the recalcitrant fungicide carbendazim. **Talanta**, vol. 221, p. 121448, 2021.

TERESA, María Teresa; QUINTERO-RONDEROS, Paula; CASTIBLANCO, John; MONTOYA-ORTÍZ, Gladis. Cell culture and cell analysis. *In*: ANAYA, J M; SHOENFELD, Y; ROJAS-VILLARRAGA, A; LEVY, R A; CERVERA, R (orgs.). **Autoimmunity: From Bench to Bedside**. Bogotá: El Rosario University Press, 2013.

THOMAS, Guillaume; DEMOISSON, Frederic; BOUDON, Julien; MILLOT, Nadine. Efficient functionalization of magnetite nanoparticles with phosphonate using a one-step continuous hydrothermal process. **Dalton Trans.**, vol. 45, p. 10821–10829, 2016.

TIAN, Chunhuan; ZHANG, Shufei; WANG, Haobo; CHEN, Chen; HAN, Zhida; CHEN, Mengling; ZHU, Yingyue; CUI, Rongjing; ZHANG, Genhua. Three-dimensional nanoporous copper and reduced graphene oxide composites as enhanced sensing platform for electrochemical detection of carbendazim. **Journal of Electroanalytical Chemistry**, vol. 847, p. 113243, 2019.

TIRADO-RIVES, Julian; JORGENSEN, William L. Performance of B3LYP Density Functional Methods for a Large Set of Organic Molecules. **Journal of Chemical Theory and Computation**, vol. 4, nº 2, p. 297–306, 2008.

TIUNOV, I A; GORBACHEVSKYY, M v; KOPITSYN, D S; KOTELEV, M S; IVANOV, E

v; VINOKUROV, V A; NOVIKOV, A A. Synthesis of Large Uniform Gold and Core – Shell Gold – Silver Nanoparticles: Effect of Temperature Control. **Russian Journal of Physical Chemistry A**, vol. 90, nº 1, p. 152–157, 2016.

TONG, Sheng; HOU, Sijian; ZHENG, Zhilan; ZHOU, Jun; BAO, Gang. Coating optimization of superparamagnetic iron oxide nanoparticles for high T2 relaxivity. **Nano Letters**, vol. 10, nº 11, p. 4607–4613, 2010.

TORRISI, V; GRAILLOT, A; VITORAZI, L; CROUZET, Q; MARLETTA, G; LOUBAT, C; BERRET, J.-F. Preventing Corona Effects: Multiphosphonic Acid Poly(ethylene glycol) Copolymers for Stable Stealth Iron Oxide Nanoparticles. **Biomacromolecules**, vol. 15, nº 8, p. 3171–3179, 2014.

TUDISCO, Cristina; OLIVERI, Valentina; CANTARELLA, Maria; VECCHIO, Graziella; CONDORELLI, Guglielmo G. Cyclodextrin anchoring on magnetic Fe_3O_4 nanoparticles modified with phosphonic linkers. **European Journal of Inorganic Chemistry**, nº 32, p. 5323–5331, 2012.

UNTERWEGER, Harald; DÉZSI, László; MATUSZAK, Jasmin; JANKO, Christina; POETTLER, Marina; JORDAN, Jutta; BÄUERLE, Tobias; SZEBENI, János; FEY, Tobias; BOCCACCINI, Aldo R. Dextran-coated superparamagnetic iron oxide nanoparticles for magnetic resonance imaging: evaluation of size-dependent imaging properties, storage stability and safety. **International journal of nanomedicine**, vol. 13, p. 1899–1915, 2018.

URBANOVA, Veronika; MAGRO, Massimiliano; GEDANKEN, Aharon; BARATELLA, Davide; VIANELLO, Fabio; ZBORIL, Radek. Nanocrystalline Iron Oxides, Composites, and Related Materials as a Platform for Electrochemical, Magnetic, and Chemical Biosensors. **Chemistry of Materials**, vol. 26, nº 23, p. 6653–6673, 9 dez. 2014.

VITT, Joseph E; JOHNSON, Dennis C. The Importance of Anodic Discharge of H_2O in Anodic Oxygen-Transfer Reactions. **Journal of The Electrochemical Society**, vol. 139, nº 3, p. 774–778, 1992.

WAHSNER, Jessica; GALE, Eric M; RODRÍGUEZ-RODRÍGUEZ, Aurora; CARAVAN, Peter. Chemistry of MRI Contrast Agents: Current Challenges and New Frontiers. **Chemical Reviews**, vol. 119, nº 2, p. 957–1057, 2019.

WALCZAK, Mary M; DRYER, Deborah A; JACOBSON, Dana D; FOSS, Michele G; FLYNN, Nolan T. pH Dependent Redox Couple: An Illustration of the Nernst Equation. **Journal of Chemical Education**, vol. 74, nº 10, p. 1195, 1997.

WALTER, Aurélie; GAROFALO, Antonio; BONAZZA, Pauline; MEYER, Florent; MARTINEZ, Hervé; FLEUTOT, Solenne; BILLOTEY, Claire; TALEB, Jacqueline; FELDER-FLESCH, Delphine; BEGIN-COLIN, Sylvie. Effect of the Functionalization Process on the Colloidal, Magnetic Resonance Imaging, and Bioelimination Properties of Mono- or Bisphosphonate-Anchored Dendronized Iron Oxide Nanoparticles. **ChemPlusChem**, vol. 82, nº 4, p. 647–659, 1 abr. 2017.

WANG, Guannan; ZHANG, Xuanjun; SKALLBERG, Andreas; LIU, Yaxu; HU, Zhangjun; MEI, Xifan; UVDAL, Kajsa. One-step synthesis of water-dispersible ultra-small Fe_3O_4 nanoparticles as contrast agents for T_1 and T_2 magnetic resonance imaging. **Nanoscale**, vol. 6, nº 5, p. 2953–2963, 2014.

WANG, Piwen; HENNING, Susanne M; HEBER, David. Limitations of MTT and MTS-Based Assays for Measurement of Antiproliferative Activity of Green Tea Polyphenols. **PLOS ONE**, vol. 5, nº 4, p. e10202, 2010.

WANG, Yi-Xiang J. Superparamagnetic iron oxide based MRI contrast agents: Current status of clinical application. **Quantitative Imaging in Medicine and Surgery**, vol. 1, nº 1, p. 35–40, 2011.

WANG, Yi-Xiang J X; HUSSAIN, Shahid M; KRESTIN, Gabriel P. Superparamagnetic iron oxide contrast agents: physicochemical characteristics and applications in MR imaging. **European Radiology**, vol. 11, nº 11, p. 2319–2331, 2001.

WANG, Yongliang; LI, Baoqiang; ZHOU, Yu; JIA, Dechang; SONG, Yang. CS-Fe(II,III) complex as precursor for magnetite nanocrystal. **Polymers for Advanced Technologies**, vol. 22, nº 12, p. 1681–1684, 2011.

WITTE, K.; BODNAR, W.; MIX, T.; SCHELL, N.; FULDA, G.; WOODCOCK, T.G.; BURKEL, E. A detailed study on the transition from the blocked to the superparamagnetic state of reduction-precipitated iron oxide nanoparticles. **Journal of Magnetism and Magnetic Materials**, vol. 403, p. 103–113, abr. 2016.

WU, Longyun; YANG, ChunYan; LV, Zhongwen; CUI, FengWen; ZHAO, Lijun; YANG, Ping. Facile one-pot synthesis of different surfactant-functionalized water-soluble Fe_3O_4 nanoparticles as magnetic resonance imaging contrast agents for melanoma tumors. **RSC Advances**, vol. 5, nº 62, p. 50557–50564, 2015.

WU, Wei; JIANG, Chang Zhong; ROY, Vellaisamy A.L. Designed synthesis and surface engineering strategies of magnetic iron oxide nanoparticles for biomedical applications. **Nanoscale**, vol. 8, p. 19421–19474, 2016.

WU, Wei; WU, Zhaohui; YU, Taekyung; JIANG, Changzhong; KIM, Woo-Sik. Recent progress on magnetic iron oxide nanoparticles: synthesis, surface functional strategies and biomedical applications. **Science and Technology of Advanced Materials**, vol. 16, nº 2, p. 023501, 2015.

XIA, Tingting; GUAN, Yueping; YANG, Mingzhu; XIONG, Wubin; WANG, Ning; ZHAO, Shen; GUO, Chen. Synthesis of polyethylenimine modified Fe_3O_4 nanoparticles with immobilized Cu^{2+} for highly efficient proteins adsorption. **Colloids and Surfaces A: Physicochemical and Engineering Aspects**, vol. 443, p. 552–559, 2014.

XIAO, Lisong; LI, Jiangtian; BROUGHAM, Dermot F.; FOX, Eoin K.; FELIU, Neus; BUSHMELEV, Alexey; SCHMIDT, Annette; MERTENS, Natascha; KIESSLING, Fabian; VALLDOR, Martin; FADEEL, Bengt; MATHUR, Sanjay. Water-soluble superparamagnetic magnetite nanoparticles with biocompatible coating for enhanced magnetic resonance imaging. **ACS Nano**, vol. 5, n° 8, p6315–6324, 2011.

XU, Fenghua; CHENG, Changming; XU, Fangjie; ZHANG, Chunfu; XU, Hong; XIE, Xuan; YIN, Duanzhi; GU, Hongchen. Superparamagnetic magnetite nanocrystal clusters: a sensitive tool for MR cellular imaging. **Nanotechnology**, vol. 20, nº 40, p. 405102, 2009.

XU, Hangxun; ZEIGER, Brad W.; SUSLICK, Kenneth S. Sonochemical synthesis of nanomaterials. **Chemical Society Reviews**, vol. 42, nº 7, p. 2555–2567, 2013.

YA, Yu; WANG, Tianshun; XIE, Liping; ZHU, Junjie; TANG, Li; NING, Dejiao; YAN, Feiyan. Highly sensitive electrochemical sensor based on pyrrolidinium ionic liquid modified ordered mesoporous carbon paste electrode for determination of carbendazim. **Analytical Methods**, vol. 7, nº 4, p. 1493–1498, 2015.

YANKE, Jenna Geralde Mbokana; DEDZO, Gustave Kenne; NGAMENI, Emmanuel. Solvent Effect on the Grafting of an Organophilic Silane Onto Smectite-type Clay: Application as Electrode Modifiers for Pesticide Detection. **Electroanalysis**, vol. 29, nº 8, p. 1894–1902, 2017.

YAO, Ye; PAN, Yue; LIU, Shiqing. Power ultrasound and its applications: A state-of-the-art review. **Ultrasonics Sonochemistry**, vol. 62, p. 104722, 2020.

YAZDANI, Farshad; SEDDIGH, Mahdieh. Magnetite nanoparticles synthesized by co-precipitation method: The effects of various iron anions on specifications. **Materials Chemistry and Physics**, vol. 184, p. 318–323, 2016.

YOU, Hongjun; FANG, Jixiang. Particle-mediated nucleation and growth of solution-synthesized metal nanocrystals: A new story beyond the LaMer curve. **Nano Today**, vol. 11, nº 2, p. 145–167, 2016.

ZENG, Jianfeng; JING, Lihong; HOU, Yi; JIAO, Mingxia; QIAO, Ruirui; JIA, Qiaojuan; LIU, Chunyan; FANG, Fang; LEI, Hao; GAO, Mingyuan. Anchoring Group Effects of Surface Ligands on Magnetic Properties of Fe_3O_4 Nanoparticles: Towards High Performance MRI Contrast Agents. **Advanced Materials**, vol. 26, nº 17, p. 2694–2698, 2014.

ZENOBI, María C; LUENGO, Carina v; AVENA, Marcelo J; RUEDA, Elsa H. An ATR-FTIR study of different phosphonic acids in aqueous solution. **Spectrochimica Acta Part A: Molecular and Biomolecular Spectroscopy**, vol. 70, nº 2, p. 270–276, 2008.

ZHANG, Weizhong; LIU, Lin; CHEN, Hongmin; HU, Kai; DELAHUNTY, Ian; GAO, Shi; XIE, Jin. Surface impact on nanoparticle-based magnetic resonance imaging contrast agents. **Theranostics**, vol. 8, nº 9, p. 2521–2548, 2018.

ZHANG, Xue; DU, Juan; WU, Dongping; LONG, Xiaoyi; WANG, Dan; XIONG, Jianhua; XIONG, Wanming; LIAO, Xiaoning. Anchoring Metallic MoS_2 Quantum Dots over MWCNTs for Highly Sensitive Detection of Postharvest Fungicide in Traditional Chinese Medicines. **ACS Omega**, vol. 6, nº 2, p. 1488–1496, 19 jan. 2021.

ZHAO, Shengzhe; YU, Xujiang; QIAN, Yuna; CHEN, Wei; SHEN, Jianliang. Multifunctional magnetic iron oxide nanoparticles: an advanced platform for cancer theranostics. **Theranostics**, vol. 10, nº 14, p. 6278–6309, 2020.

ZHELTOVA, Victoriya; VLASOVA, Anna; BOBRYSHEVA, Natalia; ABDULLIN, Ilgiz; SEMENOV, Valentin; OSMOLOWSKY, Mikhail; VOZNESENSKIY, Mikhail; OSMOLOVSKAYA, Olga. Fe_3O_4@HAp core–shell nanoparticles as MRI contrast agent: Synthesis, characterization and theoretical and experimental study of shell impact on magnetic properties. **Applied Surface Science**, vol. 531, p. 147352, 2020.

ZHENG, Xiao-Yu; ZHAO, Kai; TANG, Jinglong; WANG, Xin-Yu; LI, Lin-Dong; CHEN, Nai-Xiu; WANG, Yan-Jie; SHI, Shuo; ZHANG, Xiaodong; MALAISAMY, Sivakumar; SUN, Ling-Dong; WANG, Xiaoying; CHEN, Chunying; YAN, Chun-Hua. Gd-Dots with Strong

Ligand–Water Interaction for Ultrasensitive Magnetic Resonance Renography. **ACS Nano**, vol. 11, nº 4, p. 3642–3650, 2017.

ZHOU, Yuanzhen; CUI, Rongrong; DANG, Yuan; LI, Yang; ZOU, Yue. Doping controlled oxygen vacancies of $ZnWO_4$ as a novel and effective sensing platform for carbendazim and biomolecule. **Sensors and Actuators, B: Chemical**, vol. 296, nº 13, p. 126680, 2019.

ZHOU, Yuanzhen; LI, Yang; HAN, Ping; DANG, Yuan; ZHU, Mengyi; LI, Qian; FU, Yile. A novel low-dimensional heteroatom doped Nd_2O_3 nanostructure for enhanced electrochemical sensing of carbendazim. **New Journal of Chemistry**, vol. 43, nº 35, p. 14009–14019, 2019.

ZHOU, Zijian; ZHU, Xianglong; WU, Dongjun; CHEN, Qiaoli; HUANG, Dengtong; SUN, Chengjie; XIN, Jingyu; NI, Kaiyuan; GAO, Jinhao. Anisotropic shaped iron oxide nanostructures: Controlled synthesis and proton relaxation shortening effects. **Chemistry of Materials**, vol. 27, nº 9, p. 3505–3515, 2015.

ZHU, Chengzhou; YANG, Guohai; LI, He; DU, Dan; LIN, Yuehe. Electrochemical sensors and biosensors based on nanomaterials and nanostructures. **Analytical Chemistry**, vol. 87, n° 1, p. 230–249, 2015.

ZHU, Yun-Pei; REN, Tie-Zhen; YUAN, Zhong-Yong. Hollow cobalt phosphonate spherical hybrid as high-efficiency Fenton catalyst. **Nanoscale**, vol. 6, nº 19, p. 11395–11402, 2014.

APPENDIX A – COMPLEMENTARY DATA OF THE CHAPTER II

Figure A1 – XPS survey spectra for the samples: (A) Fe_3O_4-U, (B) H0.5, (C) H1.0 (D) U0.5 (E) U1.0 and (F) $Fe^{2+}Fe^{3+}$-DTPMP.

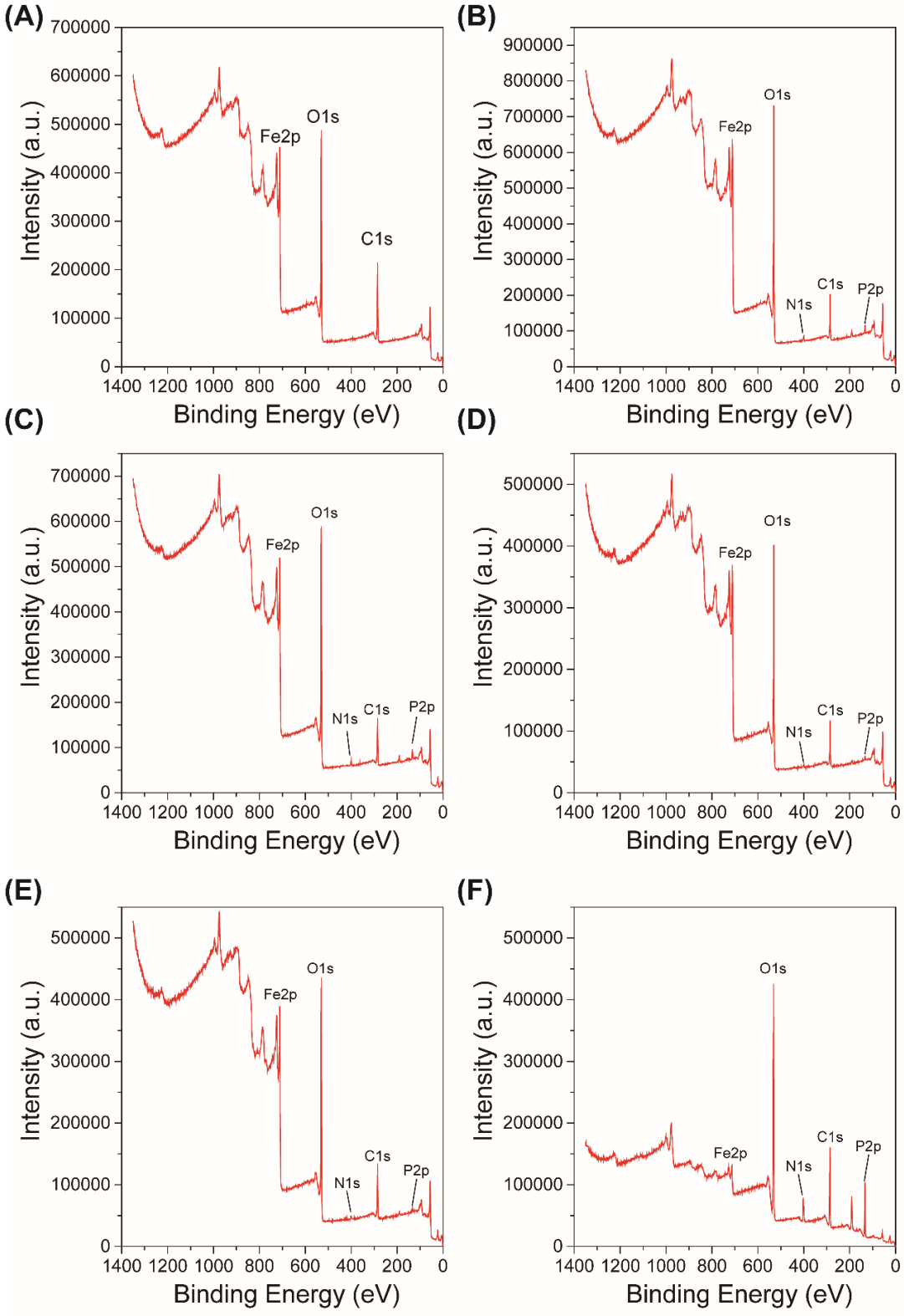

Source: author.

Figure A2 – High-resolution XPS spectra for (A) Fe2p (3/2 and 1/2), (B) just deconvoluted Fe2p 3/2 and (C) P2p.

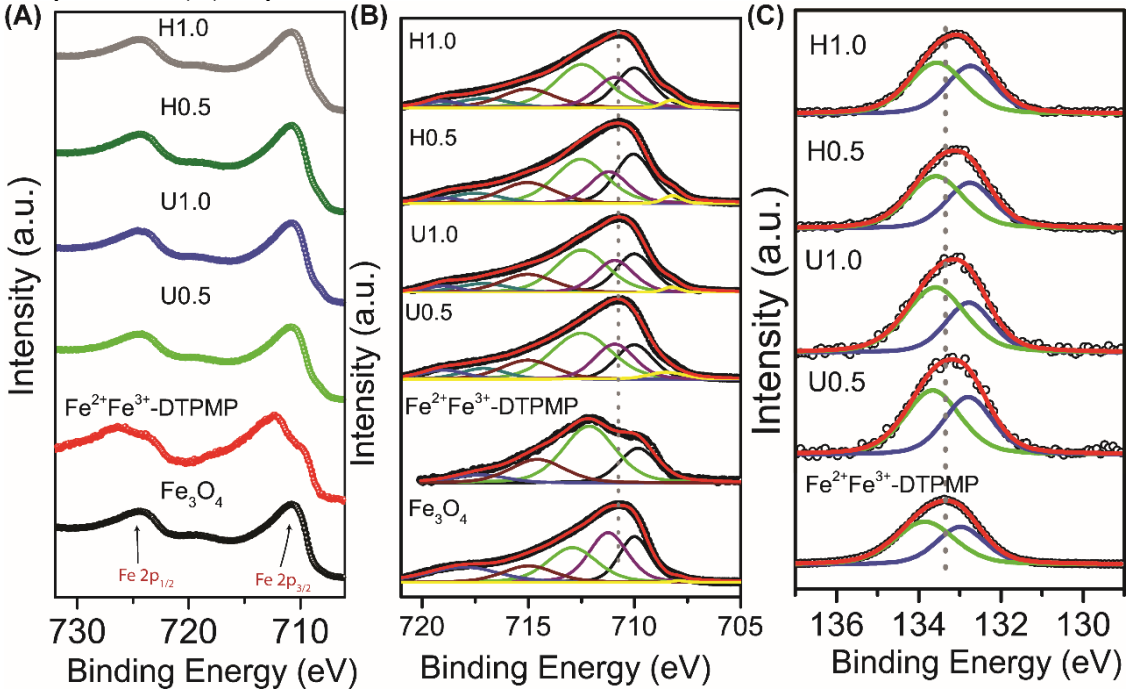

Source: author

Figure A3 – Full-range FT-IR spectra of the prepared DTPMP-coated MNPs in comparison to (A) DTPMP-Fe^{2+}-Fe^{3+} complex and (B) uncoated Fe_3O_4 NPs.

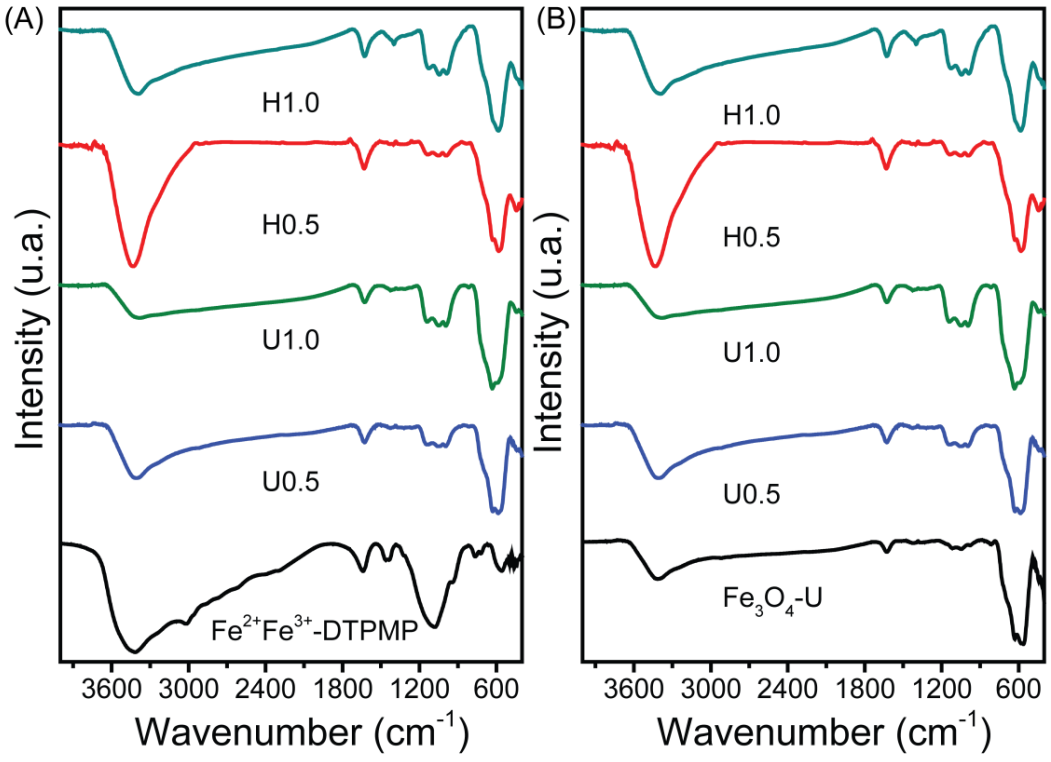

Source: author.

Table A1– Data obtained from XPS analysis.

Peak	Fe_3O_4			DTPMP-Fe^{2+}-Fe^{3+}			U0.5			U1.0			H0.5			H1.0			Attribution
	BE (eV)	A(%)	AC (%)	BE (eV)	A (%)	AC (%)	BE (eV)	A (%)	AC (%)	BE (eV)	A (%)	AC (%)	BE (eV)	A (%)	AC (%)	BE (eV)	A (%)	AC (%)	
Fe2P3/2	707.90	0.32	48.3	-	-	2.6	708.51	3.18	16.6	708.25	1.48	15.1	708.21	1.90	17.4	708.25	2.01	14.1	Fe^{3+} "pre-peak";
	709.99	21.82		709.83	21.67		710.01	16.90		710.01	21.24		710.05	24.66		710.01	21.65		Fe-DTPMP(I) and Fe^{2+}-octahedral;
	711.24	26.61		-	-		710.93	18.70		710.93	18.51		711.21	16.64		710.93	17.28		Fe^{3+}-octahedral;
	712.93	20.98		712.13	49.63		712.49	36.33		712.49	33.27		712.53	31.53		712.49	33.47		Fe-DTPMP(II) and Fe^{3+}-tetrahedral;
	714.98	13.30		714.57	21.32		715.02	13.34		715.02	14.79		715.05	15.42		715.02	15.04		Fe^{3+} surface/ Fe^{2+}satellite peak;
	718.04	16.97		717.29	7.38		717.12	6.34		717.12	7.26		717.50	7.31		717.12	7.21		satellite peak;
	-	-		-	-		719.01	5.22		719.01	3.46		718.95	2.54		719.01	3.34		satellite peak;
O1s	529.98	65.76	16.6	-	-	40.1	530.08	60.49	52.4	530.06	61.53	51.7	530.03	56.99	52.3	530.00	52.82	50.4	Fe–O of Fe_3O_4;
	531.42	22.16		531.28	71.72		531.39	29.73		531.39	28.99		531.24	37.46		531.22	40.36		Fe–OH, P–O–Fe, P=O•••Fe;
	533.40	12.08		532.84	28.28		533.94	9.78		533.93	9.48		533.72	5.54		533.57	6.82		Absorbed H_2O;
P2p	-	-		132.98	49.84	17.01	132.79	49.84	3.57	132.78	37.37	3.86	132.75	42.78	4.41	132.74	44.79	4.79	P $2p_{3/2}$;
	-	-		133.85	50.16		133.66	50.16		133.59	62.63		133.58	57.22		133.56	55.21		P $2p_{1/2}$;
C1s	-	-	35.0	-	-	31.9	-	-	26.2	-	-	27.4	-	-	23.6	-	-	27.7	-
N1s	-	-	-	399,80	35.40	8.5	399.64	64.26	1.8	399.64	61.44	1.9	399.72	67.76	2.2	399.68	68.15	3.04	R_3N^+–Fe
				402,18	64.60		401.64	35.74		401.68	38.56		401.66	32.24		401.73	31.85		R_3N^+H

BE - binding energy; A - area percentage for each component; AC – atomic percentage at the surface of NPs

Source: author

Figure A4 – DLS size distribution curves by intensity for the sample U1.0 in H_2O (blue), PB 7.4 (red) and PBS 7.4 (green).

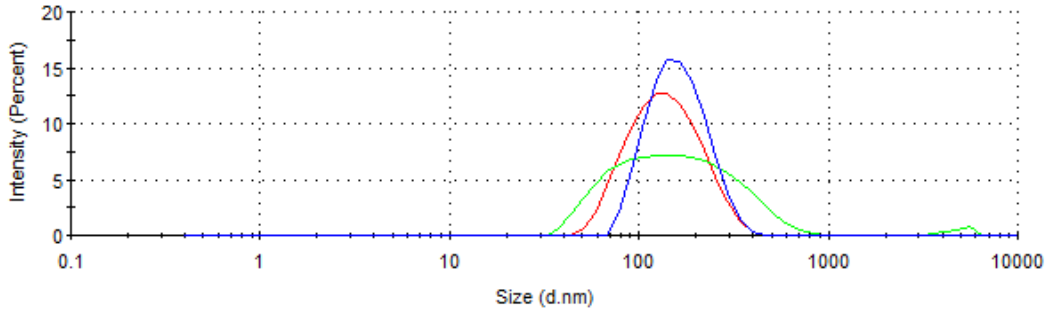

Source: author.

Figure A5 – DLS size distribution curves by intensity for the sample U0.5 in H_2O (blue), PB 7.4 (red) and PBS 7.4 (green).

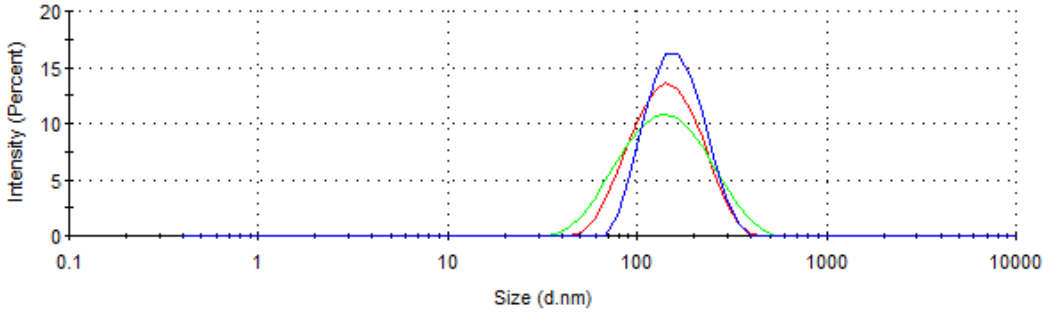

Source: author.

Figure A6 – DLS size distribution curves by intensity for the sample H1.0 in H_2O (blue), PB 7.4 (red) and PBS 7.4 (green).

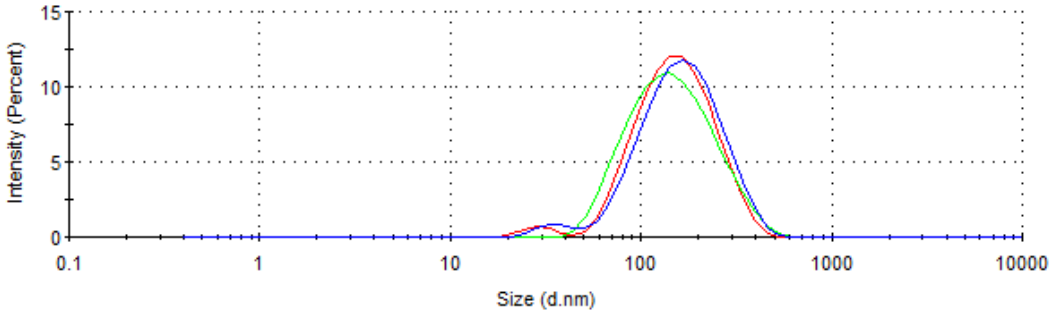

Source: author.

Figure A7 – DLS size distribution curves by intensity for the sample H1.0 in H_2O (red), PB 7.4 (green) and PBS 7.4 (blue).

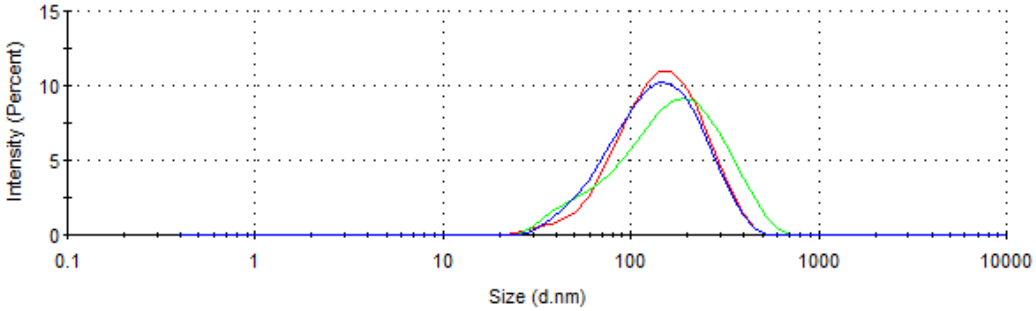

Source: author.

Figure A8 – Linear fittings of the inverse longitudinal relaxation time versus Fe concentration and r_1 relaxivity values of the samples: (A) U0.5 (B) U1.0 and (C) H0.5 and (D) H1.0.

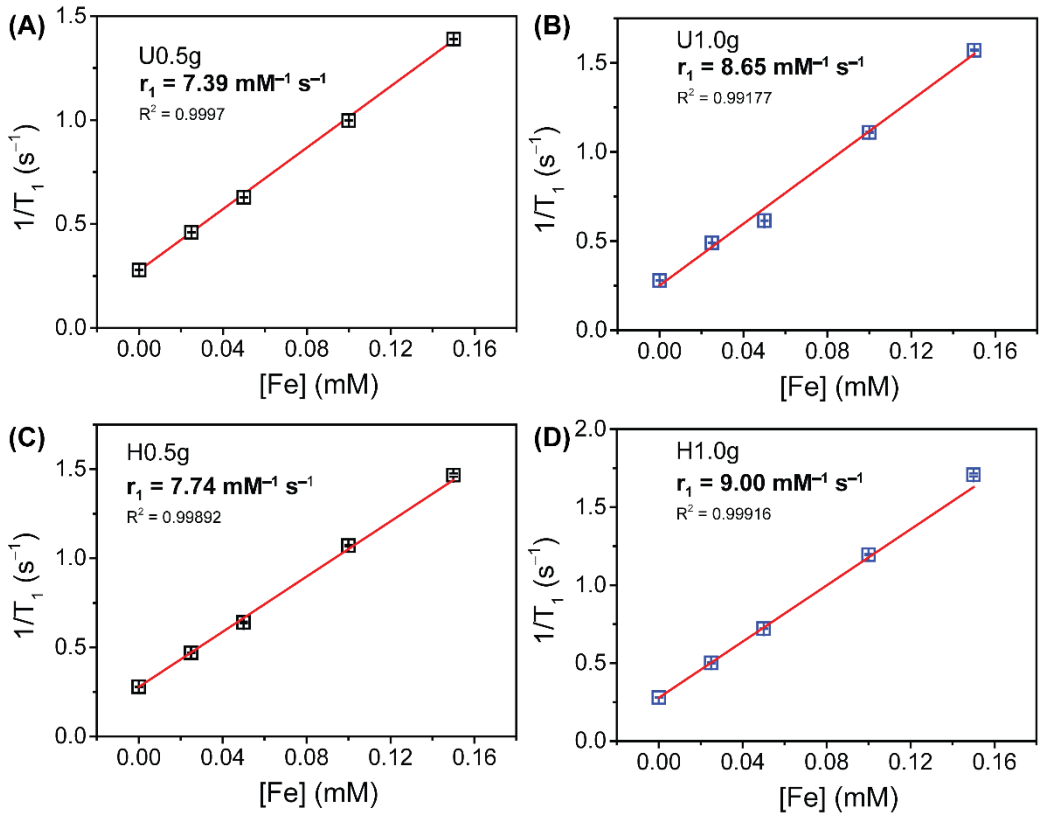

Source: author

APPENDIX B – COMPLEMENTARY DATA OF THE CHAPTER III

Figure B1 – XPS survey spectra for the MNPs synthesized in this work

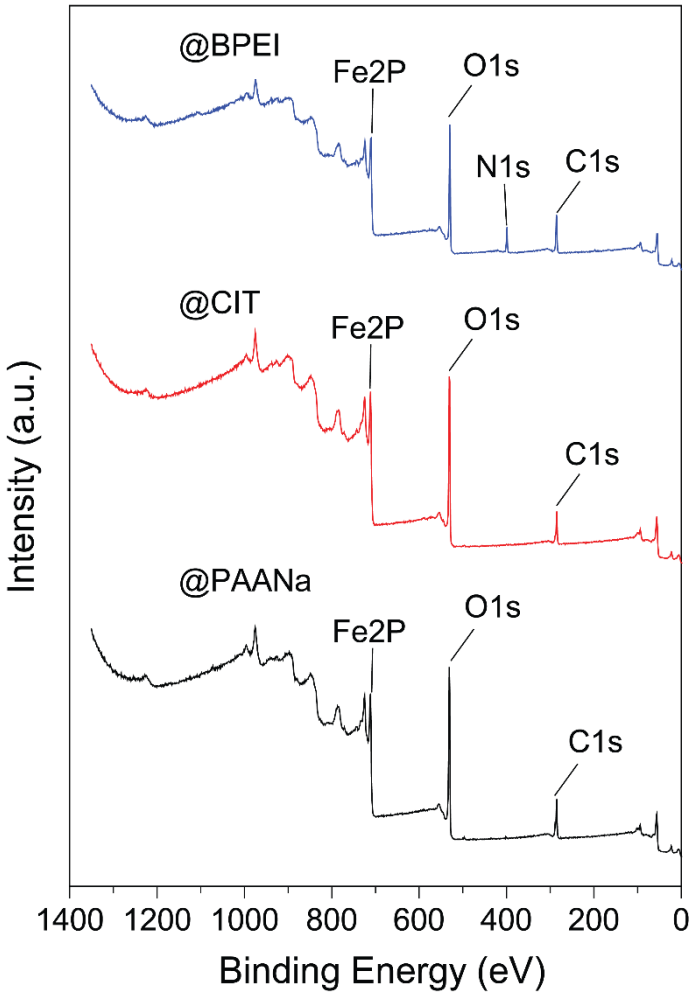

Source: author

Table B1 – Data obtained from XPS analysis.

Peak	@BPEI				@CIT				@PAANa				Assignment
	***BE* (eV)**	***A* (%)**	***AC* (%)**	**R^2**	***BE* (eV)**	***A* (%)**	***AC* (%)**	**R^2**	***BE* (eV)**	***A* (%)**	***AC* (%)**	**R^2**	
Fe2P3/2	709.98	-	12.04	-	710.78	-	14.72	-	710.78	-	14.48	-	Fe2P3/2
Fe2P1/2	723.68	-			724.38	-			724.38	-			Fe2P1/2
O1s	529.28	62.67	40.43	0.99922	530.06	54.91	56.34	0.99940	530.02	48.14	52.68	0.99919	Fe–***O*** of Fe_3O_4
	530.54	29.83			531.31	35.27			531.29	41.85			@BPEI: Fe–OH @PAANa and @CIT: Fe–**O**H, C–O and C–***O***–Fe
	533.28	5.20			533.55	7.09			533.66	7.20			@BPEI: Absorbed H_2O @PAANa and @CIT: Absorbed H_2O and C–***O***–H
	536.02	2.30			536.47	2.73			536.31	2.80			Shake-up satellites
C1s	285.35	84.92	35.32	0.99984	284.77	71.18	28.94	0.99945	284.87	72.38	32.84	0.99869	@BPEI: ***C***–N–Fe + ***C***–N; @CIT, @PAANa: ***C***–***C***
	-	-			286.45	8.43			286.53	6.49			@CIT, @PAANa: ***C***–O
	288.00	8.29			288.49	14.30			288.49	18.95			@BPEI: ***C***–N^+H_3 @CIT, @PAANa: O–***C***=O
	291.82	6.79			290.83	6.10			290.45	2.18			Shake-up satellites
N1s	399.02	85.29	12.20	0.99910	-	-	-	-	-	-	-	-	Fe–***N*** + C–***N***
	400.63	8.95											–$***N***^+H_3$
	404.20	5.76											Shake-up satellites

***BE* - binding energy; *A* - area percentage for each component; *AC* – atomic percentage at the surface of NPs**

Source: author

Figure B2 – Dependence of I_p and E_p values of $P2_a$ with (A) v and (B) $v^{0.5}$ for the CV of CBZ 9.90 µmol L^{-1} under different v (10, 25, 75, 100, 150, 200, 300, 400, 500, 600, 700, 800, 900, 1000, 1100, 1200, 1300, 1400 and 1500 mV s^{-1}). Electrolyte: BRB 0.04 mol L^{-1} pH = 3.0. Concentration of modifying agents (@BPEI): 1mg mL^{-1}. Black line in (A) is the linear regression.

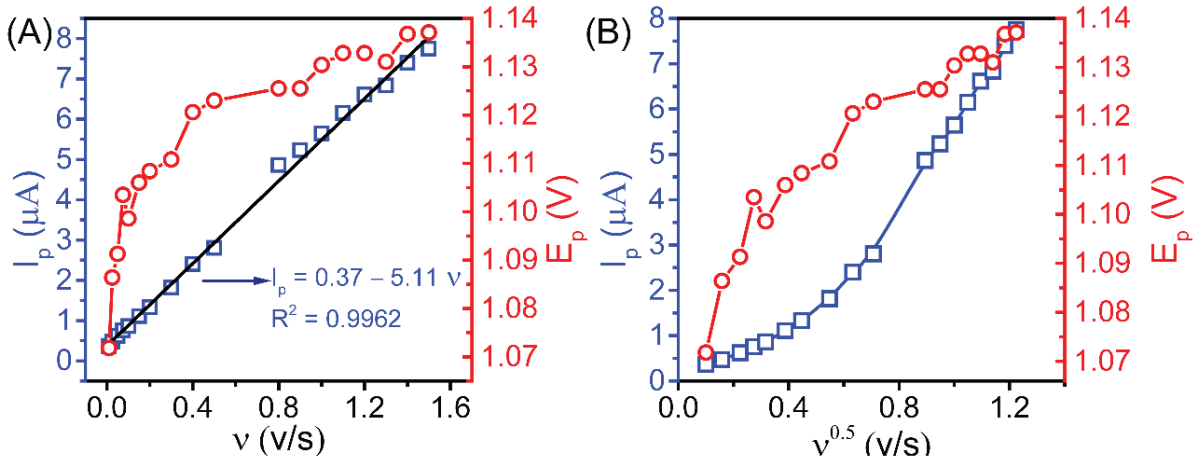

Source: author

Figure B3 – SWV in BRB 3.0 using modified GCE with @BPEI. Concentration of modifying agent (@BPEI): 1mg mL^{-1}. SWV parameters: f = 100 s^{-1}; A = 50 mV; ΔEs = 2 mV.

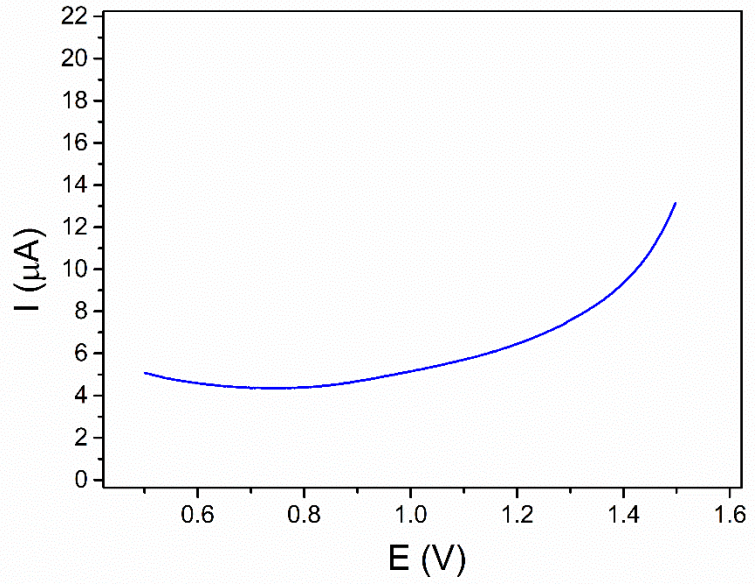

Source: author.

Figure B4 – Optimization of the pH of the electrolyte. (A) Dependence of backward peak current (I_p) and potential (E_p) with pH of the electrolyte. CBZ concentration: 9.90 µmol L^{-1}. Electrolyte: BRB 0.04 mol L^{-1} pH = 3.0, 4.0, 5.0, 7.0 and 9.0. Concentration of modifying agent (@BPEI): 1mg mL^{-1}. SWV parameters: f = 100 s^{-1}; A = 50 mV; ΔEs = 2 mV.

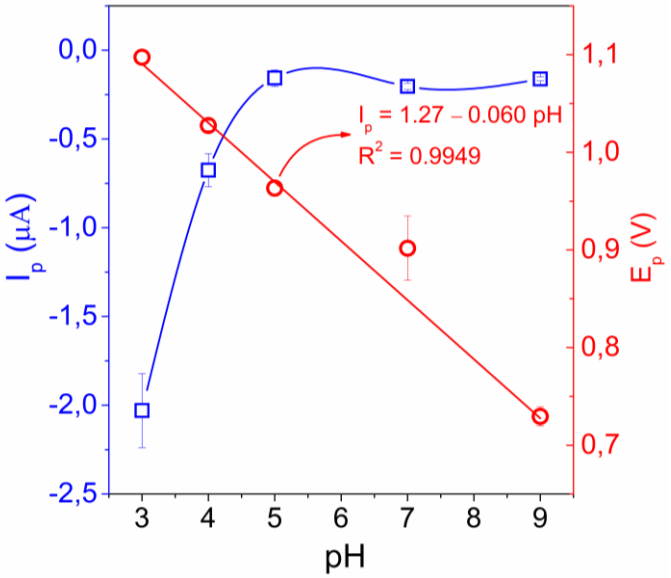

Source: author

Figure B5 – Optimization of the electrolyte at optimized pH (3.0). Mean I_p values for BRB, phosphate buffer (PO_4B) and Mcilvaine buffer (MCVB). CBZ concentration: 9.90 µmol L^{-1}. Concentration of modifying agent (@BPEI): 1mg mL^{-1}. SWV parameters: f = 100 s^{-1}; a = 50 mV; ΔEs = 2 mV.

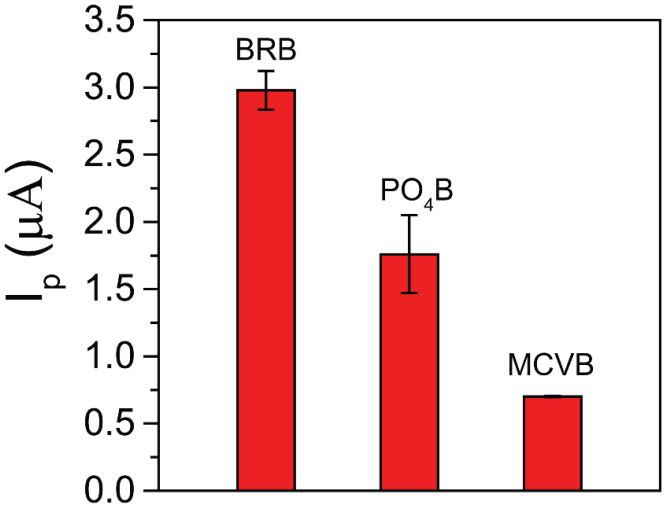

Source: author

Figure B6 – Optimization of the accumulating potential and time for SWV of CBZ 9.90 µmol L^{-1}. (A) Dependence of I_p and E_p mean values with accumulating potential, keeping constant the accumulating time of 5 s. Dependence of I_p and E_p mean values with accumulating time, keeping constant the optimized accumulating potential (0.95 V). Electrolyte: BRB 0.04 mol L^{-1} pH= 3.0. Concentration of modifying agent (@BPEI): 1mg mL^{-1}. SWV parameters: f = 100 s^{-1}; A = 50 mV; ΔEs = 2 mV.

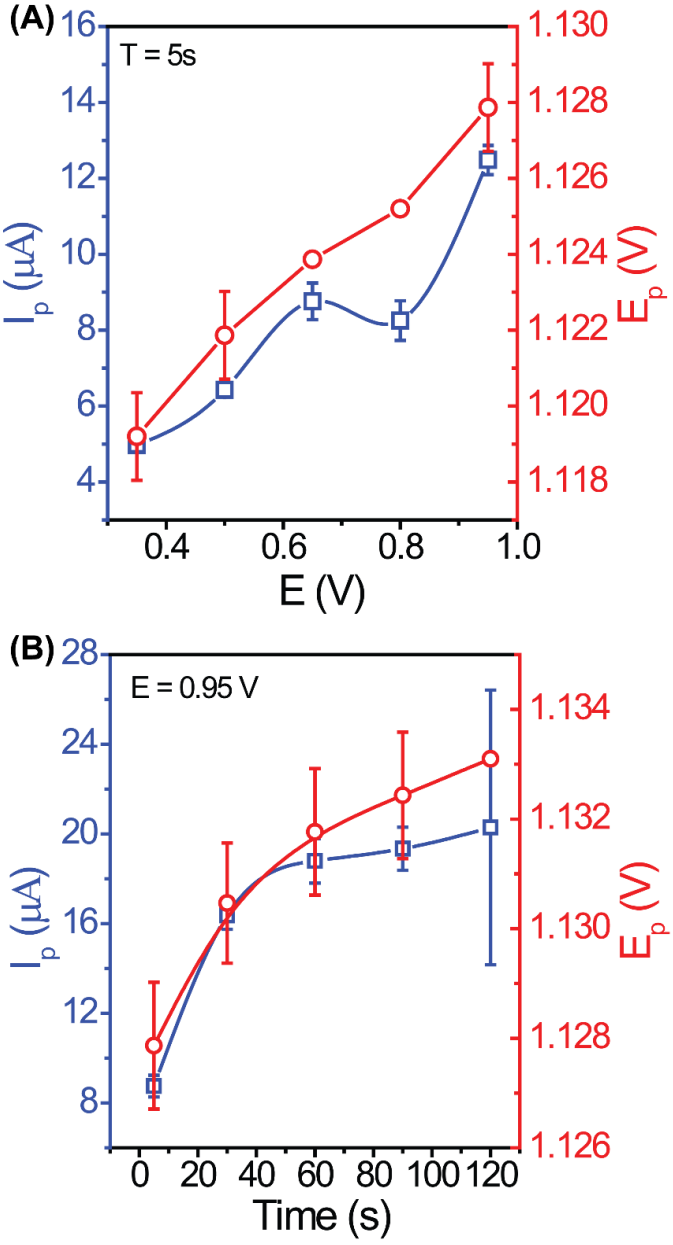

Source: author.

Figure B7 – Optimization of SWV parameters. One parameter was changed, and the two others were kept constant at theoretical values. Dependence of I_p and E_p values with (A) *f*, (B) *A* and (C) *ΔE*s. Electrolyte: BRB 0.04 mol L^{-1} pH= 3.0. Concentration of modifying agent (@BPEI): 1mg mL^{-1}. Accumulating time and potential: 60 s and 0.95 V, respectively.

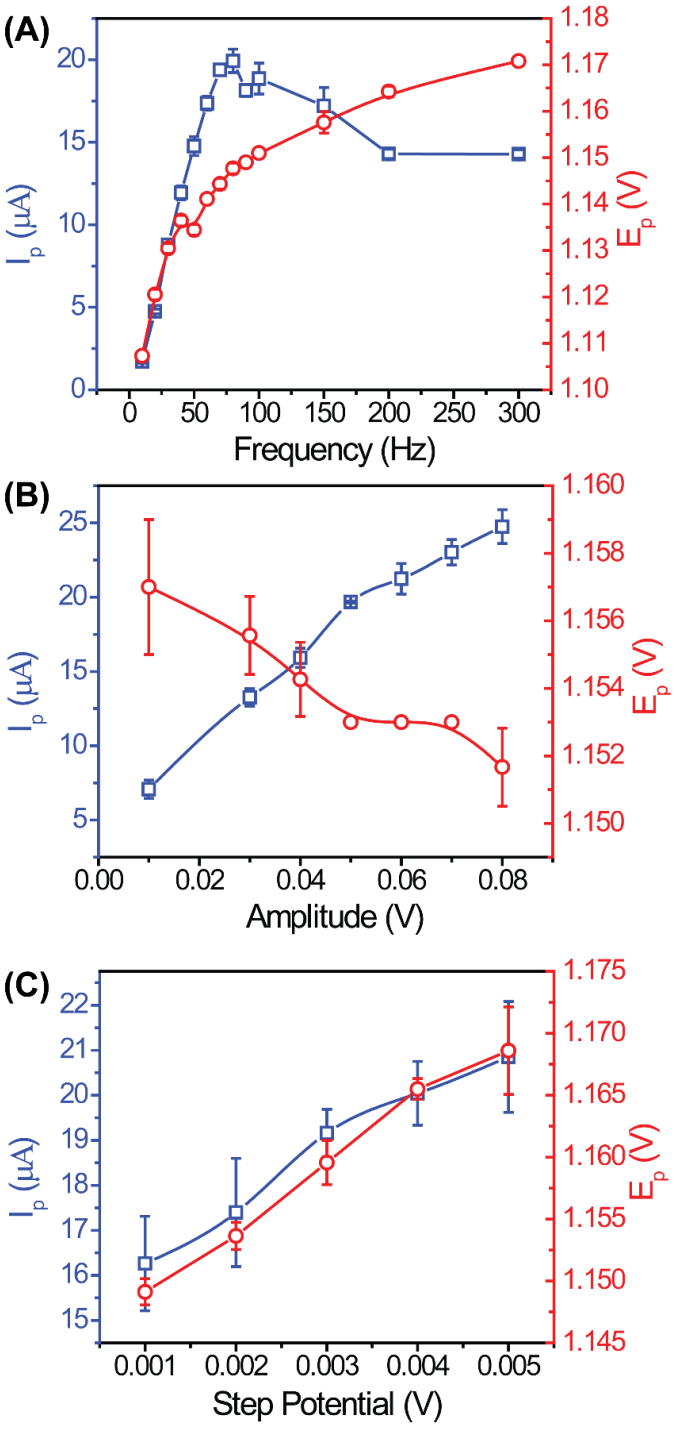

Source: author

Table B2 – Physicochemical parameters of the raw natural waters used in recovery study of CBZ using SWV.

Parameters	**Gavião**	**Acarape do meio**
Chlorophyll A (μg L^{-1})	49.02	9.29
Total Phosphorous (mg P L^{-1})	0.013	≤QL
Orthophosphate (mg P-PO_4^{-3} L^{-1})	≤ QL	≤ QL
Total Nitrogen (μg L^{-1})	0.158	0.213
Ammonia Nitrogen (mg N-NH_3 L^{-1})	≤ QL	≤ QL
NO_2^- (mg N-NO_2^- L^{-1})	≤ QL	0.008
NO_3^- (mg N-NO_3^- L^{-1})	≤ QL	≤ QL
Feofitin (μg L^{-1})	7.12	7.98

Source: author.

Figure B8 – Interference study on the oxidation of CBZ. Electrolyte: BRB 0.04 mol L^{-1} pH = 3.0. Concentration of modifying agent: 1mg mL^{-1}. Accumulating time and potential: 60 s and 0.95 V. respectively. SWV parameters: f = 70 s^{-1}; A = 50 mV; ΔEs = 2 mV. [CBZ] = 7.996 x 10^{-8} mol L^{-1}. CA: citric acid; ASA: ascorbic acid; DFC: difeconazole; IMI: imidacloprid; CHL: chlorpyrifos.

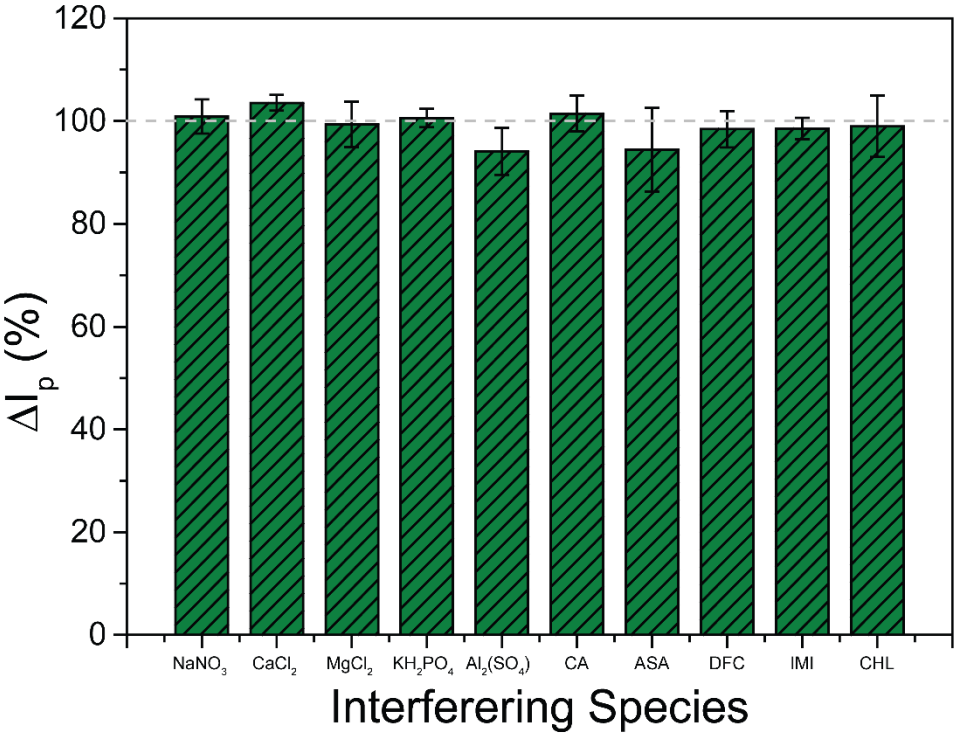

Source: author